Study on plastic pyrolysis and char smoldering for waste valorization

Ruming Pan

THÈSE

En vue de l'obtention du

DOCTORAT DE L'UNIVERSITÉ DE TOULOUSE

Délivré par :

Institut National Polytechnique de Toulouse (Toulouse INP)

Discipline ou spécialité :

Surfaces Interfaces Continentales Hydrologie

Présentée et soutenue par :

M. RUMING PAN

le mardi 26 juillet 2022

Titre :

Study on plastic pyrolysis and char smoldering for waste valorization

---

Ecole doctorale :

Sciences de l'Univers de l'Environnement et de l'Espace (SDU2E)

Unité de recherche :

Institut de Mécanique des Fluides de Toulouse (IMFT)

Directeur(s) de Thèse :

M. GERALD DEBENEST

Rapporteurs :

M. JOSE TORERO, UNIVERSITY COLLEGE LONDRES

M. VICTOR POZZOBON, UNIVERSITE PARIS-SACLAY

Membre(s) du jury :

MME GAËLLE FONTAINE, Université de Lille, Président

M. CHEN YANG, FUZHOU UNIVERSITY, Membre

M. GERALD DEBENEST, TOULOUSE INP, Membre

M. MARCIO FERREIRA MARTINS, UNIVERSITE FEDERALE ESPIRITO SANTO, Membre

M. MARCO A.B. ZANONI, National Research Council Canada, Membre

Study on plastic pyrolysis and char smoldering for waste valorization

Abstract

The European plastic production was up to 57.9 million tons in 2019, and almost half of the produced plastic becomes waste. Nearly one-quarter of plastic waste winds up in landfills. Consequently, plastic waste accumulates rapidly due to the low environmental degradability. Plastic pollution destroys ecosystems and causes harm to living creatures. Pyrolysis is considered a promising alternative to landfill disposal of plastic waste, which can simultaneously produce liquid oil similar to commercial fuels (gasoline and diesel). On the other hand, self-sustaining smoldering is increasingly popular for treating contaminated soils/sands, disposing of wastes, and realizing waste valorization. The contaminants (fuels) in the soils/sands can be destroyed by reacting with oxygen, which is a process that releases intensive heat. The smoldering heat can be used for plastic waste pyrolysis. This thesis aims to investigate the plastic waste pyrolysis driven by self-sustaining smoldering.

The pyrolysis of plastic waste is a complex chemical process. In order to better understand the pyrolysis properties of plastics, this thesis adopts different analytical methods (artificial neural network (ANN) and genetic algorithm (GA)) coupled with thermogravimetric analysis (TGA) to conduct the kinetic modeling. The findings reveal that the ANN and GA predicted thermogravimetric results are highly consistent with the experimental values. Subsequently, the

plastic waste thermal and catalytic decompositions have been conducted in a bench-scale semi-batch reactor to investigate the effects of operating parameters on the product yields. ANN-GA has also been used to establish the mathematical expressions of product yields under different conditions and optimize the conditions to obtain the highest oil yield. The pyrolysis oils under different conditions have been characterized by the Fourier-transform infrared spectroscopy (FTIR) and the gas chromatography/mass spectrometry (GC/MS). The types of oil's functional groups do not change with different operating parameters. The oils are composed of alkenes, naphthenes, alkanes, and aromatic hydrocarbons ranging from C7 to C36. The operating parameters affect the oil fractions to a great extent.

Since smoldering needs oxygen consumption whereas pyrolysis demands oxygen-free, the smoldering-driven pyrolysis reactor should be ex-situ. Due to the lack of applications of ex-situ smoldering for plastic waste pyrolysis, this thesis develops different dimensional numerical models for the smoldering-driven pyrolysis reactor. A one-dimensional (1D) smoldering model is coupled with a two-dimensional (2D) pyrolysis model to investigate the smoldering-driven pyrolysis of plastic waste. It is noteworthy that the boundary heat flux for the 1D smoldering model is determined by the global heat loss coefficient, which is calculated based on experimental data. Determining the global heat loss coefficient makes it challenging for the 1D smoldering model to conduct simulations of different reactor sizes. To improve the robustness of the smoldering-driven pyrolysis model, this thesis establishes a novel 2D pyrolysis coupled with a 2D smoldering model to address the benefits of a multi-dimensional analysis compared to the 1D smoldering approach. Moreover, a sensitivity analysis has been conducted to

investigate the effects of several parameters that can affect smoldering and pyrolysis processes. The developed model aims to provide a general design tool for the smoldering-driven pyrolysis reactor's performance, evaluation, and optimization.

Keywords: Plastic waste, pyrolysis, kinetic modeling, oil production, self-sustaining smoldering, multidimensional modeling.

Etude sur la pyrolyse du plastique et la combustion lente pour la valorisation des déchets

Résumé

La production européenne de plastique a atteint 57.9 millions de tonnes en 2019, et près de la moitié du plastique produit devient un déchet. Près d'un quart des déchets plastiques finissent dans des décharges. Par conséquent, les déchets plastiques s'accumulent rapidement en raison, majoritairement, de leur faible dégradabilité environnementale. Pourtant, la pollution plastique est préjudiciable pour les écosystèmes et nuit aux êtres vivants. Il est donc nécessaire de traiter ces déchets afin de limiter leurs impacts environnementaux.

La pyrolyse est considérée comme une alternative prometteuse à l'enfouissement des déchets plastiques, qui peut simultanément produire de l'huile liquide similaire à des carburants commerciaux (essence et diesel). D'autre part, la combustion lente autonome ou « smoldering » est de plus en plus populaire pour traiter les sols/sables contaminés, éliminer les déchets et permettre la valorisation des déchets. Les contaminants organiques (donc combustibles) dans les sols/sables peuvent être détruits en réagissant avec l'oxygène. C'est un processus qui libère une chaleur importante et qui permet dans premier temps d'entretenir le phénomène. La chaleur peut aussi être utilisée pour la permettre la pyrolyse des déchets plastiques. Cette thèse vise, en particulier, à étudier la pyrolyse des déchets plastiques générée par la combustion lente auto-entretenue ou « smoldering ».

La pyrolyse des déchets plastiques est un processus chimique complexe. Afin de mieux comprendre les phénomènes de pyrolyse des plastiques, cette thèse adopte différentes méthodes analytiques i.e. réseau de neurones artificiels (ANN) et algorithme génétique (GA), couplées à l'analyse thermogravimétrique (TGA) pour permettre la détermination de modèles de décomposition cinétique. Les résultats révèlent que les résultats thermogravimétriques prédits par ANN et GA sont très cohérents avec les valeurs expérimentales.

Par la suite, les décompositions thermique et catalytique des déchets plastiques ont été menées dans un réacteur semi-batch à petite échelle pour étudier les effets des paramètres opératoires sur les rendements en produits. Nous avons couplé l'ANN et le GA pour établir les expressions mathématiques des rendements de produits dans diverses conditions opératoires. Cela a permis d'obtenir l'optimum de la production en huile pour une condition opératoire fixée. Les huiles de pyrolyse obtenues ont été caractérisées par spectroscopie infrarouge à transformée de Fourier (notée FTIR) et la chromatographie en phase gazeuse/spectrométrie de masse (GC/MS). On a démontré que les types de groupes fonctionnels de l'huile ne changent pas avec les différents paramètres opératoires. Ainsi, on a pu déterminer que les huiles sont composées d'alcènes, de naphtènes, d'alcanes et d'hydrocarbures aromatiques allant de C7 à C36. Par contre, il convient de noter que les paramètres opératoires affectent, dans une large mesure, les fractions d'huile.

Étant donné que la combustion lente nécessite une consommation d'oxygène, si l'on veut utiliser l'énergie produite par la combustion pour alimenter le réacteur de pyrolyse, la combustion lente doit être ex-situ. En raison du manque d'applications de la combustion ex-situ

pour la pyrolyse des déchets plastiques, cette thèse développe différentes approches numériques dimensionnels pour le étudier la réponse du réacteur de pyrolyse alimenté énergétiquement par la combustion lente.

Un modèle de combustion lente unidimensionnel (1D) est couplé à un modèle de pyrolyse bidimensionnel (2D). Cela permet d'étudier la pyrolyse des déchets plastiques induite par la combustion lente. Il convient de noter que le flux de chaleur limite pour le modèle de combustion lente 1D, permettant la propagation du processus de dégradation, est déterminé par le coefficient global de perte de chaleur, lui-même estimé via une base de données expérimentales.

La détermination de ce coefficient global de perte de chaleur complique la tâche du modèle de combustion lente 1D pour effectuer des simulations de diverses tailles de réacteurs. Afin d' améliorer la robustesse du modèle de pyrolyse entrainé par la combustion lente, on a développé un modèle 2D de pyrolyse couplé à un modèle 2D de combustion lente. Ceci a pour avantage de rendre plus « physique » le modèle au regard de l'approche moyenne 1D présentée auparavant. Une analyse de sensibilité a été menée pour étudier les effets de plusieurs paramètres pouvant affecter les processus de combustion lente et de pyrolyse. Le modèle développé vise à fournir un outil de conception général pour évaluer les performances de ces deux réacteurs couplés mais aussi permettre, à terme, d'optimiser ce processus.

Mots clés: Déchets plastiques, pyrolyse, modélisation cinétique, production d'huile issue de déchets, combustion lente auto-entretenue, modélisation physique.

Publications

Published:

[1] Pan, R., Debenest, G. and Zanoni, M.A., 2022. Numerical study of plastic waste pyrolysis driven by char smoldering. Process Safety and Environmental Protection, 165, pp.46-56.

[2] Pan, R. and Debenest, G., 2022. A robust model of smoldering-driven pyrolysis reactor–Part 1: Thermal performance evaluation. Fuel, 320, p.123935.

[3] Pan, R., Debenest, G. and Zanoni, M.A., 2022. A robust two-dimensional model for the pyrolysis of plastic waste driven by self-sustaining smoldering. Process Safety and Environmental Protection, 162, pp.610-619.

[4] Pan, R. and Debenest, G., 2022. Numerical investigation of a novel smoldering-driven reactor for plastic waste pyrolysis. Energy Conversion and Management, 257, p.115439.

[5] Pan, R., Zan, Y. and Debenest, G., 2022. Oil production from waste polyethylene and polystyrene co-pyrolysis: Interactions of temperature and carrier gas flow rate. Journal of Environmental Chemical Engineering, 10(3), p.107555.

[6] Pan, R., Martins, M.F. and Debenest, G., 2022. Optimization of oil production through ex-situ catalytic pyrolysis of waste polyethylene with activated carbon. Energy, 248, p.123514.

[7] Pan, R., Duque, J.V.F. and Debenest, G., 2022. Waste Plastic Thermal Pyrolysis Analysis by a Neural Fuzzy Model Coupled with a Genetic Algorithm. Waste and Biomass Valorization, 13(1), pp.135-148.

[8] Pan, R., Martins, M.F. and Debenest, G., 2021. Pyrolysis of waste polyethylene in a semi-batch reactor to produce liquid fuel: optimization of operating conditions. Energy Conversion and Management, 237, p.114114.

[9] Pan, R., Duque, J.V.F. and Debenest, G., 2021. Investigating waste plastic pyrolysis kinetic parameters by genetic algorithm coupled with thermogravimetric analysis. Waste and Biomass Valorization, 12(5), pp.2623-2637.

[10] Pan, R., Duque, J.V.F., Martins, M.F. and Debenest, G., 2020. Application of a neural fuzzy model combined with simulated annealing algorithm to predict optimal conditions for polyethylene waste non-isothermal pyrolysis. Heliyon, 6(11), p.e05598.

Contents

List of Figures

List of Tables

Chapter 1

Introduction

1.1. Plastic crisis and sand/soil contamination

1.1.1. Plastic crisis

The production of plastic has grown promptly from 1.5 million tons in 1950 to 368 million tons in 2019 [1]. European plastic production was up to 57.9 million tons in 2019 [1], and almost half of the produced plastic became waste [2]. There are three ways to dispose of plastic waste, i.e., incineration, recycling, and landfilling (Fig. 1.1). The incineration of plastic waste can generate heat, providing energy for power plants. Note that burning plastic waste produces large amounts of greenhouse gases, and the fumes are also toxic. Therefore, the generated flue gas should be appropriately handled. It is noteworthy that nearly 25% of plastic waste winds up in landfills. Consequently, plastic waste accumulates rapidly due to the low environmental degradability.

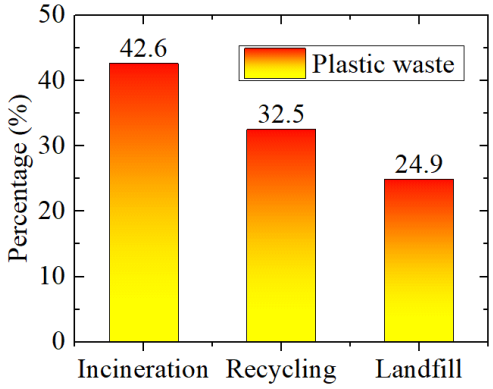

Fig. 1.1. Disposal paths for plastic waste.

Fig. 1.2 shows that the most in-demand plastic in Europe is polyethylene (PE), which accounts for 30.3% of the total demand for plastics [3]. Polypropylene (PP) accounts for 19.7% and is the second in-demand plastic-type. The remaining plastic types are all less than 10% in demand, e.g., polyvinyl chloride (PVC) for 9.6%, polyethylene terephthalate (PET) for 8.4%, polyurethane (PUR) for 7.8%, and polystyrene (PS) for 6.1%. PE is the most significant amount of plastic found in municipal solid waste (MSW) [4], which is not surprising due to the tremendous demand for PE. Plastic pollution destroys ecosystems [5] and causes harm to living creatures [6]. Therefore, there is an urgent need to find a suitable way to deal with plastic waste.

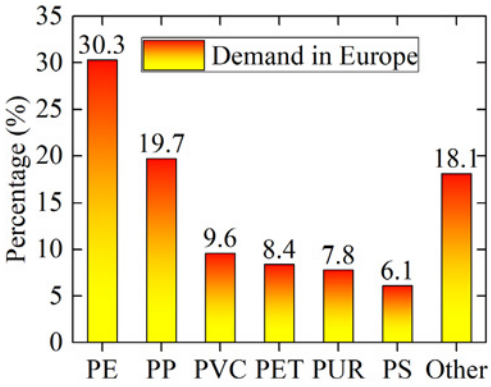

Fig. 1.2. Demand for different types of plastics in Europe.

1.1.2. Sand/soil contamination

The sand/soil is being contaminated by man-made influences. A recent accident is the Peru oil spill caused by a volcanic eruption in Tonga in 2022 (Fig. 1.3) [7]. The spilled crude oil pollutes the ocean, directly harming birds and fish, and inhibiting algae growth by reducing sunlight in the ocean. The leaked oil has also polluted the sand/soil. Plants that grow on oil-

contaminated sand/soil and organisms that live in the area are at significant risk of their survival. Per- and polyfluoroalkyl substance (PFAS) is another one of the main sources of sand/soil pollution due to its widespread use and low degradation in the environment [8]. The sand/soil contamination can cause irreversible damage to animals, plants, and humans. Consequently, the contaminated sand/soil remediation needs to find a suitable method.

Fig. 1.3. Peru oil spill in 2022.

1.2. Pyrolysis of plastic waste and contaminated sand/soil remediation by smoldering

1.2.1. Pyrolysis of plastic waste

Pyrolysis is considered a promising alternative to landfill disposal of plastic waste, which can simultaneously produce liquid oil similar to commercial fuels (gasoline and diesel) [9]. The long-chain polymers can be decomposed into short-chain hydrocarbons in the temperature range of 400–800 °C [10]. The pyrolysis can be conducted in different reactors, such as fixed bed (e.g., batch, semi-batch, kiln, drop-type, etc.) and fluidized bed [11]. The lab-scale reactors are heated indirectly by electric heating coils to reach and maintain the target temperature [12]. This makes pyrolysis a high energy-consuming process [13].

1.2.2. Contaminated sand/soil remediation by smoldering

Smoldering is flameless combustion that occurs in a porous medium, allowing sufficient oxygen diffusion [14]. Smoldering can self-sustain when the heat production rate exceeds the heat loss rate [15]. Self-sustaining smoldering is increasingly popular for treating contaminated sand/soil [8], disposing of wastes [16], and realizing waste valorization [17]. The contaminants (fuels) (e.g., char [18], bitumen [19], peat moss [20], oil [21]) in the sand/soil can be destroyed by reacting with oxygen, which is a process that releases intensive heat. The smoldering heat can be used for waste disposal and valorization [22].

1.2.3. Plastic waste pyrolysis driven by smoldering

In order to provide a more economical heat source than electricity for waste pyrolysis, Duque et al. [13] proposed a pyrolysis reactor driven by self-sustaining smoldering. This reactor has two independent chambers: the outside is a char smoldering chamber, and the inside is a semi-batch reactor. The smoldering heat is transferred to the waste treatment chamber through the boundary between the two chambers. They confirmed that char smoldering could provide enough energy for self-sustaining propagation and pyrolysis. The smoldering-driven pyrolysis reactor can be used for contaminated sand remediation (in the smoldering chamber) and plastic waste valorization (in the pyrolysis chamber).

1.3. Problems to be explored in plastic waste pyrolysis and contaminated sand/soil smoldering

1.3.1. Kinetic modeling of plastic waste pyrolysis

Plastic waste pyrolysis is a complex multistep chemical reaction, which makes it

challenging to determine the kinetic parameters (e.g., activation energy E, pre-exponential factor A and the reaction order n, etc.) of plastic waste pyrolysis. Moreover, the plastic waste pyrolysis reaction kinetic parameters are not determined simultaneously in the traditional calculation method [23][24][25][26]. For instance, the calculation of pre-exponential factor is based on the calculated activation energy. The reaction model also needs to be determined by the Coats-Redfern [23][24] or Criado methods [25]. The reaction model candidates are the representative ones, such as Power-law, Contracting geometry, Prout–Tompkins, etc. [26]. Therefore, it is necessary to explore the different methods to conduct the kinetic modeling.

1.3.2. Oil production from plastic waste pyrolysis

Pyrolysis or thermal decomposition is a promising technology to convert plastic waste into value-added fuels [27], in the form of wide product distribution, such as oil (gasoline and diesel) and gas (ethane and propane) [28]. The pyrolysis conversion is sensible to the operating parameters such as temperature, residence time, and carrier gas flow rate. Plenty of research efforts are devoted to determining the maximum pyrolysis oil production. However, most studies were conducted by adopting the One-Factor-at-a-time statistical design [29][30], which is a technique that does not capture the effects of variables interactions that are necessary to avoid misleading conclusions [31]. For this reason, we must implement a statistical technique that allows a robust parameters combination.

1.3.3. Plastic waste pyrolysis driven by contaminated sand/soil smoldering

The smoldering reactor for waste treatment can be classified as in-situ and ex-situ types. The in-situ reactor refers to the smoldering and waste treatment occurring in the same chamber.

In many cases, the waste can be combusted with oxygen to provide sufficient heat for self-sustaining smoldering [32][33]. However, it is necessary to add fuel to the reactor to increase the heat generated by smoldering to avoid quenching if the waste solely combustion does not generate enough heat [34][35]. On the other hand, the ex-situ reactor refers to the smoldering and waste treatment occurring in two chambers [13]. The smoldering heat is transferred to the waste treatment chamber through the boundary between the two chambers.

Since smoldering needs oxygen consumption whereas pyrolysis demands oxygen-free, the smoldering-driven pyrolysis reactor should be of the ex-situ type. However, most smoldering studies are performed in-situ, and only a few focus on the ex-situ applications [13][16][22]. Moreover, the numerical study of the smoldering-driven pyrolysis reactor for plastic waste pyrolysis and contaminated sand/soil remediation remains vacant to the best of our knowledge.

1.4. Thesis goals

This thesis aims to explore the plastic waste pyrolysis driven by contaminated sand smoldering. Polyethylene (PE) is the first-most component in plastic waste due to its wide range of uses. Therefore, waste polyethylene (WPE) has been chosen to study the pyrolysis behavior of plastic waste. Moreover, the contaminated sand is replaced with a mixture of char and sand to simplify. The thesis goals can be condensed as follows.

The decomposition of plastic waste is a complex chemical behavior. The pyrolysis kinetic parameters are determined by the genetic algorithm (GA) coupled with thermogravimetric analysis (TGA) using three representative reaction models. Moreover, the artificial neural network (ANN) coupled with GA is adopted to determine the optimal operating conditions over

different temperature ranges to understand WPE pyrolysis better.

The WPE pyrolysis oil is an alternative to commercial fuels. The operating conditions (temperature, residence time, and carrier gas flow rate) have complex interactive effects on oil production. The ANN coupled with GA is used to maximize the oil yield in a bench-scale semi-batch reactor. Moreover, the WPE catalytic pyrolysis is investigated to improve the quality of the pyrolysis oil.

The two multidimensional models have been developed to simulate the smoldering-driven pyrolysis reactor for the WPE pyrolysis and contaminated sand remediation. The models developed in the present thesis aim to provide general design tools for the performance, evaluation, and optimization of the smoldering-driven pyrolysis reactor.

1.5. Thesis outline

This thesis is arranged in "Integrated Article Format." Chapters 2, 3, 4, 5, 6, and 7 are based on six published/submitted papers. The contents of each chapter can be outlined as follows.

The title of Chapter 2 is "Investigating plastic waste pyrolysis kinetic parameters by genetic algorithm coupled with thermogravimetric analysis." This chapter evaluates pure PE and WPE pyrolysis kinetic parameters using GA and isoconversional methods coupled with TGA, respectively. Additionally, three representative reaction models, i.e., reaction-order, extended Prout–Tompkins, and Sestak–Berggren models, are investigated for obtaining the most suitable model, which could describe the PE and WPE pyrolysis processes more accurately. This chapter has been published in Waste and Biomass Valorization (DOI: 10.1007/s12649-020-01181-4).

The title of Chapter 3 is "Plastic waste thermal pyrolysis analysis by an artificial neural

network coupled with a genetic algorithm." This chapter investigates the process temperature, plastic waste conversion, and pyrolysis rate to guide the industrial applications of plastic waste pyrolysis. The ANN coupled with GA is adopted to determine the optimal operating conditions over different temperature ranges. This chapter has been published in Waste and Biomass Valorization (DOI: 10.1007/s12649-021-01522-x).

The title of Chapter 4 is "Pyrolysis of waste polyethylene in a semi-batch reactor to produce liquid fuel: Optimization of operating conditions." This chapter investigates the interactive effects of temperature, residence time, and carrier gas flow rate on oil production through WPE thermal pyrolysis in a bench-scale semi-batch reactor. The ANN coupled with GA optimizes operating conditions to maximize oil production. The oil sample obtained under the optimal operating conditions is analyzed by Fourier-transform infrared spectroscopy (FTIR) and gas chromatography-mass spectrometry (GC–MS). This chapter has been published in Energy Conversion and Management (DOI: 10.1016/j.enconman.2021.114114).

The title of Chapter 5 is "Optimization of oil production through ex-situ catalytic pyrolysis of waste polyethylene with activated carbon." This chapter studies the ex-situ catalytic pyrolysis of WPE with activated carbon (AC). ANN coupled with GA is used to establish the mathematical expressions of oil and gas yields under different conditions and optimize the conditions to obtain the highest oil yield. The WPE-AC catalytic pyrolysis oils under different conditions are characterized by FTIR and GC–MS. This chapter has been published in Energy (DOI: 10.1016/j.energy.2022.123514).

The title of Chapter 6 is "Numerical study of plastic waste pyrolysis driven by char smoldering." This chapter develops a multidimensional model for a novel smoldering-driven reactor for the pyrolysis of plastic waste: one-dimensional (1D) for the smoldering chamber and two-dimensional (2D) for the pyrolysis chamber. This chapter has been published in Process Safety and Environmental Protection (DOI: 10.1016/j.psep.2022.06.060).

The title of Chapter 7 is "A robust two-dimensional model for the pyrolysis of plastic waste driven by self-sustaining smoldering." This chapter establishes a novel 2D pyrolysis coupled with a 2D smoldering model to address the benefits of a multidimensional analysis compared to the 1D smoldering approach. The smoldering and pyrolysis chambers are separated by a thin layer of 2 mm stainless steel, of which the boundary heat transfer is calculated using the thermally thick approximation. Moreover, a sensitivity analysis was conducted to investigate the effects of several parameters that can affect smoldering and pyrolysis processes. This chapter has been published in Process Safety and Environmental Protection (DOI: 10.1016/j.psep.2022.04.038).

Bibliography

[1] Plastics - the Facts 2020. PlasticsEurope (2020).

[2] Karayılan, S., Yılmaz, Ö., Uysal, Ç. and Naneci, S., 2021. Prospective evaluation of circular economy practices within plastic packaging value chain through optimization of life cycle impacts and circularity. Resources, Conservation and Recycling, 173, p.105691.

[3] Plastics - the Facts 2021. PlasticsEurope (2021).

[4] Sharuddin, S.D.A., Abnisa, F., Daud, W.M.A.W. and Aroua, M.K., 2016. A review on pyrolysis of plastic wastes. Energy conversion and management, 115, pp.308-326.

[5] Zhao, S., Wang, C., Bai, B., Jin, H. and Wei, W., 2022. Study on the polystyrene plastic degradation in supercritical water/CO2 mixed environment and carbon fixation of polystyrene plastic in CO2 environment. Journal of Hazardous Materials, 421, p.126763.

[6] Ellis, L.D., Rorrer, N.A., Sullivan, K.P., Otto, M., McGeehan, J.E., Román-Leshkov, Y., Wierckx, N. and Beckham, G.T., 2021. Chemical and biological catalysis for plastics recycling and upcycling. Nature Catalysis, 4(7), pp.539-556.

[7] https://www.ndtv.com/world-news/volcanic-eruption-in-tonga-blamed-for-an-peru-oil-spill-11-000-km-away-2716360

[8] Duchesne, A.L., Brown, J.K., Patch, D.J., Major, D., Weber, K.P. and Gerhard, J.I., 2020. Remediation of PFAS-contaminated soil and granular activated carbon by smoldering combustion. Environmental Science & Technology, 54(19), pp.12631-12640.

[9] Al-Salem, S.M., Chandrasekaran, S.R., Dutta, A. and Sharma, B.K., 2021. Study of the fuel properties of extracted oils obtained from low and linear low density polyethylene pyrolysis.

Fuel, 304, p.121396.

[10] Gala, A., Catalan-Martinez, D., Guerrero, M. and Serra, J.M., 2021. Simulation-assisted design of a catalytic hydrogenation reactor for plastic pyrolysis fuels. Fuel, 287, p.119400.

[11] Wang, Z., Burra, K.G., Lei, T. and Gupta, A.K., 2021. Co-pyrolysis of waste plastic and solid biomass for synergistic production of biofuels and chemicals-A review. Progress in Energy and Combustion Science, 84, p.100899.

[12] Park, H.J., Park, Y.K., Dong, J.I., Jeon, J.K., Yim, J.H. and Jeong, K.E., 2008. Catalytic degradation of polyethylene over ferrierite. Research on Chemical Intermediates, 34(8), pp.727-735.

[13] Duque, J.V.F., Bittencourt, F.L., Martins, M.F. and Debenest, G., 2021. Developing a combustion-driven reactor for waste conversion. Energy, 237, p.121489.

[14] Torero, J.L., Gerhard, J.I., Martins, M.F., Zanoni, M.A., Rashwan, T.L. and Brown, J.K., 2020. Processes defining smouldering combustion: Integrated review and synthesis. Progress in Energy and Combustion Science, 81, p.100869.

[15] Wang, Z., Liu, N., Yuan, H., Chen, H., Xie, X., Zhang, L. and Rein, G., 2022. Smouldering and its transition to flaming combustion of polyurethane foam: An experimental study. Fuel, 309, p.122249.

[16] Bittencourt, F.L.F., Martins, M.F., Orlando, M.T.D. and Galvão, E.S., 2022. The proof-of-concept of a novel feces destroyer latrine. Journal of Environmental Chemical Engineering, 10(1), p.106827.

[17] Sun, Y., Bai, F., Liu, B., Liu, Y., Guo, M., Guo, W., Wang, Q., Lü, X., Yang, F. and Yang,

Y., 2014. Characterization of the oil shale products derived via topochemical reaction method. Fuel, 115, pp.338-346.

[18] Zanoni, M.A., Wang, J. and Gerhard, J.I., 2021. Understanding pressure changes in smouldering thermal porous media reactors. Chemical Engineering Journal, 412, p.128642.

[19] Zanoni, M.A., Torero, J.L. and Gerhard, J.I., 2019. Delineating and explaining the limits of self-sustained smouldering combustion. Combustion and Flame, 201, pp.78-92.

[20] Chen, H., Rein, G. and Liu, N., 2015. Numerical investigation of downward smoldering combustion in an organic soil column. International Journal of Heat and Mass Transfer, 84, pp.253-261.

[21] Kinsman, L., Torero, J.L. and Gerhard, J.I., 2017. Organic liquid mobility induced by smoldering remediation. Journal of Hazardous materials, 325, pp.101-112.

[22] Duque, J.V.F., Martins, M.F., Bittencourt, F.L. and Debenest, G., 2021. Relevant aspects of propagating a combustion front in an annular reactor for out-of-bed heat recovery. Experimental Thermal and Fluid Science, p.110575.

[23] Coats, A.W. and Redfern, J.P., 1964. Kinetic parameters from thermogravimetric data. Nature, 201(4914), pp.68-69.

[24] Yang, K.K., Wang, X.L., Wang, Y.Z., Wu, B., Jin, Y.D. and Yang, B., 2003. Kinetics of thermal degradation and thermal oxidative degradation of poly (p-dioxanone). European polymer journal, 39(8), pp.1567-1574.

[25] Criado, J.M., 1978. Kinetic analysis of DTG data from master curves. Thermochimica Acta, 24(1), pp.186-189.

[26] Duque, J.V.F., Martins, M.F., Debenest, G. and Orlando, M.T.D.A., 2020. The influence of the recycling stress history on LDPE waste pyrolysis. Polymer Testing, 86, p.106460.

[27] Fox, J.A. and Stacey, N.T., 2019. Process targeting: An energy based comparison of waste plastic processing technologies. Energy, 170, pp.273-283.

[28] Benavides, P.T., Sun, P., Han, J., Dunn, J.B. and Wang, M., 2017. Life-cycle analysis of fuels from post-use non-recycled plastics. Fuel, 203, pp.11-22.

[29] Parku, G.K., Collard, F.X. and Görgens, J.F., 2020. Pyrolysis of waste polypropylene plastics for energy recovery: Influence of heating rate and vacuum conditions on composition of fuel product. Fuel Processing Technology, 209, p.106522.

[30] Lopez, G., Artetxe, M., Amutio, M., Bilbao, J. and Olazar, M., 2017. Thermochemical routes for the valorization of waste polyolefinic plastics to produce fuels and chemicals. A review. Renewable and Sustainable Energy Reviews, 73, pp.346-368.

[31] Montgomery, D.C., 2017. Design and analysis of experiments. John Wiley & Sons.

[32] Ronda, A., Della Zassa, M., Gianfelice, G., Iáñez-Rodríguez, I. and Canu, P., 2019. Smouldering of different dry sewage sludges and residual reactivity of their intermediates. Fuel, 247, pp.148-159.

[33] Della Zassa, M., Ronda, A., Gianfelice, G., Zerlottin, M. and Canu, P., 2019. Scale effects and mechanisms ruling the onset of wastewater sludges self-heating. Fuel, 256, p.115876.

[34] Song, Z., He, T., Li, M., Wu, D. and You, F., 2022. Self-sustaining smoldering as a novel disposal approach for food waste with high moisture content. Fuel Processing Technology, 228, p.107144.

[35] Fabris, I., Cormier, D., Gerhard, J.I., Bartczak, T., Kortschot, M., Torero, J.L. and Cheng, Y.L., 2017. Continuous, self-sustaining smouldering destruction of simulated faeces. Fuel, 190, pp.58-66.

Introduction (Fr)

1.1. Crise plastique et contamination sable/sol

1.1.1. Crise plastique

La production de plastique est rapidement passée de 1.5 million de tonnes en 1950 à 368 millions de tonnes en 2019 [1]. La production européenne de plastique a, quant à elle, atteint 57.9 millions de tonnes en 2019 [1], et près de la moitié du plastique produit est devenue un déchet [2]. Il existe trois façons d'éliminer les déchets plastiques, à savoir l'incinération, le recyclage et la mise en décharge (Fig. 1.1). L'incinération des déchets plastiques peut générer de la chaleur, fournissant de l'énergie aux centrales électriques. Il faut noter que la combustion des déchets plastiques produit de grandes quantités de gaz à effet de serre et que les fumées sont également toxiques (production de dioxines par exemple). Par conséquent, les gaz de combustion générés doivent être traités de manière appropriée. De plus, il est à noter que près de 25 % des déchets plastiques finissent dans des décharges. Par conséquent, les déchets plastiques s'accumulent rapidement en raison de leur faible dégradabilité environnementale.

La Fig. 1.2 montre que le plastique le plus demandé en Europe est le polyéthylène (PE), qui représente 30.3 % de la demande totale de plastiques [3]. Le polypropylène (PP) représente quant à lui 19.7 % et est le deuxième type de plastique en masse. Les autres types de plastique sont moins produits à savoir :

- 9.6% en masse pour le polychlorure de vinyle (PVC),

- 8.4% pour le polyéthylène téréphtalate (PET),

- 7.8% pour le polyuréthane (PUR), et

- 6.1% pour le polystyrène (PS).

Le PE est la quantité la plus importante de plastique retrouvée dans les déchets solides municipaux (MSW) [4], ce qui n'est pas surprenant en raison de l'énorme demande faite sur ce composé. La pollution plastique est nocive pour les écosystèmes [5] et nuit aussi aux êtres vivants [6]. Par conséquent, il est urgent de trouver des moyens appropriés de traitement de ces déchets plastiques.

1.1.2. Contamination sable/sol

Les sables et sols peuvent être contaminés par des activités d'origine humaine. Un accident récent resté dans les mémoires est la marée noire qui s’est déroulée au Pérou. Elle a été causée par une éruption volcanique aux Tonga en 2022(Fig. 1.3) [7]. Le pétrole brut déversé a pollué l'océan, nuisant directement aux oiseaux et aux poissons et inhibant la croissance des algues en réduisant la lumière du soleil dans l'océan. L'huile qui s'est échappée a également pollué le sable et les sols. Les plantes qui poussent sur du sable/sol contaminé par les hydrocarbures et les organismes qui vivent dans la région courent un risque important pour leur survie. La substance per- et polyfluoroalkyle (PFAS) est une autre des principales sources de pollution par le sable/le sol en raison de son utilisation généralisée et de sa faible dégradation dans l'environnement [8]. La contamination dans les sables et sols peut causer des dommages irréversibles aux animaux, aux plantes et aux humains. Par conséquent, la dépollution des sables et sols contaminés doit se faire en utilisant des méthodes appropriées et adaptées à ce contexte précis.

1.2. Pyrolyse des déchets plastiques et assainissement des sables/sols contaminés par combustion lente

1.2.1. Pyrolyse des déchets plastiques

La pyrolyse est considérée comme une alternative prometteuse à l'enfouissement des déchets plastiques . Elle peut permettre la production d'huile liquide similaire aux carburants commerciaux (essence et diesel) [9]. Les polymères à longue chaîne peuvent être décomposés en hydrocarbures à chaîne courte dans la plage de température allant de 400 °C à 800 °C [10]. La pyrolyse peut être réalisée dans différents réacteurs, tels qu'un lit fixe (par exemple, discontinu, semi-discontinu, four, goutte à goutte, etc.) ou un lit fluidisé [11]. Les réacteurs à l'échelle du laboratoire sont chauffés indirectement par des serpentins de chauffage électriques pour atteindre et maintenir la température cible [12]. Cela fait de la pyrolyse un processus très énergivore [13].

1.2.2. Assainissement du sable/sol contaminé par combustion lente

La combustion lente ou « smoldering » est une combustion sans flamme qui se produit dans un milieu poreux, permettant une alimentation suffisante en oxygène de la réaction d’oxydation du résidu organique réactif[14]. Le « smoldering » peut s'auto-entretenir lorsque le taux de production de chaleur dépasse le taux de perte de chaleur [15]. C’est un procédés populaire pour traiter les sables et sols contaminés [8], éliminer les déchets [16] mais aussi valoriser des déchets [17]. Les contaminants (combustibles) (p. ex. charbon [18], bitume [19], tourbe [20], pétrole [21]) peuvent être détruits en réagissant avec l'oxygène. Ce processus est exothermique

et permet d’alimenter des procédés énergivores pour l'élimination et la valorisation des déchets [22].

1.2.3. Pyrolyse des déchets plastiques entraînée par « smoldering »

Afin de fournir une source de chaleur plus économique que l'électricité pour la pyrolyse des déchets, Duque et al. [13] ont proposé un réacteur de pyrolyse piloté par une combustion lente auto-entretenue. Ce réacteur a deux chambres indépendantes :

- la chambre extérieure est une chambre de combustion lente et,

- la chambre intérieure est un réacteur de pyrolyse semi-discontinu.

La chaleur de combustion lente est transférée à la chambre de traitement des déchets à travers la frontière entre les deux chambres. Ils ont démontré que la combustion lente du charbon pouvait, par exemple, fournir suffisamment d'énergie pour la propagation du phénomène de smoldering mais aussi de la pyrolyse. Le réacteur global de pyrolyse à combustion lente peut donc être utilisé pour la dépollution du sable contaminé (dans la chambre de combustion lente) et la valorisation des déchets plastiques (dans la chambre de pyrolyse).

1.3. Problèmes et enjeux à explorer pour la pyrolyse des déchets plastiques et la combustion lente du sable/sol contaminé

1.3.1. Modélisation cinétique de la pyrolyse des déchets plastiques

La pyrolyse des déchets plastiques est une réaction chimique complexe en plusieurs étapes, ce qui rend difficile la détermination des schémas et paramètres cinétiques (par exemple, l'énergie d'activation E, le facteur pré-exponentiel A et l'ordre de réaction n, etc.). De plus, les paramètres cinétiques de la réaction de pyrolyse des déchets plastiques ne sont pas déterminés

simultanément via une méthode de calcul traditionnelle [23-26]. Par exemple, le calcul du facteur pré-exponentiel nécessite une valeur numérique pour l'énergie d'activation. Le modèle de réaction doit également être déterminé par les méthodes Coats-Redfern [23][24] ou Criado [25]. Les modèles de réaction candidats sont les modèles représentatifs, tels que la loi de puissance, la géométrie contractante, Prout-Tompkins, etc. [26]. Par conséquent, il est nécessaire d'explorer les différentes méthodes pour effectuer la modélisation cinétique, puis déterminer les paramètres cinétiques.

1.3.2. Production d'huile à partir de la pyrolyse des déchets plastiques

La pyrolyse ou décomposition thermique est une technologie prometteuse pour convertir les déchets plastiques en carburants à valeur ajoutée [27], sous la forme d'une large distribution de produits, tels que le pétrole (essence et diesel) et le gaz (éthane et propane) [28]. La conversion par pyrolyse est sensible aux paramètres de fonctionnement tels que la température, le temps de séjour et le débit de gaz vecteur au travers d'un réacteur chauffé. De nombreux efforts de recherche sont consacrés à la détermination de la production maximale d'huile de pyrolyse. Cependant, la plupart des études ont été menées en adoptant la conception statistique à un facteur à la fois [29][30], qui est une technique qui ne capture pas les effets des interactions de variables qui sont nécessaires pour éviter des conclusions trompeuses [31] . Pour cette raison, nous devons mettre en œuvre une technique statistique qui permet une combinaison robuste des paramètres.

1.3.3. Pyrolyse des déchets plastiques provoquée par la combustion lente du sable/sol contaminé

Le réacteur de combustion lente pour le traitement des déchets peut être classé en deux types, i.e. *in-situ* et *ex-situ*. Le réacteur *in-situ* fait référence à la combustion lente et au traitement des déchets se produisant dans la même chambre. Dans de nombreux cas, les déchets peuvent être brûlés avec de l'oxygène pour fournir suffisamment de chaleur pour une combustion lente [32][33]. Cependant, il est nécessaire d'ajouter du combustible au réacteur pour augmenter la chaleur générée par la réaction d'oxydation afin d'éviter l'extinction du procédé [34][35]. Le réacteur *ex-situ*, quant à lui, fait référence à la combustion lente et au traitement des déchets se produisant dans deux chambres [13]. La chaleur de combustion lente est transférée à la chambre de traitement des déchets à travers la frontière entre les deux chambres.

Étant donné que la combustion lente nécessite une consommation d'oxygène alors que la pyrolyse nécessite une absence d'oxygène, le réacteur de pyrolyse entraîné par la combustion lente doit donc être du type *ex-situ*. Cependant, la plupart des études de combustion lente sont réalisées *in-situ*, et seules quelques-unes se concentrent sur les applications *ex situ* [13][16][22]. L''étude numérique du réacteur de pyrolyse à combustion lente pour la pyrolyse de déchets plastiques couplé à l'assainissement des sables et sols contaminés reste donc non étudiée dans la limite de nos connaissances.

1.4. Objectifs de la thèse

Cette thèse vise donc à explorer la pyrolyse des déchets plastiques induite par la combustion lente du sable contaminé par un résidu organique réactif. Le polyéthylène (PE) est le premier composant des déchets plastiques en raison de sa large gamme d'utilisation. Par

conséquent, les déchets de polyéthylène (WPE) ont été choisis pour étudier le comportement de pyrolyse des déchets plastiques. Le sable contaminé a été remplacé par un mélange de *char* et de sable pour simplifier les approches et bien calibrer les concentrations en réactif. Les objectifs de la thèse peuvent être résumés comme suit.

1) La décomposition des déchets plastiques est un comportement chimique complexe. Les paramètres cinétiques de pyrolyse sont déterminés par utilisation d'un algorithme génétique (GA) couplé à l'analyse thermogravimétrique (TGA) à l'aide de trois modèles de réaction représentatifs. De plus, le réseau de neurones artificiels (ANN) couplé à GA est adopté pour déterminer les conditions de fonctionnement optimales sur différentes plages de température afin de mieux comprendre la pyrolyse WPE.
2) L'huile de pyrolyse WPE est une alternative aux carburants commerciaux. Les conditions opératoires (température, temps de séjour et débit de gaz vecteur) ont des effets interactifs complexes sur la production d'huile. L'ANN couplé au GA est utilisé pour maximiser le rendement en huile dans un réacteur semi-discontinu à l'échelle du banc. De plus, la pyrolyse catalytique WPE est étudiée pour améliorer la qualité de l'huile de pyrolyse.
3) Deux modèles numériques multidimensionnels ont été développés pour simuler le réacteur de pyrolyse à combustion lente pour la pyrolyse de WPE et la dépollution du sable contaminé. Les modèles développés dans la thèse visent à fournir des outils de conception généraux pour la performance, l'évaluation et l'optimisation du réacteur de pyrolyse piloté par combustion lente.

Bibliography

[1] Plastics - the Facts 2020. PlasticsEurope (2020).

[2] Karayılan, S., Yılmaz, Ö., Uysal, Ç. and Naneci, S., 2021. Prospective evaluation of circular economy practices within plastic packaging value chain through optimization of life cycle impacts and circularity. Resources, Conservation and Recycling, 173, p.105691.

[3] Plastics - the Facts 2021. PlasticsEurope (2021).

[4] Sharuddin, S.D.A., Abnisa, F., Daud, W.M.A.W. and Aroua, M.K., 2016. A review on pyrolysis of plastic wastes. Energy conversion and management, 115, pp.308-326.

[5] Zhao, S., Wang, C., Bai, B., Jin, H. and Wei, W., 2022. Study on the polystyrene plastic degradation in supercritical water/CO2 mixed environment and carbon fixation of polystyrene plastic in CO2 environment. Journal of Hazardous Materials, 421, p.126763.

[6] Ellis, L.D., Rorrer, N.A., Sullivan, K.P., Otto, M., McGeehan, J.E., Román-Leshkov, Y., Wierckx, N. and Beckham, G.T., 2021. Chemical and biological catalysis for plastics recycling and upcycling. Nature Catalysis, 4(7), pp.539-556.

[7] https://www.ndtv.com/world-news/volcanic-eruption-in-tonga-blamed-for-an-peru-oil-spill-11-000-km-away-2716360

[8] Duchesne, A.L., Brown, J.K., Patch, D.J., Major, D., Weber, K.P. and Gerhard, J.I., 2020. Remediation of PFAS-contaminated soil and granular activated carbon by smoldering combustion. Environmental Science & Technology, 54(19), pp.12631-12640.

[9] Al-Salem, S.M., Chandrasekaran, S.R., Dutta, A. and Sharma, B.K., 2021. Study of the fuel properties of extracted oils obtained from low and linear low density polyethylene pyrolysis. Fuel, 304, p.121396.

[10] Gala, A., Catalan-Martinez, D., Guerrero, M. and Serra, J.M., 2021. Simulation-assisted design of a catalytic hydrogenation reactor for plastic pyrolysis fuels. Fuel, 287, p.119400.

[11] Wang, Z., Burra, K.G., Lei, T. and Gupta, A.K., 2021. Co-pyrolysis of waste plastic and solid biomass for synergistic production of biofuels and chemicals-A review. Progress in Energy and Combustion Science, 84, p.100899.

[12] Park, H.J., Park, Y.K., Dong, J.I., Jeon, J.K., Yim, J.H. and Jeong, K.E., 2008. Catalytic degradation of polyethylene over ferrierite. Research on Chemical Intermediates, 34(8), pp.727-735.

[13] Duque, J.V.F., Bittencourt, F.L., Martins, M.F. and Debenest, G., 2021. Developing a combustion-driven reactor for waste conversion. Energy, 237, p.121489.

[14] Torero, J.L., Gerhard, J.I., Martins, M.F., Zanoni, M.A., Rashwan, T.L. and Brown, J.K., 2020. Processes defining smouldering combustion: Integrated review and synthesis. Progress in Energy and Combustion Science, 81, p.100869.

[15] Wang, Z., Liu, N., Yuan, H., Chen, H., Xie, X., Zhang, L. and Rein, G., 2022. Smouldering and its transition to flaming combustion of polyurethane foam: An experimental study. Fuel, 309, p.122249.

[16] Bittencourt, F.L.F., Martins, M.F., Orlando, M.T.D. and Galvão, E.S., 2022. The proof-of-concept of a novel feces destroyer latrine. Journal of Environmental Chemical Engineering, 10(1), p.106827.

[17] Sun, Y., Bai, F., Liu, B., Liu, Y., Guo, M., Guo, W., Wang, Q., Lü, X., Yang, F. and Yang, Y., 2014. Characterization of the oil shale products derived via topochemical reaction method. Fuel, 115, pp.338-346.

[18] Zanoni, M.A., Wang, J. and Gerhard, J.I., 2021. Understanding pressure changes in smouldering thermal porous media reactors. Chemical Engineering Journal, 412, p.128642.

[19] Zanoni, M.A., Torero, J.L. and Gerhard, J.I., 2019. Delineating and explaining the limits of self-sustained smouldering combustion. Combustion and Flame, 201, pp.78-92.

[20] Chen, H., Rein, G. and Liu, N., 2015. Numerical investigation of downward smoldering combustion in an organic soil column. International Journal of Heat and Mass Transfer, 84, pp.253-261.

[21] Kinsman, L., Torero, J.L. and Gerhard, J.I., 2017. Organic liquid mobility induced by smoldering remediation. Journal of Hazardous materials, 325, pp.101-112.

[22] Duque, J.V.F., Martins, M.F., Bittencourt, F.L. and Debenest, G., 2021. Relevant aspects of propagating a combustion front in an annular reactor for out-of-bed heat recovery. Experimental Thermal and Fluid Science, p.110575.

[23] Coats, A.W. and Redfern, J.P., 1964. Kinetic parameters from thermogravimetric data. Nature, 201(4914), pp.68-69.

[24] Yang, K.K., Wang, X.L., Wang, Y.Z., Wu, B., Jin, Y.D. and Yang, B., 2003. Kinetics of thermal degradation and thermal oxidative degradation of poly (p-dioxanone). European polymer journal, 39(8), pp.1567-1574.

[25] Criado, J.M., 1978. Kinetic analysis of DTG data from master curves. Thermochimica Acta, 24(1), pp.186-189.

[26] Duque, J.V.F., Martins, M.F., Debenest, G. and Orlando, M.T.D.A., 2020. The influence of the recycling stress history on LDPE waste pyrolysis. Polymer Testing, 86, p.106460.

[27] Fox, J.A. and Stacey, N.T., 2019. Process targeting: An energy based comparison of waste plastic processing technologies. Energy, 170, pp.273-283.

[28] Benavides, P.T., Sun, P., Han, J., Dunn, J.B. and Wang, M., 2017. Life-cycle analysis of fuels from post-use non-recycled plastics. Fuel, 203, pp.11-22.

[29] Parku, G.K., Collard, F.X. and Görgens, J.F., 2020. Pyrolysis of waste polypropylene plastics for energy recovery: Influence of heating rate and vacuum conditions on composition of fuel product. Fuel Processing Technology, 209, p.106522.

[30] Lopez, G., Artetxe, M., Amutio, M., Bilbao, J. and Olazar, M., 2017. Thermochemical routes for the valorization of waste polyolefinic plastics to produce fuels and chemicals. A review. Renewable and Sustainable Energy Reviews, 73, pp.346-368.

[31] Montgomery, D.C., 2017. Design and analysis of experiments. John Wiley & Sons.

[32] Ronda, A., Della Zassa, M., Gianfelice, G., Iáñez-Rodríguez, I. and Canu, P., 2019. Smouldering of different dry sewage sludges and residual reactivity of their intermediates. Fuel, 247, pp.148-159.

[33] Della Zassa, M., Ronda, A., Gianfelice, G., Zerlottin, M. and Canu, P., 2019. Scale effects and mechanisms ruling the onset of wastewater sludges self-heating. Fuel, 256, p.115876.

[34] Song, Z., He, T., Li, M., Wu, D. and You, F., 2022. Self-sustaining smoldering as a novel disposal approach for food waste with high moisture content. Fuel Processing Technology, 228, p.107144.

[35] Fabris, I., Cormier, D., Gerhard, J.I., Bartczak, T., Kortschot, M., Torero, J.L. and Cheng, Y.L., 2017. Continuous, self-sustaining smouldering destruction of simulated faeces. Fuel, 190, pp.58-66.

Chapter 2

Investigating waste plastic pyrolysis kinetic parameters by genetic algorithm coupled with thermogravimetric analysis

Summary

Pyrolysis of waste plastic (WP) is a promising method to solve the plastic pollution issue. WP is mainly composed of polyethylene (PE). Moreover, the products of waste polyethylene (WPE) pyrolysis could serve as high quality fuels and the feedstocks of petrochemicals. Therefore, it is essential to investigate the WPE and WP pyrolysis process. This chapter evaluated pure PE, WPE and WP pyrolysis kinetic parameters by the use of genetic algorithm (GA) and isoconversional methods coupled with thermogravimetric analysis (TGA), respectively. Additionally, three representative reaction models, i.e., reaction-order, extended Prout–Tompkins and Sestak–Berggren models, were investigated for obtaining the most suitable model, which could describe the PE, WPE and WP pyrolysis process more accurately. Consequently, the reaction-order model turned out to be the optimal method for appropriately describing PE, WPE and WP pyrolysis processes. Hence, the pyrolysis parameters optimized by GA were proven to be accurate and reliable, in comparison of calculated values of activation energy by isoconversional methods and experimental data. Moreover, it might be applicable of GA coupled with TGA with reaction-order model to the future industrial WPE and WP pyrolysis circumstances that have variable heating rates.

Candidate contribution: Conceptualization, methodology, formal analysis, resources, data curation, writing - original draft, visualization.

2.1. Introduction

Plastic is an essential industrial product in the modern society. It has multiple usages in both daily life and industrial applications due to its superior performance. Hence, a large amount of different types of plastic produced annually worldwide. According to the literature [1], 335 million tons of plastic produced globally in 2016. Moreover, this figure is continuing increasing as the results of the global population growth [2] and economic swift development [3]. Accordingly, vast irreplaceable petroleum consumed yearly since the plastic is the chemical product based on the petroleum. Furthermore, in the entire quantity of plastic produced since 1950, nearly 70% of plastic has been obsoleted and 84% has been landfilled or discarded directly in the environment [4]. This results in severe plastic pollution because of the durable of plastic [2]. For the purpose of minimizing the plastic waste, i.e., landfill of waste plastic (WP), recycling is one of promising methods. The WP recycling could be divided into two categories, namely mechanical recycling [5] and chemical recycling [6]. Herein, owing to the exacting demand for products with high added value, WP mechanical recycling is fairly challenging contemporarily [2]. However, the products of WP chemical recycling could serve as fuels [7][8][9] and the feedstocks of petrochemicals [10]. This makes WP chemical recycling very attractive and competitive. In additional, the WP could also be utilized for energy recovery, i.e., incineration. While it turns out to be unfavorable since its low heating value (42.6 MJ/kg) [11] and hazardous dioxins producing [12].

Pyrolysis is a promising method to decompose WP, which is treated with difficulties by mechanical recycling [13]. As its price is moderate, waste polyethylene (WPE) becomes the

primary material serving as the feedstock of pyrolysis [14]. Besides, polyethylene (PE) represents more than 90% of WP [15]. Moreover, in the range of polyolefins, the PE plays a main role of the world plastic usage [1]. Therefore, it is essential to investigate the pyrolysis process of PE.

Currently, many researchers utilize the thermogravimetric analysis (TGA) to investigate the PE and other materials pyrolysis characteristics. Kple et al. [16] and Bercic et al. [17] used TGA for PE thermal pyrolysis kinetics investigation. Zheng et al. [18] and Xiang et al. [19] investigated PE co-pyrolysis behavior and thermal kinetics by TGA. Furthermore, the activation energy, calculated based on the TG experimental data, provided a reference for co-pyrolysis mechanism analysis. Das et al. [20] and Aboulkas et al. [21] conducted the thermal pyrolysis kinetics and behaviors investigations of different types of plastics by TGA. TGA was also adopted in the kinetic researches of municipal solid waste (MSW) [22] and plant seeds [23] thermal pyrolysis processes. Moreover, plenty studies have been conducted by exploiting different isoconversional methods coupled with TGA [24][25]. Wang et al. [26] investigated new and aged PE with TGA coupled with Friedman [27], Kissinger-Akahira-Sunose (KAS) [28] and Flynn-Wall-Ozawa (FWO) [29] methods. They concluded that pyrolysis of PE could be described by ‘Contracting Cylinder’ (R2) model [30]. Aboulkas et al. [21] adopted Friedman, KAS and FWO methods to calculate the PE activation energy. Furthermore, the Coats-Redfern [31][32] and Criado methods [33] were used to determine the proper reaction model for describing PE pyrolysis with accuracy. It was also reported that the ‘Contracting Cylinder’ (R2) model was suitable for the PE pyrolysis process. Vyazovkin [30] proposed an advance

isoconversional method (AIC) to promote the accuracy of the isoconversional method. Moreover, Das et al. [20] utilized AIC to investigate the PE pyrolysis in nitrogen. They compared reliability of AIC, Friedman, FWO and Starink [34] methods. Accordingly, they drew the conclusion that AIC was the more accurate method for describing PE pyrolysis process than other isoconversional methods.

In the majority of researches, the plastic pyrolysis reaction kinetic parameters (e.g., activation energy E, pre-exponential factor A and the reaction order n, etc.) are not determined simultaneously. For instance, the calculation of pre-exponential factor is based on the calculated activation energy. Moreover, the reaction model needs to be determined by the Coats-Redfern [31][32] or Criado methods [33]. The reaction model candidates are the representative ones, such as Power-law, Contracting geometry, Prout–Tompkins, etc. [35]. Therefore, some researchers turned to explore the different methods to conduct the kinetic modeling. According to the literatures [36][37][38][39], the genetic algorithm (GA) could calculate multiple parameters contemporaneously. Moreover, GA could be used for searching the global optimal parameters despite of the scopes of the parameters. Thus, GA was adopted to evaluate the reaction kinetic parameters [40]. Furthermore, Jiang et al. [41] and Chen et al. [42] conducted the kinetic study on plastic pyrolysis with GA coupled TGA. The most widespread reaction-order model was adopted in their researches. The consistency between experimental data and the GA calculated results indicated that GA is a promising method to evaluate the pyrolysis kinetic parameters of polymers.

For the purpose of instructing the further application of chemical recycling of WPE and WP,

this study adopts GA coupled with TGA to study the pyrolysis processes of WPE and WP at heating rates varied from 5 to 20 K/min in argon. Moreover, in order to obtain a better understanding of the pyrolysis processes, the pure PE from commercial corporation is utilized as a comparison. Three isoconversional methods are adopted to calculate the activation energy values. The results provide a reference to the GA calculated kinetic parameters. Additionally, three representative reaction models are investigated to determine the most favorable one which could describe the WPE and WP pyrolysis processes.

2.2. Experimental and kinetic modeling

2.2.1. Experimental

(i) Materials

Pure PE, WPE and WP utilized in this study were offered by Lukplast Ind. (ES-Brazil), as illustrated in Fig. 2.1. WPE was recycled from waste polyethylene products with the certain selection, such as plastic bags, plastic films, milk buckets and et al. While WP was recycled plastic without selection, which composed of a majority of polyethylene (PE) and a minority of polystyrene (PS) and polyethylene terephthalate (PET).

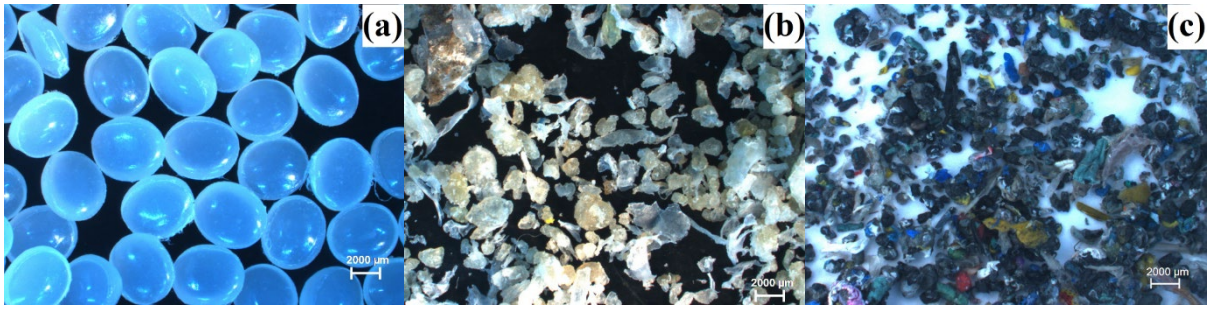

Fig. 2.1. Pictures of (a) pure PE, (b) WPE and (c) WP used in experiments.

(ii) Thermogravimetric tests

The thermogravimetric tests were using a NETZSCH STA 449F3 thermal analyzer with 60 mL/min gas flow rate of argon. Approximately 13.0 mg powder test samples were heated from room temperature to 973.15 K at four representative heating rates (i.e., 5, 10, 15, 20 K/min).

2.2.2. Kinetic modeling

(i) Pyrolysis reaction description

According to the literature [41][42], the pyrolysis of plastic could be described by:

$$plastic \rightarrow \upsilon\ residue + (1-\upsilon)\ gas \tag{2.1}$$

where ν represents reaction stoichiometry coefficient.

Based on the aforementioned Eq. (2.1), this study adopted Arrhenius Law to calculate mass loss rate (MLR) during plastic pyrolysis process. Hence, MLR could be expressed as follow:

$$MLR = (1-\upsilon)Af(\alpha)\exp\left(-E/(RT)\right) \tag{2.2}$$

where *A*, *α*, *f(α)*, *E*, *R* and *T* represent the pre-exponential factor (1/s), the conversion rate, the dependence on the conversion rate, the activation energy (kJ/mol), the universal gas constant (equals to 8.314 J/(mol·K)) and the temperature (K), respectively.

Accordingly, the mass fraction of test sample could use the following equation:

$$y = 1 - \int_0^t MLR\,dt \tag{2.3}$$

where *y* and *t* represent the mass fraction and the pyrolysis time (s), respectively.

(ii) Reaction models

According to the literature [30], three representative reaction models, namely reaction-order model, the extended Prout-Tompkins model, and the Sestak-Berggren model [43], are possible candidates for the pyrolysis description. The expressions are listed in Table 2.1.

Table 2.1. Reaction models investigated in this study.

Reaction model	Equation
Reaction-order model	$f(\alpha) = (1-\alpha)^n$
Extended Prout-Tompkins model	$f(\alpha) = \alpha^m \cdot (1-\alpha)^n$
Sestak-Berggren model	$f(\alpha) = \alpha^m \cdot (1-\alpha)^n \cdot [-ln(1-\alpha)]^p$

α, *f(α)* and *n* represent the conversion rate, the dependence on the conversion rate and the reaction order. *m* and *p* are the exponents which applied in different reaction models, respectively.

(iii) Isoconversional methods

In this study, three representative isoconversional methods, as listed in Table 2.2, were adopted for investigating the activation energy of plastic pyrolysis, namely one integral method (KAS) [28], one differential method (Friedman) [27] and AIC method [30].

Table 2.2. Isoconversional methods adopted in this study.

Method	Equation
KAS	$\ln\left(\frac{\beta}{T^2}\right) = -\frac{E}{RT} + const.$
Friedman	$\ln\left(\beta\frac{d\alpha}{dT}\right) = -\frac{E}{RT} + const.$
AIC	$\Phi(E) = \sum_{i=1}^{n}\sum_{j\neq i}^{n}\frac{I(E,T_i)/\beta_i}{I(E,T_j)/\beta_j}$ with $I(E,T_i) = \int_0^{T_i}\exp\left(-\frac{E}{RT}\right)dT$

β, *E*, *T* and *R* represent the heating rate (K/min), the activation energy (kJ/mol), temperature (K) and universal gas constant (equals to 8.314 J/(mol·K)), respectively.

(iv) Genetic algorithm

The genetic algorithm adopted in this study is described in Fig. 2.2. In each generation, there are N individuals with specific genes, such as the activation energy E, the pre-exponential

factor A, the reaction order n and et al. These individuals serve as parents. Subsequently, N parents could generate N children. This procedure is known as reproduction, also accompanied by mutation. The arithmetic expressions were illustrated in Fig. 2.1, in which i and j denote the number of individual and gene; r^i_j is a random number varied from 0 to 1; v_{mut} is the possibility of mutation, which equals to 0.05 [41]; and s is a random number varied from -0.5 to 0.5 [42]. The next procedure is to calculate the fitness of each individual. The fitness is calculated by experimental and predicted MLR and mass fraction. The fitness is served as the target function. Additionally, φ denotes the weight coefficient, which equals to 0.5 [42]. Furthermore, the best individual, which had the maximum fitness value, was selected. Lastly, offspring is undergoing selection based on the value of fitness. Individuals, of which fitness values lower than half of the maximum value fitness, would be replaced by the best individual in this generation. This process is called replacement. Therewith, the next inheritance will repeat the above processes.

In this study, the number of individuals and generations are 500 and 200, respectively. The GA was coded in Matlab. In addition, ordinary differential equation ode23s was adopted to calculate the predicted mass loss rates (MLR) and mass fractions.

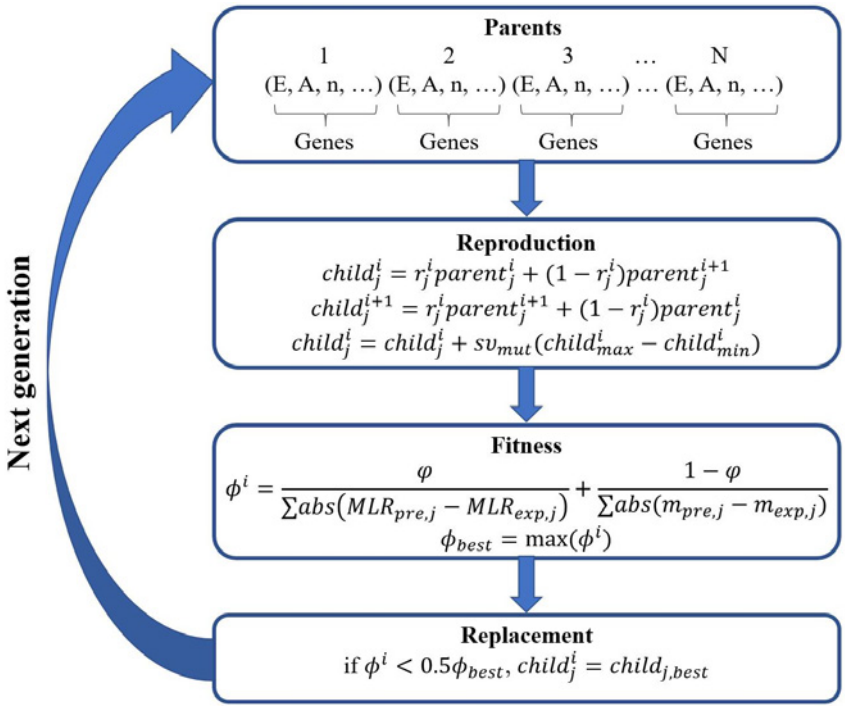

Fig. 2.2. GA schematic diagram

2.3. Results and discussions

2.3.1. Thermogravimetric analysis

Fig. 2.3 illustrates the experimental MLR and TG (relative mass loss) curves of pure PE, WPE and WP at different heating rates during the pyrolysis process under argon atmosphere. The test samples were performed under the same experimental treatment, which heated from room temperature to 973.15 K. In general, the shape of MLR and TG curves remained unchanged regardless of the variation of the heating rate. Moreover, the peak values of MLR of PE, WPE and WP increase as the heating rate increases. For instance, as depicted in Figure 3a, the peak value of MLR of PE increased from 0.2296 to 0.8751 wt%/s when the heating rate increased from 5 to 20 K/min. Additionally, a significant lateral shift to higher temperature occurred when the heating rate increased in the MLR and TG curves. It may be caused by the

pyrolysis mechanism transformation when the heating rate increased [20][44].

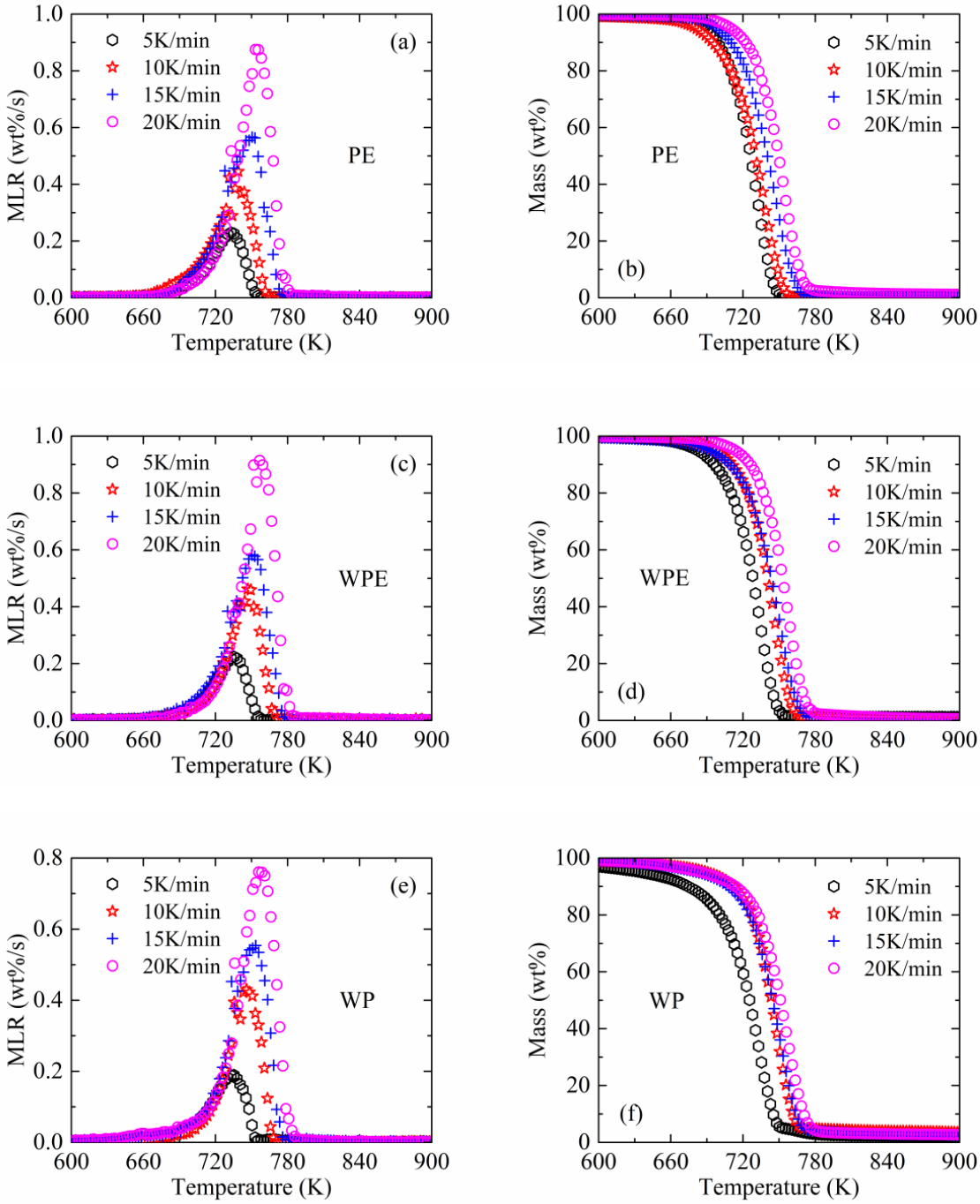

Fig. 2.3. Experimental MLR and TG curves at 5, 10, 15 and 20 K/min in argon: (a) MLR curves of PE; (b) TG curves of PE; (c) MLR curves of WPE; (d) TG curves of WPE; (e) MLR curves of WP; (f) TG curves of WP.

Fig. 2.4 demonstrates the onset temperature T_o, the end temperature T_e and the maximum

degradation temperature T_m in the PE MLR curve at 5 K/min under argon atmosphere. T_o, T_e and T_m were proposed for evaluating the plastic pyrolysis process [20]. As listed in Table 2.3, due to the pyrolysis mechanisms transformation [20], T_o, T_e and T_m of PE, WPE and WP increased with the heating rate. For instance, the onset temperature T_o of PE, WPE and WP increased from 699-719 K, 700-725 K and 697-723 K gradually when the heating rate increased from 5-20 K/min. By comparison, WP has the highest T_e and T_m, while PE has the lowest ones. As regards to T_o, there is no obvious regularities among PE, WPE and WP at different heating rates. However, the differences value between T_o and T_e are nearly constant, around 60 K, despite of the variation of the heating rate.

In consideration of the MLR maximum value, the pyrolysis processes of PE, WPE and WP are relatively fast under argon atmosphere. For example, the maximum MLR of WPE could come up to 0.9142 wt%/s at 20 K/min. Besides, the maximum values of MLR of PE, WPE and WP varied from 0.2296-0.8751 wt%/s, 0.2233-0.9142 wt%/s and 0.1912-0.7784 wt%/s at the heating rates 5-20 K/min, respectively. It could be regarded that WPE underwent a relatively faster pyrolysis process, while WP underwent a relatively slower pyrolysis process under argon atmosphere.

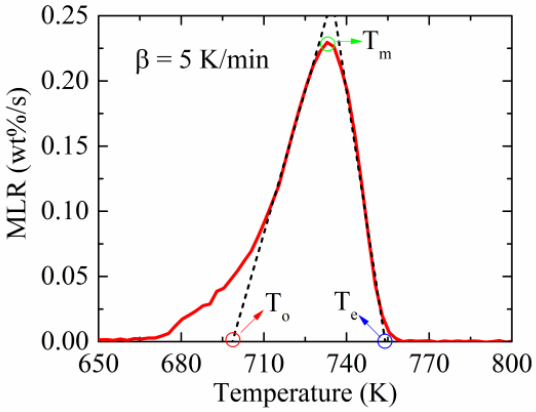

Fig. 2.4. T_o, T_e and T_m from MLR curve of PE at 5 K/min in argon.

Table 2.3. Onset, end, and maximum degradation temperatures and maximum MLR of PE, WPE, and WP in argon.

Material	Heating rate (K/min)	T_o (K)	T_e (K)	T_m (K)	MLR_{max} (wt%/s)
PE	5	699	754	733	0.2296
	10	699	764	739	0.4451
	15	707	773	750	0.5664
	20	719	777	753	0.8751
WPE	5	700	756	735	0.2233
	10	711	768	747	0.4617
	15	711	776	750	0.5820
	20	725	780	757	0.9142
WP	5	697	757	735	0.1912
	10	714	770	748	0.4442
	15	716	775	753	0.5538
	20	723	781	756	0.7784

The TG curves of PE, WPE and WP, which depicted in Fig. 2.3, indicated that they were decomposed to gaseous products (under the experimental environment) during the pyrolysis process. After PE, WPE and WP were heated from room temperature to 973.15 K, the mass fractions of the residue at different heating rates are listed in Table 2.4. Plastic pyrolysis products could be divided into char, wax/oil and gases. Moreover, the distributions of the

products are affected by the heating rates [44]. Therefore, the residues were different at different heating rates of pure PE, WPE and WP. When the pyrolysis processes finished, there were no residue of pure PE remained when the heating rates were 10 and 15 K/min. However, it existed 0.03 and 0.90 wt% residue of pure PE at 5 and 20 K/min, respectively. The values are negligible compared to the original weight. Therefore, it could be considered that pure PE can be decomposed thoroughly after the pyrolysis process under argon atmosphere [20][21]. In the case of WPE, a minor amount of residue remains after the pyrolysis process. However, a larger amount residue remained after WP pyrolysis process. As demonstrated in Table 2.4, it still remained around 2.15 wt% residue at the end of WP thermal degradation process under argon atmosphere.

Table 2.4. The mass fractions of the residue at different heating rates of pure PE, WPE, and WP.

Residue (wt%)	Heating rate (K/min)			
	5	10	15	20
PE	0.02	0	0	0.9
WPE	1.15	0.31	0.19	0.49
WP	1.08	3.16	2.1	2.26

2.3.2. Degradation kinetics by the isoconversional methods

Three isoconversional methods were adopted for calculating the activation energy E of pure PE, WPE and WP by using four sets of TG data at different heating rates. As exhibited in Table 2.5, the activation energy values of pure PE, which were calculated by KAS, Friedman, and AIC methods, are varied with the different conversion rates. However, the differences of the activation energy values are almost negligible particularly when the conversion rate varied from

0.3 to 0.9. In addition, the activation energy is relatively lowered when the conversion rate is under 0.2. This is because that the initial degradation is relatively facilitated due to the presence of weak link sites intrinsic of PE [45][46]. Furthermore, the values of PE activation energy calculated by KAS and AIC were very close. While Friedman method calculated PE activation energy values were very different from KAS and AIC. This is consistent with the results in the work of Das et al. [20]. And it indicated that the activation energy values calculated by the KAS and AIC were more convincible to a certain extent. The low-density PE activation energy value calculated by Encinar et al. [44] was 285 kJ/mol. It is close to the calculated average value of pure PE activation energy in this work. However, in the works of Das et al. [20], Xu et al. [47] and Wang et al. [26], the low-density PE activation energy values calculated by KAS were 162-242, 174.46 and 130.04-193.10 kJ/mol, respectively. The calculated results of activation energy in different literatures varied to a large extent. It may be caused by the different sources of the raw material and the varying processes of manufacturing [47].

The activation energy of WPE and WP were calculated by the same three isoconversional methods as its of pure PE. The results were listed in Table 2.6 and Table 2.7 separately. Hence, the calculated activation energy of pure PE, WPE and WP at different conversion rates by KAS, Friedman and AIC methods were plotted in Fig. 2.5. It is noticeable that the differences of activation energy, between the KAS and AIC methods, could be nearly neglected. It might be noticed that the activation energy of pure PE is larger than the one of WPE and WP. It indicates that the WPE and WP are more ignitable, whereas pure PE is relatively less ignitable [26]. Once again, we can notice the decrease of the value differences of activation energy of pure PE, WPE

and WP with the conversion rate.

Table 2.5. Calculation results of activation energy E of pure PE by KAS, Friedman, and AIC methods.

Conversion	KAS (kJ/mol)	Friedman (kJ/mol)	AIC (kJ/mol)
0.1	236.67	239.97	237.00
0.2	250.12	266.66	250.43
0.3	260.39	260.24	260.70
0.4	266.85	249.27	267.15
0.5	265.02	255.90	265.32
0.6	268.30	257.03	268.61
0.7	270.58	271.33	270.88
0.8	272.91	276.17	273.21
0.9	263.12	197.59	263.43
Average value	261.55	252.68	261.86

Table 2.6. Calculation results of activation energy E of WPE by KAS, Friedman, and AIC methods.

Conversion	KAS (kJ/mol)	Friedman (kJ/mol)	AIC (kJ/mol)
0.1	177.68	208.35	178.04
0.2	215.85	245.45	216.17
0.3	234.80	264.89	235.11
0.4	240.37	241.46	240.67
0.5	254.52	257.79	254.81
0.6	257.34	271.78	257.62
0.7	258.96	254.77	259.23
0.8	260.94	258.39	261.22
0.9	257.31	217.88	257.59
Average value	239.75	246.75	240.05

Table 2.7. Calculation results of activation energy E of WP by KAS, Friedman, and AIC methods.

Conversion	KAS (kJ/mol)	Friedman (kJ/mol)	AIC (kJ/mol)
0.1	126.75	162.39	127.20
0.2	174.64	215.20	175.02

0.3	213.99	285.69	214.32
0.4	228.82	285.04	229.14
0.5	241.26	267.45	241.57
0.6	244.28	257.55	244.60
0.7	251.43	244.72	251.74
0.8	254.55	274.89	254.86
0.9	258.38	254.81	258.70
Average value	221.57	249.75	221.91

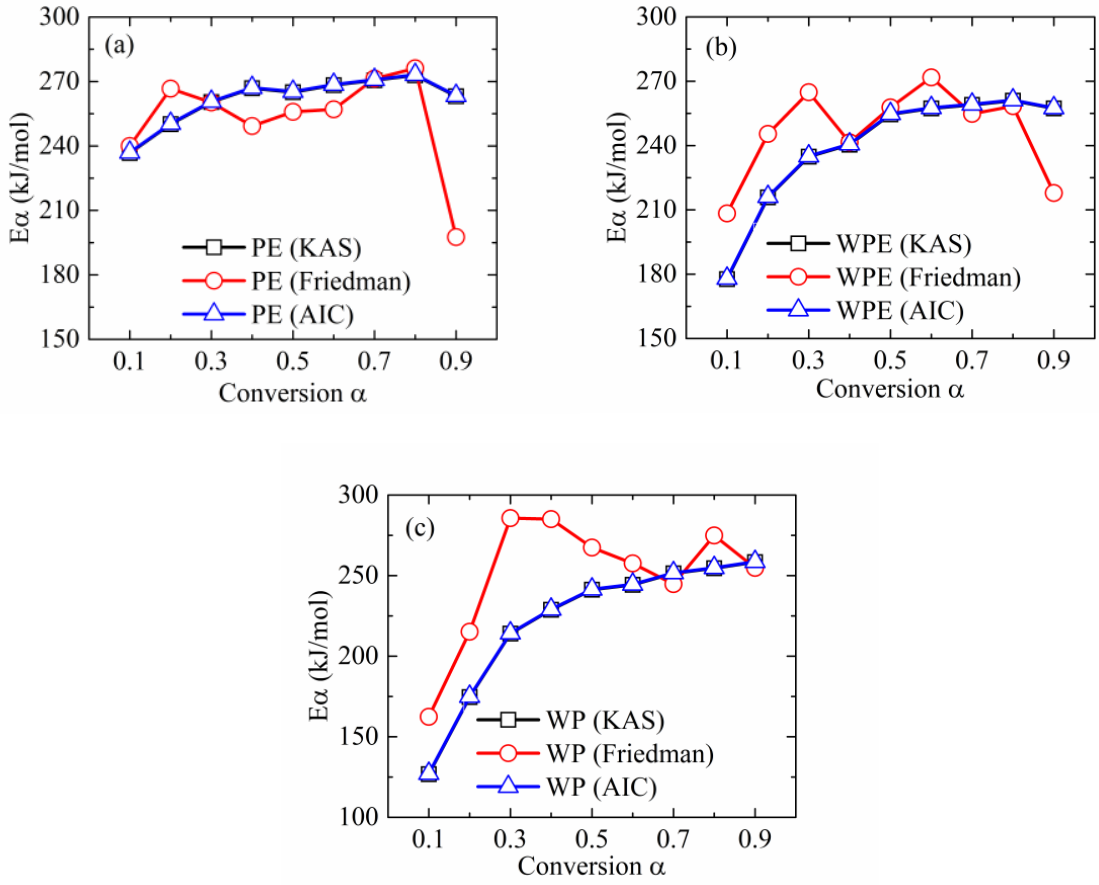

Fig. 2.5. The calculated activation energy of pure PE, WPE, and WP by different isoconversional methods.

2.3.3. Favorable reaction model selection

In order to determine which reaction model could describe the PE pyrolysis process with accuracy, three representative reaction models were adopted in this study, i.e., reaction-order,

extended Prout-Tompkins, and Sestak-Berggren models. Hence, the different reaction models coupled with GA were investigated separately for obtaining the optimal pyrolysis kinetic parameters of pure PE. Consequently, the optimized values of PE pyrolysis kinetic parameters by adopting reaction-order, extended Prout-Tompkins and Sestak-Berggren models are listed in Table 2.8. The optimized values of activation energy were 241.55, 221.21 and 217.86 kJ/mol, which were calculated with reaction-order, extended Prout-Tompkins, and Sestak-Berggren models, respectively. In comparison, the activation energy values of PE calculated by KAS, Friedman and AIC methods were 261.55, 252.68 and 261.86 kJ/mol, respectively. The GA optimized activation energy of reaction-order model is close to the value determined by the isoconversional methods.

Table 2.8. Optimized values of PE pyrolysis kinetic parameters by adopting reaction-order, extended Prout-Tompkins, and Sestak-Berggren models.

Parameters	Optimized values		
	Reaction-order	Extended Prout-Tompkins	Sestak-Berggren
lnA ($ln(s^{-1})$)	34.52	31.78	31.23
E (kJ/mol)	241.55	221.21	217.86
n	0.58	1.08	1.12
m	–	0.30	0.29
p	–	–	0.07

Accordingly, the predicted MLR and TG curves were plotted in Fig. 2.6, which with the GA optimized values of PE by adopting reaction-order, extended Prout-Tompkins, and Sestak-Berggren models at the different heating rates. It could be perceived that the predicted MLR and TG curves by using of three reaction models coupled with GA were promisingly consistent with the experimental ones. Moreover, the R-squared values between experimental and

predicted data of PE by adopting different reaction models were listed in Table 2.9. The predicted mass fraction was more precise than the predicted MLR in all three reaction models. The average R-squared value of mass fraction and MLR were ~0.998 and ~0.971, respectively. The overall average R-squared value gradually increased in reaction-order, extended Prout-Tompkins and Sestak-Berggren models. However, the increased value was almost negligible. The R-squared values of MLR and mass fraction had no obvious differences among different reaction models. To be more exact, the reaction-order and the extended Prout-Tompkins models were more accurate in the prediction of mass fraction. Whereas the Sestak-Berggren model could describe the MLR with a greater precision. In consideration of the activation energy, the GA optical value with the reaction-order was in agreement with the value calculated by using isoconversional methods. Although the activation energy calculated by isoconversional methods has no mechanistic significance and could not be utilized for extensive academic conclusions [48]. The activation parameters are possible to obtain using isoconversional methods and could provide a guidance in plastic recycling industry [21]. So, we decide to use that as a base value. Therefore, the reaction-order model coupled with GA was selected to conduct the polyethylene pyrolysis kinetic modeling. Hence, GA coupled with the reaction-order model was adopted to investigate the pyrolysis processes of WPE and WP.

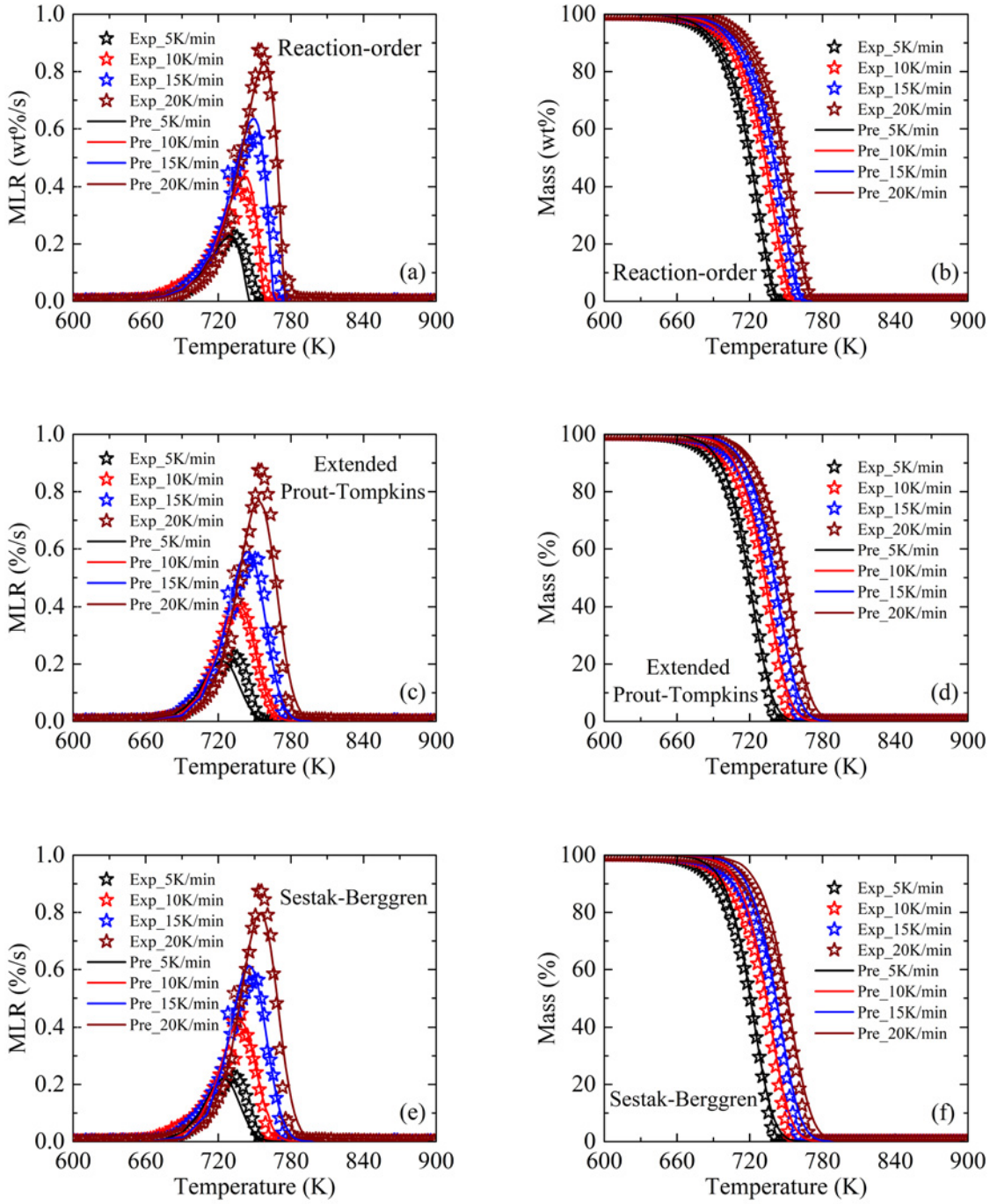

Fig. 2.6. Experimental and predicted MLR and TG curves at 5, 10, 15 and 20 K/min of pure PE by adopting reaction-order, extended Prout-Tompkins, and Sestak-Berggren models in argon.

Table 2.9. The R-squared values between experimental and predicted data of pure PE by adopting reaction-order, extended Prout-Tompkins, and Sestak-Berggren models.

Heating rate (K/min)	Reaction-order		Extended Prout-Tompkins		Sestak-Berggren	
	Mass	MLR	Mass	MLR	Mass	MLR
5	0.9948	0.9645	0.9949	0.9533	0.9966	0.9617
10	0.9992	0.9696	0.9982	0.9713	0.9968	0.9648
15	0.9995	0.9615	0.9997	0.9832	0.9992	0.9827
20	0.9990	0.9871	0.9996	0.9759	0.9991	0.9760
Average value	0.9981	0.9707	0.9981	0.9709	0.9979	0.9713
Overall average value	0.9844		0.9845		0.9846	

2.3.4. Kinetic parameters calculated by GA

According to the previous subsection discussion, GA coupled with the reaction-order model was adopted for calculating the optimal pyrolysis kinetic parameters, i.e., the pre-exponential factor A, the activation energy E, and the reaction order n of pure PE, WPE and WP. As demonstrated in Table 2.10, the optimized values of pyrolysis kinetic parameters lnA, E and n are 34.52 $\ln(s^{-1})$, 241.55 kJ/mol and 0.58 of PE; 33.84 $\ln(s^{-1})$, 239.82 kJ/mol and 0.51 of WPE; and 33.06 $\ln(s^{-1})$, 234.51 kJ/mol and 0.71 of WP, respectively. The value of calculated activation energy of PE is the largest. Moreover, the value of calculated activation energy of WP is the smallest. It is consistence with the results calculated by the KAS and AIC methods. Furthermore, the differences of calculated E by using of GA and isoconversional methods are relatively small. It indicates the reliability of GA optimized values of PE, WPE and WP pyrolysis kinetic parameters.

Table 2.10. Optimized value of pure PE, WPE, and WP pyrolysis kinetic parameters by adopting reaction-order model.

Parameters	Optimized values		
	PE	WPE	WP
lnA ($\ln(s^{-1})$)	34.52	33.84	33.06
E (kJ/mol)	241.55	239.82	234.51

n	0.58	0.51	0.71

Fig. 2.7 illustrates the experimental and predicted MLR and TG curves of PE, WPE and WP at different heating rates under argon atmosphere. The predicted MLR and mass fraction were calculated by Eqs. (2.2) and (2.3), respectively. Due to the kinetic parameters were all calculated by GA, the variables were just the temperature and the pyrolysis time. The temperature was only determined by the heating rate within the specific pyrolysis time. Therefore, the MLR and mass fraction at different heating rates could be calculated subsequently. It indicated that a high degree of consistency between experimental and predicted data was obtained. Additionally, the R-squared values between experimental and predicted data at different heating rates were listed in Table 2.11. The R-squared values of WPE mass fraction are greater than 0.999 at each heating rate. However, the R-squared values of MLR of WPE are relatively lower, which the average value is around 0.980. Moreover, in the cases of PE and WP show the same tendency as WPE. In summary, the predicted PE, WPE and WP pyrolysis kinetic parameters are relatively reliable and accurate. Furthermore, GA coupled with TGA could be applied to the more practical pyrolysis circumstances, in which have variable heating rates. This will be discussed in the future work.

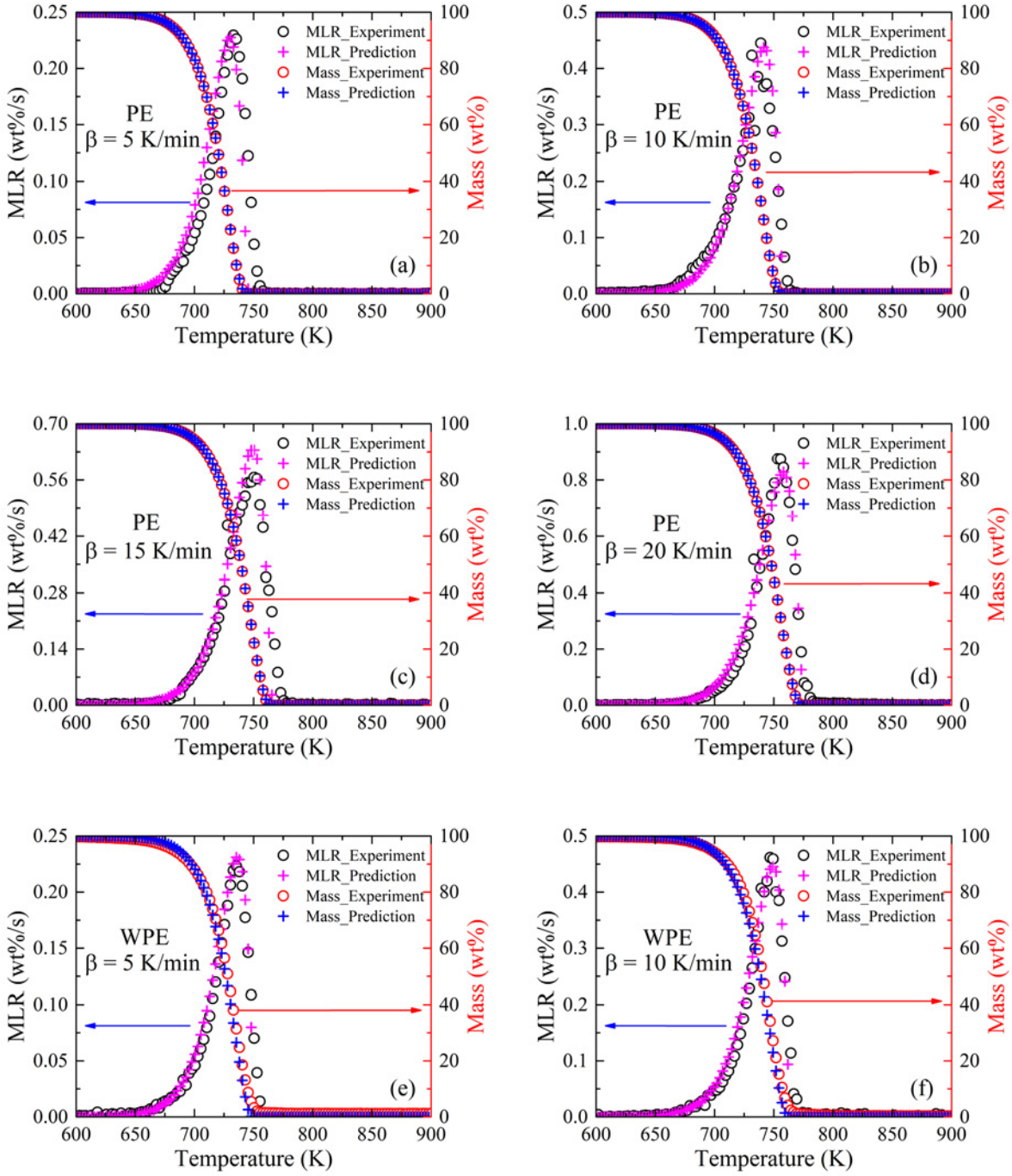
PE
β = 5 K/min
(a)
PE
β = 10 K/min
(b)
PE
β = 15 K/min
(c)
PE
β = 20 K/min
(d)
WPE
β = 5 K/min
(e)
WPE
β = 10 K/min
(f)
MLR_Experiment
MLR_Prediction
Mass_Experiment
Mass_Prediction
MLR (wt%/s)
Mass (wt%)
Temperature (K)

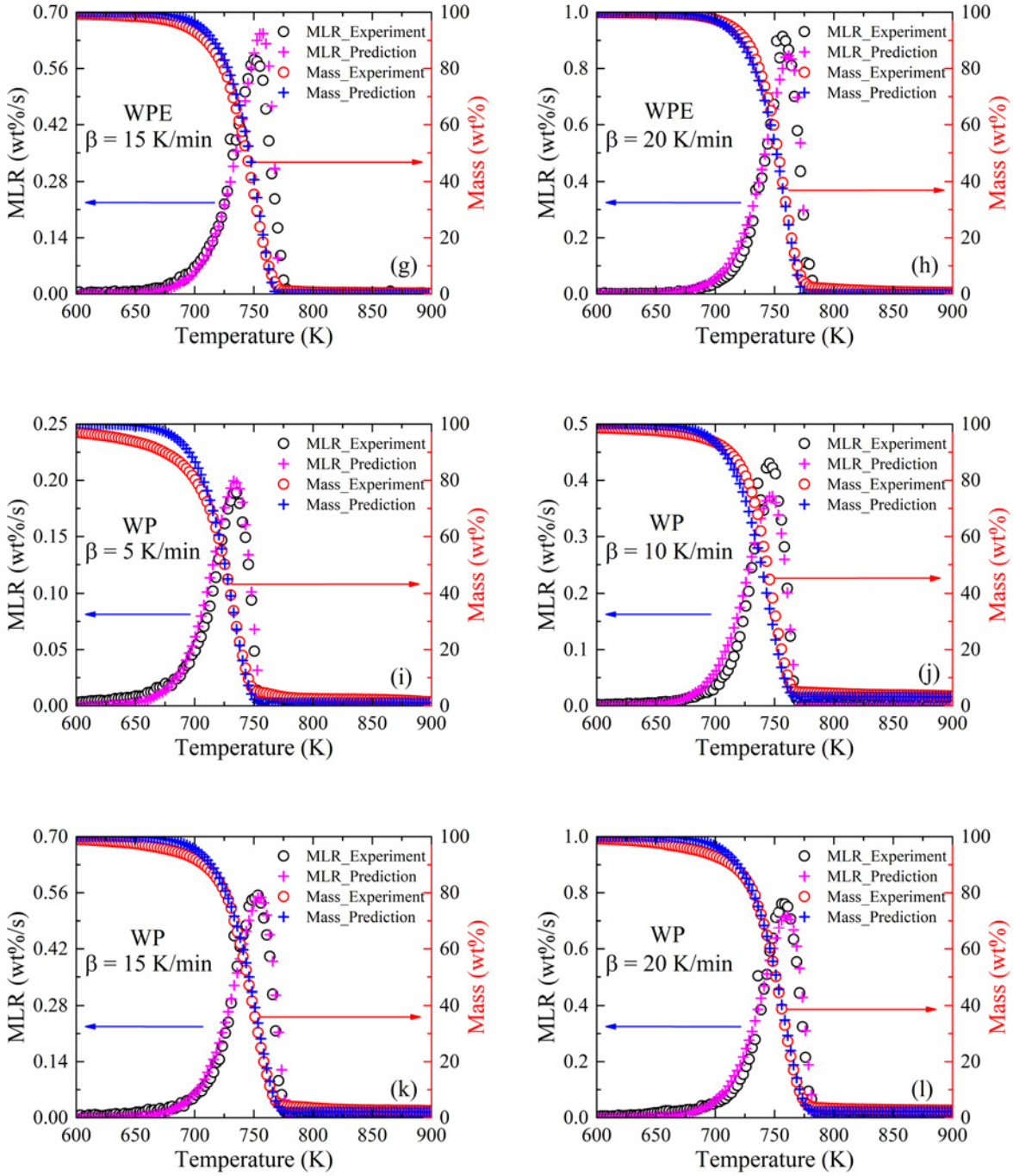

Fig. 2.7. Experimental and predicted MLR and TG curves at 5, 10, 15 and 20 K/min of pure PE, WPE, and WP in argon.

Table 2.11. The R-squared values between experimental and predicted data of pure PE, WPE, and WP at different heating rates.

Heating rate (K/min)	PE		WPE		WP	
	Mass	MLR	Mass	MLR	Mass	MLR
5	0.9948	0.9645	0.9992	0.9945	0.9966	0.9956
10	0.9992	0.9696	0.9993	0.9800	0.9966	0.9434
15	0.9995	0.9615	0.9990	0.9543	0.9990	0.9752
20	0.9990	0.9871	0.9992	0.9799	0.9992	0.9801
Average value	0.9981	0.9707	0.9992	0.9772	0.9979	0.9736
Overall average value	0.9844		0.9882		0.9857	

2.4. Conclusions

This chapter investigated the pyrolysis processes of waste polyethylene (WPE), waste plastic (WP), and pure polyethylene (PE) as a reference. Based on the pure PE, WPE and WP pyrolysis thermogravimetric experimental data at heating rates from 5 to 20 K/min under argon atmosphere, this chapter investigated the activation energy by using of three isoconversional methods, which are KAS, Friedman, and AIC methods. Three representative reaction models, i.e., reaction-order, extended Prout-Tompkins, and Sestak-Berggren models, were also investigated for determining the proper model that could describe the pyrolysis process with accuracy. Accordingly, genetic algorithm (GA) coupled with the reaction-order model was adopted for calculating the optimal pyrolysis kinetic parameters of pure PE, WPE and WP. The GA predicted optimal activation energy values are 241.55, 239.82 and 234.51 kJ/mol of pure PE, WPE and WP, respectively. It was found that the calculated activation energy values by using of GA were in good agreement with that by using of isoconversional methods. Furthermore, it compared the predicted mass fraction and mass loss rate (MLR), calculated by the GA optimized parameters, with the experimental ones. According to the results, high

consistencies between experimental and GA predicted data were obtained in pure PE, WPE and WP pyrolysis processes at heating rates of 5, 10, 15 and 20 K/min. Hence, it indicates that the predicted PE, WPE and WP pyrolysis kinetic parameters by using of GA are relatively reliable and accurate. Moreover, it might be applicable of genetic algorithm coupled with thermogravimetry analysis to the future industrial WPE and WP pyrolysis circumstances that have variable heating rates.

Bibliography

[1] Crippa, M., De Wilde, B., Koopmans, R., Leyssens, J., Muncke, J., Ritschkoff, A.C., Van Doorsselaer, K., Velis, C. and Wagner, M., 2019. A circular economy for plastics: Insights from research and innovation to inform policy and funding decisions.

[2] Sharuddin, S.D.A., Abnisa, F., Daud, W.M.A.W. and Aroua, M.K., 2016. A review on pyrolysis of plastic wastes. Energy conversion and management, 115, pp.308-326.

[3] Al-Salem, S.M., Antelava, A., Constantinou, A., Manos, G. and Dutta, A., 2017. A review on thermal and catalytic pyrolysis of plastic solid waste (PSW). Journal of environmental management, 197, pp.177-198.

[4] Jambeck, J.R., Geyer, R., Wilcox, C., Siegler, T.R., Perryman, M., Andrady, A., Narayan, R. and Law, K.L., 2015. Plastic waste inputs from land into the ocean. Science, 347(6223), pp.768-771.

[5] Al-Salem, S.M., Lettieri, P. and Baeyens, J., 2009. Recycling and recovery routes of plastic solid waste (PSW): A review. Waste management, 29(10), pp.2625-2643.

[6] Al-Salem, S.M., Lettieri, P. and Baeyens, J., 2010. The valorization of plastic solid waste (PSW) by primary to quaternary routes: From re-use to energy and chemicals. Progress in Energy and Combustion Science, 36(1), pp.103-129.

[7] Panda, A.K., Alotaibi, A., Kozhevnikov, I.V. and Shiju, N.R., 2020. Pyrolysis of plastics to liquid fuel using sulphated zirconium hydroxide catalyst. Waste and Biomass Valorization, 11(11), pp.6337-6345.

[8] Dash, A., Kumar, S. and Singh, R.K., 2015. Thermolysis of medical waste (Waste Syringe)

to liquid fuel using semi batch reactor. Waste and biomass valorization, 6(4), pp.507-514.

[9] Grigiante, M., Ischia, M., Baratieri, M., Dal Maschio, R. and Ragazzi, M., 2010. Pyrolysis analysis and solid residue stabilization of polymers, waste tyres, spruce sawdust and sewage sludge. Waste and Biomass Valorization, 1(4), pp.381-393.

[10] Sun, K., Huang, Q., Ali, M., Chi, Y. and Yan, J., 2018. Producing aromatic-enriched oil from mixed plastics using activated biochar as catalyst. Energy & Fuels, 32(4), pp.5471-5479.

[11] Kumar, S., Panda, A.K. and Singh, R.K., 2011. A review on tertiary recycling of high-density polyethylene to fuel. Resources, Conservation and Recycling, 55(11), pp.893-910.

[12] Brems, A., Baeyens, J. and Dewil, R., 2012. Recycling and recovery of post-consumer plastic solid waste in a European context. Thermal Science, 16(3), pp.669-685.

[13] Ragaert, K., Delva, L. and Van Geem, K., 2017. Mechanical and chemical recycling of solid plastic waste. Waste management, 69, pp.24-58.

[14] Sun, K., Huang, Q., Meng, X., Chi, Y. and Yan, J., 2018. Catalytic pyrolysis of waste polyethylene into aromatics by H3PO4-activated carbon. Energy & Fuels, 32(9), pp.9772-9781.

[15] Onwudili, J.A., Insura, N. and Williams, P.T., 2009. Composition of products from the pyrolysis of polyethylene and polystyrene in a closed batch reactor: Effects of temperature and residence time. Journal of Analytical and Applied Pyrolysis, 86(2), pp.293-303.

[16] Kple, M., Girods, P., Fagla, B., Anjorin, M., Ziegler-Devin, I. and Rogaume, Y., 2017. Kinetic study of low density polyethylene using thermogravimetric analysis, Part 2:

Isothermal study. Waste and biomass valorization, 8(3), pp.707-719.

[17] Berčič, G., Djinović, P. and Pintar, A., 2019. Simplified approach to modelling the catalytic degradation of low-density polyethylene (LDPE) by applying catalyst-free LDPE-TG profiles and the Friedman method. Journal of Thermal Analysis and Calorimetry, 136(3), pp.1011-1020.

[18] Zheng, Y., Tao, L., Yang, X., Huang, Y., Liu, C. and Zheng, Z., 2018. Study of the thermal behavior, kinetics, and product characterization of biomass and low-density polyethylene co-pyrolysis by thermogravimetric analysis and pyrolysis-GC/MS. Journal of Analytical and Applied Pyrolysis, 133, pp.185-197.

[19] Xiang, Z., Liang, J., Morgan Jr, H.M., Liu, Y., Mao, H. and Bu, Q., 2018. Thermal behavior and kinetic study for co-pyrolysis of lignocellulosic biomass with polyethylene over Cobalt modified ZSM-5 catalyst by thermogravimetric analysis. Bioresource technology, 247, pp.804-811.

[20] Das, P. and Tiwari, P., 2017. Thermal degradation kinetics of plastics and model selection. Thermochimica Acta, 654, pp.191-202.

[21] Aboulkas, A. and El Bouadili, A., 2010. Thermal degradation behaviors of polyethylene and polypropylene. Part I: Pyrolysis kinetics and mechanisms. Energy Conversion and Management, 51(7), pp.1363-1369.

[22] Nzioka, A.M., Kim, M.G., Hwang, H.U. and Kim, Y.J., 2019. Kinetic study of the thermal decomposition process of municipal solid waste using TGA. Waste and Biomass Valorization, 10(6), pp.1679-1691.

[23] El Abbari, H., Bentahar, S., El Marouani, M., Taibi, M., Zeriouh, A., Sebbahi, S. and Kifani-Sahban, F., 2019. Thermal and thermomechanical behavior of Moroccan Boufeggous variety date seeds. Journal of Thermal Analysis and Calorimetry, 137(5), pp.1485-1492.

[24] Ippolito, N.M., Cafiero, L., Tuffi, R. and Vecchio Ciprioti, S., 2019. Characterization of the residue of a commingled post-consumer plastic waste treatment plant: A thermal, spectroscopic and pyrolysis kinetic study. Journal of Thermal Analysis and Calorimetry, 138(5), pp.3323-3333.

[25] Wang, J. and Zhao, H., 2016. Error evaluation on pyrolysis kinetics of sawdust using iso-conversional methods. Journal of Thermal Analysis and Calorimetry, 124(3), pp.1635-1640.

[26] Wang, Z., Wei, R., Ning, X., Xie, T. and Wang, J., 2019. Thermal degradation properties of LDPE insulation for new and aged fine wires. Journal of Thermal Analysis and Calorimetry, 137(2), pp.461-471.

[27] Friedman, H.L., 1964. Kinetics of thermal degradation of char‐forming plastics from thermogravimetry. Application to a phenolic plastic. In Journal of polymer science part C: polymer symposia (Vol. 6, No. 1, pp. 183-195). New York: Wiley Subscription Services, Inc., A Wiley Company.

[28] Akahira, T. and Sunose, T., 1971. Method of determining activation deterioration constant of electrical insulating materials. Res Rep Chiba Inst Technol (Sci Technol), 16(1971), pp.22-31.

[29] Flynn, J.H. and Wall, L.A., 1966. General treatment of the thermogravimetry of polymers.

Journal of research of the National Bureau of Standards. Section A, Physics and chemistry, 70(6), p.487.

[30] Vyazovkin, S., Burnham, A.K., Criado, J.M., Pérez-Maqueda, L.A., Popescu, C. and Sbirrazzuoli, N., 2011. ICTAC Kinetics Committee recommendations for performing kinetic computations on thermal analysis data. Thermochimica acta, 520(1-2), pp.1-19.

[31] Coats, A.W. and Redfern, J.P., 1964. Kinetic parameters from thermogravimetric data. Nature, 201(4914), pp.68-69.

[32] Yang, K.K., Wang, X.L., Wang, Y.Z., Wu, B., Jin, Y.D. and Yang, B., 2003. Kinetics of thermal degradation and thermal oxidative degradation of poly (p-dioxanone). European polymer journal, 39(8), pp.1567-1574.

[33] Criado, J.M., 1978. Kinetic analysis of DTG data from master curves. Thermochimica Acta, 24(1), pp.186-189.

[34] Starink, M.J., 2003. The determination of activation energy from linear heating rate experiments: a comparison of the accuracy of isoconversion methods. Thermochimica acta, 404(1-2), pp.163-176.

[35] Duque, J.V.F., Martins, M.F., Debenest, G. and Orlando, M.T.D.A., 2020. The influence of the recycling stress history on LDPE waste pyrolysis. Polymer Testing, 86, p.106460.

[36] Lautenberger, C., Rein, G. and Fernandez-Pello, C., 2006. The application of a genetic algorithm to estimate material properties for fire modeling from bench-scale fire test data. Fire safety journal, 41(3), pp.204-214.

[37] Park, T.Y. and Froment, G.F., 1998. A hybrid genetic algorithm for the estimation of

parameters in detailed kinetic models. Computers & Chemical Engineering, 22, pp.S103-S110.

[38] Elliott, L., Ingham, D.B., Kyne, A.G., Mera, N.S., Pourkashanian, M. and Wilson, C.W., 2004. Genetic algorithms for optimisation of chemical kinetics reaction mechanisms. Progress in Energy and Combustion Science, 30(3), pp.297-328.

[39] Rein, G., Lautenberger, C., Fernandez-Pello, A.C., Torero, J.L. and Urban, D.L., 2006. Application of genetic algorithms and thermogravimetry to determine the kinetics of polyurethane foam in smoldering combustion. Combustion and flame, 146(1-2), pp.95-108.

[40] Lapene, A., Debenest, G., Quintard, M., Castanier, L.M., Gerritsen, M.G. and Kovscek, A.R., 2015. Kinetics oxidation of heavy oil. 2. Application of genetic algorithm for evaluation of kinetic parameters. Energy & Fuels, 29(2), pp.1119-1129.

[41] Jiang, L., Xiao, H.H., He, J.J., Sun, Q., Gong, L. and Sun, J.H., 2015. Application of genetic algorithm to pyrolysis of typical polymers. Fuel Processing Technology, 138, pp.48-55.

[42] Chen, R., Xu, X., Zhang, Y., Lo, S. and Lu, S., 2018. Kinetic study on pyrolysis of waste phenolic fibre-reinforced plastic. Applied Thermal Engineering, 136, pp.484-491.

[43] Šesták, J. and Berggren, G., 1971. Study of the kinetics of the mechanism of solid-state reactions at increasing temperatures. Thermochimica Acta, 3(1), pp.1-12.

[44] Encinar, J.M., Gonzalez, J.F., 2008. Pyrolysis of synthetic polymers and plastic wastes. Kinetic study. Fuel Processing Technology, 89(7), pp.678-686.

[45] Vyazovkin, S., Sbirrazzuoli, N., 2006. Isoconversional kinetic analysis of thermally stimulated processes in polymers. Macromolecular Rapid Communications, 27(18),

pp.1515-1532.

[46] Peterson, J.D., Vyazovkin, S., Wight, C.A., 2001. Kinetics of the thermal and thermo‐oxidative degradation of polystyrene, polyethylene and poly (propylene). Macromolecular Chemistry and Physics, 202(6), pp.775-784.

[47] Xu, F.F., Wang, B., Yang, D., Hao, J.H., Qiao, Y.Y., Tian, Y.Y., 2018. Thermal degradation of typical plastics under high heating rate conditions by TG-FTIR: Pyrolysis behaviors and kinetic analysis. Energy Conversion and Management, 171, pp.1106-1115.

[48] Simon, P., 2004. Isoconversional methods. Journal of Thermal Analysis and Calorimetry, 76(1), pp.123-132.

Chapter 3

Waste plastic thermal pyrolysis analysis by an artificial neural network coupled with a genetic algorithm

Summary

In Chapter 2, the genetic algorithm (GA) coupled with thermogravimetric analysis (TGA) was used to conduct the kinetic modeling of waste plastic (WP) thermal pyrolysis. The results indicated that the predicted WP conversion and pyrolysis rate, calculated by the GA optimized parameters, agreed well with the experimental ones. However, this method was based on the reaction-order model. Moreover, it simplified WP pyrolysis into a one-step reaction, which might not be applicable in the real-life WP with complex components. Therefore, a more robust model-free method should be developed to simulate the WP pyrolysis behavior.

This chapter investigated the WP pyrolysis to provide a direction for prospective industrial and commercial productions. The process temperature, the WP conversion and the pyrolysis rate are the decisive factors for industrial applications. Therefore, thermogravimetric (TG) experiments were conducted at different heating rates to obtain the experimental WP mass fraction, the WP conversion, and the pyrolysis rate, which varied with the temperature and heating rate. Furthermore, an artificial neural network (ANN) and a genetic algorithm (GA) were adopted to determine the optimal operating conditions over different temperature ranges. The ANN predicted WP conversion and pyrolysis rate were highly consistent with the experimental results, indicating the high accuracy of the ANN method for this application. Moreover, the WP conversion and the pyrolysis rate optimized by the GA were 97.68 % at 5.00 ℃/min and 497.89 ℃, and 60.66 wt%/min at 20.00 ℃/min and 492.09 ℃, respectively.

Candidate contribution: Conceptualization, methodology, experimental design and execution, formal analysis, resources, data curation, writing - original draft, visualization.

3.1. Introduction

Waste plastic (WP) has caused large-scale environmental pollution and a health hazard to many organisms. Historically, a large amount of WP was disposed of via landfill or incineration [1]. Several methods have been proposed for treating WP in a more responsible way, namely, mechanical recycling, chemical recycling, and energy recovery methods [2]. Among these methods, chemical recycling is a favorable method which can utilize the WP to produce fuels [3]. Moreover, WP thermal pyrolysis, which is performed in the absence of oxygen [4], is a most promising chemical recycling method. It can strongly reduce WP pollution while producing useful by-products such as biochar, bio-oil and syngas [5][6][7][8]. According to the literature [4], the temperature and heating rate are the determining factors in the WP pyrolysis process. Besides these, considering the economical aspect, the temperature, the conversion and the pyrolysis rate are also critical parameters for practical applications of WP pyrolysis [9][10][11].

Much research in thermogravimetric analysis (TG) has been conducted to try to obtain a better understanding about the WP pyrolysis process. Paraschiv et al. [12] adopted TG experimental results to determine the optimal operating parameters for hospital-based WP pyrolysis on different scales for a fixed bed reactor. Chen et al. [13] utilized TG analysis to investigate the WP co-pyrolysis process. Additionally, Navarro et al. [14] used TG analysis coupled with a distributed activation energy model to conduct a WP co-pyrolysis kinetic study. Chen et al. [15] investigating a waste phenolic fibre-reinforced plastic thermal pyrolysis process based on TG experiments with different heating rates. Singh et al. [16] adopted TG analysis to

investigate the influence of the heating rate on the WP pyrolysis process. Moreover, Ippolito et al. [17] conducted TG experiments to determine the WP pyrolysis kinetic values. In conclusion, TG analysis is a promising method to investigate the WP pyrolysis process as it can provide important parameters - the WP relative weight over time and the temperature at different heating rates [18][19]. However, TG experiments so-far could only provide the discrete mass fraction curves at disparate heating rates. This creates difficulties in determining the optimal conditions of the WP pyrolysis process. For the purpose of investigating the optimal conversion, Teng et al. [19] creatively adopted an artificial neural network (ANN) coupled with TG analysis and applied it to the Chlorella vulgaris pyrolysis process. In consequence, the Chlorella vulgaris conversion turned out to be a continuous function of the temperature and the heating rate. Subsequently, a mathematical algorithm was utilized to obtain the optimal operating parameters over different temperature ranges. Therefore, the application of artificial intelligence coupled with TG analysis could, ideally, determine the optimal operating conditions of the WP pyrolysis process.

The artificial neural network (ANN), from artificial intelligence theory, is a promising method which could establish an arithmetic expression to describe the relationship between multiple independent variables and dependent variables [20]. Sadeghizadeh et al. [21] and Ronda et al. [22] investigated the effects of multiple operating conditions on the Pb (II) adsorption efficiency using ANN. Calero et al. [23] adopted ANN to determine the optimal copper biosorption capacity under the influence of three operational parameters. Iáñez-Rodríguez et al. [24] conducted research on the optimal temperature and residence time during

a crop torrefaction process using ANN. Nevertheless, the values of the response variables predicted by the afore-mentioned researchers using ANN were discrete. Arithmetic expressions, established by ANN between the multiple operating parameters and the response variables however, are continuous. Therefore, the robustness of predicted optimal operating conditions can be improved. Hence, it is necessary to adopt a mathematical calculation method for determining the optimal operating parameters in accordance with the arithmetic expression established using ANN.

Regarding the global extremum calculation, the genetic algorithm (GA) is a promising method to find the optimal operating parameters based on the existing mathematical models. Javed et al. [25] utilized GA for optimization of a hybrid energy storage system. Tuchler et al. [26] optimized the radial compressor of an automobile by evaluating the isentropic efficiency with the GA. Ascione et al. [27] conducted an optimization design of an envelope enclosure with the GA with multiple objective functional assessments. Rezaie et al. [28] adopted multiple objective functions to evaluate heat recovery in a steam generator. Subsequently, GA was used to optimize the thermal design.

As there has been little research into the optimal WP conversion and pyrolysis rates with different temperatures and heating rates, this work aims to fully investigate the WP pyrolysis process, to provide guidance for industrial and commercial applications. This study investigated the optimal operating parameters - the temperature and the heating rate of the WP thermal pyrolysis conversions and the pyrolysis rates over different temperature ranges. Four TG experiments with different heating rates were conducted to obtain the experimental WP mass

fraction during the pyrolysis process. Subsequently, the experimental WP conversion (calculated as WP conversion = 1 – WP relative weight) and the pyrolysis rate (by derivation) were obtained. As previously discussed, ANN was adopted to establish arithmetic expressions to describe the relationships between the independent and dependent variables. The ANN predicted WP mass fraction, conversion, and pyrolysis rate were highly accurate. Finally, the optimal operating conditions were determined using GA.

3.2. Experiments and methods

3.2.1. TG experiments

The WP used for pyrolysis experiments, illustrated in Fig. 3.1a, was provided by Wanbei Plastic Recycling Development Base (Anhui-China). The WP is mainly composed of polyethylene (PE). In order to ensure the uniform composition of the WP, the WP was heated and melted and made into 3mm pellets. As shown in Fig. 3.1b, the WP's main functional groups are $–CH_2–$, –CH, $–CH_3$, and –OH [29]. The TG experiments were conducted at temperatures ranging from 25 ℃ to 600 ℃ at five representative heating rates - 5, 10, 12, 15 and 20 ℃/min [30][31][32]. Consequently, the WP mass fraction m variation with time was obtained for different heating rates. Hence, the conversion α and the pyrolysis rate r_p were determined by the following equations.

$$\alpha = 1 - m \tag{3.1}$$

$$r_p = (m_{i+1} - m_i)/(t_{i+1} - t_i) \tag{3.2}$$

where m_i and t_i represent the ith mass fraction (wt%) and time (min) and m_{i+1} and t_{i+1} represent the $(i+1)th$ mass fraction (wt%) and time (min).

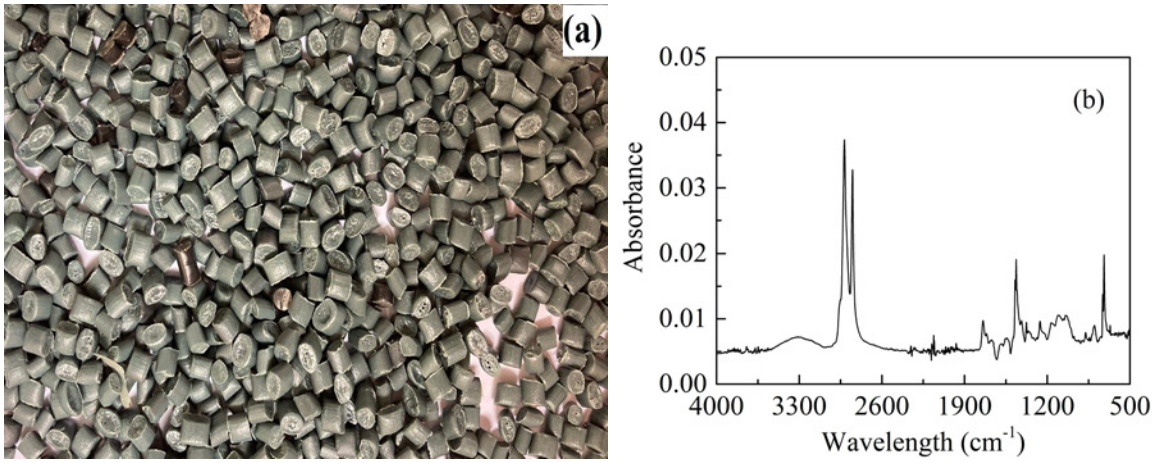

Fig.3.1. WP used for pyrolysis experiments in this study: (a) WP pellets; (b) FTIR spectrum.

3.2.2. Methods

(i) ANN

ANN is inspired by the humanoid reasoning and the neural network' structure. ANN was adopted for predicting the mass fractions and the WP conversion and pyrolysis rates based on the TG experimental data previously described. In the present study, there were two independent variables, i.e., the temperature and the heating rate. The certain dependent variable could be predicted by the following equation [20][21]:

$$y_{pre} = \Sigma_{i=1}^{n}(a_i \cdot FR_i)/\Sigma_{i=1}^{n} FR_i \quad (3.3)$$

where y_{pre}, n, a_i and FR_i represent the predicted value, the number of rules, the constant of each rule and the fuzzy rule, respectively.

The fuzzy rule can be expressed with the following equation:

$$FR_i = \Pi_{i=1}^{m}\mu_i(x_i, x_i(\Theta)) \quad (3.4)$$

where m, x_i, $x_i(\Theta)$ and $\mu_i(x_i(\Theta))$ represent the number of independent values, the evaluation value of the level of the independent variable, the value of independent variable and the

membership function, respectively.

According to previous studies [20][23], the Gaussian membership function $\mu_i(x_i(\Theta))$ can predict the dependent variables most accurately. Therefore, in the present study, the Gaussian membership function $\mu_i(x)$ was adopted. It can be expressed using the following equation:

$$\mu_i(x_i, x_i(\Theta)) = \exp\left(-0.5 \cdot ((x_i - x_i(\Theta))/L)^2\right) \quad (3.5)$$

where L represents the Gaussian distribution width.

(ii) GA

When the experimental data was processed with ANN, the constant of each rule a_i and the Gaussian distribution width L could be obtained. Accordingly, GA was adopted to determine the optimal operating conditions of the WP pyrolysis process. GA is literally developed according to evolution theory and is designed to obtain an optimal condition containing multiple chosen parameters [33][34][35][36][37].

The WP conversion, for example, was determined by two parameters, i.e., the temperature and the heating rate. Hence, a single value for the WP conversion was considered to be an individual. It contained two “genes”, the temperature and the heating rate. A population was studied, composed of N individuals. In the first generation, these N individuals were treated as “parents”. N children were reproduced after N sets of parents underwent mutation and crossover processes. The next step was to calculate the fitness values of these N children. Children with worse fitness were replaced by children with better fitness to complete the first generation. In the next generation, these N children would be treated as the “parents” and follow the same processes as mentioned before. Therefore, the GA optimization procedure could be described

using the following equations:

The mutation is expressed according to the following equation:

$$child_i^j = v_{mut} \cdot (1 - t/iter)^2 \cdot parent_i^j \tag{3.6}$$

where *i*, *j*, v_{mut}, *t*, and *iter* represent the number of individuals, the number of genes, the probability of mutation, the number of the generation and the number of total generations, respectively.

The crossover is expressed using the following equation:

$$if\ r_{i,cro} < v_{cro}, child_i^j = child_n^j \tag{3.7}$$

where $r_{i,cro}$, v_{cro}, and *n* represent a random number value between 0 and 1, the probability of a crossover and the random number iteration between 1 and N, respectively.

The fitness of an individual and the highest fitness could be expressed using the following equations:

$$fitness_i = \Sigma_{i=1}^{n}(a_i \cdot FR_i)/\Sigma_{i=1}^{n} FR_i \tag{3.8}$$

$$fitness_{best} = \max\ (fitness_i) \tag{3.9}$$

where $fitness_i$ and $fitness_{best}$ represent the fitness of the *i-th* individual and the maximum value of fitness, respectively. The best child is the one with the maximum fitness value.

The replacement can be expressed with the following equation:

$$If\ fitness_i < 0.2 \cdot (max(fitness_i) - min(fitness_i)) + min(fitness_i),$$

$$child_i^j = child_{i,best}^j \tag{3.10}$$

where $child_{i,best}^j$ represents the best child.

In the present study, the number of individuals N and generations *iter* are 1000 and 1000.

The probabilities of mutation v_{mut} and crossover v_{cro} are 0.2 and 0.2. Moreover, ANN used in the present study is from the Matlab software toolbox. GA was also coded in Matlab.

3.3. Results and discussion

3.3.1. TG analysis

Fig. 3.2 illustrates the experimental WP mass fractions and pyrolysis rates (which vary with the pyrolysis temperature) for heating rates of 5, 10, 12, 15 and 20 ℃/min. The pyrolysis onset temperature To, the end pyrolysis temperature Te and the maximum pyrolysis temperature Tm are also shown. To, Te and Tm were proposed to describe the pyrolysis process more precisely [38][39][40]. The onset pyrolysis temperature To occurs at the intersection of the tangent to the pyrolysis rate rise curve and the temperature-axis; The end pyrolysis temperature Tm occurs at the intersection of the tangent to the falling part of the pyrolysis rate curve and the temperature-axis; The maximum pyrolysis temperature Tm is the temperature coordinate value at the pyrolysis rate curve's peak. As shown in Fig. 3.2a, the WP mass fraction curves have the same trend regardless of the different heating rates. The WP mass fraction curve decreases slowly at the initial pyrolysis stage and the WP decomposed at a relatively high speed over a narrow temperature range. Finally, at high temperatures, the WP mass fraction curve flattened out again. Besides that, the WP mass fraction curve shifted laterally to a higher temperature when the heating rate was increased from 5 to 20 ℃/min.

In terms of the pyrolysis rate, the WP had one peak at all heating rates. The single peak only represents the overall conversion rate, which does not indicate the WP is pyrolyzed in a one-step mechanism [41][42]. The WP is decomposed into short-chain hydrocarbons via

random and Beta scission reactions [43][44]. The peak of WP pyrolysis rate curves shifted laterally to a higher temperature when the heating rate was increased from 5 to 20 ℃/min, which had the same trend as the WP mass fraction curves. Higher heating rates resulted in the thermal hysteresis from the TG instrument to WP, thereby extending the time to reach the WP's initial pyrolysis heat [45]. On the other hand, higher heating rates could accelerate the WP pyrolysis process by providing sufficient heat [46]. Therefore, the maximum pyrolysis rate increased with the increasing heating rate. The WP pyrolysis rate curves were more complex compared to those for the individual plastic types [13][14], e.g., PE, PS, PET, etc. This is because that the pyrolysis mechanism transformations are caused by the co-pyrolysis effects from the different individual plastics [15][16].

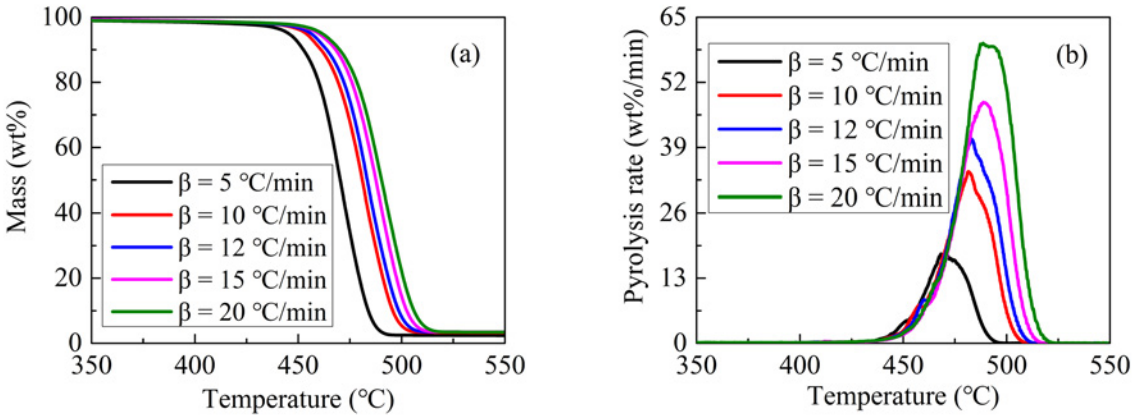

Fig.3.2. Experimental WP (a) mass fractions and (b) pyrolysis rates at different heating rates.

To, Te, Tm, and the maximum pyrolysis rates of the WP at different heating rates are listed in Table 3.1. The values of To, Te and Tm increased with the heating rate, which is consistent with the literature results [47][48]. While it was noticeable that the difference between To and Te was quite constant, at the different heating rates, they shifted by up to 50 ℃. Moreover, the

WP was undergoing pyrolysis at a relatively high-speed considering the maximum pyrolysis rate values. For instance, the maximum WP pyrolysis rate could reach up to 59.82 wt%/min at a heating rate of 20 ℃/min. Additionally, the pyrolysis rate also increased with the heating rate.

Table 3.1. To, Te, Tm, and the WP maximum pyrolysis rates for different heating rates.

Heating rate (℃/min)	To (℃)	Te (℃)	Tm (℃)	Maximum pyrolysis rate (wt%/min)
5	442.54	485.14	468.05	17.60
10	451.57	498.64	478.49	34.19
12	454.58	502.39	480.72	40.65
15	459.05	506.59	486.78	48.02
20	460.15	510.19	487.77	59.82

3.3.2. ANN predicted results

In Fig. 3.3, the WP mass fraction and the pyrolysis rate were determined as functions of the temperature and the heating rate using ANN. Experimental data obtained for different heating rates - 5, 10, 15 to 20 ℃/min was used. In order to reduce the calculation time, the data set used by ANN to predict the WP mass fraction and pyrolysis rate was sampled to be one fifth the size of the experimental data. The experimental data was chosen with equal time intervals. As depicted in Fig. 3.3a, the WP mass fraction predicted by ANN followed the same trend as the experimental data. The slope of the predicted WP mass fraction surface was small in the temperature range of 300-400 ℃. Subsequently, the slope became very steep at the temperature range of 400-500 ℃. However, the predicted WP mass fraction surface became flat again after a pyrolysis temperature of 500 ℃. Regarding the effect of the heating rate on the WP mass fraction during the pyrolysis process, the surface becomes bumpy when the heating rate is close

to 10 ℃/min. In addition, the WP mass fraction decreased faster at a higher heating rate, which was consistent with the results obtained experimentally for the WP mass fraction, as depicted in Fig. 3.2.

As for the predicted pyrolysis rate of the WP, it was noteworthy that the peak value increased with the heating rate as illustrated in Fig. 3.3b. This was in good agreement with the experimental WP pyrolysis rate as shown in Fig. 3.2b. At first, the predicted pyrolysis rate increased with temperature, then at higher temperatures it decreased. The temperature of the maximum pyrolysis rate became higher when the heating rate increased.

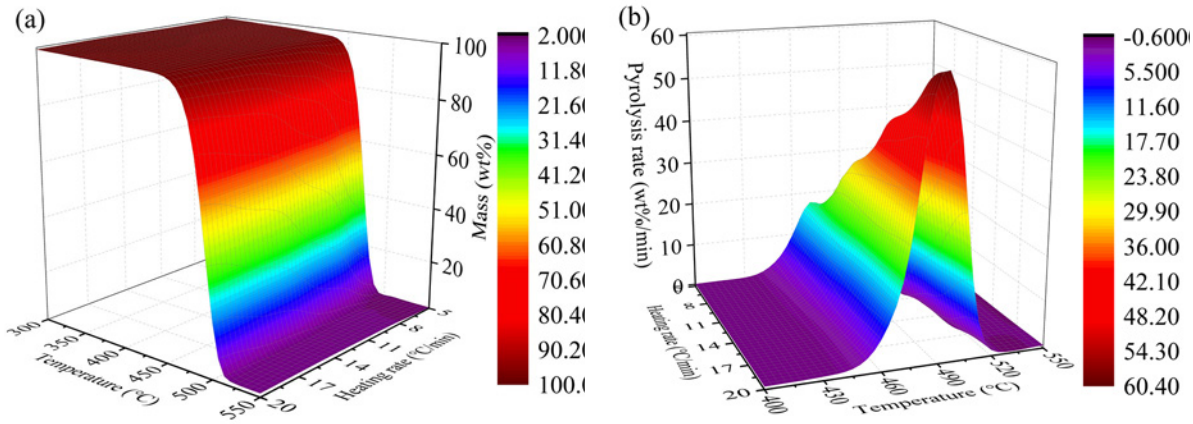

Fig.3.3. The ANN predicted (a) WP mass fraction and (b) pyrolysis rate.

3.3.3. The accuracy of ANN

In Figs. 3.4a, 3.4b, 3.4c and 3.4d the WP mass fraction and pyrolysis rate obtained experimentally were compared with the ANN predictions at different heating rates of 5, 10, 15 and 20 ℃/min, respectively. Additionally, we calculated the R-squared values between the experimental and the predicted WP mass fraction and pyrolysis rates to determine the accuracy of ANN. The R-squared values of the WP mass fraction and the pyrolysis rates at heating rates

of 5, 10, 15 and 20 ℃/min are depicted in Figs. 3.4e and 3.4f, respectively. In Figs. 3.4a-d, the predicted WP mass fraction and the pyrolysis rate are in good agreement with the experimental values regardless of the temperature and heating rate. The coincidence degrees between the experimental and the predicted WP mass fraction were very high at all heating rates. As demonstrated in Fig. 3.4e, the R-squared values of the WP mass fraction were 0.99999 at heating rates of 5, 10, 15 and 20 ℃/min. The R-squared values were close to 1 for every heating rate which indicated that the ANN predicted values were highly accurate [45].

As for the WP pyrolysis rate, the ANN predicted results also coincided with the experimental results to a great extent. For a heating rate of 5 ℃/min, as illustrated in Fig. 3.4a, the predicted and the experimental WP pyrolysis rates had the same trend. The maximum experimental WP pyrolysis rate was 17.18 wt%/min at 467.5 ℃. The maximum predicted WP pyrolysis rate was 17.73 wt%/min at 472.5 ℃. The agreement between the experimental and the predicted maximum pyrolysis rates was within 3.2 %. For the heating rate of 10 ℃/min, as depicted in Fig. 3.4b, the maximum experimental and the predicted WP pyrolysis rates were 33.80 wt%/min at 482.5 ℃, and 32.59 wt%/min at 482.5 ℃, respectively. The difference between the experimental and the predicted maximum pyrolysis rates was around 3.6 %. As shown in Fig. 3.4c, the peak values of the experimental and the predicted WP pyrolysis rate curves at 15 ℃/min were 47.81 wt%/min at 490.0 ℃, and 47.59 wt%/min at 487.5 ℃, respectively. The error of the peak values between the experimental and the predicted maximum pyrolysis rates was 0.46 %. For a heating rate of 20 ℃/min, as illustrated in Fig. 3.4d, the maximum experimental and the predicted WP pyrolysis rates were 59.51 wt%/min at 489.3 ℃,

and 60.63 wt%/min at 491.7 ℃, respectively. The difference between the experimental and the predicted maximum pyrolysis rates was 1.9 % at a rate of 20 ℃/min. As described in Fig. 3.4f, the R-squared values of the WP pyrolysis rate were 0.99674, 0.99697, 0.99923 and 0.99934 at heating rates of 5, 10, 15 and 20 ℃/min, respectively. In conclusion, the ANN allowed for a high accuracy in predicting the WP mass fractions and pyrolysis rates.

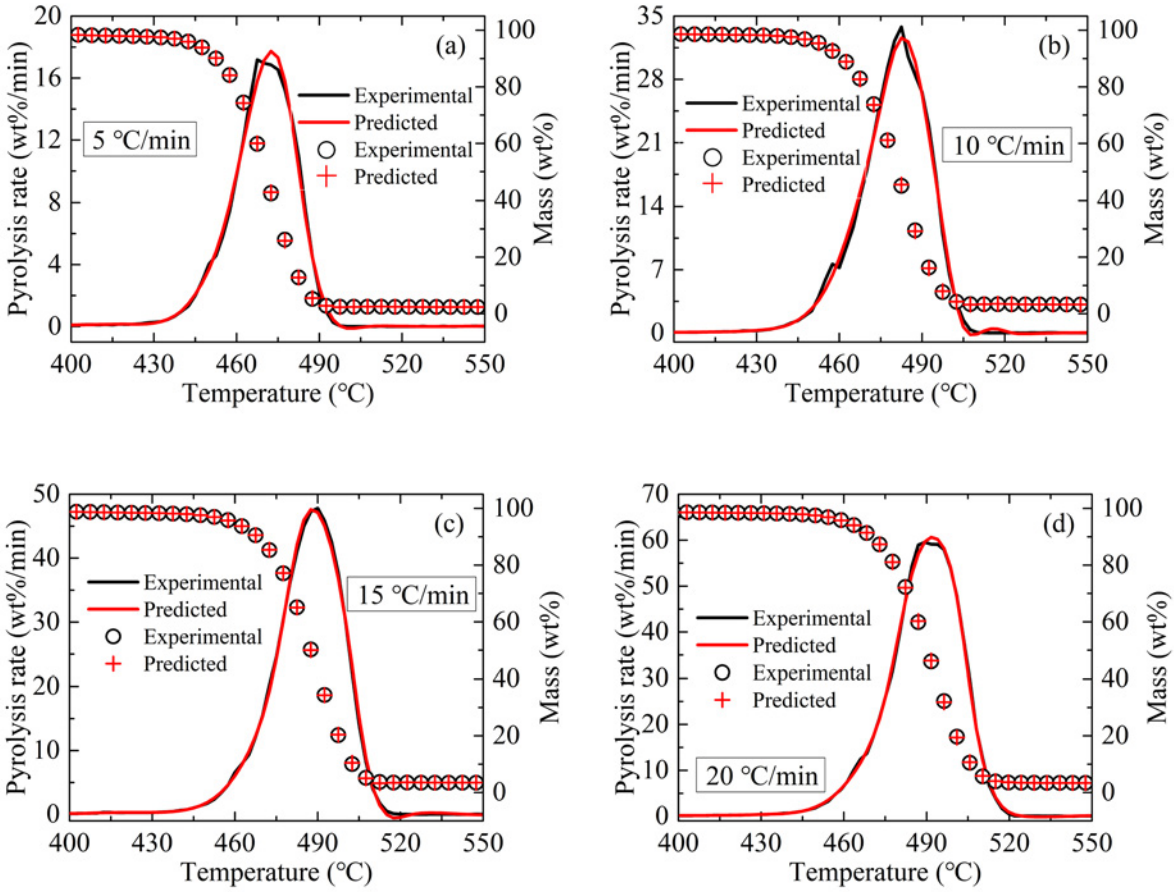

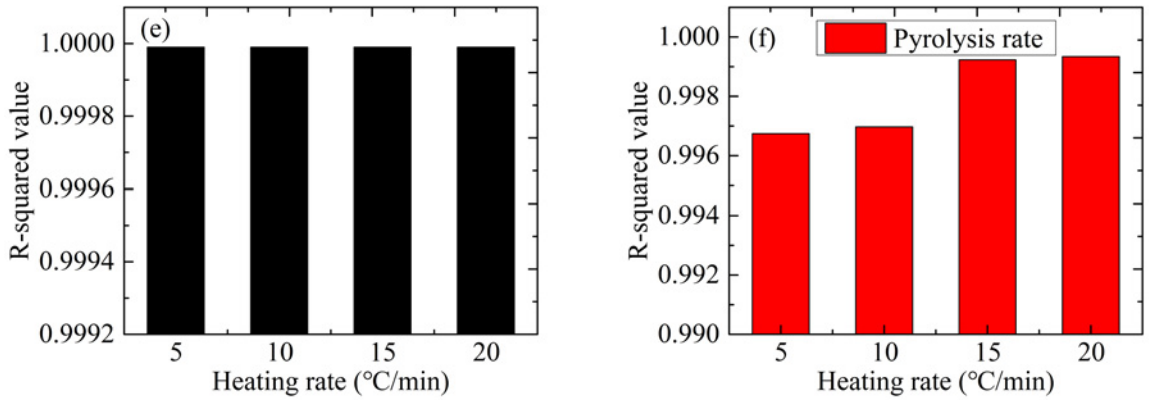

Fig.3.4. Comparisons of the experimental WP mass fraction and the pyrolysis rate with the ANN predicted values: (a) At 5 ℃/min; (b) At 10 ℃/min; (c) At 15 ℃/min; (d) At 20 ℃/min; (e) R-squared values of the WP mass fraction; (f) R-squared values of the WP pyrolysis rate.

3.3.4. GA optimization

GA is a promising optimization method to determine the multiple operating parameters needed to obtain the optimal objective results. In this study, GA is used to calculate the optimal WP conversions and pyrolysis rates in different pyrolysis temperature ranges, based on ANN predicted data. From the experimental WP mass fractions described in Fig. 3.2, it could be concluded that the WP pyrolysis process started at about 300 ℃ and finished at around 550 ℃. Simultaneously, the WP pyrolysis process proceeded relatively slowly before 400 ℃. Hence, according to [19], 6 temperature ranges were chosen to investigate the optimal WP conversions: 300-400 ℃, 400-430 ℃, 430-460 ℃, 460-490 ℃, 490-520 ℃, and 520-550 ℃, in this sequence. The optimal WP conversions in different temperature ranges calculated using GA are shown in Figs. 3.5a-f. As depicted in Fig. 3.5a, generally a larger WP conversion was obtained for a higher pyrolysis temperature and lower heating rate. For instance, the WP conversion increased from 0.66 % to 1.37 % when the pyrolysis temperature increased from 300 ℃ to 400 ℃ at

20 ℃/min. Furthermore, the WP conversions were enhanced from 1.37 % to 1.64 % when the heating rate decreased from 20 to 5 ℃/min. Additionally, a hollow appeared at around 15 ℃/min on the WP conversion surface, as seen in Fig. 3.5a. The same situation occurred for the temperature range of 400-430 ℃ shown in Fig. 3.5b. Subsequently, the optimal WP conversion determined using the GA was 1.64 % at 5.00 ℃/min and 400 ℃. The optimal WP conversions were 2.35 % at 5.00 ℃/min and 430.00 ℃, 20.31 % at 5.00 ℃/min and 460.00 ℃, 96.24 % at 5.00 ℃/min and 490.00 ℃, 97.68 % at 5.00 ℃/min and 497.89 ℃, and 97.63 % at 5.00 ℃/min and 550 ℃ in the temperature ranges of 400-430 ℃, 430-460 ℃, 460-490 ℃, 490-520 ℃, and 520-550 ℃, respectively. It is noteworthy that the predicted WP conversion slightly lowered from 97.68 % to 97.63 % when the temperature increased from 497.89 ℃ to 550 ℃, which contradicted the other results of the experiment. However, the difference value was just -0.05 %, which is almost negligible.

Figs. 3.5g-h depict the experimental and predicted optimal WP conversions for temperature ranges of 300-400 ℃, 400-430 ℃, 430-460 ℃, 460-490 ℃, 490-520 ℃ and 520-550 ℃. These temperature intervals are denoted as 1 to 6, respectively in Figs. 3.5g-h. As shown in Fig. 3.5g, the experimental WP conversions were 1.59 %, 2.43 %, 20.11 %, 96.39 %, 97.51 % and 97.63 % at a heating rate of 5.00 ℃/min, and at temperatures of 400.00 ℃, 430.00 ℃, 460.00 ℃, 490.00 ℃, 497.89 ℃ and 550.00 ℃, respectively. Moreover, as demonstrated in Fig. 3.5h, the relative errors between the experimental and the predicted optimal WP conversions for different temperature ranges were 3.18 %, -3.25 %, 0.96 %, -0.16 %, 0.17 % and 0.00 %. The absolute values of the relative error were less than 3.50 %. Moreover, the deviation

percentage *Dev%* between the experimental and predicted WP conversions was 0.13, which satisfied the fitting acceptability *Dev%* < 4, according to [49]. This also indicated a satisfactory accuracy for the WP conversions predicted by ANN.

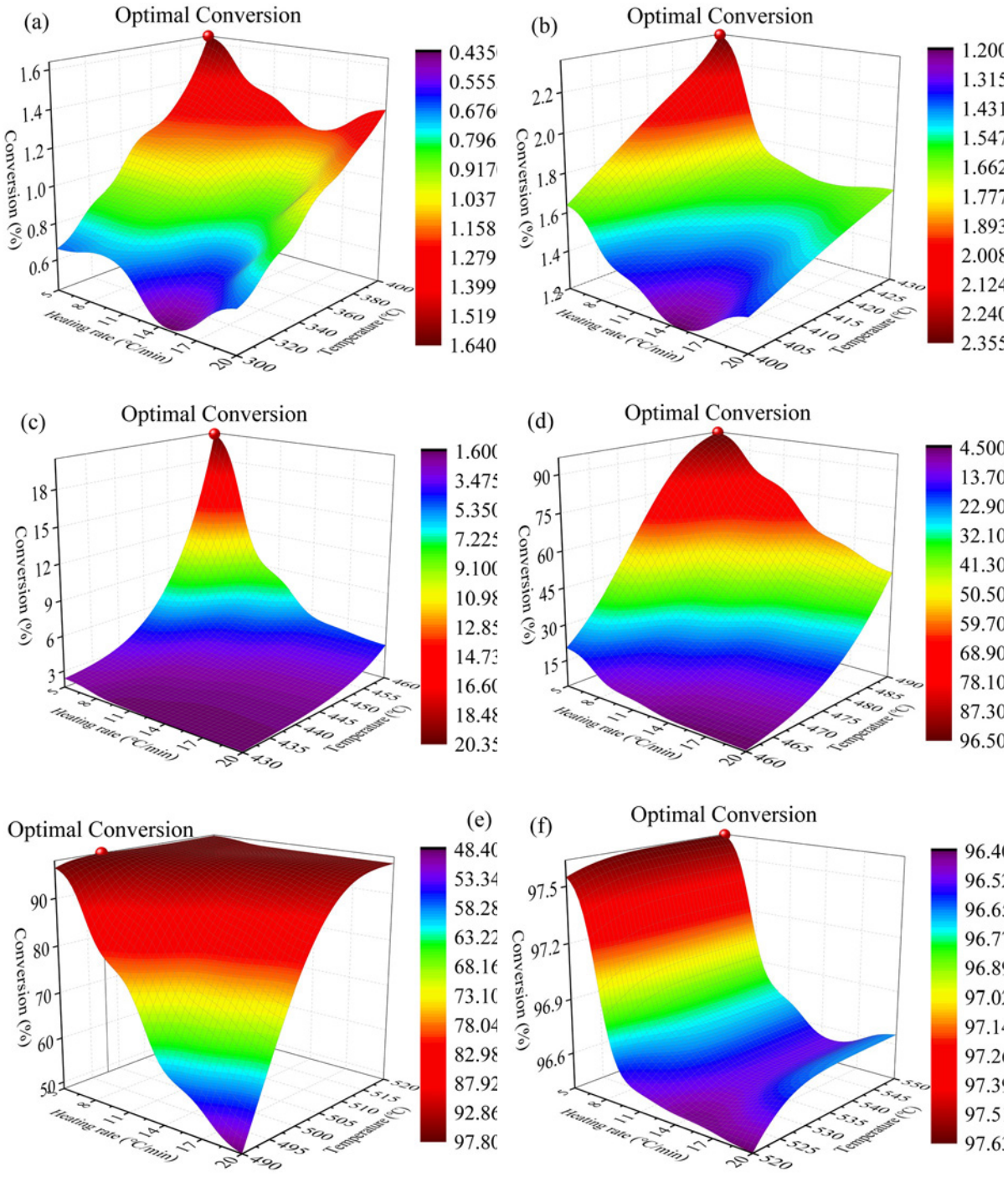

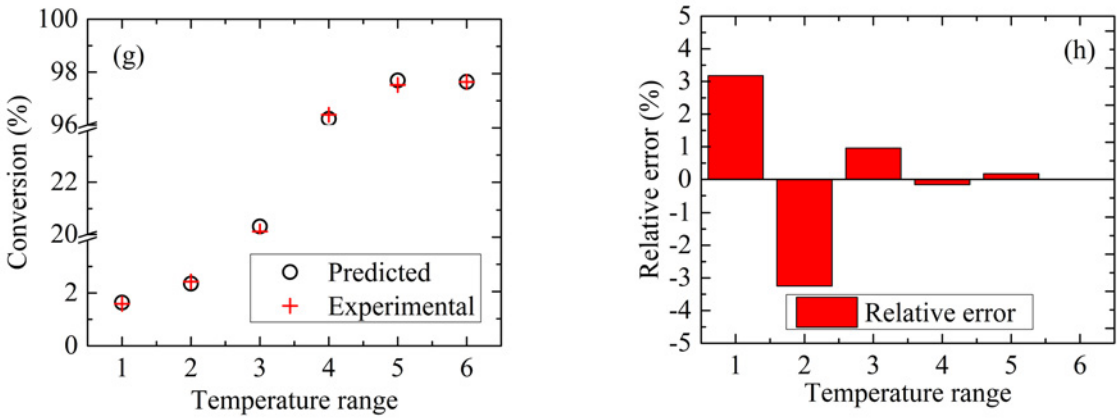

Fig.3.5. Optimal WP conversions in different temperature ranges calculated using GA: (a) 300-400 ℃; (b) 400-430 ℃; (c) 430-460 ℃; (d) 460-490 ℃; (e) 490-520 ℃; (f) 520-550 ℃; (g) Experimental and predicted optimal conversions; (h) Relative errors between experimental and predicted optimal conversions.

Fig. 3.6 describes the optimal WP pyrolysis rates for the different temperature ranges calculated using the GA. Because of the low pyrolysis rate before 400 ℃ and after 550 ℃, 5 temperature ranges were used to investigate the WP optimal pyrolysis rates, i.e., 400-430 ℃, 430-460 ℃, 460-490 ℃, 490-520 ℃, and 520-550 ℃, in this sequence [19]. The GA determined optimal WP pyrolysis rates in different temperature ranges are depicted in Figs. 6a-e. As shown in Fig. 3.6a, the WP pyrolysis rate decreased with a heating rate of around 5-10 ℃/min, while it increased with a heating rate of around 10-20 ℃/min in a temperature range of around 400-405 ℃. Moreover, in the temperature range of 405-425 ℃, the WP pyrolysis rate decreased with a heating rate from around 5-10 ℃/min, increased with a heating rate of around 10-15 ℃/min, and decreased again with a heating rate of around 15-20 ℃/min. Consequently, the optimal WP pyrolysis rate determined by GA was 0.39 wt%/min at 20.00 ℃/min and 430.00 ℃ in the temperature range of 400-430 ℃. Furthermore, as depicted in Figs. 3.6b-e, the GA optimized WP pyrolysis rates were 9.78 wt%/min at 5.00 ℃/min and

460.00 ℃, 60.07 wt%/min at 20.00 ℃/min and 490.00 ℃, 60.66 wt%/min at 20.00 ℃/min and 492.09 ℃, and 0.84 wt%/min at 20.00 ℃/min and 520.00 ℃ in the temperature ranges of 430-460 ℃, 460-490 ℃, 490-520 ℃, and 520-550 ℃, respectively. In conclusion, the optimal heating rate is 20 ℃/min in the lower temperature range (400-430 ℃) and the higher temperature range (460-550 ℃), while the optimal heating rate is 5 ℃/min in the medium temperature range (430-460 ℃). Higher heating rates could accelerate the WP's mass loss, thereby increasing the pyrolysis rate [4]. However, higher heating rates can also cause thermal hysteresis, which is not conducive to the thermal decomposition of WP [3]. The thermal hysteresis might have a stronger influence on the WP's pyrolysis than the acceleration of WP's mass loss in the medium temperature range, thus the lowest heating rate was most conducive to the reaction rate of WP's pyrolysis. Moreover, the maximum WP pyrolysis rate was obtained at 492.09 ℃ and 20.00 ℃/min.

Figs. 3.6f-g illustrate the experimental and the GA optimized WP pyrolysis rates in the temperature ranges of 400-430 ℃, 430-460 ℃, 460-490 ℃, 490-520 ℃, and 520-550 ℃, denoted 1 to 5 respectively in Figs. 3.6f-g. As demonstrated in Fig. 3.6f, the experimental WP pyrolysis rates were 0.39 wt%/min, 9.68 wt%/min, 59.25 wt%/min, 59.14 wt%/min, and 0.53 wt%/min in the temperature ranges of 400-430 ℃, 430-460 ℃, 460-490 ℃, 490-520 ℃, and 520-550 ℃, respectively. Furthermore, as described in Fig. 3.6g, the relative errors between the experimental and the predicted optimal WP pyrolysis rates in the different temperature ranges were 0.57 %, 1.04 %, 1.39 %, 2.57 %, and 57.63 %. Except for the temperature range of 520-550 ℃, the absolute values of relative error between the experimental and the predicted optimal

pyrolysis rates were less than 2.6 %. The temperature range of 520-550 ℃ was approaching the end of the WP pyrolysis [43], in which the highest pyrolysis rate was merely 0.53 wt%/min. Although the relative error was high, the difference between predicted and the experimental optimal pyrolysis rates was only 0.31 wt%/min in the temperature range of 520-550 ℃. Besides, the deviation percentage *Dev%* between the experimental and predicted WP pyrolysis rates was 1.33, which showed the high accuracy of the ANN predicted results [14][49].

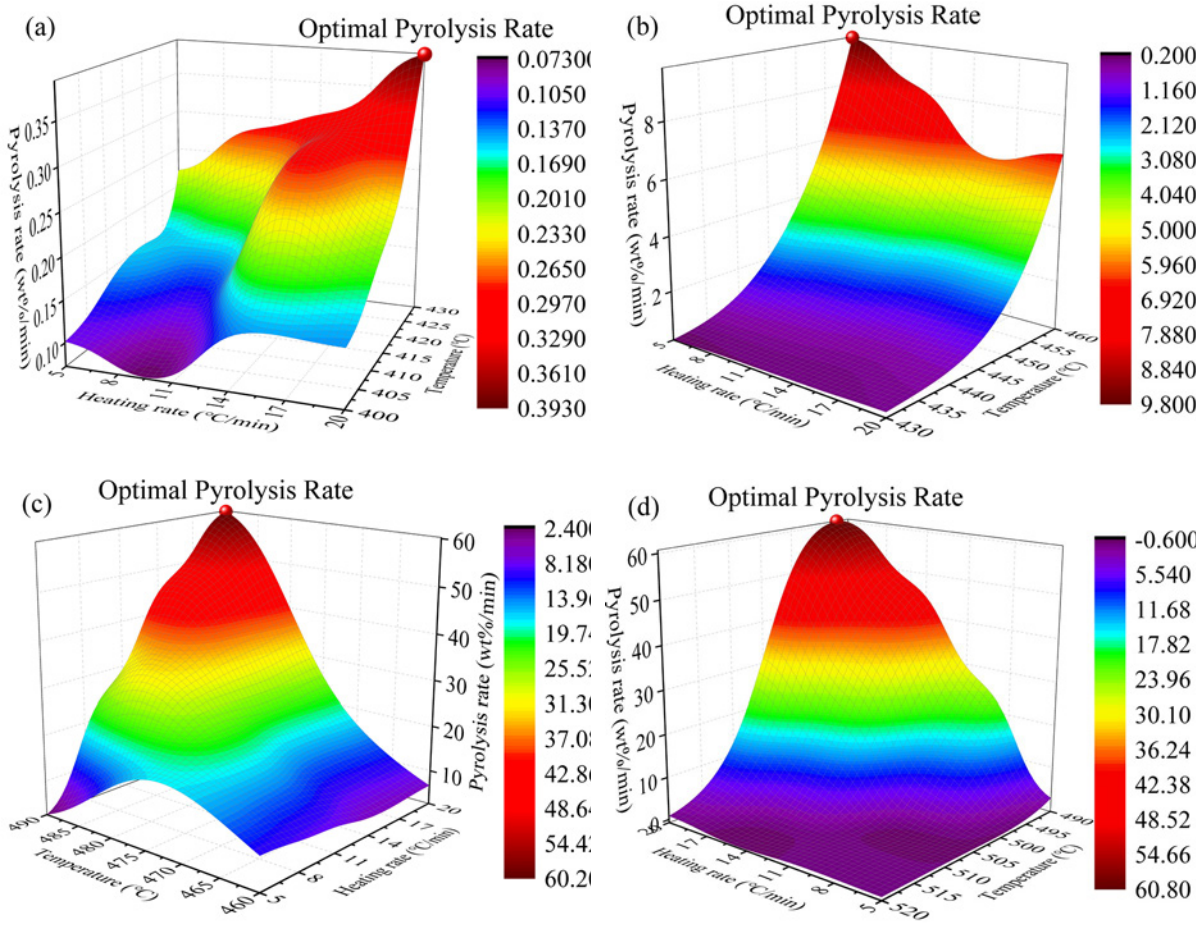

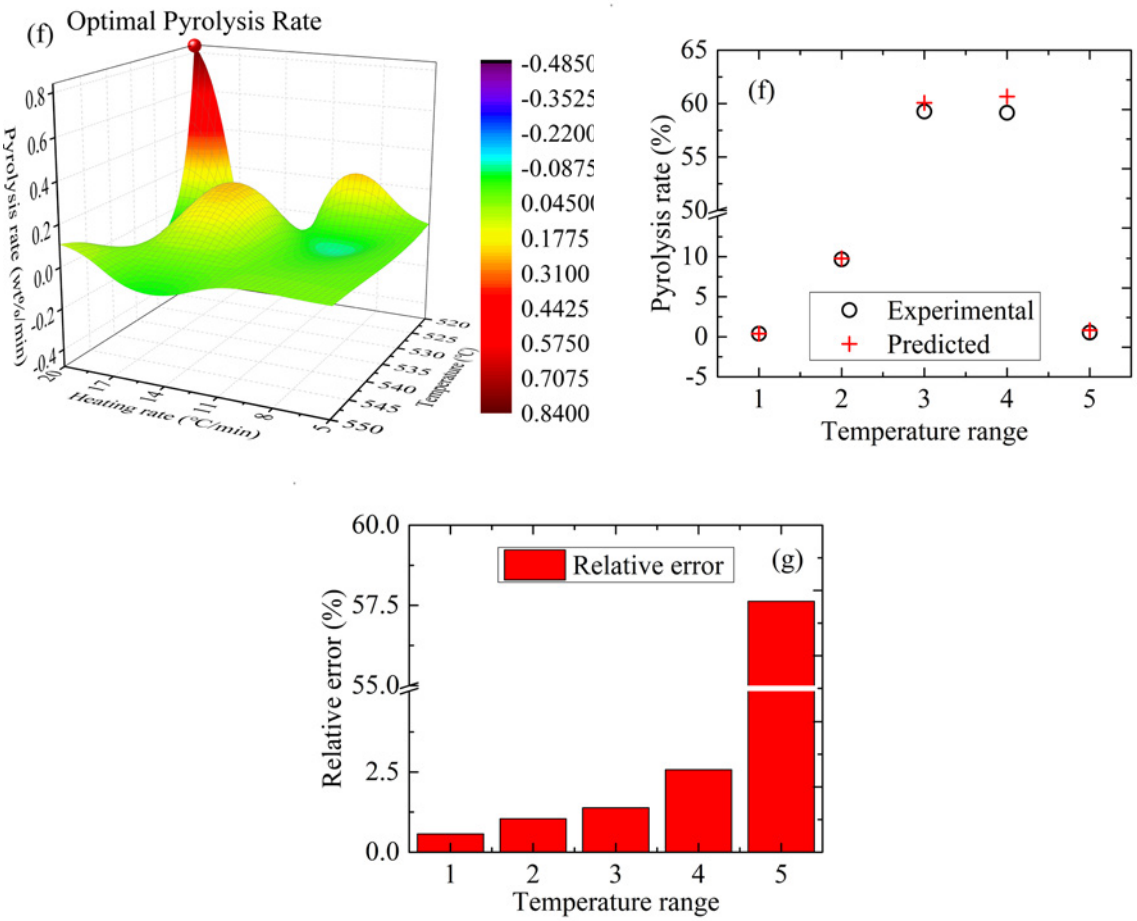

Fig.3.6. Optimal WP pyrolysis rates in different temperature ranges calculated using GA: (a) 400-430 ℃; (b) 430-460 ℃; (c) 460-490 ℃; (d) 490-520 ℃; (e) 520-550 ℃; (f) Experimental and predicted optimal pyrolysis rates; (g) Relative errors between experimental and predicted optimal pyrolysis rates.

3.3.5. Applicability of ANN

For the purpose of certifying the applicability of ANN, one fifth of the experimental data for the WP conversion and the pyrolysis rate, different from that used for predicting by ANN, was sampled at equal interval for comparison with the ANN predicted results. Figs. 3.7a-e illustrate the comparison between the experimental and predicted WP mass fractions and pyrolysis rates at heating rates of 5-20 ℃/min, respectively. Overall, the predicted WP mass fraction and the pyrolysis rate were consistent with the experimental data. Moreover, in order to determine the reliability of the ANN predicted data, the R-squared values of the WP

conversion and the pyrolysis rate were calculated, as depicted in Figs. 3.7f-g. It was noteworthy that the accuracy of the ANN predicted WP mass fraction was lower at 12 ℃/min compared to the predicted data at heating rates of 5, 10, 15 and 20 ℃/min. As shown in Fig. 3.7e, the R-squared value of the WP conversion at 12 ℃/min was 0.99996, while the R-squared values of the WP conversion were all 0.99999 at heating rates of 5, 10, 15 and 20 ℃/min, respectively. The R-squared values of the WP mass fraction were all close to 1 at heating rates of 5-20 ℃/min, exhibiting a high accuracy for the ANN predicted values.

In terms of the WP pyrolysis rate, the ANN predicted results were in good agreement with the experimental data. As described in Fig. 3.7a, the predicted and experimental WP pyrolysis rate curves almost coincided with each other at 5 ℃/min. Moreover, the predicted and the experimental maximum pyrolysis rates were 17.66 wt%/min at 473.8 ℃, and 17.73 wt%/min at 468.8 ℃, respectively. The relative error between the predicted and the experimental maximum pyrolysis rates was around 0.39 %. As depicted in Fig. 3.7b, the predicted and the experimental maximum pyrolysis rates at 10 ℃/min were 32.62 wt%/min at 483.7 ℃, and 34.04 wt%/min at 481.2 ℃, respectively. The agreement between the predicted and the experimental maximum pyrolysis rates was within 4.18 %. As illustrated in Fig. 3.7c, the peak values of the predicted and experimental WP pyrolysis rate curves were 47.61 wt%/min and 48.02 wt%/min at 488.8 ℃, respectively. The relative error of the peak values between the predicted and the experimental maximum pyrolysis rates was 0.84 %. As shown in Fig. 3.7d, the predicted and the experimental maximum pyrolysis at 20 ℃/min were 60.61 wt%/min at 492.7 ℃, and 59.52 wt%/min at 488.0 ℃, respectively. The relative error between the

experimental and predicted maximum pyrolysis rates was around -1.84 %. Additionally, as demonstrated in Fig. 3.7f, the R-squared values of the WP pyrolysis rates were 0.99675, 0.99658, 0.99911 and 0.99926 at heating rates of 5, 10, 15 and 20 ℃/min, respectively. Moreover, the R-squared value of the WP pyrolysis rate was 0.99449 at 12 ℃/min, which indicated that the ANN predicted values were highly precise.

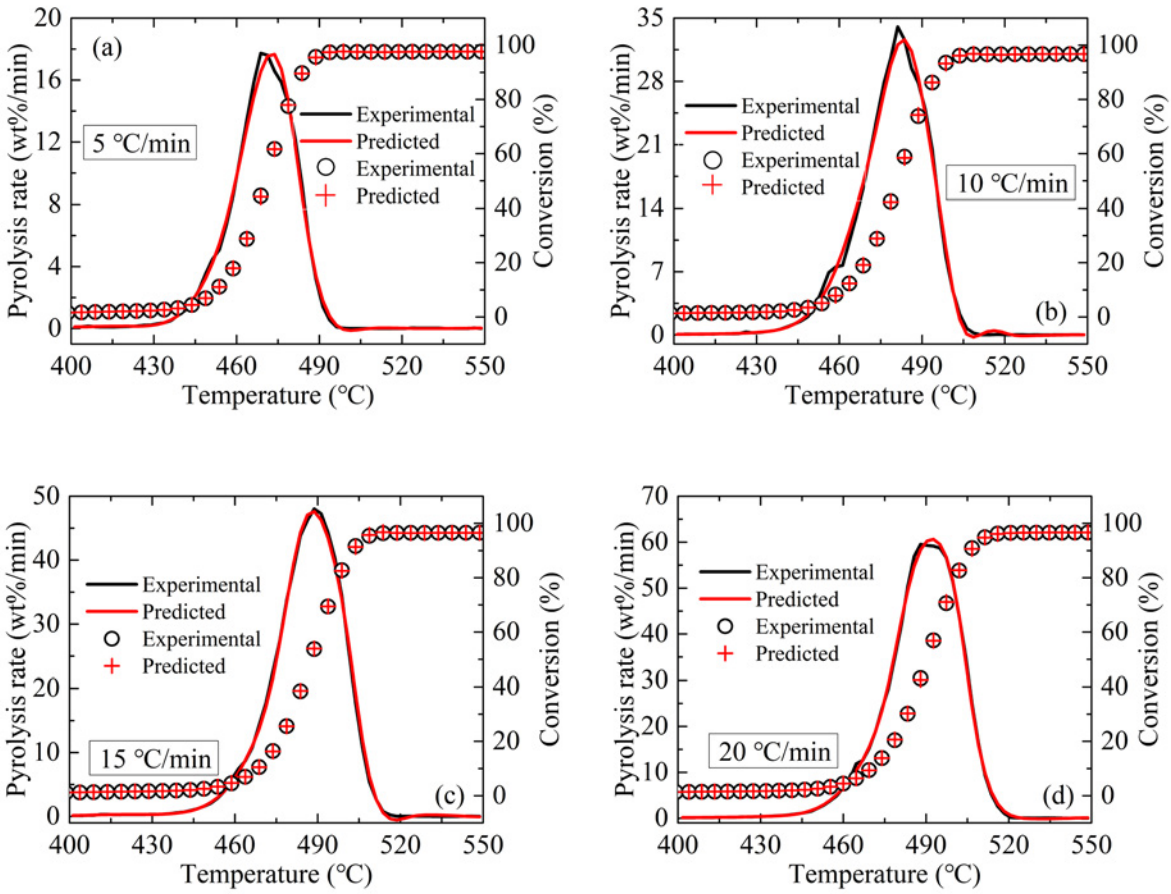

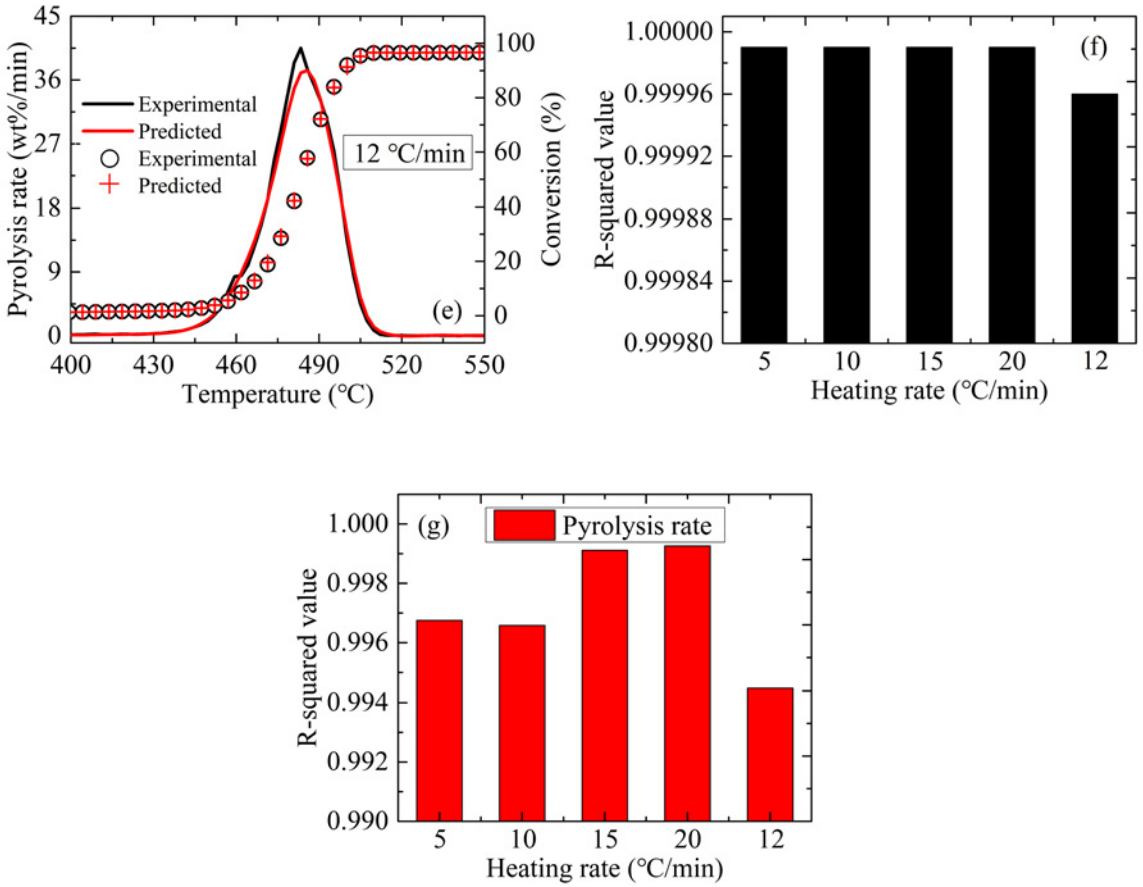

Fig.3.7. Applicability of ANN: (a) At 5 ℃/min; (b) At 10 ℃/min; (c) At 15 ℃/min; (d) At 20 ℃/min; (e) At 12 ℃/min; (f) R-squared values of the WP mass fraction; (g) R-squared values of the WP pyrolysis rate.

3.4. Conclusions

This chapter investigated the WP thermal pyrolysis process to provide guidance for prospective industrial and commercial applications. The temperature, the conversion and the pyrolysis rate are the determining factors for industrial applications. Therefore, TG experiments were conducted at different heating rates of 5, 10, 12, 15 and 20 ℃/min to obtain the WP mass fraction, the conversion, and the pyrolysis rate, which varied with the temperature and heating rate. ANN was adopted to predict the WP conversion and the pyrolysis rate based on the experimental TG data. According to the experimental results, the WP conversion and the

pyrolysis rate were investigated for the temperature ranges of 300-550 ℃ and 400-550 ℃, respectively. Furthermore, GA was adopted to determine the optimal operating conditions in the different temperature ranges. ANN was validated using the comparison of the experimental and predicted results. The accuracy of ANN predicted results was investigated by determining the R-squared values of the mass fraction (~ 1) and the pyrolysis rate (> 0.994) compared with the available experimental observations. Subsequently, the GA optimized WP conversion and the pyrolysis rate were 97.68 % at 5.00 ℃/min and 497.89 ℃, and 60.66 wt%/min at 20.00 ℃/min and 492.09 ℃, respectively. Additionally, the ANN predicted results were consistent with the supplementary experimental data, which certified the applicability of ANN. The hybrid algorithm of ANN coupled with GA could be used to model and analyze the co-pyrolysis behavior of WP and other materials (biomass, waste paper, etc.).

Bibliography

[1] Rabl, A., Spadaro, J.V., Zoughaib. A., 2008. Waste Management & Research, 26(2), 147-162.

[2] Al-Salem, S.M., Lettieri, P., Baeyens, J., 2009. Recycling and recovery routes of plastic solid waste (PSW): A review. Waste Management, 29(10), 2625-2643.

[3] Al-Salem, S.M., Antelava, A., Constantinou, A., Manos, G., Dutta, A., 2017. A review on thermal and catalytic pyrolysis of plastic solid waste (PSW). Journal of Environmental Management, 197, 177-198.

[4] Sharuddin, S.D.A., Abnisa, F., Daud, W.M.A.W., Aroua, M.K., 2016. A review on pyrolysis of plastic wastes. Energy Conversion and Management, 115, 308-326.

[5] Zhang, D.Q., Tan, S.K., Gersberg, R.M., 2010. Municipal solid waste management in China: status, problems and challenges. Journal of Environmental Management, 91(8), 1623-1633.

[6] Nisar, J., Ali, G., Shah, A., Iqbal, M., Khan, R.A., Sirajuddin, Anwar, F., Ullah, R., Akhter, M.S., 2019. Fuel production from waste polystyrene via pyrolysis: Kinetics and products distribution. Waste Management, 88, 236-247.

[7] Mishra, R.K., Iyer, J.S., Mohanty, K., 2019. Conversion of waste biomass and waste nitrile gloves into renewable fuel. Waste Management, 89, 397-407.

[8] Veses, A., Sanahuja-Parejo, O., Callen, M.S., Murillo, R., Garcia, T., 2020. A combined two-stage process of pyrolysis and catalytic cracking of municipal solid waste for the production of syngas and solid refuse-derived fuels. Waste Management, 101, 171-179.

[9] Blazquez, F.C., Gonzalez, A.G., Sanchez, C.S., Rodriguez, V.D., Salcedo, F.C., 2018. Waste valorization as an example of circular economy in extremadura (Spain). Journal of Cleaner Production, 181, 136-144.

[10] Hidalgo, D., Martin-Marroquin, J.M., Corona, F., 2019. A multi-waste management concept as a basis towards a circular economy model. Renewable & Sustainable Energy Reviews, 11, 481-489.

[11] Antoniou, N., Monlau, F., Sambusiti, C., Ficara, E., Barakat, A., Zabaniotou, A., 2019. Contribution to Circular Economy options of mixed agricultural wastes management: Coupling anaerobic digestion with gasification for enhanced energy and material recovery. Journal of Cleaner Production, 209, 505-514.

[12] Paraschiv, M., Kuncser, R., Tazerout, M., Prisecaru, T., 2015. New energy value chain through pyrolysis of hospital plastic waste. Applied Thermal Engineering, 87, 424-433.

[13] Chen, L., Wang, S.Z., Meng, H.Y., Wu, Z.Q., Zhao, J., 2017. Synergistic effect on thermal behavior and char morphology analysis during co-pyrolysis of paulownia wood blended with different plastics waste. Applied Thermal Engineering, 111, 834-846.

[14] Navarro, M.V., Lopez, J.M., Veses, A., Callen, M.S., Garcia, T., 2018. Kinetic study for the co-pyrolysis of lignocellulosic biomass and plastics using the distributed activation energy model. Energy, 165, 731-742.

[15] Chen, R.Y., Xu, X.K., Zhang, Y., Lo, SM., Lu, S.X., 2018a. Kinetic study on pyrolysis of waste phenolic fibre-reinforced plastic. Applied Thermal Engineering, 136, 484-491.

[16] Singh, R.K., Ruj, B., Sadhukhan, A.K., Gupta, P., 2019. Impact of fast and slow pyrolysis

on the degradation of mixed plastic waste: Product yield analysis and their characterization. Journal of the Energy Institute, 92(6), 1647-1657.

[17] Ippolito, N.M., Cafiero, L., Tuffi, R., Ciprioti, S.V., 2019. Characterization of the residue of a commingled post-consumer plastic waste treatment plant: a thermal, spectroscopic and pyrolysis kinetic study. Journal of Thermal Analysis and Calorimetry, 138(5), 3323-3333.

[18] Chhabra, V., Bhattachary, S., Shastri, Y., 2019. Pyrolysis of mixed municipal solid waste: Characterisation, interaction effect and kinetic modelling using the thermogravimetric approach. Waste Management, 90, 152-167.

[19] Teng, S.Y., Loy, A.C.M., Leong, W.D., How B.S., Chin, B.L.F., Masa, V., 2019. Catalytic thermal degradation of Chlorella vulgaris: Evolving deep neural networks for optimization. Bioresource Technology, 292, 121971.

[20] Quesada, L., Perez, A., Godoy, V., Peula, F.J., Calero, M., Blazquez, G., 2019. Optimization of the pyrolysis process of a plastic waste to obtain a liquid fuel using different mathematical models. Energy Conversion and Management, 188, 19-26.

[21] Sadeghizadeh, A., Ebrahimi, F., Heydari, M., Tahmasebikohyani, M., Ebrahimi, F., Sadeghizadeh, A., 2019. Adsorptive removal of Pb (II) by means of hydroxyapatite/chitosan nanocomposite hybrid nanoadsorbent: ANFIS modeling and experimental study. Journal of Environmental Management, 232, 342-353.

[22] Ronda, A., Martín-Lara, M.A., Almendros, A.I., Pérez, A., Blázquez, G., 2015. Comparison of two models for the biosorption of Pb(II) using untreated and chemically treated olive stone: Experimental design methodology and adaptive neural fuzzy inference

system (ANFIS). Journal of the Taiwan Institute of Chemical Engineers, 54, 45-56.

[23] Calero, M., Ianez-Rodriguez, I., Perez, A., Martin-Lara, M.A., Blazquez, G., 2018. Neural fuzzy modelization of copper removal from water by biosorption in fixed-bed columns using olive stone and pinion shell. Bioresource Technology, 252, 100-109.

[24] Iáñez-Rodríguez, I., Martín-Lara, M.Á., Blázquez, G., Pérez, A., Calero, M., 2017. Effect of torrefaction conditions on greenhouse crop residue: Optimization of conditions to upgrade solid characteristics. Bioresource Technology, 244, 741-749.

[25] Javed, M.S., Song, A.T., Ma, T., 2019. Techno-economic assessment of a stand-alone hybrid solar-wind-battery system for a remote island using genetic algorithm. Energy, 176, 704-717.

[26] Tuchler, S., Chen, Z.H., Copeland, C.D., 2018. Multipoint shape optimisation of an automotive radial compressor using a coupled computational fluid dynamics and genetic algorithm approach. Energy, 165, 543-561.

[27] Ascione, F., Bianco, N., Mauro, G.M., Napolitano, D.F., 2019. Building envelope design: Multi-objective optimization to minimize energy consumption, global cost and thermal discomfort. Application to different Italian climatic zones. Energy, 174, 359-374.

[28] Rezaie, A., Tsatsaronis, G., Hellwig, U., 2019. Thermal design and optimization of a heat recovery steam generator in a combined-cycle power plant by applying a genetic algorithm. Energy, 168, 346-357.

[29] Akgün, H., Yapıcı, E., Günkaya, Z., Özkan, A., Banar, M., 2021. Utilization of liquid product through pyrolysis of LDPE and C/LDPE as commercial wax. Environmental

Science and Pollution Research, 28(33), pp.45971-45984.

[30] Chen, R.Y., Xu, X.K., Lu, S.X., Zhang, Y., Lo, S.M., 2018. Pyrolysis study of waste phenolic fibre-reinforced plastic by thermogravimetry/Fourier transform infrared/mass spectrometry analysis. Energy Conversion and Management, 165, 555-566.

[31] Aboulkas, A., El Harfi, K., El Bouadili, A., 2010. Thermal degradation behaviors of polyethylene and polypropylene. Part I: Pyrolysis kinetics and mechanisms. Energy Conversion and Management, 51(7), 1363-1369.

[32] Mumbach, G.D., Alves, J.L.F., Da Silva, J.C.G., De Sena, R.F., Marangoni, C., Machado, R.A.F., Bolzan, A., 2019. Thermal investigation of plastic solid waste pyrolysis via the deconvolution technique using the asymmetric double sigmoidal function: Determination of the kinetic triplet, thermodynamic parameters, thermal lifetime and pyrolytic oil composition for clean energy recovery. Energy Conversion and Management, 200, 112031.

[33] Sousa, V., Meireles, I., Oliveira, V., Dias-Ferreira, C., 2019. Prediction performance of separate collection of packaging waste yields using genetic algorithm optimized support vector machines. Waste and Biomass Valorization, 10(12), 3603-3612.

[34] Michailos, S., Parker, D., Webb, C., 2019. Design, sustainability analysis and multiobjective optimisation of ethanol production via syngas fermentation. Waste and Biomass Valorization, 10(4), 865-876.

[35] Barik, D., Murugan, S., 2015. An artificial neural network and genetic algorithm optimized model for biogas production from co-digestion of seed cake of karanja and cattle dung. Waste and Biomass Valorization, 6(6), 1015-1027.

[36] Perez-Gallardo, J.R., Azzaro-Pantel, C., Astier, S., 2018. A multi-objective framework for assessment of recycling strategies for photovoltaic modules based on life cycle assessment. Waste and Biomass Valorization, 9(1), 147-159.

[37] Niu, B., Jia, M., Xu, G.F., Chang, Y.C., Xie, M.Z., 2018. Efficient approach for the optimization of skeletal chemical mechanisms with multiobjective genetic algorithm. Energy & Fuels, 32(6), 7086-7102.

[38] Das, P., Tiwari, P., 2017. Thermal degradation kinetics of plastics and model selection. Thermochimica Acta, 654, 191-202.

[39] Das, P., Tiwari, P., 2019. Thermal degradation study of waste polyethylene terephthalate (PET) under inert and oxidative environments. Thermochimica Acta, 679, 178340.

[40] Pan, R.M., Duque, J.V.F., Debenest, G., 2021. Investigating waste plastic pyrolysis kinetic parameters by genetic algorithm coupled with thermogravimetric analysis. Waste and Biomass Valorization, 12, 2623-2637.

[41] Pan, R.M., Duque, J.V.F., Martins, M.F., Debenest, G., 2020. Application of a neural fuzzy model combined with simulated annealing algorithm to predict optimal conditions for polyethylene waste non-isothermal pyrolysis. Heliyon, 6(11), e05598.

[42] Duque, J.V.F., Martins, M.F., Debenest, G., Orlando, M.T.D., 2020. The influence of the recycling stress history on LDPE waste pyrolysis. Polymer Testing, 86, 106460.

[43] Majid, M., Chin, B.L.F., Jawad, Z.A., Chai, Y.H., Lam, M.K., Yusup, S., Cheah, K.W., 2021. Particle swarm optimization and global sensitivity analysis for catalytic co-pyrolysis of Chlorella vulgaris and plastic waste mixtures. Bioresource Technology, 329, 124874.

[44] Pan, R.M., Martins, M.F., Debenest, G., 2021. Pyrolysis of waste polyethylene in a semi-batch reactor to produce liquid fuel: Optimization of operating conditions. Energy Conversion and Management, 237, 114114.

[45] Bong, J.T., Loy, A.C.M., Chin, B.L.F., Lam, M.K., Tang, D.K.H., Lim, H.Y., Chai, Y.H., Yusup, S., 2020. Artificial neural network approach for co-pyrolysis of Chlorella vulgaris and peanut shell binary mixtures using microalgae ash catalyst. Energy, 207, 118289.

[46] Liew, J.X., Loy, A.C.M., Chin, B.L.F., AlNouss, A., Shahbaz, M., Al-Ansari, T., Govindan, R., Chai, Y.H., 2021. Synergistic effects of catalytic co-pyrolysis of corn cob and HDPE waste mixtures using weight average global process model. Renewable Energy, 170, 948-963.

[47] Singh, R.K., Ruj, B., Sadhukhan, A.K., Gupta, P., 2019b. Thermal degradation of waste plastics under non-sweeping atmosphere: Part 1: Effect of temperature, product optimization, and degradation mechanism. Journal of Environmental Management, 239, 395-406.

[48] Wang, X.B., Liang, Q.M., Wang, J.N., Bai, S.J., Mikulčić, H., Vujanović, M., Tan, H.Z., 2019. Synergistic effect of biomass and polyurethane waste co-pyrolysis on soot formation at high temperatures. Journal of Environmental Management, 239, 306-315.

[49] Zhang, J.Z., Chen, T.J., Wu, J.L., Wu, J.H., 2014. A novel Gaussian-DAEM-reaction model for the pyrolysis of cellulose, hemicellulose and lignin. RSC Advances, 4, 17513-17520.

Chapter 4

Pyrolysis of waste polyethylene in a semi-batch reactor to produce liquid fuel: Optimization of operating conditions

Summary

This chapter investigated the interactive effects of temperature, residence time, and carrier gas flow rate on the liquid fuel production through the pyrolysis of waste polyethylene (WPE) in a bench-scale semi-batch reactor. To enhance the liquid fuel production, fifteen experiments were conducted based on a central composite design. Artificial neural network (ANN) was adopted to establish the relationship between liquid fuel production and operating conditions. The R-squared value of the experimental and ANN predicted that liquid fuel production was 0.9934. Four additional experimental results verified the ANN's applicability. Subsequently, the genetic algorithm (GA) was adopted to optimize operating conditions to maximize liquid fuel production. The GA optimized operating conditions (temperature, residence time, and carrier gas flow rate) were: 488 ℃, 20 min, and 20 mL/min. The liquid fuel under the optimal operating conditions was analyzed by Fourier-transform infrared spectroscopy (FTIR) and gas chromatography-mass spectrometry (GC-MS). The liquid fuel had similar main functional groups as diesel. The components of the liquid fuel were mainly 1-alkenes and n-alkanes ranging from C7 to C36. The effects of operating conditions on liquid fuel fractions and mean molecular weight were also investigated.

Candidate contribution: Conceptualization, methodology, experimental design and execution, formal analysis, resources, data curation, writing - original draft, visualization.

4.1. Introduction

Municipal solid waste (MSW) is accumulating rapidly due to the enormous resource consumption and inefficient recycling worldwide. It is estimated that within 34 years (from 2016 to 2050), MSW will increase from 2.01 billion tons to 3.40 billion tons [1]. Plastic waste accounts for a large part of Municipal Solid Waste (MSW) due to its wide range of uses [2]. Moreover, the waste polyethylene (WPE) accounts for 40 % of plastics in MSW [3]. Also, about 70 % of the total produced plastics have been directly discarded in the environment [4]. These combinations of mismanagement have aggravated environmental pollution and endangered human health [5]. Therefore, the recycling of waste plastics, especially the WPE, needs to be further promoted.

It is reported that pyrolysis is an efficient way to recycle the WPE [6][7]. The polymer is thermally decomposed into gas, liquid fuel, and char products in an oxygen-free atmosphere. Moreover, slow pyrolysis with low heating rates can enhance liquid fuel production [8]. The thermal lag phenomenon can also be diminished by adopting low heating rates [9]. The uniform temperature distributions inside the reactor and the reactants can be achieved during slow pyrolysis [10][11]. This is conducive to heat and mass transfer and liquid fuel production [8], [12]. The distribution of products is determined by the reactor type, the presence of catalysts, and operating conditions, such as temperature, residence time, and carrier gas flow rate [6]. Many studies on the thermal pyrolysis of polyethylene (PE) have been conducted in semi-batch reactors. It has been reported that high liquid fuel yields can be obtained [13][14][15][16][17][18].

In terms of operating conditions, the temperature is the dominant parameter during plastics' pyrolysis [6]. Onwudili et al. [3][19] reported that the virgin low-density PE was completely pyrolyzed at temperatures above 425 ℃. The liquid fuel yield reached 89.5 wt% at 425 ℃. They also found that liquid oil production dropped drastically as the temperature increased beyond 425 ℃. Tiikma et al. [20] stated that the optimal temperature for the liquid oil production from the pyrolysis of the WPE was 450 ℃. Quesada et al. [21][22] and Rodríguez-Luna et al. [23] investigated WPE and high-density PE thermal pyrolysis processes in a temperature range of 450-550 ℃, respectively. They both reported that the optimal temperature for liquid fuel production was 500 ℃. Sharuddin et al. [6] also concluded that temperatures below 500 ℃ were suitable for plastics' pyrolysis to produce liquid fuel.

According to [3], the residence time was related to the experiment's duration at the target temperature. It has been reported that the residence time is also a critical factor in determining the composition of pyrolysis products [3][21]. Quesada et al. [21][22] found that a long residence time could enhance the liquid fuel yield. Muhammad et al. [24] investigated the effect of the carrier gas flow rate on PE's pyrolysis in a 200 mL bench-scale semi-batch reactor with nitrogen as the carrier gas. They investigated the production changes of liquid fuel and char with gas flow rates in the range of 0-60 mL/min. Also, they found that the carrier gas flow rate could also determine the distribution of thermal pyrolysis products of PE. A higher carrier gas flow rate would increase the liquid fuel yield and reduce the char yield.

In short, on the one hand, many research works have been done to investigate the effects of the operating conditions (temperature, residence time, and carrier gas flow rate) on the liquid

fuel yield through the pyrolysis of PE; On the other, most of them investigated such effects by varying operating conditions one-by-one. However, according to [21], the operating conditions have complex interactive effects on liquid fuel production, which requires establishing a multiparameter mathematical expression for evaluating the yield of liquid fuel. For these reasons, one-by-one relationship interaction makes the optimal operating conditions determined in such a way not particularly convincing.

Artificial neural network (ANN) [25][26] is a suitable mathematical method that can set up relations between attributive variables and multiple arguments. Paramasivam [27] adopted ANN to analyze the CI engine performance through engine load and fuel mixture ratio. High accuracy was obtained between the experimental, and the ANN predicted results. Pan et al. [28] established the mathematical relationship between the PE pyrolysis rate and the operating conditions (temperature and heating rate). The high R-squared value (> 0.999) between the experimental and predicted values exhibited the ANN's reliability. Dubdub et al. [29] utilized ANN to conduct the thermogravimetric modeling of high-density PE catalytic pyrolysis. A good agreement between the experimental and predicted data was also obtained. Quesada et al. [21] adopted different mathematical models to establish the relationships between the yields of plastic waste pyrolysis products and operating conditions. They concluded that the ANN predicted results were more accurate and reliable.

In this perspective, this study aims to comprehensively investigate the interactive effects of temperature, residence time, and carrier gas flow rate on the liquid fuel production through the slow pyrolysis (heating rate of 6 °C/min) [30] of the WPE in a bench-scale semi-batch reactor.

ANN [25][26] was adopted to determine the liquid oil production by the operating conditions (temperature, residence time, and carrier gas flow rate). Genetic algorithm (GA) is a promising method to determine the extremums of complicated functions [7][31]. Due to the complex expressions established by ANN, GA was exploited to ascertain the maximum liquid fuel production's operating conditions. ANN was also used to investigate the effects of operating conditions on the gas yield through thermal pyrolysis of WPE. The pyrolysis liquid fuel under the optimal operating conditions was analyzed by Fourier-transform infrared spectroscopy (FTIR) and gas chromatography-mass spectrometry (GC-MS). Lastly, the effects of operating conditions on liquid fuel fractions and mean molecular weight were also investigated.

4.2. Material and methods

4.2.1. Material

WPE was provided from Wanbei Plastic Recycling Development Base in Anhui Province, China. It was recycled from MSW and cut into approximately 3 mm pellets.

4.2.2. Experimental setup

Fig. 4.1 illustrates the experimental schematic diagram of the pyrolysis of WPE for liquid fuel production. The reactor is a 200 mL bench-scale semi-batch reactor. The WPE weighing approximately 5 g was used in each experiment. The reactor was purged with nitrogen at a 100 mL/min flow rate for 30 min before each experiment to ensure an inert atmosphere, and then nitrogen flow was adjusted to the target flow rate. The internal pressure of the reactor was maintained at 0.1 MPa during the whole experiment. The reactor was heated from room temperature (20 ℃) to the target temperature at a heating rate of 6 ℃/min [30] in each

experiment. Subsequently, the reactor was maintained at the target temperature for the specified duration (the residence time).

WPE was pyrolyzed into volatilized gas (liquid fuel and gas). The volatilized gas was purged out of the reactor by the carrier gas through the outlet pipe. The outer wall of the outlet pipe is equipped with metal cooling fins. The volatilized gas can be cooled to about 50 ℃ through the outlet pipe. Part of volatilized gas was condensed into liquid fuel during this process. The liquid fuel flowed through the rubber tube [24] into the glass bottle. The rest volatilized gas was condensed into a liquid by the ice-water mixture (0 ℃) [23][24][32] and collected by two in-sequence glass bottles. It is worth mentioning that liquid fuel was entirely collected in the first glass bottle. There was no liquid fuel collected in the second glass bottle. The WPE pyrolysis gas product was collected in the gas bag. Lastly, the reactor was taken out of the heating device and promptly cooled by water. The remaining contents in the reactor were char and involatile remnants [24][33][34]. The reactor was opened when it was cooled to 20 ℃. The residue was then collected and weighed.

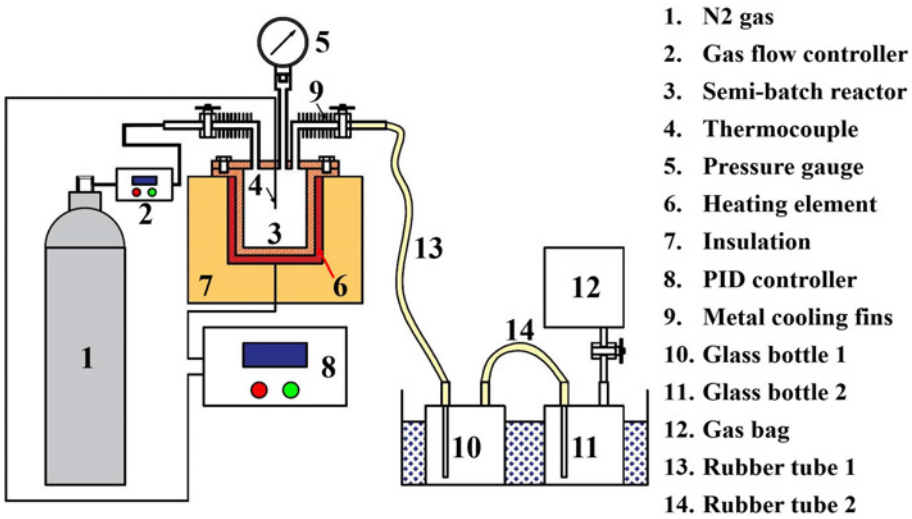

Fig. 4.1. The experimental schematic diagram of the pyrolysis of WPE for liquid fuel production.

The semi-batch reactor and the glass bottle (1) and the two glass bottles are connected by the rubber tubes. The liquid fuel also excites inside the metal outlet pipe and the rubber tubes. To reduce the experimental errors, two glass bottles and two rubber tubes are all weighted. The substance inside the metal outlet pipe is also collected and weighted. The weight of liquid fuel is calculated by the following equation,

$$W_{liquid} = \left(W_{b1,f} + W_{b2,f} + W_{t1,f} + W_{t2,f}\right) - \left(W_{b1,i} + W_{b2,i} + W_{t1,i} + W_{t2,i}\right) + W_{op} \quad (4.1)$$

where W_{liquid}, $W_{b1,f}$, $W_{b2,f}$, $W_{t1,f}$, $W_{t2,f}$, $W_{b1,i}$, $W_{b2,i}$, $W_{t1,i}$, $W_{t2,i}$ and W_{op} represent the weight of liquid fuel, the final weight of glass bottle (1), the final weight of glass bottle (2), the final weight of rubber tube (1), the final weight of rubber tube (2), the initial weight of glass bottle (1), the initial weight of glass bottle (2), the initial weight of rubber tube (1), the initial weight of rubber tube (2) and the substance weight inside the metal outline pipe, respectively.

The weight of gas is calculated by the following equation,

$$W_{gas} = W_{WPE} - W_{liquid} - W_{residue} \quad (4.2)$$

where W_{gas}, W_{WPE}, and $W_{residue}$ represent the weights of gas, initial WPE and residue, respectively.

A central composite design [21][35] was used to determine the optimal operating conditions of liquid fuel production. A total number of fifteen experiments were conducted to obtain the experimental results [21]. Furthermore, a mathematical expression with independent variables (temperature, residence time, and carrier gas flow rate) was established by ANN to investigate the production of liquid fuel. The experiments were conducted under different operating conditions, as tabulated in Table 1. Fifteen experiments were numbered from E1 to E15. Four

additional experiments were conducted to validate the mathematical model established by ANN. Four validation experiments were numbered from V1 to V4. Each experiment was conducted two times to ensure repeatability.

Table 4.1. Experiments performed under different operating conditions.

Number	Temperature (℃)	Residence time (min)	Carrier gas flow rate (mL/min)
E1	425	20	20
E2	425	20	100
E3	425	40	60
E4	425	60	20
E5	425	60	100
E6	475	20	60
E7	475	40	20
E8	475	40	60
E9	475	40	100
E10	475	60	60
E11	525	20	20
E12	525	20	100
E13	525	40	60
E14	525	60	20
E15	525	60	100
V1	450	30	80
V2	450	50	40
V3	500	30	80
V4	500	50	40

4.2.3. Methods

(i) Artificial neural network (ANN)

Fig. 4.2 depicts the ANN network structure for determining liquid fuel production. ANN utilizes the subsistent input and output data to determine the network structure's parameters [25][28]. The network structure connections are established by the IF-THEN fuzzy rules [26].

In this study, the network structure has three input variables (temperature, residence time, and carrier gas flow rate) and two output variables (liquid fuel and gas yields). According to [21], the temperature was divided into three levels (high, medium, and low); the residence time was divided into two levels (high and low); the carrier gas flow rate was divided into two levels (high and low). The input membership functions were combined into twelve fuzzy rules, which were determined by the Gaussian dependency function [28]. The output membership functions of constant type were served as the defuzzification functions. The weighted values of the fuzzy rules were calculated by the input and output membership functions. Lastly, the summation of the weighted values of twelve fuzzy rules was the liquid fuel production value. ANN is described in detail by [21][25][26][28].

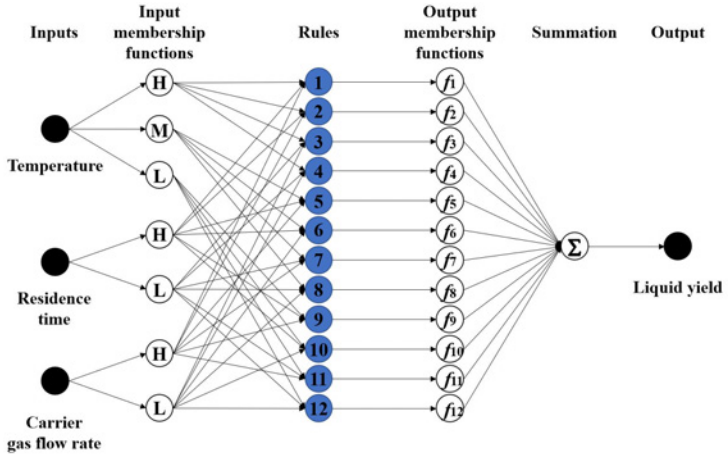

Fig. 4.2. The network structure of ANN for determining liquid fuel production.

(ii) Genetic algorithm (GA)

Genetic algorithm (GA) is a widespread optimization method [36]. GA is derived from the theory of evolution [7]. GA's core contents are the mutation and the crossover of individuals' genes, and survival of the fittest in each generation. In this study, operating conditions

(temperature, residence time, and carrier gas flow rate) were three “genes”. Liquid fuel fraction is the fitness of each individual. GA, coupled with the ANN, was utilized to optimize the operating conditions to maximize liquid fuel production. The generations and individuals were 1000 and 1000, respectively [7]. The probabilities of the mutation and the crossover of individuals’ genes were 0.005 and 0.005, respectively.

(iii) Fourier-transform infrared spectroscopy (FTIR)

FTIR test was conducted to determine the liquid fuel’s main functional groups. The FTIR spectra were recorded from 4000 to 400 cm^{-1} with 4 cm^{-1} resolution by the Thermo Nicolet 6700 FTIR optical spectrometer.

(iv) Gas chromatography-mass spectrometry (GC-MS)

The specific components of the liquid fuel were determined by gas chromatography-mass spectrometry (GC-MS). The experiments were conducted by using a low-resolution Thermo Scientific TRACE 1300/1310 gas chromatograph coupled to a TSQ 9000 triple quadrupole mass spectrometer from Thermo Fisher (USA).

The temperatures of the GC front inlet and the MS transfer line were set at 280 ℃. The GC front inlet was operated in the split mode. Helium was used as the carrier gas with a 1 mL/min flow rate. A polar phase ZB-5MS capillary column (30m × 0.25 mm, ID × 0.25 μm film) was utilized. The GC oven was set to hold at 70 ℃ for 2 min, then increased to 250 ℃ with a heating rate of 10 ℃/min and hold for 10 min, and lastly, increased to 300 ℃ with a heating rate of 20 ℃/min and hold for 27.5 min. The MS was performed under the following conditions: ion source temperature, 230 ℃; full scan, 30 Da-800 Da. The components were identified by the

National Institute of Standards and Technology (NIST) mass spectrum library.

4.3. Results and discussion

4.3.1. Liquid fuel production

(i) Accuracy of ANN

Fig. 4.3 illustrates the experimental and the ANN predicted liquid fuel productions under different operating conditions. It is worth noting that liquid fuel's appearance resembles wax at room temperature [21][22].

Fig. 4.3a shows that the ANN predicted liquid fuel production results were close to the experimental ones (E1-E15). The absolute relative errors between the predicted and the experimental values were within 1.3 %. Moreover, the R-squared value between the experimental and the ANN predicted liquid fuel productions was 0.9934. Figure 3b exhibits the ANN's applicability through the four additional experiments (V1-V4). The absolute relative errors between the predicted and the experimental values were within 1.4 %. It reveals that the ANN predicted liquid fuel production is accurate and reliable.

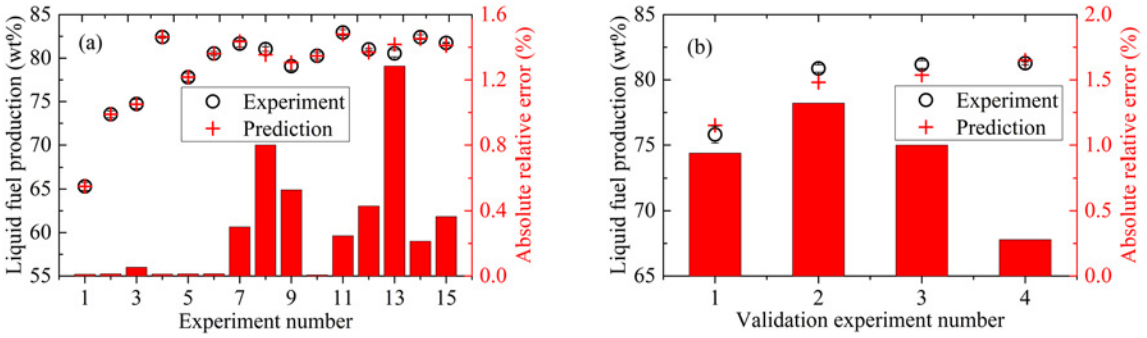

Fig. 4.3. The experimental and the ANN predicted liquid fuel productions: (a) Training; (b) Testing.

(ii) Interactive effects of residence time and carrier gas flow rate on liquid fuel

production

Figs. 4.4a, 4.4b, and 4.4c demonstrate the interactive effects of the residence time and the carrier gas flow rate on liquid fuel production at temperatures of 425 ℃, 475 ℃, and 525 ℃, respectively. The liquid fuel production varied from 65.32 wt% to 82.43 wt% at 425 ℃; from 79.05 wt% to 83.00 wt% at 475 ℃; and from 80.65 wt% to 82.73 wt% at 525 ℃, respectively. Das and Tiwari [32] obtained around 81.4 wt% liquid fuel through thermal pyrolysis of virgin PE under the operating conditions of 400 ℃, 8 h and 200 mL/min in a 1000 mL semi-batch reactor. They also obtained around 82.7 wt% liquid fuel under the operating conditions of 500 ℃, 30 min, and 100 mL/min in the same reactor [8]. Onwudili et al. [3] obtained 89.5 wt% liquid fuel production at 425 ℃ in a batch reactor. However, Quesada et al. [21] obtained relatively lower liquid fuel production through the pyrolysis of WPE at 450 ℃, which varied from 13.61 wt% to 48.38 wt%. This is because that they conducted the experiments under higher heating rates (20-50 ℃/min).

As depicted in Fig. 4.4a, a higher carrier gas flow rate could increase liquid fuel production under a shorter residence time at 425 ℃. For instance, the liquid fuel production was increased from 65.32 wt% to 73.54 wt% when the carrier gas flow rate varied from 20 mL/min to 100 mL/min under residence time of 20 min. Muhammad et al. [24] investigated liquid fuel production by the thermal pyrolysis of linear low-density PE at 450-460 ℃. The liquid fuel production increased from 45.0 wt% to 75.0 wt% when the carrier gas flow rate varied from 0 to 60 mL/min. This is consistent with the results of this study. The increase in liquid fuel production could be attributed to the higher carrier gas flow rate, which can quickly carry

volatile products out of the reactor, thereby inhibiting the secondary reactions that consume liquid fuel [37]. However, the liquid fuel production was decreased with the increasing carrier gas flow rate under a longer residence time at 425 ℃. For example, the liquid fuel production was decreased from 82.43 wt% to 77.81 wt% when the carrier gas flow rate increased from 20 mL/min to 100 mL/min under residence time of 60 min. The reduction of liquid fuel production could be attributed to that the higher carrier gas flow rate inhibited polycondensation and repolymerization reactions of the pyrolysis gas for liquid fuel formation [38]. As for the liquid fuel production at higher temperatures, as shown in Figs. 4.4b and 4.4c, increasing the carrier gas flow rate would inhibit the liquid fuel production under the residence time ranging from 20 min to 60 min. This is because higher temperatures can promote the liquid fuel's secondary cracking to generate the shorter-chain pyrolysis gas [39].

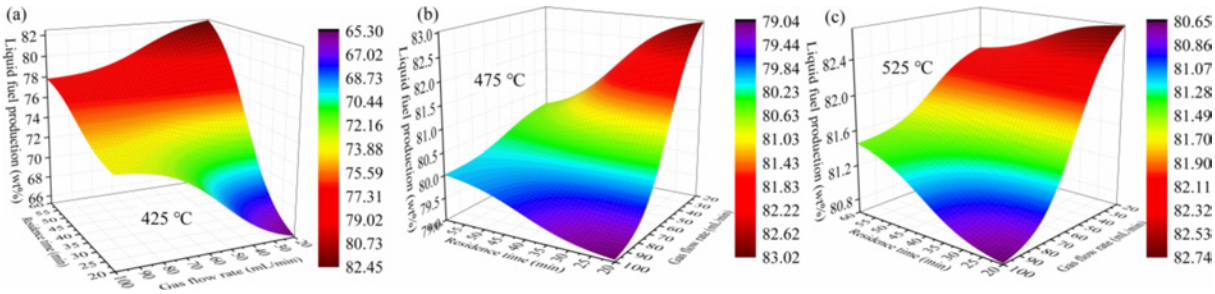

Fig. 4.4. Interactive effects of residence time and carrier gas flow rate on liquid fuel production at different temperatures: (a) 425 ℃; (b) 475 ℃; (c) 525 ℃.

(iii) Interactive effects of temperature and carrier gas flow rate on liquid fuel production

Figs. 4.5a, 4.5b, and 4.5c show the interactive effects of the temperature and the carrier gas flow rate on liquid fuel production under residence times of 20 min, 40 min, and 60 min, respectively. The liquid fuel production had the same variation tendency under a higher carrier

gas flow rate regardless of the residence time changes. The liquid fuel productions were increased when the temperature increased from 425 ℃ to 525 ℃ for all residence times. The liquid fuel production was increased from 73.54 wt% to 80.65 wt% (20 min), from 75.53 wt% to 81.02 wt% (40 min), and from 77.81 wt% to 81.45 wt% (60 min) when temperature increased from 425 ℃ to 525 ℃, respectively. The increase in the liquid fuel production could be attributed to more intense random scission reactions of WPE at higher temperatures [11]. The temperature has a more complex influence on liquid fuel production under the lowest carrier gas flow rate (20 mL/min). This is due to the interaction between the random scission reactions of WPE and the liquid fuel's secondary cracking reactions [37]. As illustrated in Fig. 4.5a, the liquid fuel production was firstly increased from 65.32 wt% to 83.63 wt% when temperature increased from 425 ℃ to 488 ℃ under residence time of 20 min. The increase in temperature had a greater impact on promoting random scission reactions of WPE in this temperature range. Therefore, the liquid fuel production increased with the increasing temperature. However, liquid fuel's secondary cracking reactions hold a dominant position in the higher temperature range. The liquid fuel production was then decreased from 83.63 wt% to 82.73 wt% when temperature increased from 488 ℃ to 525 ℃ under residence time of 20 min. While the changing trend of liquid fuel production under residence time of 60 min, as shown in Fig. 4.5c, was a reversal from the one under residence time of 20 min. It indicated that the dominance of the random scission reactions of WPE and the secondary cracking reactions of the liquid fuel had been reversed under the longest residence time (60 min).

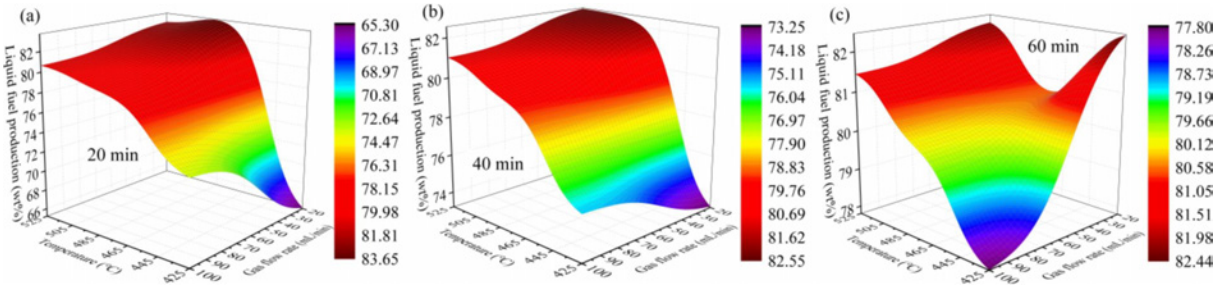

Fig. 4.5. Interactive effects of temperature and carrier gas flow rate on liquid fuel production under different residence times: (a) 20 min; (b) 40 min; (c) 60 min.

(iv) Interactive effects of temperature and residence time on liquid fuel production

Figs. 4.6a, 4.6b, and 4.6c display the interactive effects of the temperature and the residence time on liquid fuel production under carrier gas flow rates of 20 mL/min, 60 mL/min, and 100 mL/min, respectively. The temperature has a more significant impact on liquid fuel production when the residence time is shorter under all carries gas flow rates. The residence time has less impact at higher temperatures [21]. As depicted in Fig. 4.6c, the liquid fuel production was increased with the increasing residence time regardless of the temperature. WPE could be fully decomposed into short-chain hydrocarbons with longer residence time through random scission reactions in the reactor [23]. Therefore, compared with the shorter residence time, the liquid fuel production was higher under longer residence time. The thermochemical conversion is an endothermic reaction, thereby increasing temperature is conducive to the thermal pyrolysis of WPE [40]. Thus, a higher temperature could improve liquid fuel production. It is noteworthy that liquid fuel production was decreased with the temperature above 500 ℃ under carries gas flow rate of 20 mL/min in the lower range of the residence time. Sharuddin et al. [6] also suggested that temperatures below 500 ℃ are more conducive to liquid fuel production. It could be attributed to that the liquid fuel was further decomposed into low-molecular pyrolysis gas

through β cleavage reactions at temperatures over 500 ℃ [41][42].

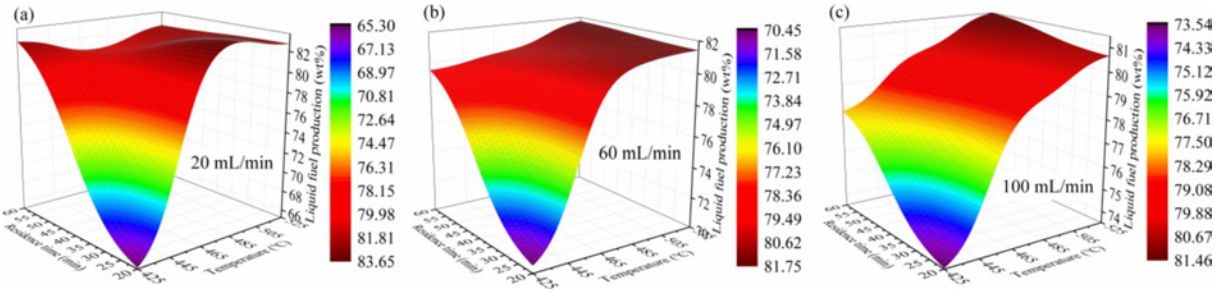

Fig. 4.6. Interactive effects of temperature and residence time on liquid fuel production under different carrier gas flow rates: (a) 20 mL/min; (b) 60 mL/min; (c) 100 mL/min.

4.3.2. Gas production

(i) Accuracy of ANN

Fig. 4.7 depicts the experimental and the ANN predicted gas production results under different operating conditions. As illustrated in Fig. 4.7a, the gas productions predicted by ANN were all close to the experimental ones (E1-E15). The absolute relative errors between the predicted and the experimental values were within 4.6 %. Besides, the R-squared value between the experimental and the ANN predicted gas production was 0.9719. The predicted gas production was relatively less accurate than the predicted liquid fuel production. This is because the gas production was calculated from the difference between the initial WPE mass and the masses of liquid fuel and residue. Errors in gas production were accumulated, and thereby gas production became more inaccurate [21]. Fig. 4.7b shows the applicability of the ANN predicted gas production. The absolute relative errors between the predicted and the experimental values were within 6.8 %. Quesada et al. [21] adopted the fuzzy neural model to predict the WPE thermal pyrolysis's energy efficiency. The maximum absolute relative error was approximately 6.4 %. The errors of the predicted gas production were in a reasonable range

in this study. Therefore, ANN is qualified to predict gas production.

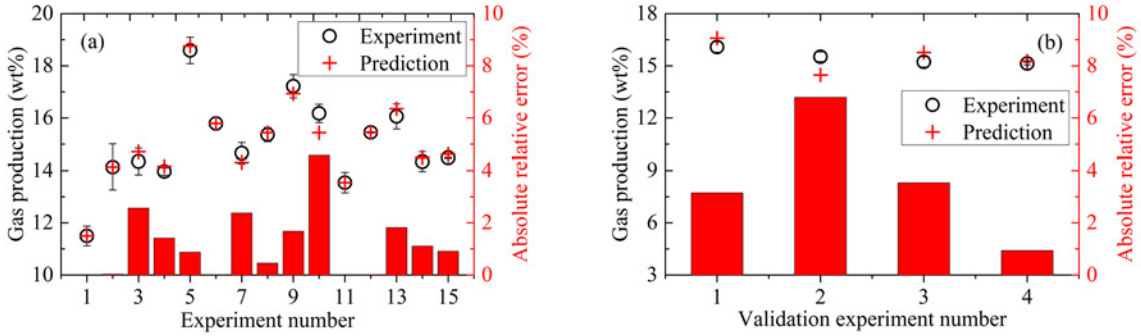

Fig. 4.7. The comparisons of the experimental and the ANN predicted gas productions: (a) Training; (b) Testing.

(ii) Interactive effects of residence time and carrier gas flow rate on gas production

Figs. 4.8a, 4.8b, and 4.8c illustrate the interactive effects of the residence time and the carrier gas flow rate on gas production at temperatures of 425 ℃, 475 ℃, and 525 ℃, respectively. The gas production varied from 11.50 wt% to 18.75 wt% at 425 ℃; from 12.40 wt% to 16.93 wt% at 475 ℃; and from 13.54 wt% to 16.35 wt% at 525 ℃, respectively. Onwudili et al. [3] obtained 10 wt% and 25wt% gas productions through thermal pyrolysis of low-density PE in a batch reactor at temperatures of 425 ℃ and 450 ℃, respectively. These results were similar to the ones reported by [8][32]. Gas productions of 16.58-22.53 wt% and 17.80-27.52 wt% were obtained through thermal pyrolysis of virgin low-density PE and high-density PE within the temperature ranging from 350 ℃ to 400 ℃, respectively [32]. Also, approximately 17 wt% of gas was obtained at a temperature of 500 ℃ [8].

As demonstrated in Fig. 4.8a, a longer residence time would increase the gas production under the lowest (20 mL/min) and the highest (100 mL/min) carrier gas flow rates at 425 ℃. When the residence time was increased from 20 min to 60 min, the gas production was

increased from 11.50-14.17 wt% and 14.14-18.75 wt% under the carrier gas flow rates of 20 mL/min and 100 mL/min, respectively. Onwudili et al. [3] also found that gas production was increased from 8.70 wt% to 16.30 wt% at 450 ℃ when the residence time increased from 0 min to 30 min. This is because the random scission reactions of WPE were not intense to produce pyrolysis gas at low temperatures [37]. Extending the residence time could make the random scission reactions of WPE proceed more thoroughly to obtain higher gas yields. As shown in Fig. 4.8b, the carrier gas flow rate had a stronger impact on gas production under the lowest residence time (20 min) at 475 ℃. The gas production was first increased from 12.40 wt% to 15.82 wt% when the carrier gas flow rate increased from 20 mL/min to 64 mL/min. The increase in gas production could be attributed to the inhibition of polycondensation and repolymerization reactions of the pyrolysis gas at low carrier gas flow rates [38]. While the excessive carrier gas flow rate would reduce the heat transfer efficiency inside the reactor, thereby inhibiting the gas production [37]. Thus, gas production decreased from 15.82 wt% to 14.72 wt% when the carrier gas flow rate varied from 64 mL/min to 100 mL/min. The thermal pyrolysis of linear low-density PE at 450-460 ℃ has a similar phenomenon [24]. The gas production was first increased from 15.5 wt% to 20.0 wt% (by difference) when the carrier gas flow rate increased from 0 mL/min to 30 mL/min. Then, the gas production decreased from 20.0 wt% to 17.5 wt% when the carrier gas flow rate varied from 30 mL/min to 60 mL/min. At 525 ℃, as depicted in Fig. 4.8c, a longer residence time would increase gas production under the lowest carrier gas flow rate (20 mL/min). The gas production was increased from 13.54 wt% to 14.49 wt% when the residence time increased from 20 min to 60 min. This is because that longer residence time

enhanced the possibility of β cleavage reactions for pyrolysis gas formation [41].

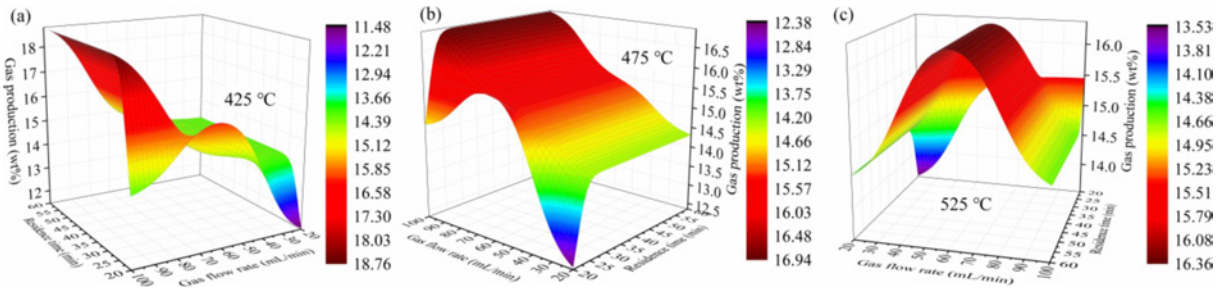

Fig. 4.8. Interactive effects of residence time and carrier gas flow rate on gas production at different temperatures: (a) 425 ℃; (b) 475 ℃; (c) 525 ℃.

(iii) Interactive effects of temperature and carrier gas flow rate on gas production

Figs. 4.9a, 4.9b, and 4.9c present the interactive effects of the temperature and the carrier gas flow rate on gas production under residence times of 20 min, 40 min, and 60 min, respectively. The carrier gas flow rate had a stronger influence on gas production at the lowest temperature (425 ℃) regardless of residence time changes. As illustrated in Fig. 4.9a, the temperature had a similar influence on gas production under the lowest (20 mL/min) and the highest (100 mL/min) carrier gas flow rates. The gas productions were both increased with the increasing temperature. The liquid fuel's secondary cracking reactions were more intense to generate pyrolysis gas at higher temperatures [37]. However, the temperature had an opposite impact on the gas production under the medium (60 mL/min) carrier gas flow rate. The gas production was decreased from 16.17 wt% to 15.30 wt% when the temperature increased from 425 ℃ to 525 ℃. The gas production was also decreased from 55.46 wt% to 32.63 wt% when the temperature varied from 450 ℃ to 550 ℃ in [21]. The increase in temperature promoted polycondensation and repolymerization reactions of the pyrolysis gas, resulting in a reduction in gas production. It also suggested that the polycondensation and repolymerization reactions

of the pyrolysis gas played a dominant role, compared to the secondary cracking reactions of the liquid fuel, under the medium carrier gas flow rate (60 mL/min). As depicted in Figs. 4.9b and 4.9c, the temperature and the carrier gas flow rate had the same influences on gas production under the residence times of 40 min and 60 min. The lowest gas productions were obtained under the same operating conditions (temperature of 425 ℃ and carrier gas flow rate of 20 mL/min). While the highest gas productions were both obtained under 425 ℃ and 100 mL/min. It indicated that a higher carrier gas flow rate could suppress the polycondensation and repolymerization reactions for the pyrolysis gas consumption under the residence times of 40 min and 60 min.

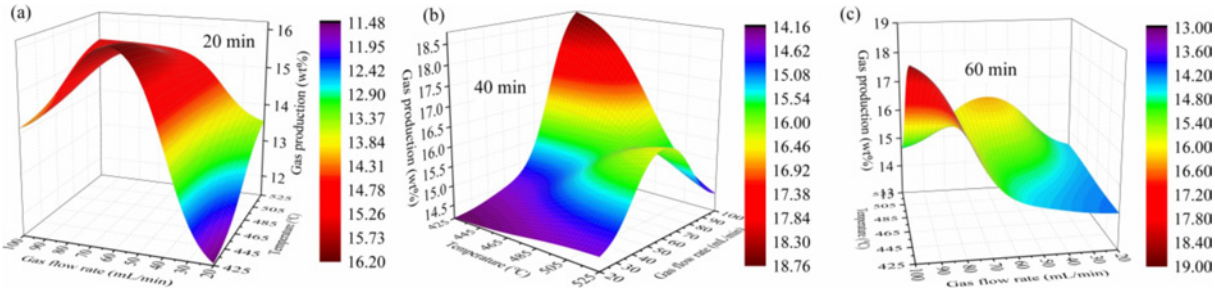

Fig. 4.9. Interactive effects of temperature and carrier gas flow rate on gas production under different residence times: (a) 20 min; (b) 40 min; (c) 60 min.

(iv) Interactive effects of temperature and residence time on gas production

Figs. 4.10a, 4.10b, and 4.10c demonstrate the interactive effects of the temperature and the residence time on gas production under carrier gas flow rates of 20 mL/min, 60 mL/min, and 100 mL/min, respectively. As shown in Fig. 4.10a, the temperature could enhance gas production under the carrier gas flow rate of 20 mL/min regardless of the residence time changes. As depicted in Figs. 4.10b and 4.10c, the interactive effects of the temperature and the residence time became more complicated on gas production under the carrier gas flow rates of

60 mL/min and 100 mL/min. For example, as demonstrated in Fig. 4.10b, the gas production was decreased from 16.17 wt% to 14.71 wt% when the residence time increased from 20 min to 60 min at 425 ℃ and 60 mL/min. The reason for the decrease in gas production was the promotion of the pyrolysis gas polymerization reactions at a longer residence time. Concurrently, the gas production was increased from 15.30 wt% to 16.35 wt% when the residence time varied from 20 min to 60 min at 525 ℃ and 60 mL/min. The longer residence time enhanced the possibility of char gasification and β cleavage reactions for pyrolysis gas formation [37]. As depicted in Fig. 4.10c, the residence time's influence on gas production was opposite under 100 mL/min, compared with the results under 60 mL/min. Longer residence times would enhance the gas production at 425 ℃; while it would inhibit the gas production at 525 ℃.

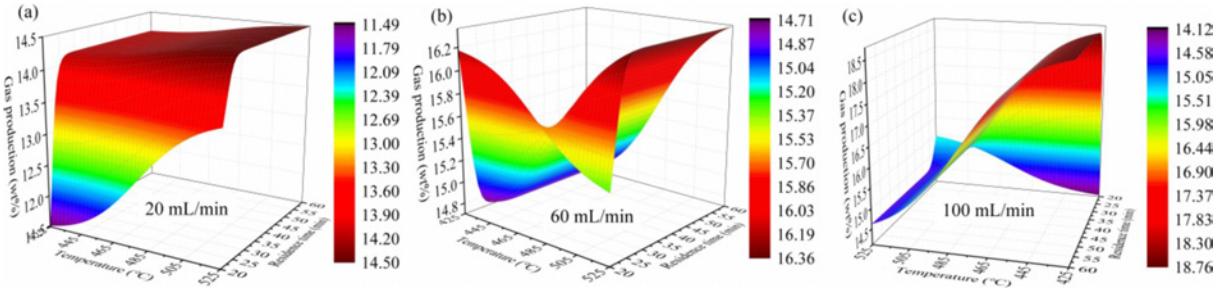

Fig. 4.10. Interactive effects of temperature and residence time on gas production under different carrier gas flow rates: (a) 20 mL/min; (b) 60 mL/min; (c) 100 mL/min.

4.3.3. Optimization of operating conditions by GA

As discussed in Section 4.3.1, the operating conditions (temperature, residence time, and carrier gas flow rate) had very complex interactive effects on liquid fuel production. To obtain the maximum liquid fuel production, GA was adopted to determine the optimal operating conditions. Fig. 4.11a exhibits the variations of the average and the optimal values of 1000

individuals' fitness in 1000 iterations. In this study, fitness was liquid fuel production. The optimal value reached stability after 100 iterations, while the average value was stabled after 800 iterations.

Fig. 4.11b shows the maximum liquid fuel production under the optimal operating conditions. The GA optimized operating conditions were 488 ℃, 20 min, and 20 mL/min. The optimal liquid fuel production was 83.63 wt%. Rodríguez-Luna et al. [23] reported 500 ℃ was the most suitable temperature for pyrolysis of high-density PE to produce liquid fuel in a semi-batch reactor. Quesada et al. [21] concluded that the optimal operating conditions for liquid fuel production were 500 ℃ and 120 min. The experiments were conducted in a horizontal tubular reactor. The optimized temperature was close to the one in this study. While the optimized residence time was much longer than the one in this study. This is because the experiments in [21] were conducted under higher heating rates (20-50 ℃/min) and a faster carrier gas flow rate (833 mL/min). Sharuddin et al. [6] also concluded that temperatures below 500 ℃ were suitable for liquid fuel production.

The experiment under GA optimized operating conditions (488 ℃, 20 min, and 20 mL/min) was conducted to verify the GA predicted results. The experimental liquid fuel production was 83.50 ± 0.59 wt%. The absolute relative error between the predicted and the experimental values was within 0.16 %. It suggests that the GA optimized results were accurate and reliable.

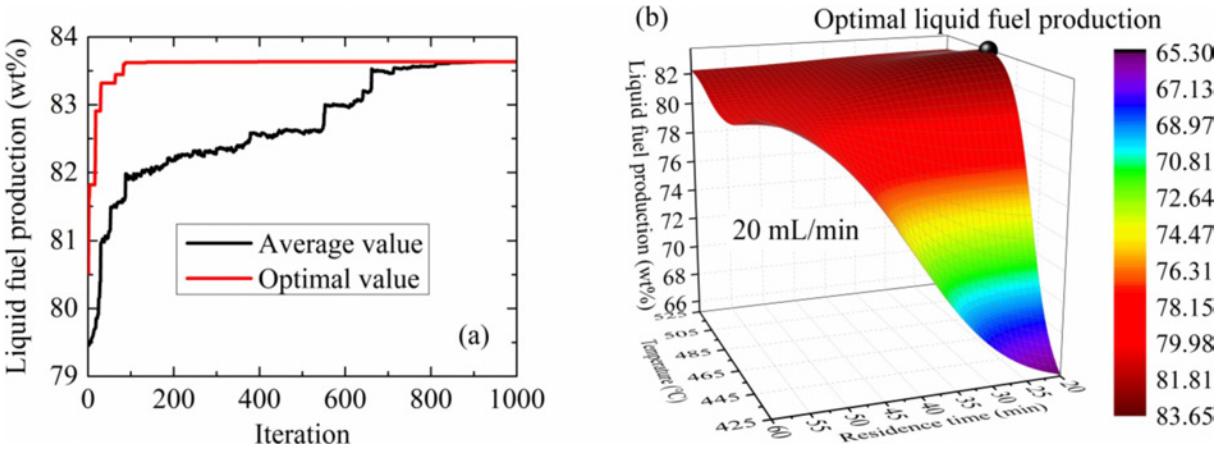

Fig. 4.11. Illustrations of optimized operating conditions by GA: (a) Optimization process; (b) Liquid fuel production under optimal operating conditions.

4.3.4. FTIR analysis

Fig. 4.12 shows the FTIR results of liquid fuels from this study and Quesada et al. [22]. The main functional groups of liquid fuels do not change under different operating conditions [22]. Therefore, the liquid fuel under the optimal operating conditions (488 ℃, 20 min, and 20 mL/min) was chosen to conduct the FTIR analysis. As illustrated in Fig. 4.12, the following functional groups in liquid fuel of this study were determined: C-H stretch at 2916-2848 cm^{-1} [43]; C=C stretching at 1642 cm^{-1} and 1462 cm^{-1}; C-H scissor and bend at 1377 cm^{-1}; C-H out of the plane bend at 909 cm^{-1}; and C-H bend at 719 cm^{-1}. The linear alkanes were generated by intermolecular hydrogen transfer reactions [44]. While the β cleavage coupled with the intramolecular hydrogen transfer reactions are responsible for the alkenes yields during the pyrolysis of WPE [23].

Fig. 4.12 also demonstrates the FTIR results of liquid fuel from Quesada et al. [22] and diesel. The liquid fuel sample in [22] was obtained under 500 ℃, 80 min, and 833 mL/min. The liquid fuel from this study had the same characteristic peaks like the one in [22]. It also suggests

that the operating conditions do not change the main functional groups of WPE thermal pyrolysis liquid fuels. Besides, the liquid fuel from this study had similar characteristic peaks as diesel.

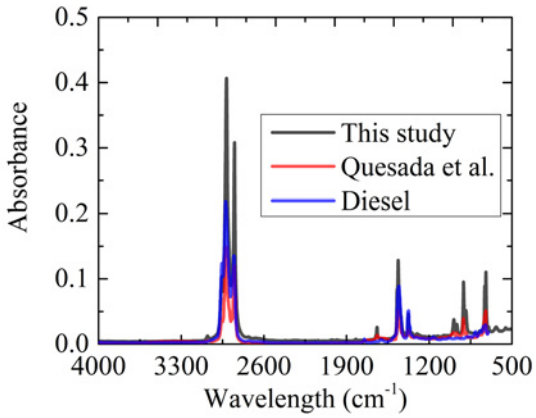

Fig. 4.12. FTIR analysis of liquid fuels from this study and Quesada et al. [22], and diesel [22].

4.3.5. GC-MS analysis

The GC-MS analysis was conducted to determine the specific components of the liquid fuel. Fig. 4.13 demonstrates the liquid fuel chromatogram under the optimal operating conditions (488 ℃, 20 min, and 20 mL/min). The identified compounds present in the liquid fuel under the optimal operating conditions are tabulated in Table 4.2. The components of the liquid fuel were mainly 1-alkenes and n-alkanes ranging from C7 to C36. The liquid fuel's mean molecular weight was 291 g/mol.

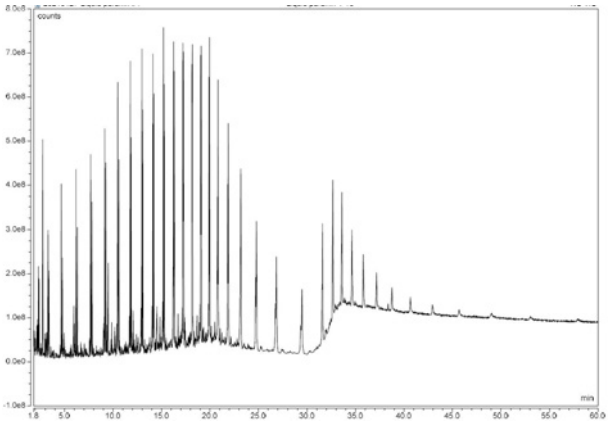

Fig. 4.13. GC-MS analysis of the liquid fuel under the optimal operating conditions (488 ℃, 20 min, and 20 mL/min).

Table 4.2. Identified compounds present in the liquid fuel under the optimal operating conditions (488 ℃, 20 min, and 20 mL/min).

Peak	Time (min)	Compound	Relative area (%)	Molecular weight
1	2.32	cyclopentane (C7)	0.71	98
2	2.38	n-heptane (C7)	0.63	100
3	2.76	1-octene (C8)	1.67	112
4	2.98	n-octane (C8)	0.20	114
5	3.31	1-nonene (C9)	1.41	126
6	3.40	n-nonane (C9)	0.74	128
7	4.66	1-decene (C10)	1.33	140
8	4.79	n-decane (C10)	0.78	142
9	6.19	1-undecene (C11)	1.51	154
10	6.31	n-undecane (C11)	1.01	156
11	7.70	1-dodecene (C12)	1.53	168
12	7.82	n-dodecane (C12)	1.21	170
13	9.15	1-tridecene (C13)	1.75	182
14	9.26	n-tridecane (C13)	2.12	184
15	10.50	1-tetradecene (C14)	2.09	196
16	10.60	n-tetradecane (C14)	1.47	198
17	11.78	1-pentadecene (C15)	2.18	210
18	11.87	n-pentadecane (C15)	1.66	212
19	12.99	1-hexadecene (C16)	2.45	224
20	13.07	n-hexadecane (C16)	2.01	226
21	14.13	1-heptadecene (C17)	2.62	238
22	14.20	n-heptadecane (C17)	2.08	240

23	15.21	1-octadecene (C18)	2.87	252
24	15.28	n-octadecane (C18)	2.39	254
25	16.24	1-nonadecene (C19)	2.74	266
26	16.30	n-nonadecane (C19)	2.35	268
27	17.21	1-eicosene (C20)	2.54	280
28	17.27	n-eicosane (C20)	2.50	282
29	18.15	1-heneicosene (C21)	2.66	294
30	18.20	n-heneicosane (C21)	2.64	296
31	19.04	1-docosene (C22)	2.62	308
32	19.09	n-docosane (C22)	2.89	310
33	19.90	1-tricosene (C23)	2.24	322
34	19.94	n-tricosane (C23)	2.63	324
35	20.79	1-tretacosene (C24)	2.10	336
36	20.83	n-tretacosane (C24)	2.75	338
37	21.83	1-pentacosene (C25)	1.93	350
38	21.88	n-pentacosane (C25)	2.76	352
39	23.11	1-hexacosene (C26)	1.66	364
40	23.17	n-hexacosane (C26)	2.71	366
41	24.71	1-heptacosene (C27)	1.22	378
42	24.79	n-heptacosane (C27)	2.59	380
43	26.75	1-octacosene (C28)	1.31	392
44	26.84	n-octacosane (C28)	2.60	394
45	29.36	1-nonacosene (29)	0.88	406
46	29.47	n-nonacosane (29)	2.37	408
47	31.56	1-triacontene (C30)	0.82	420
48	31.60	n-triacontane (C30)	2.27	422
49	33.60	n-hentriacontane (C31)	2.18	436
50	34.64	n-dotriacontane (C32)	1.80	450
51	35.81	n-tritriacontane (C33)	1.54	464
52	37.16	n-tetratriacontane (C34)	1.00	478
53	38.76	n-pentatriacontane (C35)	0.72	492
54	40.67	n-hexatriacontane (C36)	0.58	506

Figs. A.1-15 illustrate the chromatograms of the liquid fuels E1-15, respectively. The liquid fuels E1-15 had the same component types as the liquid fuel under the optimal operating conditions (mostly 1-alkenes and n-alkanes ranging from C7 to C36). However, the specific component proportions of the liquid fuels were different. This indicated that the operating

conditions had effects on the composition of the liquid fuel produced by the thermal pyrolysis of waste polyethylene. The liquid fuel was classified into light (C_7 – C_{11}), middle (C_{12} – C_{20}) and heavy (C_{21} – C_{36}) fractions [8]. Fig. 4.14 shows the liquid fuel fractions and mean molecular weight under different operating conditions. The light, middle and heavy fractions varied from 3.61-6.79 %, 28.65-42.54 % and 50.72-66.83 %, respectively. Moreover, the liquid fuel's mean molecular weight was varied from 291.00 g/mol to 325.23 g/mol.

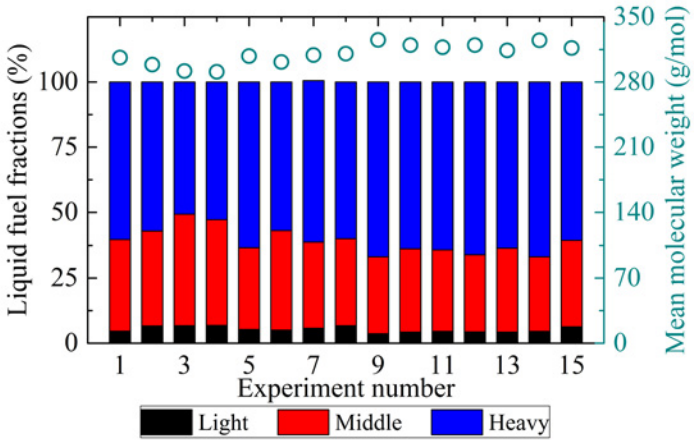

Fig. 4.14. Liquid fuel fractions and mean molecular weight under different operating conditions.

Fig. 4.15 demonstrates the effects of operating conditions on liquid fuel fractions and mean molecular weight. Samples of E3, E8 and E13 were taken into consideration to analyze the effect of temperature on the liquid fuel composition. As shown in Fig. 4.15a, the light and middle fractions were decreased from 6.74-4.25 % and 42.54-32.22 % when the temperature was increased from 425 ℃ to 525 ℃, respectively. In comparison, the heavy fraction was increased from 50.72 % to 63.53 % when the temperature was increased from 425 ℃ to 525 ℃. Besides, the liquid fuel's mean molecular weight was also increased from 291.78 g/mol to 313.96 g/mol. This indicates that high temperature is conducive to the formation of the heavy

fraction in the liquid fuel. It can be ascribed to that higher temperature would enhance the possibility of secondary reactions of liquid fuel's light and middle fractions for pyrolysis gas formation [8].

Fig. 4.15b illustrates the effect of residence time on liquid fuel fractions and mean molecular weight (E6, E8 and E10). The middle fraction was decreased from 38.18 % to 32.02 %, whereas the heavy fraction was increased from 56.80 % to 63.73 % when residence time was increased from 20 min to 60 min. The light fraction was firstly increased from 5.02 % to 6.73 % when residence time was increased from 20 min to 40 min. The light fraction was then decreased from 6.73 % to 4.25 % when residence time varied from 40 min to 60 min. The longer residence time enhanced the possibility of β cleavage reactions of liquid fuel's light and middle fractions [8][37]. Therefore, the liquid fuel's mean molecular weight was increased from 301.54 g/mol to 319.73 g/mol when residence time was increased from 20 min to 60 min.

Fig. 4.15c shows the effect of carrier gas flow rate on liquid fuel fractions and mean molecular weight (E7, E8 and E9). The light, middle and heavy fractions varied from 3.61-6.73 %, 29.57-33.42 % and 59.86-66.82 %, respectively. Moreover, the liquid fuel's mean molecular weight was increased from 309.02 g/mol to 325.23 g/mol when the carrier gas flow rate increased from 20 mL/min to 100 mL/min. The increase in liquid fuel's mean molecular weight could be attributed to the higher carrier gas flow rate, which can quickly carry volatile products out of the reactor, thereby inhibiting β cleavage reactions of liquid fuel's heavy fraction [37] and polycondensation and repolymerization reactions of the pyrolysis gas [38] for the light and middle fractions' liquid fuel formation.

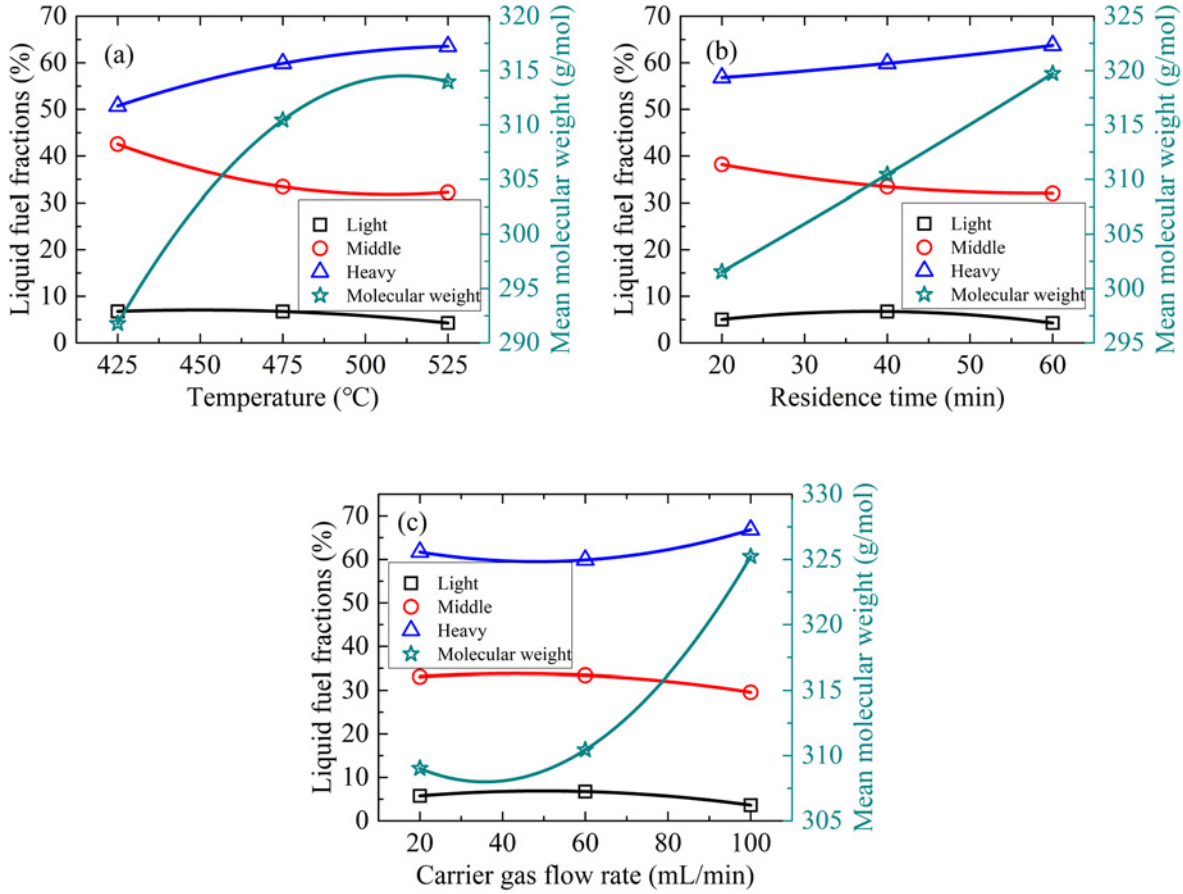

Fig. 4.15. Effects of operating conditions on liquid fuel fractions and mean molecular weight: (a) Temperature; (b) Residence time; (c) Carrier gas flow rate.

4.4. Conclusions

This chapter aims to obtain the optimal operating conditions for liquid fuel production through thermal pyrolysis of waste polyethylene in a bench-scale semi-batch reactor. Three operating conditions were considered, i.e., the temperature, the residence time, and the carrier gas flow rate. ANN comprehensively described the interactive effects of operating conditions on liquid fuel production. The R-squared value between the experimental and the ANN predicted liquid fuel production was 0.9934. It revealed that the ANN predicted liquid fuel production was accurate and reliable.

Subsequently, genetic algorithm (GA) was adopted to optimize the operating conditions to maximize liquid fuel production. The GA optimized liquid fuel production was 83.63 wt% under the operating conditions of 488 ℃ (temperature), 20 min (residence time) and 20 mL/min (carrier gas flow rate). The experimental liquid fuel production was 83.50 wt% under these operating conditions, a value very close to the GA predicted one. It indicated that the ANN coupled with GA was qualified to optimize the operating conditions for liquid fuel production through thermal pyrolysis of waste polyethylene.

FTIR and GC-MS analyses were conducted to determine the liquid fuels' main functional groups and the chemical components. It was found that the operating conditions did not change the liquid fuels' main functional groups. The waste polyethylene thermal pyrolysis liquid fuels had similar characteristic peaks as commercial diesel. The liquid fuels had the same component types under different operating conditions (mostly 1-alkenes and n-alkanes ranging from C7 to C36). However, the specific component proportions of the liquid fuels varied with the operating conditions. It could be concluded that high temperature, long residence time, and high carrier gas flow rate were conducive to formation of the liquid fuel's heavy fraction. While low temperature, short residence time, and low carrier gas flow rate were beneficial to form light and middle fractions in liquid fuel.

Bibliography

[1] Kaza, S., Yao, L., Bhada-Tata, P. and Van Woerden, F., 2018. What a waste 2.0: a global snapshot of solid waste management to 2050. World Bank Publications.

[2] Quesada, L., Calero, M., Martín-Lara, M.A., Perez, A. and Blazquez, G., 2020. Production of an alternative fuel by pyrolysis of plastic wastes mixtures. Energy & Fuels, 34(2), pp.1781-1790.

[3] Onwudili, J.A., Insura, N. and Williams, P.T., 2009. Composition of products from the pyrolysis of polyethylene and polystyrene in a closed batch reactor: Effects of temperature and residence time. Journal of Analytical and Applied Pyrolysis, 86(2), pp.293-303.

[4] Geyer, R., Jambeck, J.R. and Law, K.L., 2017. Production, use, and fate of all plastics ever made. Science advances, 3(7), p.e1700782.

[5] Crippa, M., De Wilde, B., Koopmans, R., Leyssens, J., Muncke, J., Ritschkoff, A.C., Van Doorsselaer, K., Velis, C. and Wagner, M., 2019. A circular economy for plastics: Insights from research and innovation to inform policy and funding decisions.

[6] Sharuddin, S.D.A., Abnisa, F., Daud, W.M.A.W. and Aroua, M.K., 2016. A review on pyrolysis of plastic wastes. Energy conversion and management, 115, pp.308-326.

[7] Pan, R., Duque, J.V.F. and Debenest, G., 2021. Investigating waste plastic pyrolysis kinetic parameters by genetic algorithm coupled with thermogravimetric analysis. Waste and Biomass Valorization, 12(5), pp.2623-2637.

[8] Das, P. and Tiwari, P., 2018. The effect of slow pyrolysis on the conversion of packaging waste plastics (PE and PP) into fuel. Waste Management, 79, pp.615-624.

[9] Ceamanos, J., Mastral, J.F., Millera, A. and Aldea, M.E., 2002. Kinetics of pyrolysis of high density polyethylene. Comparison of isothermal and dynamic experiments. Journal of Analytical and Applied Pyrolysis, 65(2), pp.93-110.

[10] Mazloum, S., Awad, S., Allam, N., Aboumsallem, Y., Loubar, K. and Tazerout, M., 2021. Modelling plastic heating and melting in a semi-batch pyrolysis reactor. Applied Energy, 283, p.116375.

[11] Al-Salem, S.M., Antelava, A., Constantinou, A., Manos, G. and Dutta, A., 2017. A review on thermal and catalytic pyrolysis of plastic solid waste (PSW). Journal of environmental management, 197, pp.177-198.

[12] Kunwar, B., Cheng, H.N., Chandrashekaran, S.R. and Sharma, B.K., 2016. Plastics to fuel: a review. Renewable and Sustainable Energy Reviews, 54, pp.421-428.

[13] Manos, G., Garforth, A. and Dwyer, J., 2000. Catalytic degradation of high-density polyethylene on an ultrastable-Y zeolite. Nature of initial polymer reactions, pattern of formation of gas and liquid products, and temperature effects. Industrial & engineering chemistry research, 39(5), pp.1203-1208.

[14] Manos, G., Yusof, I.Y., Gangas, N.H. and Papayannakos, N., 2002. Tertiary recycling of polyethylene to hydrocarbon fuel by catalytic cracking over aluminum pillared clays. Energy & Fuels, 16(2), pp.485-489.

[15] Quesada, L., Calero de Hoces, M., Martín-Lara, M.A., Luzón, G. and Blázquez, G., 2020. Performance of different catalysts for the in situ cracking of the oil-waxes obtained by the pyrolysis of polyethylene film waste. Sustainability, 12(13), p.5482.

[16] Kassargy, C., Awad, S., Burnens, G., Kahine, K. and Tazerout, M., 2017. Experimental study of catalytic pyrolysis of polyethylene and polypropylene over USY zeolite and separation to gasoline and diesel-like fuels. Journal of Analytical and Applied Pyrolysis, 127, pp.31-37.

[17] Al-Salem, S. M., 2019. Thermal pyrolysis of high density polyethylene (HDPE) in a novel fixed bed reactor system for the production of high value gasoline range hydrocarbons (HC). Process Safety and Environmental Protection, 127, pp.171-179.

[18] Yan, G., Jing, X., Wen, H. and Xiang, S., 2015. Thermal cracking of virgin and waste plastics of PP and LDPE in a semibatch reactor under atmospheric pressure. Energy & Fuels, 29(4), pp.2289-2298.

[19] Insura, N., Onwudili, J.A. and Williams, P.T., 2010. Catalytic pyrolysis of low-density polyethylene over alumina-supported noble metal catalysts. Energy & fuels, 24(8), pp.4231-4240.

[20] Tiikma, L., Tamvelius, H. and Luik, L., 2007. Coprocessing of heavy shale oil with polyethylene waste. Journal of analytical and applied pyrolysis, 79(1-2), pp.191-195.

[21] Quesada, L., Pérez, A., Godoy, V., Peula, F.J., Calero, M. and Blázquez, G., 2019. Optimization of the pyrolysis process of a plastic waste to obtain a liquid fuel using different mathematical models. Energy Conversion and Management, 188, pp.19-26.

[22] Quesada, L., Calero, M., Martín-Lara, M.A., Pérez, A. and Blázquez, G., 2019. Characterization of fuel produced by pyrolysis of plastic film obtained of municipal solid waste. Energy, 186, p.115874.

[23] Rodríguez-Luna, L., Bustos-Martínez, D. and Valenzuela, E., 2021. Two-step pyrolysis for waste HDPE valorization. Process Safety and Environmental Protection, 149, pp.526-536.

[24] Muhammad, I., Makwashi, N. and Manos, G., 2019. Catalytic degradation of linear low-density polyethylene over HY-zeolite via pre-degradation method. Journal of Analytical and Applied Pyrolysis, 138, pp.10-21.

[25] Karaboga, D. and Kaya, E., 2019. Adaptive network based fuzzy inference system (ANFIS) training approaches: a comprehensive survey. Artificial Intelligence Review, 52(4), pp.2263-2293.

[26] Jang, J.S.R., 1993. ANFIS: adaptive-network-based fuzzy inference system. IEEE transactions on systems, man, and cybernetics, 23(3), pp.665-685

[27] Paramasivam, B., 2020. Fuzzy prediction and RSM optimization of CI engine performance analysis: aegle marmelos non-edible seed cake pyrolysis oil as a diesel alternative. Energy Sources, Part A: Recovery, Utilization, and Environmental Effects, pp.1-17.

[28] Pan, R., Duque, J.V.F., Martins, M.F. and Debenest, G., 2020. Application of a neural fuzzy model combined with simulated annealing algorithm to predict optimal conditions for polyethylene waste non-isothermal pyrolysis. Heliyon, 6(11), p.e05598.

[29] Al-Yaari, M. and Dubdub, I., 2020. Application of artificial neural networks to predict the catalytic pyrolysis of HDPE using non-isothermal TGA data. Polymers, 12(8), p.1813.

[30] Fakhrhoseini, S. M. and Dastanian, M., 2013. Predicting pyrolysis products of PE, PP, and PET using NRTL activity coefficient model. Journal of Chemistry, 2013.

[31] Ighose, B. O., Adeleke, I.A., Damos, M., Junaid, H.A., Okpalaeke, K.E. and Betiku, E.,

2017. Optimization of biodiesel production from Thevetia peruviana seed oil by adaptive neuro-fuzzy inference system coupled with genetic algorithm and response surface methodology. Energy conversion and Management, 132, pp.231-240.

[32] Das, P. and Tiwari, P., 2018. Valorization of packaging plastic waste by slow pyrolysis. Resources, Conservation and Recycling, 128, pp.69-77.

[33] Lin, Y.H. and Yen, H.Y., 2005. Fluidised bed pyrolysis of polypropylene over cracking catalysts for producing hydrocarbons. Polymer degradation and Stability, 89(1), pp.101-108.

[34] Lin, Y.H. and Yang, M.H., 2007. Catalytic pyrolysis of polyolefin waste into valuable hydrocarbons over reused catalyst from refinery FCC units. Applied Catalysis A: General, 328(2), pp.132-139.

[35] Wang, C., Lei, H., Qian, M., Huo, E., Zhao, Y., Zhang, Q., Mateo, W., Lin, X., Kong, X., Zou, R. and Ruan, R., 2020. Application of highly stable biochar catalysts for efficient pyrolysis of plastics: a readily accessible potential solution to a global waste crisis. Sustainable Energy & Fuels, 4(9), pp.4614-4624.

[36] Lu, X., Wu, Y., Lian, J., Zhang, Y., Chen, C., Wang, P. and Meng, L., 2020. Energy management of hybrid electric vehicles: A review of energy optimization of fuel cell hybrid power system based on genetic algorithm. Energy Conversion and Management, 205, p.112474.

[37] Jiang, G., Fenwick, R., Seville, J., Mahood, H.B., Thorpe, R.B., Bhattacharya, S., Monsalve, D.S. and Leeke, G.A., 2022. Lumped kinetic modelling of polyolefin pyrolysis:

A non-isothermal method to estimate rate constants. Journal of Analytical and Applied Pyrolysis, 164, p.105530.

[38] Heidari, A., Stahl, R., Younesi, H., Rashidi, A., Troeger, N. and Ghoreyshi, A.A., 2014. Effect of process conditions on product yield and composition of fast pyrolysis of Eucalyptus grandis in fluidized bed reactor. Journal of Industrial and Engineering Chemistry, 20(4), pp.2594-2602.

[39] Wei, F., Cao, J.P., Zhao, X.Y., Ren, J., Wang, J.X., Fan, X. and Wei, X.Y., 2017. Nitrogen evolution during fast pyrolysis of sewage sludge under inert and reductive atmospheres. Energy & Fuels, 31(7), pp.7191-7196.

[40] Morato-Godino, A., Sánchez-Delgado, S., García-Hernando, N. and Soria-Verdugo, A., 2018. Pyrolysis of Cynara cardunculus L. samples–Effect of operating conditions and bed stage on the evolution of the conversion. Chemical Engineering Journal, 351, pp.371-381.

[41] Cai, N., Li, X., Xia, S., Sun, L., Hu, J., Bartocci, P., Fantozzi, F., Williams, P.T., Yang, H. and Chen, H., 2021. Pyrolysis-catalysis of different waste plastics over Fe/Al2O3 catalyst: High-value hydrogen, liquid fuels, carbon nanotubes and possible reaction mechanisms. Energy Conversion and Management, 229, p.113794.

[42] Vollmer, I., Jenks, M.J., Roelands, M.C., White, R.J., van Harmelen, T., de Wild, P., van Der Laan, G.P., Meirer, F., Keurentjes, J.T. and Weckhuysen, B.M., 2020. Beyond mechanical recycling: Giving new life to plastic waste. Angewandte Chemie International Edition, 59(36), pp.15402-15423.

[43] Ghenai, C., Rasheed, M.A., Alshamsi, M.J., Alkamali, M.A., Ahmad, F.F. and Inayat, A.,

2020. Design of hybrid solar photovoltaics/shrouded wind turbine power system for thermal pyrolysis of plastic waste. Case Studies in Thermal Engineering, 22, p.100773.

[44] McCaffrey, W.C., Cooper, D.G. and Kamal, M.R., 1998. Tertiary recycling of polyethylene: mechanism of liquid production from polyethylene by thermolysis/reactive distillation. Polymer degradation and stability, 62(3), pp.513-521.

Chapter 5

Optimization of oil production through ex-situ catalytic pyrolysis of waste polyethylene with activated carbon

Summary

Chapter 4 investigated the oil production from plastic thermal pyrolysis. The thermal pyrolysis oil had a large proportion of heavy fraction, making it challenging as a commercial fuel alternative. Therefore, the investigation of plastic catalytic pyrolysis should be conducted to improve the pyrolysis oil's quality.

This chapter studied the ex-situ catalytic pyrolysis of waste polyethylene (WPE) with activated carbon (AC). It was found that the operating parameters and AC/WPE mass ratio had complex interactions on the WPE-AC catalytic pyrolysis oil and gas yields. A hybrid method of artificial neural network (ANN) coupled with genetic algorithm (GA) was used to establish the mathematical expressions of oil and gas yields under different conditions and optimize the conditions to obtain the highest oil yield. The R^2 values and the average absolute relative errors between the experimental and the ANN predicted values were 0.9992 and 0.60 %, and 0.9830 and 5.01 % in the training and the testing tests, respectively. The optimal oil production calculated by ANN-GA was 69.16 wt% under 479 °C, the AC/WPE mass ratio of 1, and 10 mL/min. The experimental oil yield was 69.63 wt% under the optimal parameters, which was close to the predicted value of ANN-GA. The WPE-AC catalytic pyrolysis oils under different conditions were characterized by the Fourier-transform infrared spectroscopy (FTIR) and the gas chromatography/mass spectrometry (GC/MS). The types of oil's functional groups did not change with different operating parameters and AC/WPE mass ratios. The oils were composed

of alkenes, naphthenes, alkanes, and aromatic hydrocarbons ranging from C8 to C33. The operating parameters and AC/WPE mass ratio affected the oil fractions to a great extent.

Candidate contribution: Conceptualization, methodology, experimental design and execution, formal analysis, resources, data curation, writing - original draft, visualization.

5.1. Introduction

Municipal solid waste (MSW) increases by ~2.01 billion tons per year due to global urbanization and population growth [1]. It has been reported that ~33 % of MSW is not adequately managed [2]. Waste plastics account for a large proportion (5.6–27.6 wt%) of MSW [3]. Moreover, waste polyethylene (WPE) takes up the most significant proportion (38–62 wt%) of plastic in MSW [4]. Mass production of plastics and improper handling of waste plastics has led to a waste plastic crisis [5]. For example, landfilling would generate microplastics that harm ecosystems and living things [6]. In terms of the incineration of waste plastics, it causes a large amount of greenhouse gas emissions [7]. Therefore, it is necessary to adopt appropriate methods to dispose of waste plastics, WPE in particular.

Pyrolysis, without the presence of oxygen, is a promising method to convert WPE into value-added oil, gas, and char [8][9]. The pyrolysis oil is considered a substitute for commercial gasoline or diesel, so it has aroused the research interest of many researchers [5][10][11]. In the absence of catalysis, the WPE pyrolysis oil contains a large proportion of macromolecular wax that is solid at room temperature [12][13][14]. To be a suitable alternative to commercial fuels, researchers use catalysts to improve the quality of WPE pyrolysis oil.

It has been reported that activated carbon (AC) could effectively reduce wax in WPE pyrolysis oil. Duan et al. [15] reported that low-density PE could be pyrolyzed with AC (mass ratio of 1:1) at 550 °C to obtain ~45 wt% pyrolysis oil containing only C8–C16 hydrocarbons. Huo et al. [16] used AC to catalytically pyrolyze low-density PE (mass ratio of 2:1) at 500 °C to obtain 56.0 wt% oil, which was 100 % jet fuel. Zhang et al. [11] also recovered 54.0 wt%

high-quality oil from low-density PE ex-situ catalytic pyrolysis with AC under the AC/low-density PE mass ratio of 2 and 571 °C. Besides, Zhang et al. [17] also found that AC could enhance the aromatics' selectivity in the oil obtained from co-pyrolysis of biomass and high-density PE.

It can be concluded that the WPE pyrolysis oil could be upgraded by catalytic pyrolysis in the presence of AC. The effects of temperature and AC/WPE mass ratio on the yield and composition of WPE pyrolysis oil have also been comprehensively investigated. Nevertheless, according to [14][18], the flow rate of carrier gas is also a significant parameter, determining the oil yield and composition to a great extent. However, few studies were conducted to investigate the interactions of temperature and carrier gas flow rate on the WPE-AC catalytic pyrolysis oil yield to the best of our knowledge. Therefore, this study investigates the effect of AC/WPE mass ratio on the WPE catalytic pyrolysis affected by two operating parameters: the temperature and flow rate of carrier gas. Based on the mentioned studies, the target ranges for the temperature, the flow rate of carrier gas, and the AC/WPE mass ratio are 425–525 °C, 10–30 mL/min, and 1–2, respectively.

Since the correlation of the operating parameters and AC/WPE mass ratio is expected to be ill-posed, the methodology of artificial neural network (ANN) coupled with a genetic algorithm (GA) is used to establish the mathematical expression to estimate oil yield under different conditions and then maximize the oil yield. The recovered oils are characterized by Fourier-transform infrared spectroscopy (FTIR) and gas chromatography/mass spectrometry (GC/MS). The main functional groups and components of the oil are analyzed under different operating

parameters and AC/WPE mass ratios.

5.2. Experiments and methods

5.2.1. Materials

WPE (~3 mm particles) was recovered from MSW and provided by Zhoushan Jinke Renewable Resources Co., China. The AC sample was purchased from Sigma-Aldrich, Germany (100 mesh, CAS: 7440-44-0). The AC's BET surface area, average pore diameter, and average particle size are 876.45 m^2/g, 3.33 nm, and 19.27 μm, respectively [19].

Fig. 5.1 shows the thermogravimetric analysis of WPE. The sample was heated from 20 °C to 550 °C at a heating rate of 6 °C/min. 2.81 wt% of residue remained after the thermogravimetric analysis. The WPE's onset, end, and maximum degradation temperatures [20] were 452.1 °C, 494.1 °C, and 474.9 °C, respectively. Moreover, the maximum mass loss rate was 21.44 wt%/min.

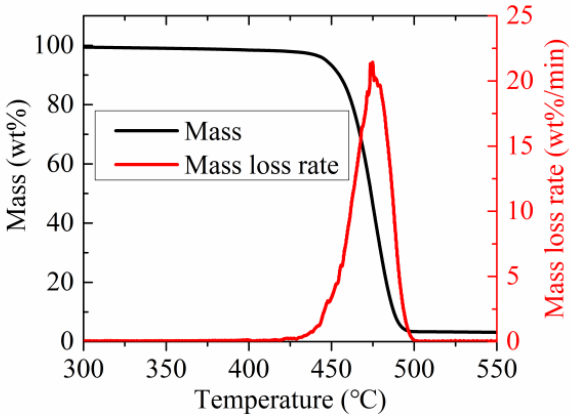

Fig.5.1. Thermogravimetric analysis of WPE.

5.2.2. Experiments

Fig. 5.2 shows the experimental setup for ex-situ catalytic pyrolysis of WPE with AC.

Nitrogen is severed as the purge gas (purge for 30 min under 100 mL/min) to create the oxygen-free atmosphere for WPE-AC catalytic pyrolysis. The flow rate of nitrogen is controlled by the gas flow controller with the range of 0–250 mL/min. The pyrolysis is carried out in a 99% Al_2O_3 crucible (Φ40 mm × 60 mm, wall thickness 3 mm) placed in a 200 mL reactor. As shown in Fig. 5.2, ~2 g of WPE is evenly spread on the crucible bottom. The 2nd, 3rd, and fourth layers are quartz wool, AC, and quartz wool. The reactor is heated to the target temperature under 6 °C/min and stays at the target temperature for 20 min. The pyrolysis oil is cooled by the water-chiller condenser and condensed in the glass bottles placed in a mixture of ice and water. A 10 L gas bag is used to collect the pyrolysis gas.

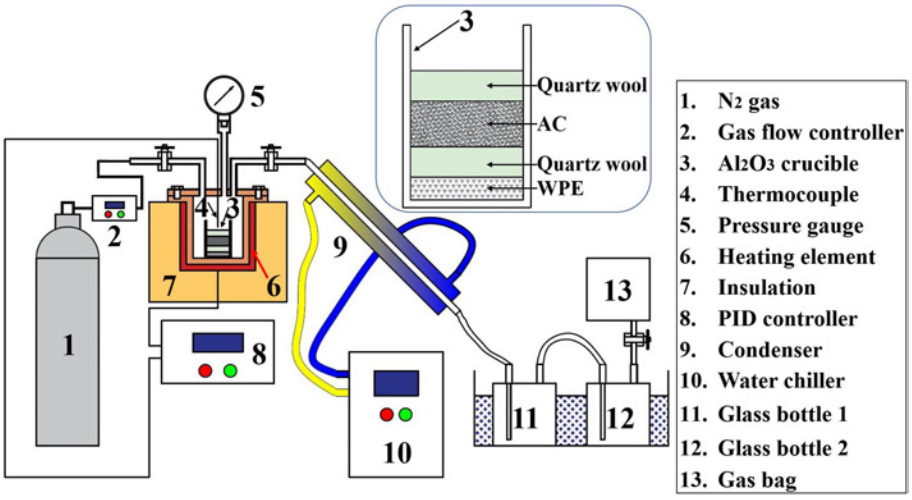

Fig.5.2. Experimental setup for ex-situ catalytic pyrolysis of WPE with AC.

Table 5.1 shows the experimental design of ex-situ catalytic pyrolysis of WPE with AC based on the central-composite design [11][14]. The temperature, AC/WPE mass ratio, and flow rate of carrier gas were investigated in the ranges of 425–525 °C, 1–2, and 10–30 mL/min, respectively. Experiments of R1–R16 were carried out to obtain the training data for ANN-GA, and V1–V6 were conducted to gain the testing data.

Table 5.1. Experimental design of ex-situ catalytic pyrolysis of WPE with AC.

Run	Temperature (°C)	AC/WPE mass ratio	Carrier gas flow rate (mL/min)
R1	425	1	10
R2	425	1	30
R3	425	1.5	20
R4	425	2	10
R5	425	2	30
R6	475	1	20
R7	475	1.5	10
R8	475	1.5	20
R9	475	1.5	30
R10	475	2	20
R11	475	2	30
R12	525	1	10
R13	525	1	30
R14	525	1.5	20
R15	525	2	10
R16	525	2	30
V1	450	1	10
V2	450	1.25	25
V3	450	1.75	15
V4[a]	479	1	10
V5	500	1.25	25
V6	500	1.75	15

[a] Conditions optimized by ANN-GA.

5.2.3. Characterization methods for recovered oil

FTIR (Thermo Nicolet 6700) and GC/MS (Thermo Scientific TRACE 1300/1310 coupled Thermo Fisher TSQ 9000) analyses were conducted to identify the recovered oils' functional groups and specific compositions. The operating details are wholly described in the previous study [14].

5.2.4. ANN-GA

Fig. 5.3 shows the flow schematic of ANN coupled with GA, which has been described in detail in previous studies [14][21][22]. This study adopted ANN-GA to investigate the triplet of parameters: pyrolysis temperatures, AC/WPE mass ratios, and flow rates of carrier gas. ANN trained the experimental gas and oil yields under the triplet combination, and then the mathematical expressions of gas and oil yields were expressed in terms of the triplet of parameters. Subsequently, the oil yield was optimized by GA to obtain the highest value.

In order to verify the applicability of ANN-GA, this study used ANN-GA to optimize the required heat and exergy efficiency during the WPE gasification process [23]. Hasanzadeh et al. [23] investigated the interactions of temperature and steam to polyethylene waste ratio (S/P ratio) on the WPE gasification's required heat and exergy efficiency. They used the response surface methodology (RSM) to establish the mathematical expressions of required heat and exergy efficiency expressed in terms of temperature and S/P ratio. A total of 13 sets of tests were conducted to obtain the training data. The comparison of the predicted results of RSM and ANN-GA was described in detail in Appendix B. The ANN-GA predicted results were more consistent with the original data and more accurate than the RSM predicted ones. It can be concluded that ANN-GA can predict and optimize other researches' data.

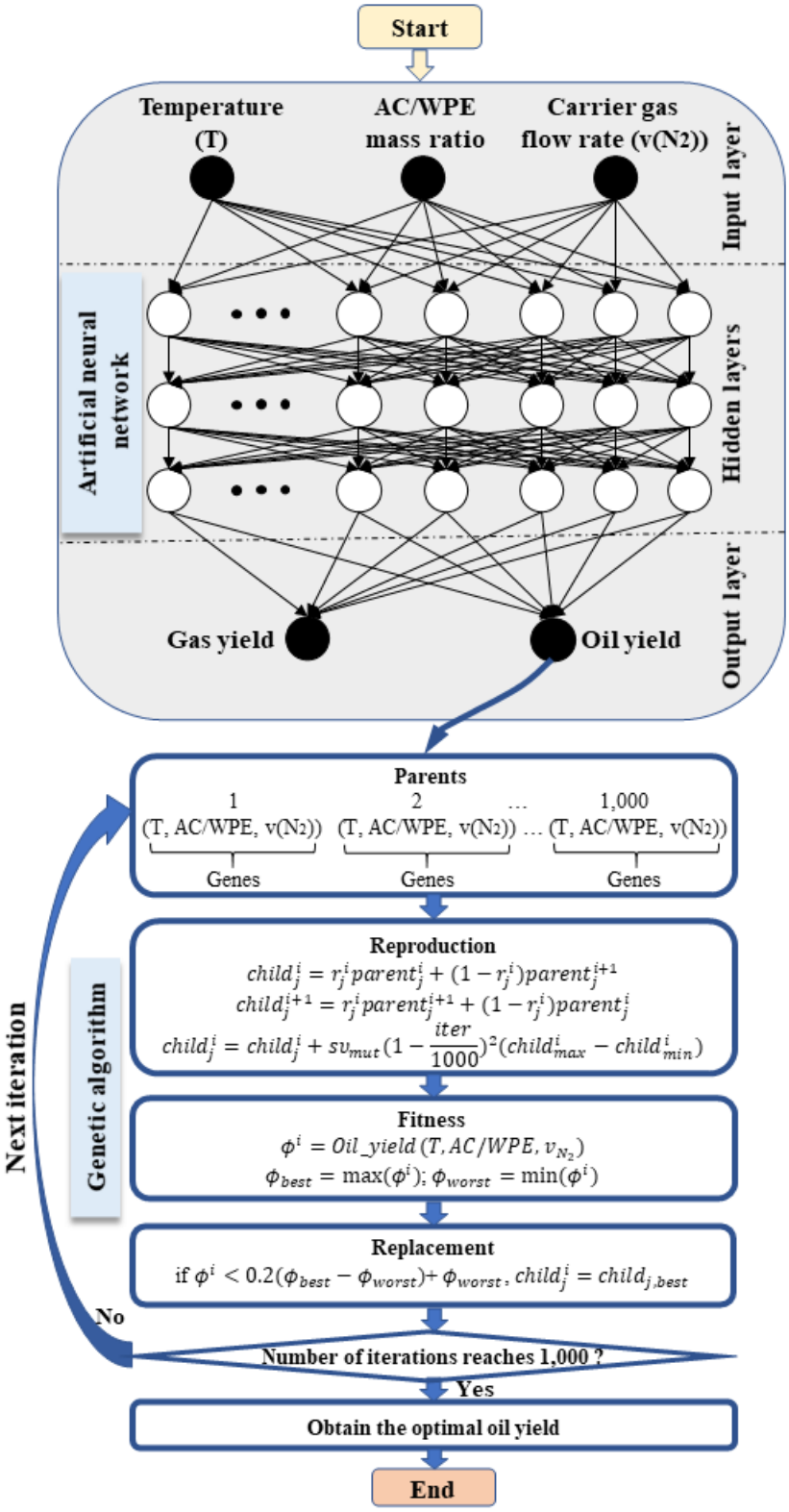

Fig.5.3. Flow schematic of ANN coupled with GA for the context of the present work.

5.3. Results and discussion

5.3.1. Accuracy of ANN

Fig. 5.4 shows the experimental and the ANN predicted oil and gas productions from the WPE-AC catalytic pyrolysis in the training and testing sets. The experimental oil and gas yields oscillated between 56.31–69.63 wt% and 21.18–42.46 wt%, respectively. It is noteworthy that the WPE thermal pyrolysis oil yield (65.31–83.50 wt%) was higher than the WPE-AC catalytic pyrolysis one, whereas the WPE thermal pyrolysis gas yield (11.50–18.59 wt%) was lower than the WPE-AC catalytic pyrolysis one within the same temperature range of 425–525 °C [14]. It was because that the WPE could be decomposed into the shorter-chain hydrocarbons in the presence of catalysts [24]. Santos et al. [25] recovered approximately 21–59 wt% oil and 16–50 wt% gas from the high-density PE catalytic pyrolysis with H-ZSM-5 (1 wt%) in a relatively lower temperature range 430–470 °C. Zhang et al. [11] recovered 38.5–73.0 wt% high-quality oil and 10.9–44.8 wt% gas from the low-density PE catalytic pyrolysis with AC in the temperature range of 430–571 °C. These results were close to the values presented in this study.

Fig. 5.4 also illustrates the absolute relative errors (AREs) between the experimental and the ANN predicted oil and gas yields. It could be seen that the predicted oil yields (AREs within 3.1 %) were more accurate than the predicted gas yields (AREs within 11.8 %). It might be because the gas production was calculated by the difference method, which caused the accumulation of errors in gas yield [14]. Moreover, the R^2 values and average AREs between the experimental and ANN predicted values were 0.9992 and 0.60 %, 0.9830 and 5.01 % in the training and testing tests. The high R^2 values and low average AREs revealed the high accuracies of ANN-predicted oil and gas yields.

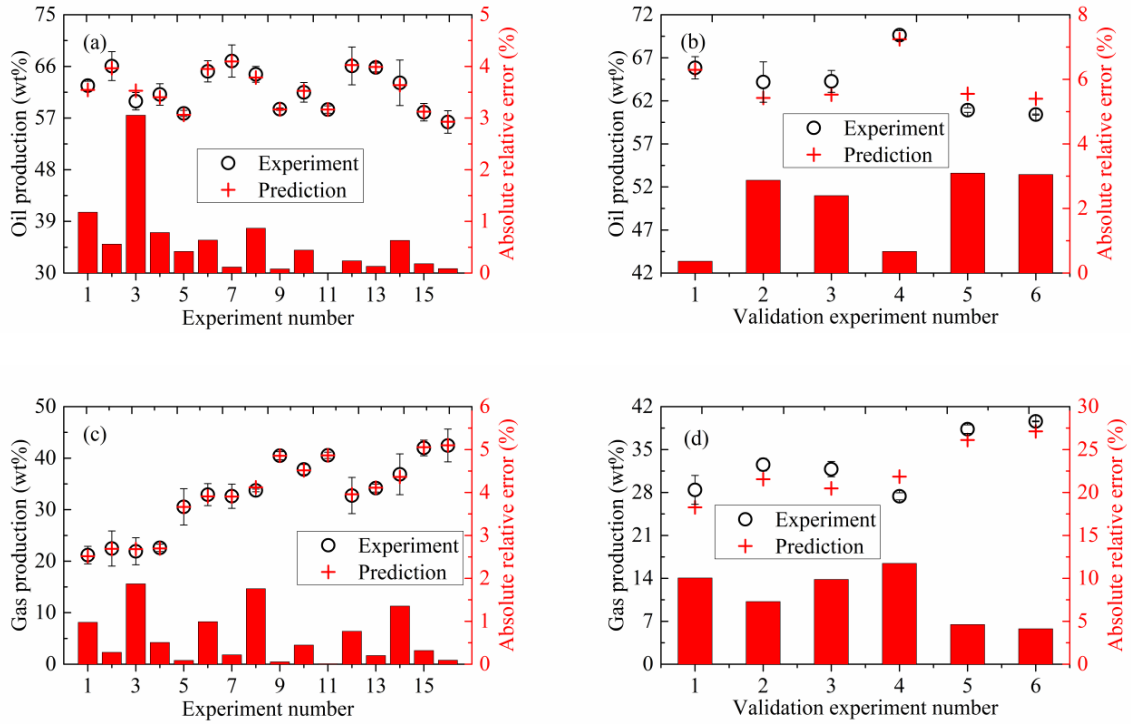

Fig.5.4. Experimental and ANN predicted oil and gas productions in training and testing sets: (a) Oil production in the training set; (b) Oil production in the testing set; (c) Gas production in the training set; (d) Gas production in the testing set.

5.3.2. Interactions of temperature and AC/WPE mass ratio

Fig. 5.5 shows the interactions of temperature and AC/WPE mass ratio on oil and gas productions under different carrier gas flow rates. The variation ranges of oil and gas productions under different carrier gas flow rates are tabulated in Table 5.2. It can be found that under the highest AC/WPE mass ratio of 2, the oil production increased with the increasing temperature in the range of 425–475 °C, regardless of the variation of carrier gas flow rate. Higher temperatures aggravated the random scissions of WPE, resulting in more volatile products [26]. Therefore, gas production was also enhanced when the temperature increased [27]. However, enhancing temperature above 475 °C intensified the secondary cracking of pyrolysis oil, leading to a decrease in oil production and an increase in gas production [28]. It

is noteworthy that the effect of temperature on oil and gas yields was more complicated under 30 mL/min (Figs. 5.5e–f). Under the lowest AC/WPE mass ratio of 1, the oil production decreased from 65.68 wt% at 425 °C, reached the minimum yield of 58.53 wt% at 475 °C, and increased thenceforth. The gas recondensation might cause an increase in oil yield at higher temperatures [29]. In this perspective, the gas yield decreased by 6.15 wt% (from 40.40 wt% to 34.25 wt%) as the temperature increased from 475 °C to 525 °C, which might be ascribed to promoting the Diels-Alder reaction for gas aromatized by AC [30].

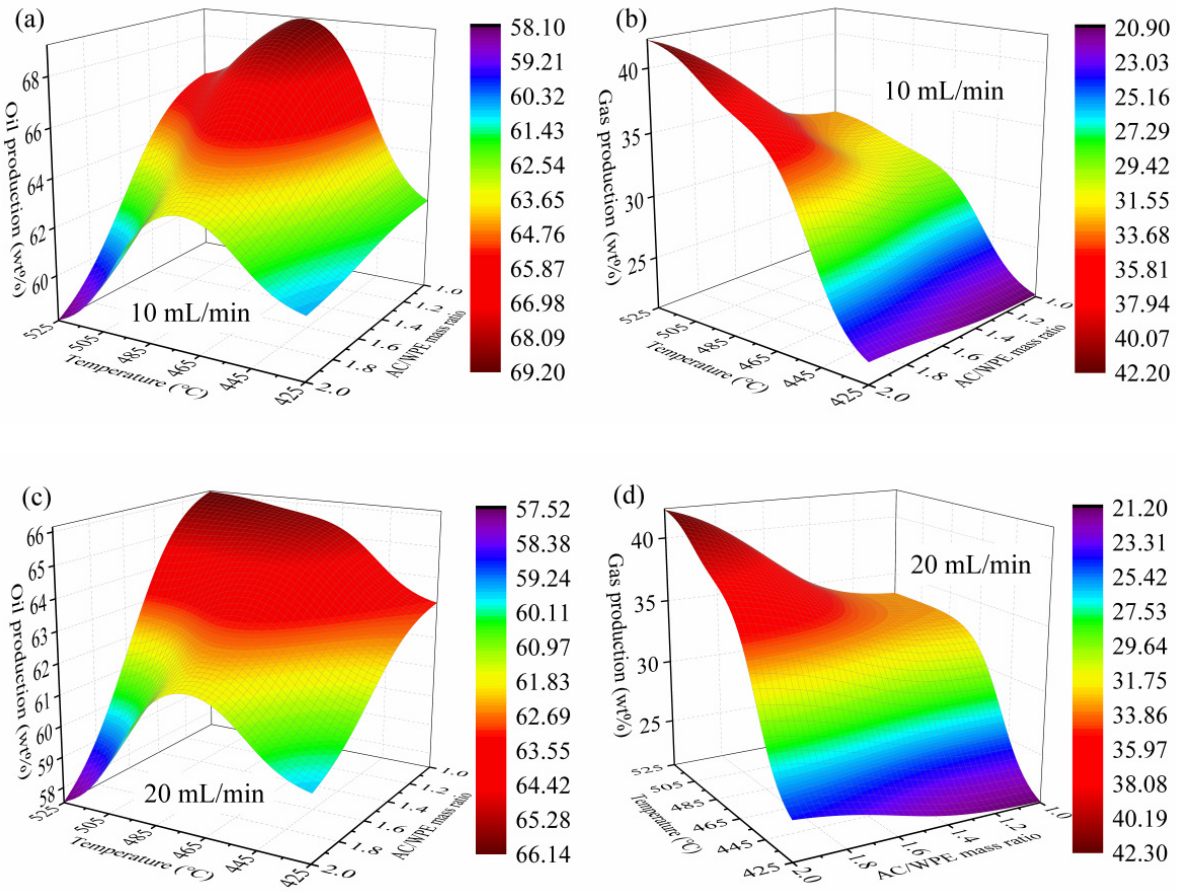

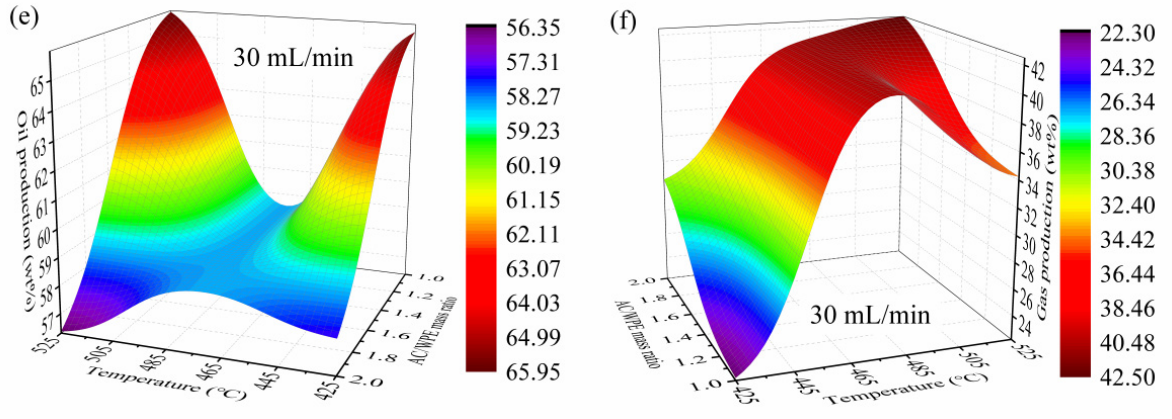

Fig.5.5. Interactions of temperature and AC/WPE mass ratio on oil and gas productions under different carrier gas flow rates: (a) Oil production under 10 mL/min; (b) Gas production under 10 mL/min; (c) Oil production under 20 mL/min; (d) Gas production under 20 mL/min; (e) Oil production under 30 mL/min; (f) Gas production under 30 mL/min.

Table 5.2. WPE catalytic pyrolysis oil and gas productions under different carrier gas flow rates.

Temperature: 425–525 °C; AC/WPE mass ratio: 1.0–2.0			
Yield	Under 10 mL/min	Under 20 mL/min	Under 30 mL/min
Oil	58.12–69.16 wt%	57.53–66.13 wt%	56.36–65.90 wt%
Gas	20.97–42.11 wt%	21.29–42.20 wt%	22.39–42.50 wt%

5.3.3. Interactions of AC/WPE mass ratio and carrier gas flow rate

Fig. 5.6 illustrates the interactions of AC/WPE mass ratio and carrier gas flow rate on oil and gas productions under different temperatures. Table 5.3 exhibits the variation ranges of oil and gas productions under different temperatures. It can be concluded that a higher AC/WPE mass ratio would reduce oil production and enhance gas production, regardless of the variations of carrier gas flow rate and temperature. More catalytic sites exacerbated WPE backbone cracking and oil secondary cracking, thereby led to a decrease in oil yield and an increase in

gas yield [11][31]. The AC/WPE mass ratio faintly impacted the oil production under 10mL/min and 425 °C (Fig. 5.6a). The oil yield merely decreased by 1.27 wt% as the AC/WPE mass ratio increased. It may be ascribed to that partial polyene radicals also formed light oils via rearrangement, cyclization, and aromatization in the catalytic sites [29][32]. However, as carrier gas flow rate increased to 30 mL/min (Fig. 5.6b), oil secondary cracking was more intense than gas recondensation reaction [14], resulted in a dramatic reduction (of 8.11 wt%) of oil yield as the AC/WPE mass ratio increased.

The AC/WPE mass ratio had an inconspicuous impact on oil and gas yields under 30 mL/min and 475 °C (Figs. 5.6c–d). Fan et al. [10] also found that the oil yield almost unchanged when the MgO/LDPE mass ratio enhanced from 1/10 to 1/3. They attributed it to the fact that excess catalyst would not further promote the secondary cracking reaction. On the other hand, higher carrier gas flow rates would lead to heavier oil production [14]. It might block the AC's pores to decrease the catalyst activity, which led to the practically constant oil and gas yields as the AC/WPE mass ratio increased [11]. However, increasing the AC/WPE mass ratio led to a decrease of 5.70 wt% in oil yield and an increase of 6.47 wt% in gas yield under 10 mL/min and 475 °C. Moreover, the oil yield decreased by approximately 8 wt%, and the gas yield enhanced by approximately 8wt% when the AC/WPE mass ratio increased from 1 to 2 under 525 °C, regardless of carrier gas flow rate's variation. It indicated that higher AC/WPE mass ratios could promote the oil secondary cracking for the oil consumption and the gas formation by providing more active sites [33].

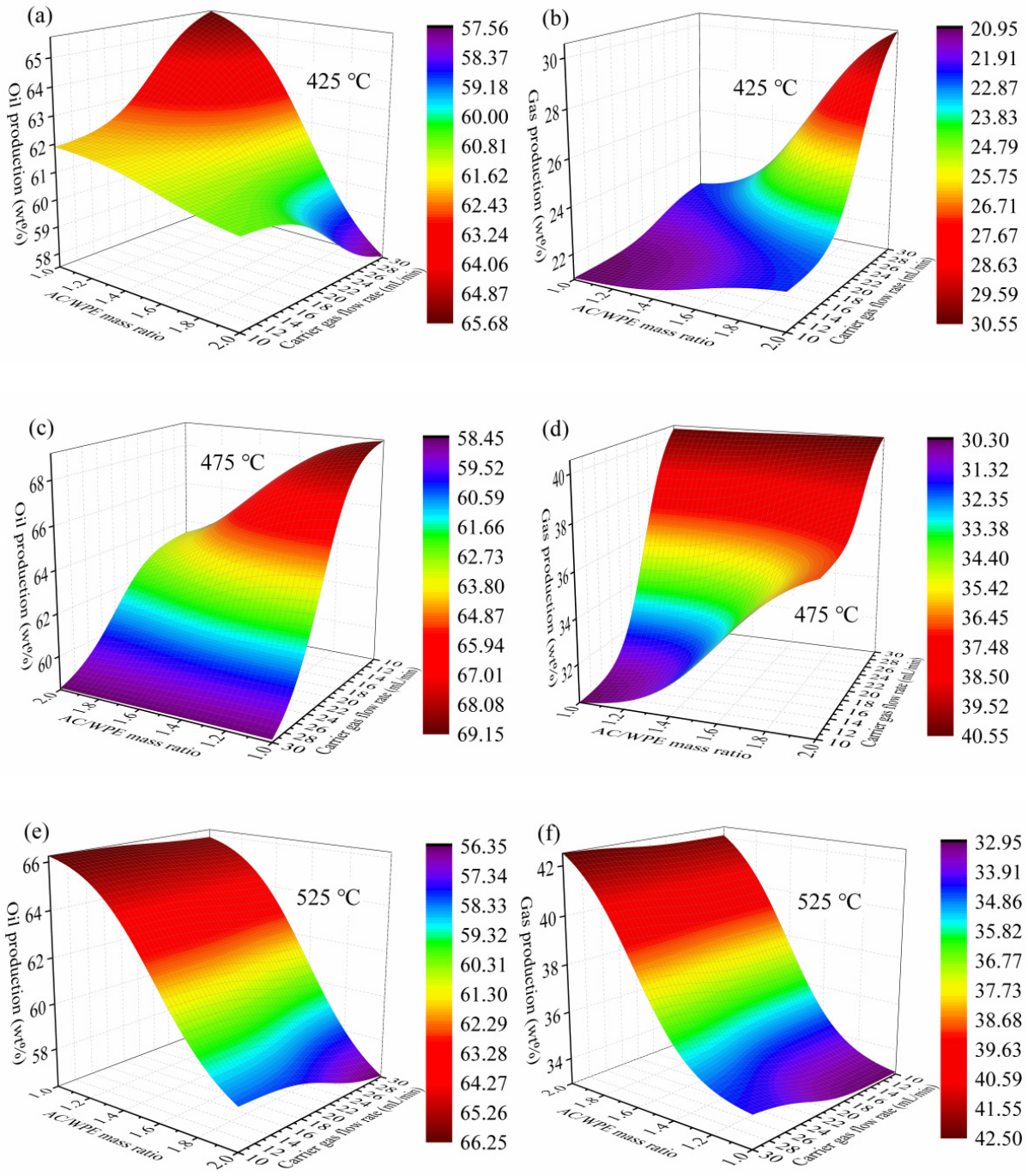

Fig.5.6. Interactions of AC/WPE mass ratio and carrier gas flow rate on oil and gas productions under different temperatures: (a) Oil production under 425 °C; (b) Gas production under 425 °C; (c) Oil production under 475 °C; (d) Gas production under 475 °C; (e) Oil production under 525 °C; (f) Gas production under 525 °C.

Table 5.3. WPE catalytic pyrolysis oil and gas productions under different temperatures.

Carrier gas flow rate: 10–30 mL/min; AC/WPE mass ratio: 1.0–2.0			
Yield	Under 425 °C	Under 475 °C	Under 525 °C
Oil	57.57–65.68 wt%	58.48–69.10 wt%	56.36–66.24 wt%
Gas	20.97–30.52 wt%	30.31–40.54 wt%	32.99–42.50 wt%

5.3.4. Interactions of carrier gas flow rate and temperature

Fig. 5.7 shows the interactions of carrier gas flow rate and temperature on oil and gas productions under different AC/WPE mass ratios. Table 5.4 tabulates the variation ranges of oil and gas productions under different AC/WPE mass ratios. As shown in Figs. 5.7a (AC/WPE mass ratio = 1), 5.7c (AC/WPE mass ratio = 1.5), and 5.7e (AC/WPE mass ratio = 2), enhancing the flow rate of carrier gas led to an increase of 3.78 wt%, an increase of 0.11 wt%, and a reduction of 3.06 wt% in oil yields under the lowest temperature of 425 °C, respectively. More significant carrier gas flow rates could inhibit the oil secondary cracking, thereby increased the oil yield [18]. On the other hand, increasing the flow rate of carrier gas would purge the produced volatiles out of the reactor faster, thereby suppressing the formation of light oils from the partial polyene radicals via rearrangement, cyclization, and aromatization [11][32]. As the flow rate of carrier gas increased, the oil yield would enhance when the gas recondensation reaction was more violent than the oil secondary cracking, while it would reduce as the oil secondary cracking dominated. It can be seen that the secondary cracking of oil was dominant in the middle-temperature range of 450–500 °C. Therefore, enhancing the flow rate of carrier gas led to a decrease in oil yield and an increase in gas yield under all AC/WPE mass ratios. However, the flow rate of carrier gas became an inconspicuous parameter on both oil and gas

yields when the temperature was higher than 500 °C. It might be ascribed that higher temperature would increase the heavy fraction in oil [14] and decrease the alkenes in gas [34]. Both the secondary cracking of oil and the recondensation of gas were at low reactivity, and thereby the oil and gas yields did not change with the flow rate of carrier gas under higher temperatures.

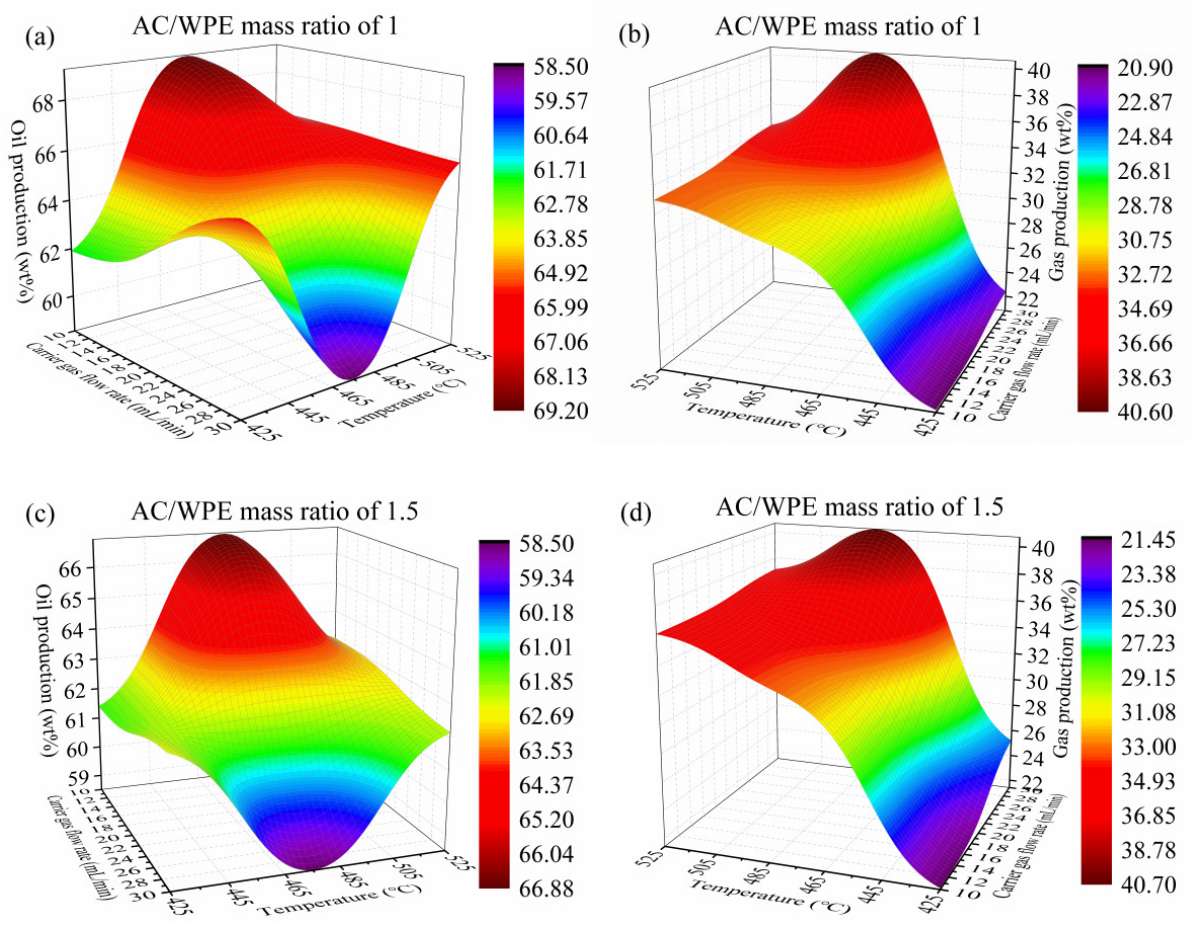

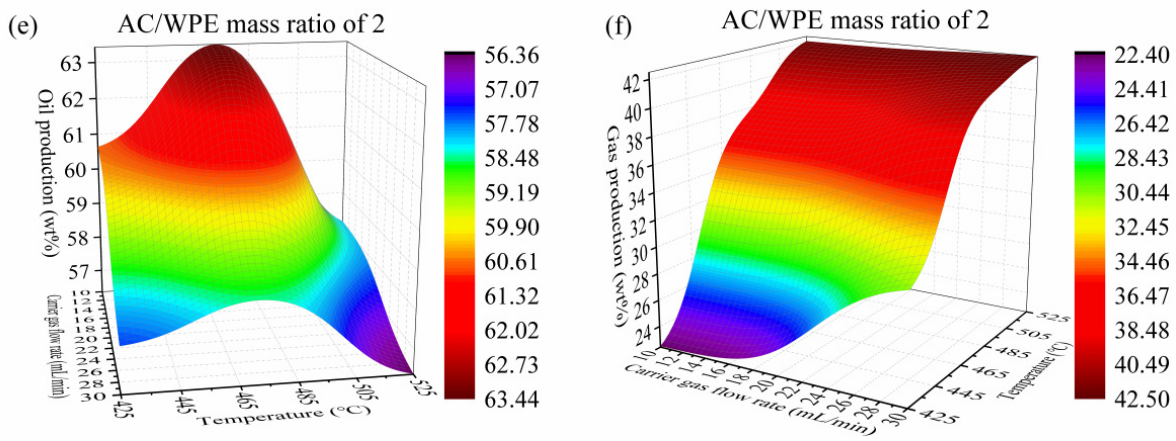

Fig.5.7. Interactions of carrier gas flow rate and temperature on oil and gas productions under different AC/WPE mass ratios: (a) Oil production under AC/WPE mass ratio of 1; (b) Gas production under AC/WPE mass ratio of 1; (c) Oil production under AC/WPE mass ratio of 1.5; (d) Gas production under AC/WPE mass ratio of 1.5; (e) Oil production under AC/WPE mass ratio of 2; (f) Gas production under AC/WPE mass ratio of 2.

Table 5.4. WPE catalytic pyrolysis oil and gas productions under different AC/WPE mass ratios.

Temperature: 425–525 °C; Carrier gas flow rate: 10–30 mL/min			
Yield	Under AC/WPE mass ratio of 1	Under AC/WPE mass ratio of 1.5	Under AC/WPE mass ratio of 2
Oil	58.53–69.16 wt%	58.51–66.86 wt%	56.36–63.42 wt%
Gas	20.97–40.58 wt%	21.49–40.69 wt%	22.48–42.50 wt%

5.3.5. ANN-GA optimization

Fig. 5.8 shows the ANN-GA optimization process and optimal conditions for oil production through the ex-situ catalytic pyrolysis of WPE with AC. As shown in Fig. 5.8a, the highest oil production was determined at the 200th iteration. Fig. 5.8b illustrates that the optimal oil production calculated by ANN-GA was 69.16 wt% under 479 °C, the AC/WPE mass ratio of 1, and 10 mL/min. It indicated that the moderate temperature (≤ 500 °C) [30][35], the low

AC/WPE mass ratio [36][37], and the low flow rate of carrier gas [38][39] were beneficial to oil production. The experimental oil yield was 69.63 wt% under the optimal parameters. The absolute relative error was 0.67 % between the experimental and the ANN-GA determined oil yields, which exhibited the high accuracy of ANN-GA. Moreover, the optimal temperature for WPE thermal pyrolysis was 488 °C [14], a value higher than the optimal temperature for WPE-AC catalytic pyrolysis. Therefore, it can be concluded that the presence of AC could decrease the optimal pyrolysis temperature of WPE.

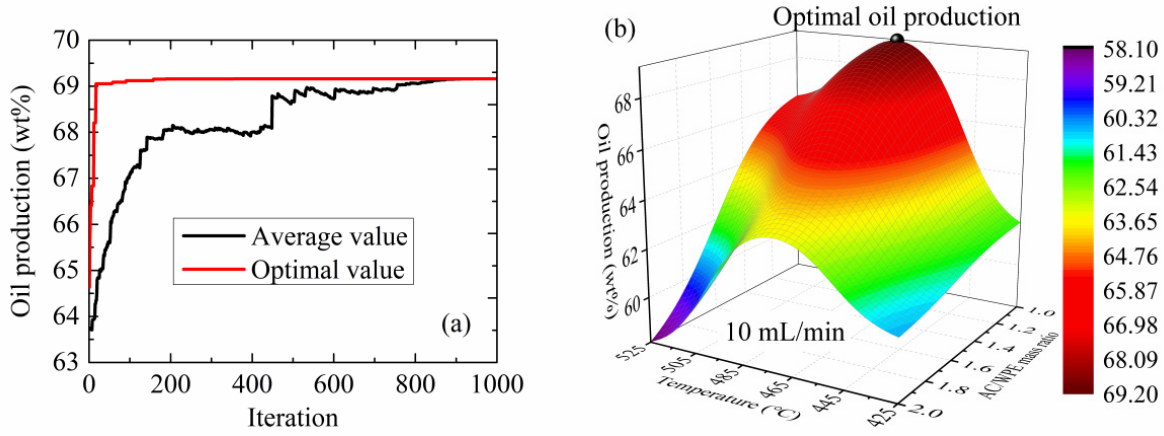

Fig.5.8. Optimal conditions optimized by ANN-GA for maximum oil production: (a) Optimization process; (b) Optimal conditions for oil production.

5.3.6. FTIR analysis

Fig. 5.9 shows the FTIR spectrum of oil samples under different conditions (oil samples of R3, R6, R7, R8, R9, R10, and R14). It can be seen that the oil's FTIR characteristic peaks did not change with the temperature, the AC/WPE mass ratio, and the flow rate of carrier gas. The oils were composed of alkenes, naphthenes, alkanes, and aromatic hydrocarbons, which indicated that WPE-AC catalytic pyrolysis underwent random and Beta scissions [25], hydrogen transfers (both inter- and intra-molecular) [40], and molecular cyclization and

aromatization [41].

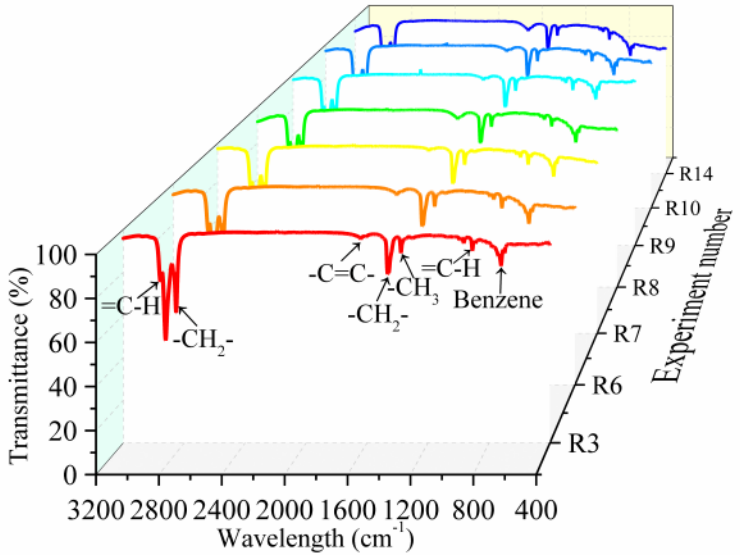

Fig.5.9. FTIR spectrum of oil samples under different conditions.

5.3.7. GC-MS analysis

Fig. 5.10 shows carbon number distribution and fractions of the WPE-AC catalytic and thermal pyrolysis oils. The thermal and catalytic pyrolysis (R14) were performed under the same operating parameters (525 °C, 20 mL/min, 20 min). It can be seen that the WPE thermal pyrolysis oil was composed of C7–C36 hydrocarbons with a large proportion of C21–C24 and C30 (> 6 %) [14], while the WPE-AC catalytic pyrolysis oil was composed of C8–C33 hydrocarbons with a large proportion of C9–C12 and C15 (> 7 %). AC could accelerate the hydrogen-ion abstraction reaction of the WPE hydrocarbon long chain to form more carbonium-ion free radicals, which was conducive to generating shorter chain hydrocarbons with lower carbon numbers [42][43]. Therefore, as shown in Fig. 5.10b, the light (C7–C11) and middle (C12–C20) frictions significantly increased from 4.55 % to 27.40 %, from 31.27 % to 57.24 %, and the heavy friction (> C20) reduced dramatically from 64.18 % to 15.36 % in the presence

of AC.

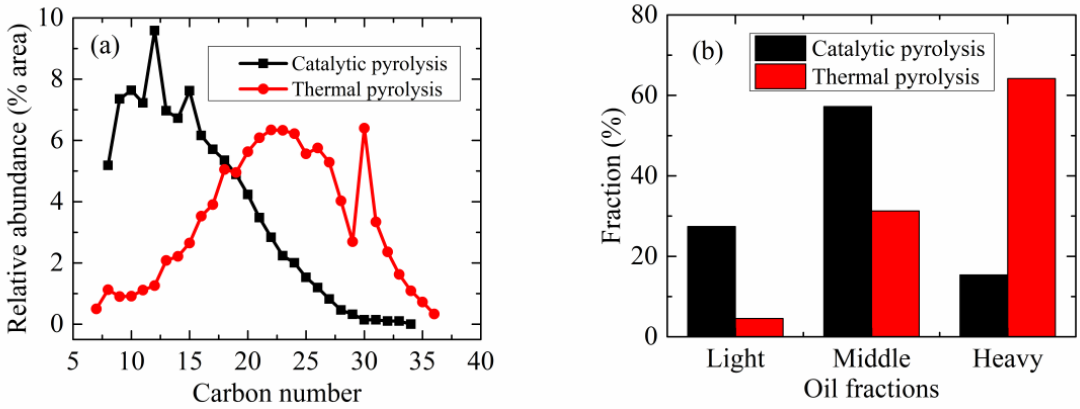

Fig.5.10. Carbon number distribution and fractions of the WPE catalytic and thermal pyrolysis oils: (a) Carbon number distribution; (b) Oil fractions.

(i) Effect of temperature on carbon number distribution and oil fractions

Fig. 5.11 shows the effect of temperature on the carbon number distribution and the fractions of WPE-AC catalytic pyrolysis oil. As depicted in Fig. 5.11a, the carbon number distribution trends were similar under different temperatures. Hydrocarbons with the carbon numbers of C8–C18 were all greater than 4 %, which together accounted for ~75 % of the WPE-AC catalytic pyrolysis oils. Moreover, the hydrocarbons with carbon numbers above C30 only took up ~1 % in oils under all operating temperatures.

As shown in Fig. 5.11b, the light-fraction increased from 28.70 % to 35.96 % as the temperature enhanced from 425 °C to 475 °C, whereas it decreased to 27.40 % as the temperature continuously increased to 525 °C. The middle-fraction firstly decreased from 55.09 % to 46.70 % when the temperature increased from 425 °C to 475 °C, while it increased to 57.24 % under 525 °C. The heavy-fraction oscillated in a narrow range of 15.36–17.34 %, which was not significantly affected by the temperature [44]. Therefore, it could conclude that

improving the temperature from 425 °C was beneficial to convert the WPE-AC catalytic pyrolysis oil's middle-fraction to light-fraction at first, thereby leading to an increase in the light-fraction and a decrease in the middle-fraction [35][41][45]. However, continuously increasing the temperature to 525 °C resulted in the over-cracking of light-fraction, which contributed to the reduction of light-fraction and the enhancement of middle-fraction in the WPE-AC catalytic pyrolysis oil [35][46].

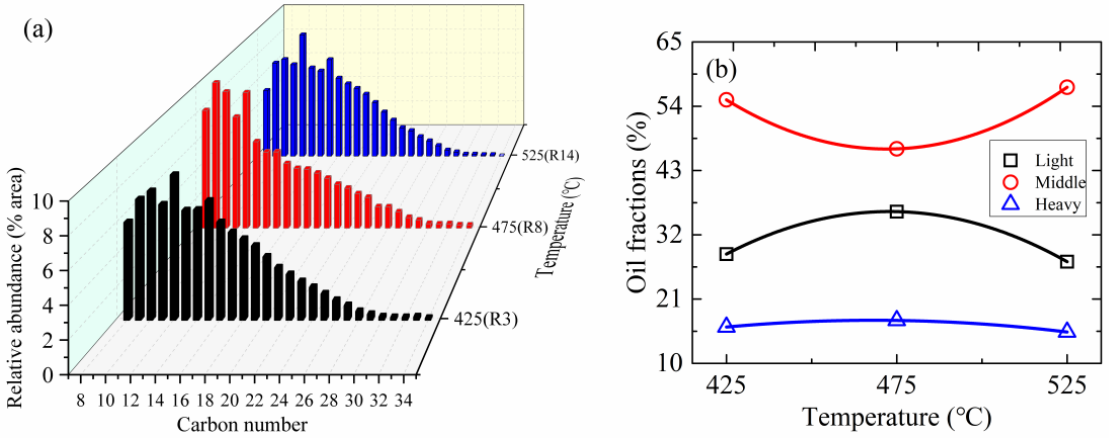

Fig.5.11. Effect of temperature on the carbon number distribution and the fractions of WPE catalytic pyrolysis oil: (a) Carbon number distribution; (b) Oil fractions.

(ii) Effect of AC/WPE mass ratio on carbon number distribution and oil fractions

Fig. 5.12 demonstrates the effect of AC/WPE mass ratio on the carbon number distribution and the fractions of WPE-AC catalytic pyrolysis oil. As illustrated in Fig. 5.12a, the oil under the AC/WPE mass ratio of 1.5 had more hydrocarbons with the carbon numbers of C8–C11 than the oils under the AC/WPE mass ratios of 1 and 2. The oil under the AC/WPE mass ratio of 2 had the most abundant hydrocarbons with the carbon numbers of C12–C15. On the other hand, the highest content of hydrocarbons above C15 was obtained under the lowest AC/WPE mass ratio of 1.

Consequently, as depicted in Fig. 5.12b, the light-fraction enhanced from 23.46 % to 35.96 % as the AC/WPE mass ratio increased from 1 to 1.5, while decreased to 29.18 % as the AC/WPE mass ratio sequentially enhanced to 2. The middle-fraction initially reduced from 55.48 % to 46.70 % when the AC/WPE mass ratio improved from 1 to 1.5, whereas it increased to 53.56 % under the AC/WPE mass ratio of 2. Moreover, the heavy-fraction gradually decreased from 21.06 % to 17.26 % as the AC/WPE mass ratio enhanced. The reductions of middle-fraction and heavy-fraction and the enhancement of light-fraction might be attributed to the sufficient acid sites for the secondary cracking of middle-fraction and heavy-fraction in oil when the AC/WPE mass ratio enhanced from 1 to 1.5 [15]. However, the excessive acid sites might conduce to the over-cracking of oil's light-fraction, which correspondingly led to an increase in gas production [15][45].

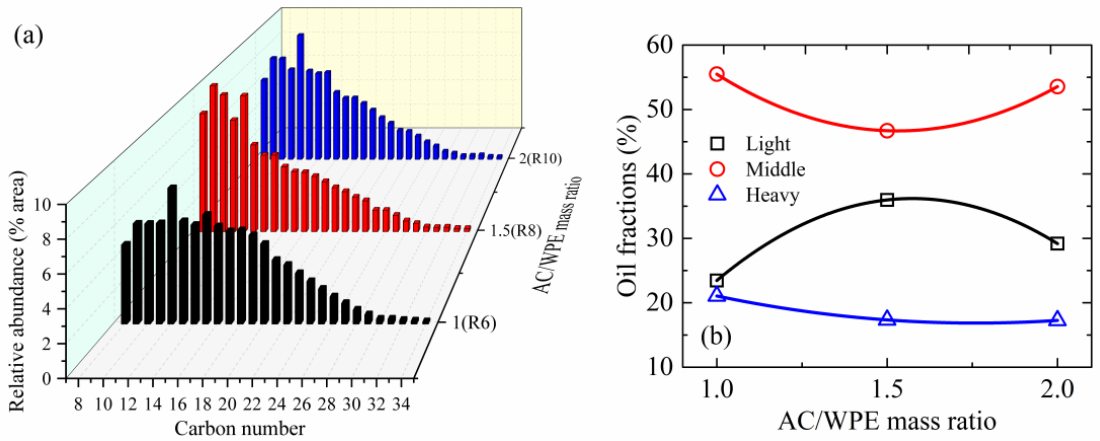

Fig.5.12. Effect of AC/WPE mass ratio on the carbon number distribution and the fractions of WPE catalytic pyrolysis oil: (a) Carbon number distribution; (b) Oil fractions.

(iii) Effect of carrier gas flow rate on carbon number distribution and oil fractions

Fig. 5.13 illustrates the effect of carrier gas flow rate on the carbon number distribution and the fractions of WPE-AC catalytic pyrolysis oil. As shown in Fig. 5.13a, the hydrocarbons with

carbon numbers of C8–C12 in the oil under 20 mL/min were richer than those in the oils under 10 mL/min and 30 mL/min. The oil under the lowest flow rate of carrier gas (10 mL/min) had the most abundant hydrocarbons with the carbon numbers of C14–C24 compared to the oils under 20 mL/min and 30 mL/min. In comparison, the highest content of hydrocarbons above C24 was obtained under the highest flow rate of carrier gas (30 mL/min), which together accounted for around 7 % in the WPE-AC catalytic pyrolysis oil.

Accordingly, as illustrated in Fig. 5.13b, the light-fraction increased from 19.46 % to 35.96 % as the flow rate of carrier gas enhanced from 10 mL/min to 20 mL/min, whereas reduced to 26.61 % as the flow rate of carrier gas subsequently enhanced to 30 mL/min. The middle-fraction firstly decreased from 59.40 % to 46.70 % as the flow rate of carrier gas improved from 10 mL/min to 20 mL/min, while enhanced to 53.19 % under 30 mL/min. The heavy-fraction fluctuated between 17.34 % and 21.13 %, which was not significantly influenced by the flow rate of carrier gas. The enhancement of light-fraction and the reductions of middle-fraction and heavy-fraction might be ascribed to the suppression of the light-fraction's over-cracking as the flow rate of carrier gas enhanced from 10 mL/min to 20 mL/min [47]. However, the excessive flow rate of carrier gas shortened the residence time of volatile gas and suppressed the gas recondensation and the secondary cracking of middle-fraction and heavy-fraction, which further decreased the oil's light-fraction formation [47][48][49].

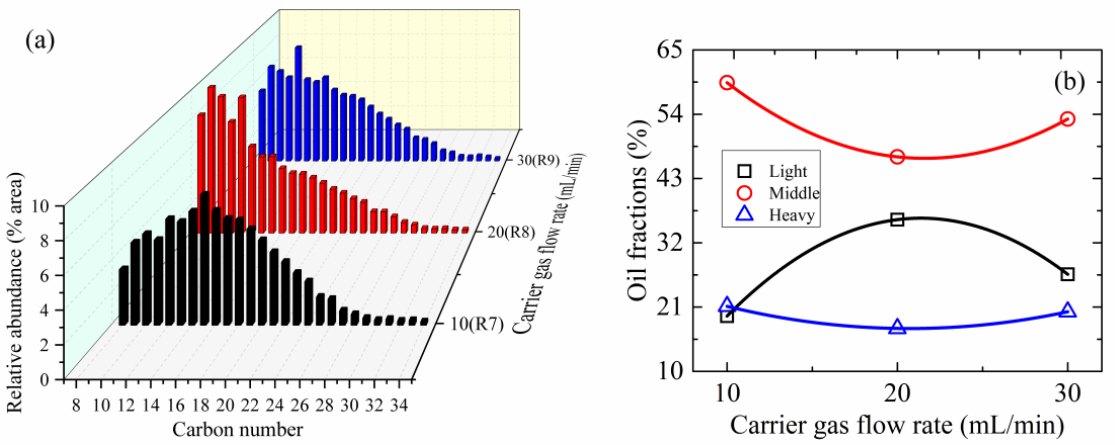

Fig.5.13. Effect of carrier gas flow rate on the carbon number distribution and the fractions of WPE catalytic pyrolysis oil: (a) Carbon number distribution; (b) Oil fractions.

5.4. Conclusions

This chapter investigated the ex-situ catalytic pyrolysis of waste polyethylene (WPE) with activated carbon (AC). The pyrolysis experiments were carried out in a bench-scale semi-batch reactor. The operating parameters of temperature and carrier gas flow rate, and AC/WPE mass ratio were investigated in the ranges of 425–525 °C, 1–2, and 10–30 mL/min, respectively. It was found that the operating parameters and AC/WPE mass ratio had complex interactions on the WPE-AC catalytic pyrolysis oil and gas yields. Therefore, a hybrid method of artificial neural network (ANN) coupled with genetic algorithm (GA) was used to establish the mathematical expressions of oil and gas yields under different conditions and optimize the conditions to obtain the highest oil yield. It should be noted that the correlations obtained in this study have application limitations delimited by the experimental apparatus and process conditions. Nonetheless, ANN-GA has been proved to have good robustness, which can provide guidance for industrial process optimization. The main findings and conclusions are outlined as follows.

- The oil production optimized by ANN-GA was 69.63 wt% under 479 °C, the AC/WPE mass ratio of 1, and 10 mL/min.
- The oils were composed of alkenes, naphthenes, alkanes, and aromatic hydrocarbons in the range of C8–C33.
- Improving the temperature from 425 °C was firstly beneficial to convert the middle-fraction into the light-fraction in the WPE-AC catalytic pyrolysis oil, while continuously increasing the temperature to 525 °C resulted in a decrease in the light-fraction and an increase in the middle-fraction.
- Increasing the AC/WPE mass ratio led to an increase in the light-fraction and a decrease in the middle-fraction when the AC/WPE mass ratio was low (1–1.5); However, the excessive AC/WPE mass ratio (1.5–2) decreased the light-fraction and increased the middle-fraction in the pyrolysis oil.
- A lower carrier gas flow rate led to a higher proportion of light-fraction and lower middle- and heavy-fraction proportions.

Bibliography

[1] Usmani, Z., Kumar, V., Varjani, S., Gupta, P., Rani, R. and Chandra, A., 2020. Municipal solid waste to clean energy system: a contribution toward sustainable development. In Current Developments in Biotechnology and Bioengineering (pp. 217-231). Elsevier.

[2] Shah, A.V., Srivastava, V.K., Mohanty, S.S. and Varjani, S., 2021. Municipal solid waste as a sustainable resource for energy production: State-of-the-art review. Journal of Environmental Chemical Engineering, 9(4), p.105717.

[3] Wen, Y., Zaini, I.N., Wang, S., Mu, W., Jönsson, P.G. and Yang, W., 2021. Synergistic effect of the co-pyrolysis of cardboard and polyethylene: A kin

[4] Sophonrat, N., Sandström, L., Johansson, A.C. and Yang, W., 2017. Co-pyrolysis of mixed plastics and cellulose: an interaction study by Py-GC× GC/MS. Energy & Fuels, 31(10), pp.11078-11090.

[5] Zhang, F., Zeng, M., Yappert, R.D., Sun, J., Lee, Y.H., LaPointe, A.M., Peters, B., Abu-Omar, M.M. and Scott, S.L., 2020. Polyethylene upcycling to long-chain alkylaromatics by tandem hydrogenolysis/aromatization. Science, 370(6515), pp.437-441.

[6] Weckhuysen. B.M., 2020. Creating value from plastic waste. Science, 370(6515), pp.400-401.

[7] Jeswani, H., Krüger, C., Russ, M., Horlacher, M., Antony, F., Hann, S. and Azapagic, A., 2021. Life cycle environmental impacts of chemical recycling via pyrolysis of mixed plastic waste in comparison with mechanical recycling and energy recovery. Science of the Total Environment, 769, p.144483.

[8] Wen, Y., Wang, S., Mu, W., Yang, W. and Jönsson, P.G., 2020. Pyrolysis performance of peat moss: A simultaneous in-situ thermal analysis and bench-scale experimental study. Fuel, 277, p.118173.

[9] Wen, Y., Shi, Z., Wang, S., Mu, W., Jönsson, P.G. and Yang, W., 2021. Pyrolysis of raw and anaerobically digested organic fractions of municipal solid waste: Kinetics, thermodynamics, and product characterization. Chemical Engineering Journal, 415, p.129064.

[10] Fan, L., Zhang, Y., Liu, S., Zhou, N., Chen, P., Liu, Y., Wang, Y., Peng, P., Cheng, Y., Addy, M. and Lei, H., 2017. Ex-situ catalytic upgrading of vapors from microwave-assisted pyrolysis of low-density polyethylene with MgO. Energy Conversion and Management, 149, pp.432-441.

[11] Zhang, Y., Duan, D., Lei, H., Villota, E. and Ruan, R., 2019. Jet fuel production from waste plastics via catalytic pyrolysis with activated carbons. Applied Energy, 251, p.113337.

[12] Quesada, L., Calero, M., Martín-Lara, M.A., Pérez, A. and Blázquez, G., 2019. Characterization of fuel produced by pyrolysis of plastic film obtained of municipal solid waste. Energy, 186, p.115874.

[13] Akgün, H., Yapıcı, E., Günkaya, Z., Özkan, A. and Banar, M., 2021. Utilization of liquid product through pyrolysis of LDPE and C/LDPE as commercial wax. Environmental Science and Pollution Research, 28(33), pp.45971-45984.

[14] Pan, R., Martins, M.F. and Debenest, G., 2021. Pyrolysis of waste polyethylene in a semi-batch reactor to produce liquid fuel: optimization of operating conditions. Energy

Conversion and Management, 237, p.114114.

[15] Duan, D., Feng, Z., Dong, X., Chen, X., Zhang, Y., Wan, K., Wang, Y., Wang, Q., Xiao, G., Liu, H. and Ruan, R., 2021. Improving bio-oil quality from low-density polyethylene pyrolysis: Effects of varying activation and pyrolysis parameters. Energy, 232, p.121090.

[16] Huo, E., Lei, H., Liu, C., Zhang, Y., Xin, L., Zhao, Y., Qian, M., Zhang, Q., Lin, X., Wang, C. and Mateo, W., 2020. Jet fuel and hydrogen produced from waste plastics catalytic pyrolysis with activated carbon and MgO. Science of The Total Environment, 727, p.138411.

[17] Zhang, D., Lin, X., Zhang, Q., Ren, X., Yu, W. and Cai, H., 2020. Catalytic pyrolysis of wood-plastic composite waste over activated carbon catalyst for aromatics production: Effect of preparation process of activated carbon. Energy, 212, p.118983.

[18] Jalalifar, S., Abbassi, R., Garaniya, V., Salehi, F., Papari, S., Hawboldt, K. and Strezov, V., 2020. CFD analysis of fast pyrolysis process in a pilot-scale auger reactor. Fuel, 273, p.117782.

[19] Singh, V.K. and Kumar, E.A., 2017. Measurement of CO2 adsorption kinetics on activated carbons suitable for gas storage systems. Greenhouse Gases: Science and Technology, 7(1), pp.182-201.

[20] Pan, R., Duque, J.V.F. and Debenest, G., 2022. Waste Plastic Thermal Pyrolysis Analysis by a Neural Fuzzy Model Coupled with a Genetic Algorithm. Waste and Biomass Valorization, 13(1), pp.135-148.

[21] Pan, R., Duque, J.V.F., Martins, M.F. and Debenest, G., 2020. Application of a neural fuzzy

model combined with simulated annealing algorithm to predict optimal conditions for polyethylene waste non-isothermal pyrolysis. Heliyon, 6(11), p.e05598.

[22] Pan, R., Duque, J.V.F. and Debenest, G., 2021. Investigating waste plastic pyrolysis kinetic parameters by genetic algorithm coupled with thermogravimetric analysis. Waste and Biomass Valorization, 12(5), pp.2623-2637.

[23] Hasanzadeh, R., Mojaver, M., Azdast, T. and Park, C.B., 2021. Polyethylene waste gasification syngas analysis and multi-objective optimization using central composite design for simultaneous minimization of required heat and maximization of exergy efficiency. Energy Conversion and Management, 247, p.114713.

[24] Jie, X., Li, W., Slocombe, D., Gao, Y., Banerjee, I., Gonzalez-Cortes, S., Yao, B., AlMegren, H., Alshihri, S., Dilworth, J. and Thomas, J., 2020. Microwave-initiated catalytic deconstruction of plastic waste into hydrogen and high-value carbons. Nature Catalysis, 3(11), pp.902-912.

[25] Santos, E., Rijo, B., Lemos, F. and Lemos, M.A.N.D.A., 2021. A catalytic reactive distillation approach to high density polyethylene pyrolysis–Part 2–Middle olefin production. Catalysis Today, 379, pp.212-221.

[26] Wang, W., Lu, Y., Xu, K., Wu, K., Zhang, Z. and Duan, J., 2021. Experimental and simulated study on fluidization characteristics of particle shrinkage in a multi-chamber fluidized bed for biomass fast pyrolysis. Fuel Processing Technology, 216, p.106799.

[27] Santos, E., Rijo, B., Lemos, F. and Lemos, M.A.N.D.A., 2019. A catalytic reactive distillation approach to high density polyethylene pyrolysis–Part 1–Light olefin production.

Chemical Engineering Journal, 378, p.122077.

[28] Bagi, E. and Baseri, H., 2021. Pyrolysis of Ligustrum vulgare waste and the effects of various operating parameters on bio-oil upgrading. Biomass Conversion and Biorefinery, pp.1-11.

[29] Fan, L., Liu, L., Xiao, Z., Su, Z., Huang, P., Peng, H., Lv, S., Jiang, H., Ruan, R., Chen, P. and Zhou, W., 2021. Comparative study of continuous-stirred and batch microwave pyrolysis of linear low-density polyethylene in the presence/absence of HZSM-5. Energy, 228, p.120612.

[30] Sun, K., Wang, W., Themelis, N.J., Bourtsalas, A.T. and Huang, Q., 2021. Catalytic co-pyrolysis of polycarbonate and polyethylene/polypropylene mixtures: Promotion of oil deoxygenation and aromatic hydrocarbon formation. Fuel, 285, p.119143.

[31] Zhang, Y., Fu, P., Yi, W., Li, Z., Li, Z., Wang, S. and Li, Y., 2021. Species transport and reaction characteristics between gas and solid phases for ex-situ catalytic pyrolysis of biomass. Energy, 225, p.120212.

[32] Xu, F., Wang, B., Yang, D., Hao, J., Qiao, Y. and Tian, Y., 2018. Thermal degradation of typical plastics under high heating rate conditions by TG-FTIR: Pyrolysis behaviors and kinetic analysis. Energy Conversion and Management, 171, pp.1106-1115.

[33] Wang, C., Lei, H., Kong, X., Zou, R., Qian, M., Zhao, Y. and Mateo, W., 2021. Catalytic upcycling of waste plastics over nanocellulose derived biochar catalyst for the coupling harvest of hydrogen and liquid fuels. Science of The Total Environment, 779, p.146463.

[34] Das, P. and Tiwari, P., 2018. Valorization of packaging plastic waste by slow pyrolysis.

Resources, Conservation and Recycling, 128, pp.69-77.

[35] Costa, C.S., Muñoz, M., Ribeiro, M.R. and Silva, J.M., 2021. H-USY and H-ZSM-5 zeolites as catalysts for HDPE conversion under a hydrogen reductive atmosphere. Sustainable Energy & Fuels, 5(4), pp.1134-1147.

[36] Ukarde, T.M. and Pawar, H.S., 2021. A Cu doped TiO2 catalyst mediated Catalytic Thermo Liquefaction (CTL) of polyolefinic plastic waste into hydrocarbon oil. Fuel, 285, p.119155.

[37] Fan, Y., Liu, C., Kong, X., Han, Y., Lei, M. and Xiao, R., 2021. A new perspective on polyethylene-promoted lignin pyrolysis with mass transfer and radical explanation. Green Energy & Environment.

[38] Muhammad, I. and Manos, G., 2021. Simultaneous pretreatment and catalytic conversion of polyolefins into hydrocarbon fuels over acidic zeolite catalysts. Process Safety and Environmental Protection, 146, pp.702-717.

[39] Das, S. and Goud, V.V., 2021. RSM-optimised slow pyrolysis of rice husk for bio-oil production and its upgradation. Energy, 225, p.120161.

[40] Qian, M., Lei, H., Villota, E., Zhao, Y., Huo, E., Wang, C., Mateo, W. and Zou, R., 2021. Enhanced production of renewable aromatic hydrocarbons for jet-fuel from softwood biomass and plastic waste using hierarchical ZSM-5 modified with lignin-assisted re-assembly. Energy Conversion and Management, 236, p.114020.

[41] Wang, C., Lei, H., Zou, R., Qian, M., Mateo, W., Lin, X. and Ruan, R., 2021. Biochar-driven simplification of the compositions of cellulose-pyrolysis-derived biocrude oil coupled with the promotion of hydrogen generation. Bioresource Technology, 334,

p.125251.

[42] Kassargy, C., Awad, S., Burnens, G., Kahine, K. and Tazerout, M., 2017. Experimental study of catalytic pyrolysis of polyethylene and polypropylene over USY zeolite and separation to gasoline and diesel-like fuels. Journal of Analytical and Applied Pyrolysis, 127, pp.31-37.

[43] Wong, S.L., Ngadi, N., Abdullah, T.A.T. and Inuwa, I.M., 2017. Conversion of low density polyethylene (LDPE) over ZSM-5 zeolite to liquid fuel. Fuel, 192, pp.71-82.

[44] Das, P. and Tiwari, P., 2018. The effect of slow pyrolysis on the conversion of packaging waste plastics (PE and PP) into fuel. Waste Management, 79, pp.615-624.

[45] Wang, C., Lei, H., Qian, M., Huo, E., Zhao, Y., Zhang, Q., Mateo, W., Lin, X., Kong, X., Zou, R. and Ruan, R., 2020. Application of highly stable biochar catalysts for efficient pyrolysis of plastics: a readily accessible potential solution to a global waste crisis. Sustainable Energy & Fuels, 4(9), pp.4614-4624.

[46] Saeaung, K., Phusunti, N., Phetwarotai, W., Assabumrungrat, S. and Cheirsilp, B., 2021. Catalytic pyrolysis of petroleum-based and biodegradable plastic waste to obtain high-value chemicals. Waste Management, 127, pp.101-111.

[47] Varma, A.K. and Mondal, P., 2017. Pyrolysis of sugarcane bagasse in semi batch reactor: Effects of process parameters on product yields and characterization of products. Industrial Crops and Products, 95, pp.704-717.

[48] Russell, J.M., Gracida-Alvarez, U.R., Winjobi, O. and Shonnard, D.R., 2020. Update to "Effect of Temperature and Vapor Residence Time on the Micropyrolysis Products of Waste

High Density Polyethylene". Industrial & Engineering Chemistry Research, 59(22), pp.10716-10719.

[49] Xu, F., Ming, X., Jia, R., Zhao, M., Wang, B., Qiao, Y. and Tian, Y., 2020. Effects of operating parameters on products yield and volatiles composition during fast pyrolysis of food waste in the presence of hydrogen. Fuel Processing Technology, 210, p.106558.

Chapter 6

Numerical study of plastic waste pyrolysis driven by char smoldering

Summary

Pyrolysis is a promising method for the valorization of plastic waste (PW). However, traditional pyrolysis processes have high energy consumption. On the other hand, smoldering has been proven as an effective and economic process to treat waste, becoming an attractive application for developing countries. Therefore, this chapter proposes a novel reactor design for PW pyrolysis driven by char smoldering. A proof-of-concept was the development of a multidimensional numerical model to verify the feasibility of the proposed reactor and evaluate its performance. It was found that PW was pyrolyzed stably driven by a self-sustaining char smoldering front. The model revealed that the air inlet velocity and char concentration determined the duration of the PW pyrolysis process and tar and gas yields by controlling the peak temperature and the front velocity. The carrier gas inlet velocity controlled the residence time of tar in the PW pyrolysis chamber and further affected the tar and gas yields.

Candidate contribution: Conceptualization, methodology, formal analysis, resources, data curation, writing - original draft, visualization.

6.1. Introduction

A significant number of plastics are produced annually due to their wide range of uses in packaging, building, automotive, etc. The production of plastics increased from 359 million tons in 2018 to 368 million tons in 2019 globally [1]. Specifically, polyethylene (PE) is the most in demand plastic type, accounting for 29.8 % of total plastic production in 2019. Mass-produced plastics also generate a large amount of plastic waste (PW). The recycling amount of PW in Europe has increased from 4.7 million tons to 9.4 million tons, doubled from 2006 to 2018. While the landfill rate of PW in 2018 was still as high as 25 % [1]. The amount of European PW processed through energy recovery or incineration was 12.4 million tons, accounting for 42.8 % of total PW. Direct landfilling of PW will pollute the environment and even endanger human health [2]. Energy recovery or incineration also generates hazardous gases [2]. Therefore, it is urgent to adopt a proper method to handle the massive PW.

Pyrolysis is a promising method to convert PW (PE) into valuable liquid (tar) and fuel gas [3]. The long-chain PW can be decomposed into short-chain hydrocarbons in the temperature range of 400–800 °C [4]. The pyrolysis can be conducted in different reactors, such as fixed bed (e.g., batch, semi-batch, kiln, drop-type, etc.) and fluidized bed [5]. The lab-scale reactors are heated indirectly by electric heating coils to reach and maintain the target temperature [6]. This makes pyrolysis a high energy-consuming process [7]. On the other hand, the high thermal resistance of plastic causes uneven temperature distribution in the reactor and makes it difficult to reach the target temperature [8-9].

In order to provide a more economical heat source than electricity for PW pyrolysis, Duque

et al. [7] proposed a pyrolysis reactor driven by self-sustaining smoldering. This reactor has two independent chambers: the outside is a char smoldering chamber, and the inside is a semi-batch reactor. Smoldering is a flameless combustion that sustains itself through an exothermic oxidation reaction [10-11]. They confirmed that char smoldering could provide enough energy for self-sustaining propagation and pyrolysis. However, the main drawback of this reactor is that the smoldering propagation speed and temperature are unstable [12]. Because it is a reactive bed with no inert conductive material, bed shrinkage results in a semi-batch reactor temperature unevenly distributed and much lower than the wall temperature.

Mixing char with sand has been proved to be an economical and convenient way to solve the instability of smoldering propagation created during the smoldering of char alone [7,11]. Zanoni et al. [13-14] conducted studies on the smoldering of liquid (bitumen) and solid (char) fuels embedded in the sand. Smoldering propagated at a steady front velocity and maintained an almost constant peak temperature due to the high heat capacity of sand. On the other hand, adding high thermal conductivity porous matrix can increase the efficiency of heat and mass transfer in the fixed bed reactor [15].

The char concentration is considered to be one of the most important parameters in the self-sustaining smoldering process [7,12]. The increase in char concentration has a dominant influence on the local net energy rate and thus leads to an increase in both peak temperature and front velocity [16]. The air velocity dominates the local energy leaving the smoldering front by controlling convection, and further affects the front velocity. Moreover, the local char oxidation rate is affected by the air velocity, which causes the peak temperature fluctuation due

to the variation of the local net energy rate [16]. The carrier gas velocity is a vital operating parameter in the PW pyrolysis process [17]. The carrier gas velocity can determine the residence time of pyrolysis products inside the pyrolysis reactor, thereby affecting the product composition [18]. A higher carrier gas velocity shortens the residence time of tar in the reaction zone and reduces tar cracking into non-condensable gas, leading to an increase in tar yield and a decrease in gas yield [19].

In this study, a 1D smoldering model based on the previous work [20] was coupled with a 2D pyrolysis model based on the previous research [21-22] to simulate the PW pyrolysis driven by char smoldering. The 1D smoldering model and the 2D pyrolysis model were validated and verified based on previous experiments and numerical modeling [11,19]. Then, the validated multidimensional model was used to simulate the PW pyrolysis front and estimate tar and gas yields under different smoldering (air inlet velocity and char concentration) and pyrolysis (carrier gas inlet velocity) operating conditions. The pyrolysis tar and gas are value-added fuels, which can be used as alternatives to fossil fuels. The model developed in the present study intends to provide a general tool to evaluate the performance of the novel pyrolysis reactor driven by smoldering, which can remediate contaminated sands and pyrolyze wastes.

6.2. Methodology

The physical model for the numerical work is described in Section 6.2.1. The reaction kinetics of char smoldering and PW pyrolysis are discussed in Section 6.2.2. Section 6.2.3 describes the governing equations and boundary conditions of the numerical model.

6.2.1. Physical model

Fig. 6.1 shows the numerical domain representing a pyrolysis reactor for plastic waste driven by char smoldering, i.e., the heat generated by smoldering will be used to pyrolyze the plastic waste. The model developed in this study is axisymmetric. The system is separated into two domains: i) char smoldering (mixture of sand and char); and ii) plastic waste pyrolysis (mixture of plastic waste and porous matrix). The smoldering domain contains a heating element simulated by a constant heat flux at the top boundary (z = 0.73 m), which provides the initial energy for char ignition. The air supply was simulated by a constant air flux at the top boundary (z = 0.73 m). Therefore, smoldering propagation is forward-downwards. The pyrolysis domain contains a nitrogen supply at the bottom boundary (z = 0 m), carrying the pyrolysis products upwards.

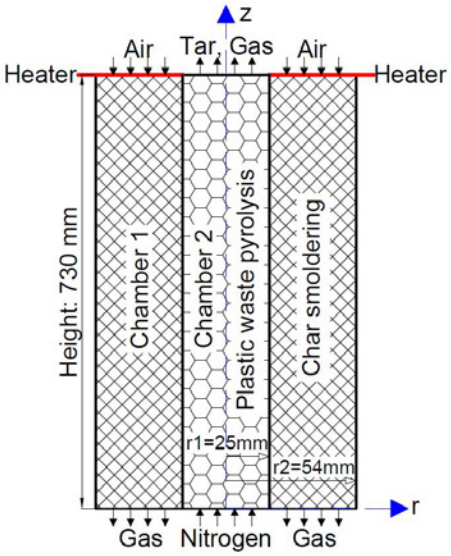

Fig.6.1. Illustration of the numerical domain for PW pyrolysis driven by char smoldering: Char smoldering in Chamber 1 and PW pyrolysis in Chamber 2.

Table 6.1 shows the numerical model input parameters.

Table 6.1. Numerical model input parameters.

Case	Air inlet velocity (m/s)	Initial char concentration (%)	Carrier gas inlet velocity (m/s)

Base case			
1	0.050	2.2	0.10
Air inlet velocity			
2	0.030	2.2	0.10
3	0.035	2.2	0.10
4	0.040	2.2	0.10
5	0.045	2.2	0.10
Char concentration			
6	0.050	2.4	0.10
7	0.050	2.6	0.10
8	0.050	2.8	0.10
9	0.050	3.0	0.10
Carrier gas inlet velocity			
10	0.050	2.2	0.02
11	0.050	2.2	0.04
12	0.050	2.2	0.06
13	0.050	2.2	0.08

6.2.2. Reaction kinetics

Char smoldering was assumed as a one-step oxidation reaction [11,23]:

$$Char + v_{O_2} O_2 \xrightarrow{R_{Char}} gases \tag{6.1}$$

where v_{O_2} represents the reaction coefficient of oxygen. Since the correction of CO_2 and CO in combustion products is not clear, no distinction was made between gases [24]. The char smoldering reaction rate R_{Char} (1/s) follows:

$$R_{Char} = A_{Char} \exp\left(-E_{Char}/(R_g T_s)\right) Y_{Char}^{n_C} Y_{O_2}^{n_O} \tag{6.2}$$

where A_{Char}, E_{Char}, R_g, T_s, Y_{Char}, and Y_{O_2} represent the pre-exponential factor, activation energy, ideal gas constant (8.314 $J \cdot mol^{-1} \cdot K^{-1}$), solid temperature, local char mass fraction(initial value is 1), and oxygen mass fraction, respectively.

The plastic waste (PW) is polyethylene recycled from municipal solid waste [19]. It should

be noted that the melted PW is supposed to be a stationary fluid due to the high viscosity (> 1000 Pa·s) [25] of molten polyethylene. The heat absorbed by the melting process has been taken into account in the pyrolysis enthalpy of PW (ΔH_{PW}). PW pyrolysis adopted a two-step reaction mechanism [15,25-28]:

$$PW \xrightarrow{R_{PW}} v_{Tar}Tar + v_{Gas}Gas + v_{Res}Residue \tag{6.3}$$

$$Tar \xrightarrow{R_{Tar}} Gas \tag{6.4}$$

where v_{Tar}, v_{Gas}, and v_{Res} represent the reaction coefficients of tar, pyrolysis gas, and residue, respectively. The pyrolysis rates for PW (R_{PW}, kg·m^{-3}·s^{-1}) and tar (R_{Tar}, kg·m^{-3}·s^{-1}) follow:

$$R_{PW} = A_{PW}\exp\left(-E_{PW}/(R_g T_{PW})\right)\rho_{PW} \tag{6.5}$$

$$R_{Tar} = A_{Tar}\exp\left(-E_{Tar}/(R_g T_{PW})\right)\rho_{Tar} \tag{6.6}$$

where T_{PW}, ρ_{PW}, and ρ_{Tar} represent the PW temperature, PW mass concentration, tar mass concentration, respectively. Hence, the reaction rates of tar (R_T, kg·m^{-3}·s^{-1}) and gas (R_G, kg·m^{-3}·s^{-1}) are:

$$R_T = v_{Tar}R_{PW} - R_{Tar} \tag{6.7}$$

$$R_G = v_{Gas}R_{PW} + R_{Tar} \tag{6.8}$$

The PW conversion (PW_{conv}), tar yield (Y_{Tar}), and gas yield (Y_{Gas}) are calculated by:

$$PW_{conv} = 1 - m_{PW}/m_{PW,0} \tag{6.9}$$

$$Y_{Tar} = m_{Tar}/m_{PW,0} \tag{6.10}$$

$$Y_{Gas} = m_{Gas}/m_{PW,0} \tag{6.11}$$

where $m_{PW,0}$, m_{PW}, m_{Tar}, and m_{Gas} are the initial PW weight, residual solid weight, tar

weight, and gas wight, respectively.

Table 6.2 shows the kinetic parameters for the char smoldering and PW pyrolysis reaction mechanisms.

Table 6.2. Kinetic parameters of char smoldering and PW pyrolysis.

Par.	Value	Unit	Ref.
A_{Char}	707.9	1/s	[11]
E_{Char}	6.8×10^{4}	J/mol	[11]
ΔH_{Char}	-30.82×10^{6}	J/kg	[11]
A_{PW}	2.92×10^{15}	1/s	[26]
E_{PW}	2.487×10^{5}	J/mol	[26]
ΔH_{PW}	9.75×10^{5}	J/kg	[15]
A_{Tar}	4.25×10^{6}	1/s	[28]
E_{Tar}	1.08×10^{5}	J/mol	[28]
ΔH_{Tar}	-4.2×10^{4}	J/kg	[15]
n_C	1	-	[11]
n_O	1	-	[11]
v_{O2}	1.15	-	[11]
v_{Tar}	0.8350	-	[19]
v_{Gas}	0.1285	-	[19]
v_{Res}	0.0365	-	[19]

6.2.3. Governing equations

(i) Char smoldering

The smoldering model was developed as a one-dimensional (1D) model, while the PW pyrolysis was developed as a two-dimensional (2D) model. It is noteworthy that the smoldering chamber has been developed to a small diameter to minimize 2D effects.

The mass conservation equations for char and air:

$$\frac{\partial}{\partial t}(Y_{Char}) = -R_{Char} \tag{6.12}$$

$$\frac{\partial}{\partial t}(\varepsilon_{p,smo}\rho_g) + \frac{\partial}{\partial z}(\rho_g u_g) = \rho_{Char} R_{Char} \tag{6.13}$$

where ρ_{Char} is the initial char bulk density, the air density ρ_g follows the ideal gas law, the smoldering chamber porosity is $\varepsilon_{p,smo} = \varepsilon_{p,smo,0} - Y_{Char}\rho_{Char}/\rho_{Char,par}$, and the superficial air velocity u_g is calculated by Darcy's Law:

$$u_g = -(\kappa_{p,smo}/\mu_g)\frac{\partial}{\partial z}p_g \tag{6.14}$$

where $\varepsilon_{p,smo,0}$, C_{Char}, $\kappa_{p,smo}$, μ_g, and p_g represent the initial smoldering chamber porosity, char concentration, permeability of smoldering chamber, air viscosity, and pressure, respectively.

The oxygen transport equation is given by:

$$\frac{\partial}{\partial t}(\varepsilon_{p,smo}\rho_g Y_{O_2}) + \frac{\partial}{\partial z}(\rho_g u_g Y_{O_2}) = \frac{\partial}{\partial z}(\varepsilon_{p,smo}\rho_g D_g \frac{\partial}{\partial z}Y_{O_2}) - \rho_{Char} v_{O_2} R_{Char} \tag{6.15}$$

where D_g represents the diffusion coefficient of gas.

The energy conservation equations for solid (T_s) and air (T_g) are given by:

$$\frac{\partial(\rho C_p)_{eff,smo}T_s}{\partial t} = \frac{\partial}{\partial z}\left(k_{eff,smo}\frac{\partial}{\partial z}T_s\right) + \frac{A_{inner}}{V_{smo}}h_{inner}(T_{PW} - T_s) + \frac{A_{outer}}{V_{smo}}h_{outer}(T_\infty - T_s) + h_{sg}(A_{s,sp}/V_{sp})(T_g - T_s) - \rho_{Char}\Delta H_{Char}R_{Char} \tag{6.16}$$

$$\frac{\partial \varepsilon_{p,smo}(\rho_g C_{p,g})T_g}{\partial t} + \frac{\partial \rho_g C_{p,g} u_g T_g}{\partial z} = \frac{\partial}{\partial z}\left(\varepsilon_{p,smo}k_g\frac{\partial}{\partial z}T_g\right) + h_{sg}(A_{s,sp}/V_{sp})(T_s - T_g) \tag{6.17}$$

where ΔH_{Char}, $C_{p,g}$, and k_g are the heat of char smoldering (exothermic), air heat capacity, and thermal conductivity, respectively. The solid effective properties of $(\rho C_p)_{eff,smo}$ and $k_{eff,smo}$ follow:

$$(\rho C_p)_{eff,smo} = (1 - \varepsilon_{p,smo,0})\rho_{Sand,par}C_{p,Sand} + Y_{Char}\rho_{Char}C_{p,Char} \tag{6.18}$$

$$k_{eff,smo} = (1 - \varepsilon_{p,smo,0})(k_{Sand} + k_{rad}) + Y_{Char}(\varepsilon_{p,smo,0} - \varepsilon_{p,smo})k_{Char} \tag{6.19}$$

where $\rho_{Sand,par}$, $C_{p,Sand}$, $C_{p,Char}$, k_{Sand}, and k_{Char} are the sand particle density, sand

particle specific heat capacity, char particle specific heat capacity, sand particle heat conductivity, and char particle thermal conductivity. It should be noted that the irradiative conductivity of char particle has been ignored due to its low content. The irradiative conductivity k_{rad} follows Rosseland approximation [23]:

$$k_{rad} = 16\sigma d_{p,Sand} {T_s}^3/3 \tag{6.20}$$

Local Thermal Non-Equilibrium (LTNE) was used to determine the heat transfer between solid and air. The interfacial heat transfer coefficient h_{sg} [29] and the surface area per unit volume $A_{s,sp}/V_{sp}$ [11] follow:

$$Nu = \frac{h_{sg} d_{p,Sand}}{k_g} = 0.001(Re^{1.97} Pr^{1/3}) \tag{6.21}$$

$$A_{s,sp}/V_{sp} = 6(1 - \varepsilon_{p,smo})/d_{p,Sand} \tag{6.22}$$

where Re, Pr, and $d_{p,Sand}$ are Reynolds number (valid for $0.5 < Re < 31$), Prandtl number, and sand particle diameter (valid for $0.125\ \text{mm} < d_{p,Sand} < 2.000\ \text{mm}$). The correlation of Nusselt number Nu was established by the empirical results [29].

The smoldering model input parameters are presented in Table 6.3. Table 6.4 shows the initial conditions and parameters for the simulation and the constraints on the model's conditions.

Table 6.3. Model inputs and materials' physical parameters of smoldering model.

Par.	Value	Description	Ref.
H	0.73	Height of smoldering chamber, m	[11]
r_{smo}	0.054	Outer radius of smoldering chamber, m	[11]
A_{inner}	$2\pi r_{py} H$	Inner surface area of smoldering chamber, m^2	Calibrated
A_{outer}	$2\pi r_{smo} H$	Outer surface area of smoldering chamber, m^2	Calibrated

V_{smo}	$\pi(r_{smo}^2 - r_{py}^2)H$	Volume of smoldering chamber, m^3	Calibrated
$d_{p,Sand}$	0.88	Sand particle diameter, mm	[11]
D_g	4.53×10^{-5}	Diffusion coefficient of gas, m^2/s	[30]
μ_g	$-9\times10^{-12}(T_g^2)+4\times10^{-8}(T_g)+6\times10^{-6}$	Air viscosity, Pa·s	[29]
k_{Char}	0.25	Thermal conductivity of char, W/(m·K)	[31]
k_{Sand}	$0.000541(T_s)+0.1044$	Thermal conductivity of sand, W/(m·K)	[29]
k_g	$-1\times10^{-8}(T_g^2)+8\times10^{-5}(T_g)+4.3\times10^{-3}$	Thermal conductivity of gas, W/(m·K)	[29]
m_{Char}	0.207	Initial char mass, kg	[11]
m_{Sand}	10.34	Sand mass, kg	[11]
C_{Char}	$m_{Char,0}/m_{Sand}$=2.0	Initial char concentration, %	Calibrated
ρ_{Char}	$m_{Char,0}/V_{smo}$=31.80	Char bulk density, kg/m^3	[11]
$\rho_{Char,par}$	550	Char particle density, kg/m^3	This study
ρ_{Sand}	1620	Sand bulk density, kg/m^3	[29]
$\rho_{Sand,par}$	2650	Sand particle density, kg/m^3	[29]
$C_{p,Char}$	1100	Heat capacity of char, J/(kg·K)	[31]
$C_{p,Sand}$	$2.49(T_s)+39.06$	Heat capacity of sand, J/(kg·K)	[29]
$C_{p,g}$	$-3\times10^{-5}(T_g^2)+0.2261\ (T_g)+940.35$	Heat capacity of air, J/(kg·K)	[29]
$\kappa_{p.smo}$	2.54×10^{-10}	Permeability of smoldering chamber, m^2	[11]
M_g	28.97	Molecular weight of air, g/mol	[11]
$\varepsilon_{p,smo,0}$	0.4	Initial porosity of smoldering chamber	[11]
R_g	8.314	Ideal gas constant, J/(mol·K)	[24]
σ	5.67×10^{-8}	Stefan–Boltzmann constant, $W/(m^2\cdot K^4)$	[11]
h_{inner}	359	Inner boundary solid heat transfer coefficient, $W/(m^2\cdot K)$	[32]
h_{outer}	5	Outer boundary solid heat transfer coefficient, $W/(m^2\cdot K)$	[11]
q_{in}	25000	Input heat flux, W/m^2	[29]
$u_{g,in}$	0.05	Air inlet velocity, m/s	[11]
t_g	1020	Air supply starting time, s	[11]
t_h	4320	Heating end time, s	[11]
t_{end}	30000	Smoldering end time, s	[11]
T_∞	293.15	Ambient temperature, K	This study

Table 6.4. Initial and boundary conditions of smoldering model.

Eq.	Initial Condition	Boundary Condition

(23)	t=0s: $Y_{Char} = 1$	-
(24)	t=0s: $p_g = 101375\text{Pa}$	z=0.000m: $p_g = 101375\text{Pa}$
		z=0.730m: $\begin{cases} t = (0, t_g): u_g = 0 \\ t = (t_g, t_{end}): u_g = u_{g,in} \end{cases}$
(25)	t=0s: $Y_{O_2} = 0.204$	z=0.000m: $-\varepsilon_{p,smo} D_g \frac{\partial}{\partial z}(\rho_g Y_{O_2}) = 0$
		z=0.730m: $Y_{O_2} = 0.204$
(26)	t=0s: $T_s = 293.15\text{K}$	z=0.000m: $-k_{eff,smo} \frac{\partial}{\partial z} T_s = 0$
		z=0.730m: $\begin{cases} t = (0, t_h): -k_{eff,smo} \frac{\partial}{\partial z} T_s = 25\text{kW/m}^2 \\ t = (t_h, t_{end}): -k_{eff,smo} \frac{\partial}{\partial z} T_s = 0 \end{cases}$
(27)	t=0s: $T_g = 293.15\text{K}$	z=0.000m: $-k_g \frac{\partial}{\partial z} T_g = 0$
		z=0.730m: $T_g = 293.15\text{K}$

(ii) PW pyrolysis

The 2D pyrolysis model considers the mass conservation equations for PW and fluid as:

$$\frac{\partial}{\partial t}(\rho_{PW}) = -R_{PW} \tag{6.28}$$

$$\frac{\partial}{\partial t}\left(\varepsilon_{p,py}\rho_f\right) + \nabla \cdot \left(\rho_f \mathbf{u}\right) = R_T + R_G \tag{6.29}$$

where the fluid density ρ_f follows the ideal gas law, the pyrolysis chamber porosity is $\varepsilon_{p,py} = \varepsilon_{p,bed} - \left(\varepsilon_{p,bed} - \varepsilon_{p,py,0}\right)\rho_{PW}/\rho_{PW,0}$, and the superficial fluid velocity **u** is calculated by Darcy's Law:

$$\mathbf{u} = -(\kappa_{p,py}/\mu_f)\nabla p_f \tag{6.30}$$

where $\kappa_{p,py}$, μ_f, and p_f represent the permeability of pyrolysis chamber, fluid viscosity, and pressure, respectively.

The tar transport and gas transport equations are given by:

$$\frac{\partial}{\partial t}\left(\varepsilon_{p,py}\rho_{Tar}\right) + \nabla \cdot (\rho_{Tar}\mathbf{u}) = \nabla \cdot \left(\varepsilon_{p,py} D_{Tar} \nabla \rho_{Tar}\right) + R_T \tag{6.31}$$

$$\frac{\partial}{\partial t}\left(\varepsilon_{p,py}\rho_{Gas}\right) + \nabla \cdot (\rho_{Gas}\mathbf{u}) = \nabla \cdot \left(\varepsilon_{p,py}D_{Gas}\nabla\rho_{Gas}\right) + R_G \quad (6.32)$$

where D_{Tar} and D_{Gas} are the diffusion coefficients of tar and gas.

The interfacial heat transfer coefficient correlation in the pyrolysis model has not been established yet. Therefore, the local thermal equilibrium (LTE) assumption is used to calculate the temperature of the pyrolysis model as a first approach. LTE assumes a single temperature for the solid and fluid phases. The energy conservation equation is given by:

$$\frac{\partial(\rho C_p)_{eff,py}T_{PW}}{\partial t} + \nabla \cdot ((\rho C_p)_{eff,py}\mathbf{u}T_{PW}) = \nabla \cdot \left(k_{eff,py}\nabla T_{PW}\right) - R_{PW}\Delta H_{PW} - R_{Tar}\Delta H_{Tar} \quad (33)$$

where the effective volumetric heat capacity $(\rho C_p)_{eff,py}$ and the effective thermal conductivity $k_{eff,py}$ follow:

$$(\rho C_p)_{eff,py} = \left(1 - \varepsilon_{p,bed}\right)\rho_{bed}C_{p,bed} + \left(\varepsilon_{p,bed} - \varepsilon_{p,py}\right)\rho_{PW,par}C_{p,PW} + \varepsilon_{p,py}\rho_f C_{p,f} \quad (6.34)$$

$$k_{eff,py} = \left(1 - \varepsilon_{p,bed}\right)k_{bed} + \left(\varepsilon_{p,bed} - \varepsilon_{p,py}\right)k_{PW} + \varepsilon_{p,py}k_f \quad (6.35)$$

where ρ_{bed}, $C_{p,bed}$, $\rho_{PW,par}$, $C_{p,PW}$, $C_{p,f}$, k_{bed}, k_{PW}, and k_f represent the fixed bed material density, heat capacity of fixed bed material, PW particle density, heat capacity of PW, heat capacity of fluid, thermal conductivity of fixed bed material, thermal conductivity of PW, and heat capacity of fluid, respectively.

The pyrolysis model input parameters, initial and boundary conditions are presented in Tables 6.5 and 6.6. It is worth mentioning that the smoldering chamber was developed in 1D due to its high height-to-thickness ratio of 25.2. The input heat flux of the pyrolysis chamber was assumed to be transferred from the centerline of the smoldering chamber to the pyrolysis chamber wall, which is given by Eq. (6.41) in Table 6.6.

Table 6.5. Model inputs and materials' physical parameters of pyrolysis model.

Par.	Value	Description	Ref.
r_{py}	0.025	Outer radius of pyrolysis chamber, m	This study
r_c	0.001	Radius of fixed bed particle, m	This study
D_0	5.6×10^{-5}	Diffusion coefficient of fluid, m^2/s	[33]
D_{Tar}	$D_0(T_{PW}/273)^{1.7}$	Diffusion coefficient of Tar, m^2/s	[33]
D_{Gas}	$D_0(T_{PW}/273)^{1.7}$	Diffusion coefficient of Gas, m^2/s	[33]
μ_f	3.0×10^{-5}	Fluid viscosity, Pa·s	[15]
k_{PW}	0.335	Thermal conductivity of PW, W/(m·K)	[15]
k_f	0.02557	Thermal conductivity of fluid, W/(m·K)	[15]
k_{bed}	10	Thermal conductivity of fixed bed material, W/(m·K)	[15]
$\varepsilon_{p,py,0}$	0.2	Initial porosity of pyrolysis chamber	This study
$\varepsilon_{p,bed}$	0.4	Fixed bed porosity	[15]
$\rho_{PW,par}$	920	PW particle density, kg/m^3	[15]
$\rho_{PW,0}$	$\rho_{PW,par}(\varepsilon_{p,bed}-\varepsilon_{p,py,0})=184$	Initial PW mass concentration, kg/m^3	Calibrated
ρ_{bed}	2650	Fixed bed material density, kg/m^3	[15]
$C_{p,PW}$	2100	Heat capacity of PW, J/(kg·K)	[15]
$C_{p,f}$	2356.3	Heat capacity of fluid, J/(kg·K)	[9]
$C_{p,bed}$	800	Heat capacity of fixed bed material, J/(kg·K)	[15]
$\kappa_{p,py}$	$r_c^2\varepsilon_{p,py}^3/(180(1-\varepsilon_{p,py})^2)$	Permeability of pyrolysis chamber, m^2	[34]
M_{Tar}	100	Molecular weight of tar, g/mol	[15]
M_{Gas}	30	Molecular weight of pyrolysis gas, g/mol	[15]
M_{N2}	28	Molecular weight of nitrogen, g/mol	[10]
$u_{f,in}$	0.10	Carrier gas inlet velocity, m/s	This study

Table 6.6. Initial and boundary conditions of pyrolysis model.

Eq.	Initial Condition	Boundary Condition
(36)	t=0s:$\rho_{PW} = 184\text{kg/m}^3$	-
(37)	t=0s: $\rho_{Tar} = 0\text{kg/m}^3$	r=0.000m&0.025m: $-\mathbf{n}\cdot(-D_{Tar}\nabla\rho_{Tar} + \mathbf{u}\rho_{Tar}) = 0$
(38)	t=0s: $\rho_{Gas} = 0\text{kg/m}^3$	r=0.000m&0.025m: $-\mathbf{n}\cdot(-D_{Gas}\nabla\rho_{Gas} + \mathbf{u}\rho_{Gas}) = 0$
(39)	t=0s: $\varepsilon_{p,py} = 0.2$	-
(40)	t=0s: $\begin{cases}\mathbf{u} = 0\text{m/s}\\ p_f = 101375\text{Pa}\end{cases}$	z=0.000m: $\begin{cases}u_z = u_{in}\\ u_r = 0\text{m/s}\end{cases}$ z=0.730m: $p_f = 101375\text{Pa}$

		r=0.000m: $\mathbf{u} \cdot \mathbf{n} = 0\mathrm{m/s}$	
		r=0.025m: $\mathbf{u} = 0\mathrm{m/s}$	
(41)	t=0s: $T_{PW} = 293.15\mathrm{K}$	z=0.000m: $T_{PW} = 293.15\mathrm{K}$	
		z=0.730m: $k_{eff,py}\frac{\partial T_{PW}}{\partial z} = 0$	
		r=0.000m: $k_{eff,py}\frac{\partial T_{PW}}{\partial r} = 0$	
		r=0.025m: $k_{eff,py}\frac{\partial T_{PW}}{\partial r} = h_{inner}(T_s - T_{PW})$	

6.3. Results and discussion

The developed numerical model is validated in Section 6.3.1. Section 6.3.2 assesses the numerical results in detail. Sections 6.3.3–6.3.5 discuss the effects of air inlet velocity, char concentration, and carrier gas inlet velocity, respectively.

6.3.1. Model verification

Since there is no experimental data on the PW pyrolysis driven by char smoldering embedded in inert media, we have separately verified the simulations of char smoldering and PW pyrolysis. The model developed in this study was implanted and simulated in COMSOL. The method of time stepping is the backward differentiation formula with a time step of 60 s. The duration of the whole simulation process is 30000 s. Moreover, a grid-independence test was conducted (Fig. C.1, Supplementary Material) and showed that the simulations have a good accuracy and low computational time when the mesh is divided into 4,000 elements.

(i) Smoldering verification

Fig. 6.2 shows the comparison between the experimental [11], numerical results by [11], and the numerical results using the model developed in this work. The smoldering chamber is

a fixed bed with 0.73 m height and 0.054 m radius. The air inlet velocity $u_{g,in}$ and char concentration C_{Char} are 0.050 m/s and 2.0 %, respectively. Eqs. (6.12–6.22) and initial and boundary conditions in Tables 6.3 and 6.4 were used in these simulations. The differences between the numerical results in [11] and the present study are attributed to the different mesh sizes and time steps. It can be concluded that the simulated temperature and pressure are in good agreement with the experimental results, with errors equal to 3.6 % and 14.2 %, respectively. Moreover, as shown in Fig. C.2, the average numerical peak temperature $T_{s,p}$ (the subscript "p" refers to peak value) and front velocity $v_{f,s}$ (635 °C and 0.054 mm/s) agree well with experimental data (631 °C and 0.057 mm/s) and numerical results by [11] (657 °C and 0.056 mm/s). This also proves that char smoldering can provide a stable heat source for PW pyrolysis.

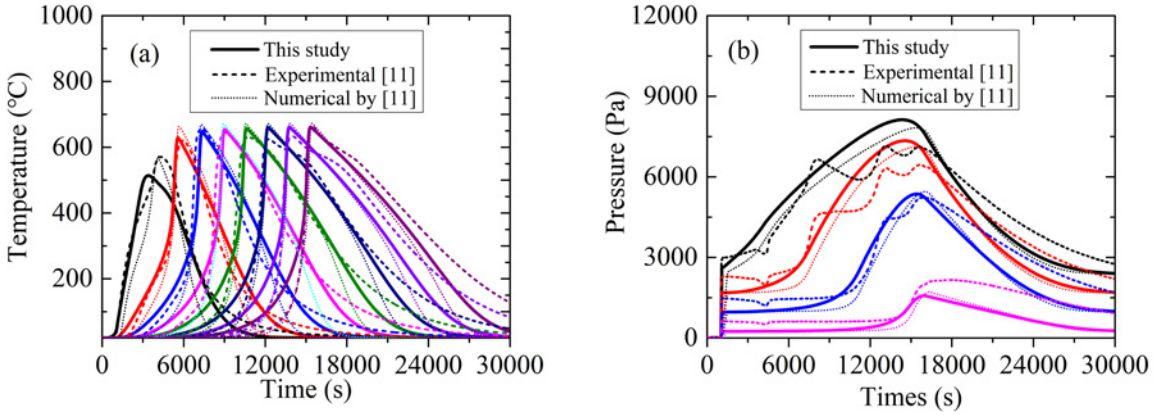

Fig.6.2. Temperature and pressure profiles in different locations: (a) Temperature profiles at z=0.06–0.69 m, distributed with a spacing of 0.09 m; (b) Pressure profiles at z=0.07–0.70 m, distributed with a spacing of 0.21 m; (c) $T_{s,p}$; (d) $v_{f,s}$.

(ii) Pyrolysis verification

Table 6.7 illustrates the experimental and predicted PW pyrolysis tar and gas yields. The

PW pyrolysis experiment was conducted to produce tar and gas. Nitrogen was served as the purge and carrier gas. The experimental conditions are described in Table 6.7 and more details can be found in [19]. For the PW pyrolysis simulation, the domain's temperature was programed according to the experimental conditions. These experiments were simulated with the model developed in Section 6.2.3 (ii) using Eqs. (6.23–6.27). Here, tar and gas yields were calculated with Eqs. (6.10–6.11) and then compared with experimental data.

As shown in Table 6.7, the increase in temperature leads to a decrease in tar yield and an increase of gas yield, which can be attributed to the tar cracking at higher temperatures. The model was able to accurately simulate the production of tar and gas, with errors equal to 4.0 % and 5.9 %, respectively.

Table 6.7. Experimental and numerical PW pyrolysis tar and gas yields in different cases [19].

Case	Temperature (°C) [a]	Residence time (min) [b]	Carrier gas inlet velocity (m/s) [c]	Experimental			Numerical		
				Tar (wt.%)	Gas (wt.%)	PW_{conv} (%)	Tar (wt.%)	Gas (wt.%)	PW_{conv} (%)
1	425	60	0.1	82.42	13.97	100	73.10	12.29	89.1
2	475	20	0.1	80.53	15.79	100	80.98	15.36	100
3	525	40	0.1	80.54	16.06	100	80.75	15.59	100

[a] Temperature increases from 20°C to the target value at 6°C/min.

[b] Residence time is the duration after reaching the target temperature.

[c] Carrier gas inlet velocity for the numerical model.

6.3.2. Assessments of modeling results

Fig. 6.3 illustrates the coupling of the 1D smoldering model with 2D pyrolysis model. In the smoldering chamber (Fig. 6.3a), the smoldering front propagates from the top to the bottom

of the reactor. When air starts to enter the reactor, the gas temperature (T_g) is gradually increased by convective heat transfer from the solid phase (T_s). T_g is higher than T_s in the lower part of the reactor because the air velocity is faster than heat conduction in the solid. In addition, heat radiation corresponds to a large fraction of heat transfer in the smoldering chamber [35]. In the pyrolysis chamber (Fig. 6.3b), the PW temperature (T_{PW}) shows a similar trend to the smoldering temperatures due to the boundary heat transfer between smoldering and pyrolysis chambers. It is worth noting that the T_s peak in the char smoldering is sharp, while the T_{PW} peak in the PW pyrolysis is round due to the PW's low thermal conductivity (compared to the fixed bed material). Figs. 6.3c–d shows that the smoldering oxidation occurs in a narrow region (z=0.35–0.38 m), i.e., the thickness of the smoldering front is very thin (0.03 m), which led to a sharp peak in T_s profile. The PW pyrolysis is dominated by endothermic processes and driven by the heat generated in the char smoldering. Note that the PW pyrolysis chamber continuously receives the heat from the smoldering chamber; thus, the temperature peaks increase along the reactor. Fig. 6.3d shows that the pyrolysis front is relatively wide (0.09 m) mainly occurring at z=0.36–0.45 m, resulting in a round T_{PW} peak.

By comparing Figs. 6.3a and b, there is a temperature difference of ~80 °C between $T_{s,p}$ and $T_{PW,p}$ (Fig. C.3a, Supplementary Material), which could be attributed to the endothermic PW pyrolysis. As shown in Fig. C.3b (Supplementary Material), the heat propagation of PW pyrolysis ($v_{f,PW}$=0.050 mm/s) is slightly slower than that of char smoldering ($v_{f,s}$=0.051 mm/s). Moreover, it takes a longer time for the local T_{PW} to reach its maximum value compared to T_s because of the thermal inertia (Fig. C.3c). In other words, the heat propagation of PW pyrolysis

is lagging (~550 s) behind that of char smoldering.

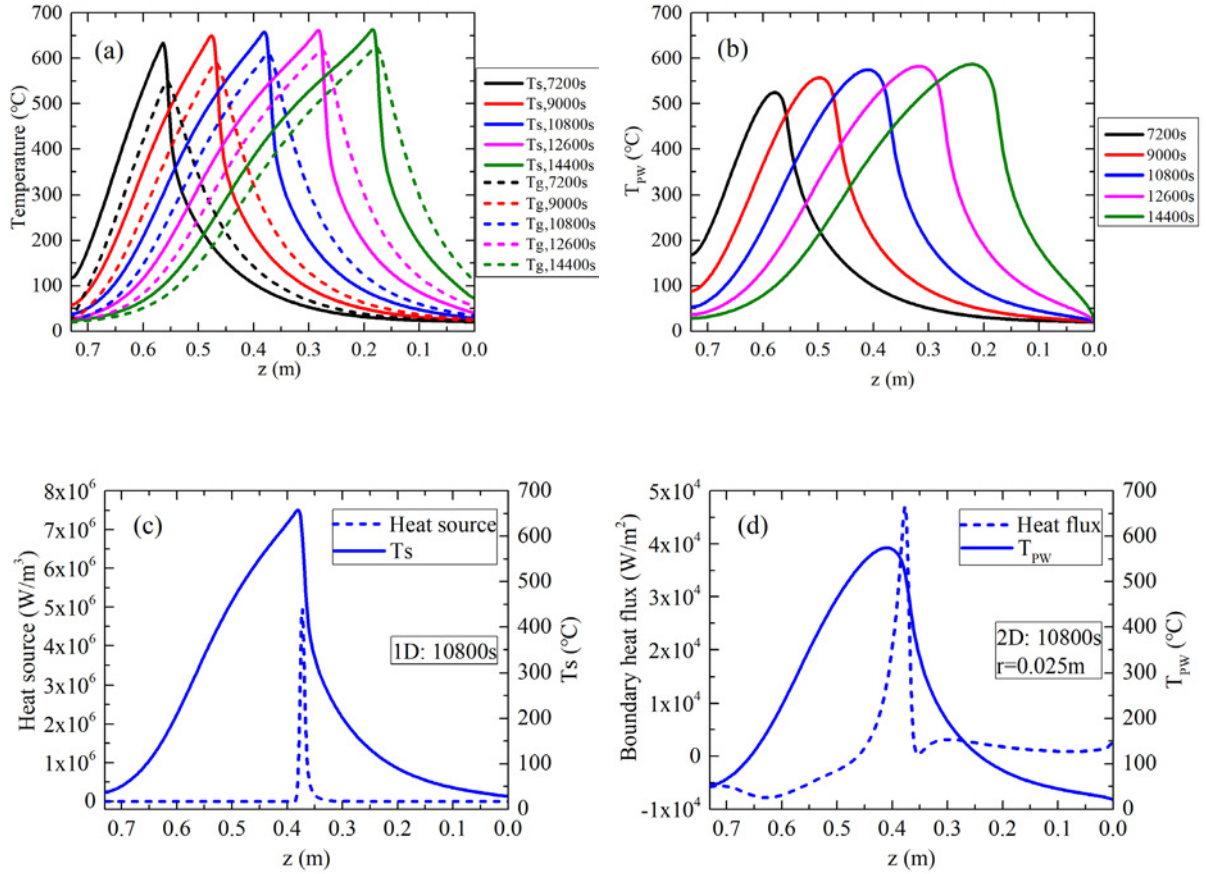

Fig.6.3. T_s, T_g, T_{PW} profiles at t=7200–14400 s with intervals of 1800 s: (a) T_s and T_g; (b) T_{PW} at r=0.025 m; (c) T_s and smoldering heat generation at 10800 s; (d) T_{PW} and boundary heat flux at 10800 s and r=0.025 m.

Fig. 6.4 shows that the pyrolysis front propagates downwards as time increases (Fig. 6.4a), which is consistent with the direction of char smoldering propagation. The PW pyrolysis rate (R_{PW}) increases over time with a maximum R_{PW} equals to ~7.3 kg·m^{-3}·s^{-1} at z=0.180 m, r=0.025 m and t=14400 s (Fig. 6.4b). This is attributed to the increase in $T_{PW,p}$ (Fig. 6.3b). The pyrolysis front thickness of PW decreases with time due to the higher R_{PW} (Fig. 6.4b), which decomposes PW into vapors (tar and gas) when T_{PW} reaches the onset temperature [25]. Therefore, the downward propagation of T_{PW} leads to a decrease in the PW mass concentration (ρ_{PW}) and an

increase in the fixed bed porosity ($\varepsilon_{p,py}$), Figs. 6.4c–d. It is worth noting that PW at the top of the reactor is not completely pyrolyzed (Fig. 6.4c) due to lower temperatures at that region. Fig. 6.2a shows that T_s peak at z=0.69 m is 572 °C, while the T_s peak in the lower part of the reactor is around 666 °C. This is because the char smoldering has just started, and the accumulated heat is not enough to completely pyrolyze the PW on the top of the reactor [11]. Moreover, the maximum temperature region is in the post-reaction zone (Fig. 6.4a) due to the countercurrent flow of carrier gas relative to the temperature wave propagation direction.

Fig. 6.4a also shows the velocity fields in the pyrolysis chamber at different times, which correspond to volatile tar and gases generated during pyrolysis along with nitrogen. Note that the arrows corresponding to the velocity field are bigger close to the wall. This is because T_{PW} at the reactor wall ($r \to 0.025m$) is higher than that at the center ($r \to 0m$), which results in a faster gas flow at that region.

It is noteworthy that the model developed in the present study can be used to simulate the contaminated sands/soils remediation, other wastes pyrolysis, and energy storage [36–38].

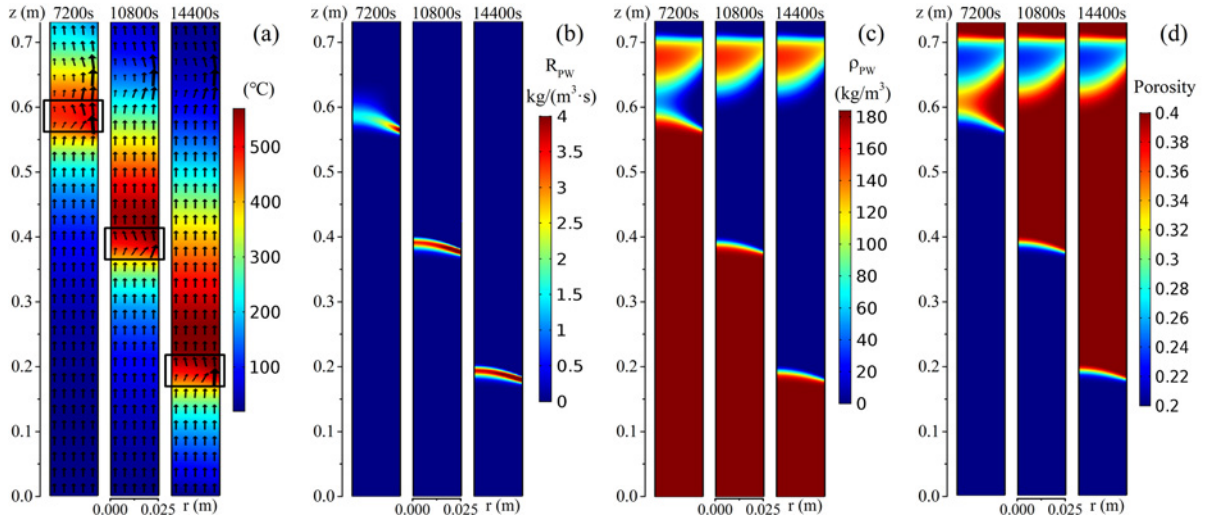

Fig.6.4. Modeling results in PW pyrolysis chamber at t=7200–14400 s with intervals of 3600 s: (a) T_{PW} and

velocity field; (b) R_{PW}; (c) PW mass concentration; (d) Bed porosity.

6.3.3. Effect of air inlet velocity in smoldering chamber

Fig. 6.5 illustrates the effect of air inlet velocity on the smoldering temperature T_s and pyrolysis temperature T_{PW} (at r=0.025 m) profiles. As shown in Figs. 6.5a–b, the increase in the air inlet velocity leads to a decrease in T_s and T_{PW} peak at z=0.69 m due to convective cooling. However, higher air inlet velocities can also increase the char combustion rate and thus increase the local net energy rate, which further leads to an increase in $T_{s,p}$ (Fig. 6.5c) [16]. Moreover, the increase in air inlet velocity could accelerate the local energy leaving the smoldering front, thereby increasing the $v_{f,s}$. The increase in $T_{s,p}$ and $v_{f,s}$ leads to the corresponding increase in $T_{PW,p}$ and $v_{f,PW}$, which is cause by the increase in boundary heat flux. The higher temperature in pyrolysis chamber increases the R_{PW} (Fig. C.4, Supplementary Material), which can be attributed to the intensified random scission of C–C bond in PW [19].

PW conversion increases with time due to the production of tar and gas (Fig. C.5, Supplementary Material). In Fig. C.5 (Supplementary Material), the pyrolysis of PW is completed (maximum PW conversion) earlier (from 21660 s to 18060 s) under higher air inlet velocities. These results revealed good insights into future practical application, because just increasing the air inlet velocity in the smoldering chamber from 0.03 m/s to 0.05 m/s can shorten the PW pyrolysis process by ~3600 s. Moreover, the increase in air inlet velocity leads to a decrease in Y_{Tar} and an increase in Y_{Gas} due to the increase in T_{PW} (Fig. 6.5b), which accelerates the chain-end scission of tar and thus generates more gaseous hydrocarbons (C1–C4) [39-40]. As illustrated in Fig. 6.5d, the PW conversion is enhanced by higher $T_{PW,p}$ (Fig. 6.5c) under

higher air inlet velocities in the range of 0.03–0.04 m/s. However, when the air inlet velocity continues to increase to 0.05 m/s, the PW at the top of the reactor is not completely pyrolyzed (Fig. C.4, Supplementary Material) due to the low local T_{PW} (Fig. 6.5b), which decreases the PW conversion to 88.8 wt%.

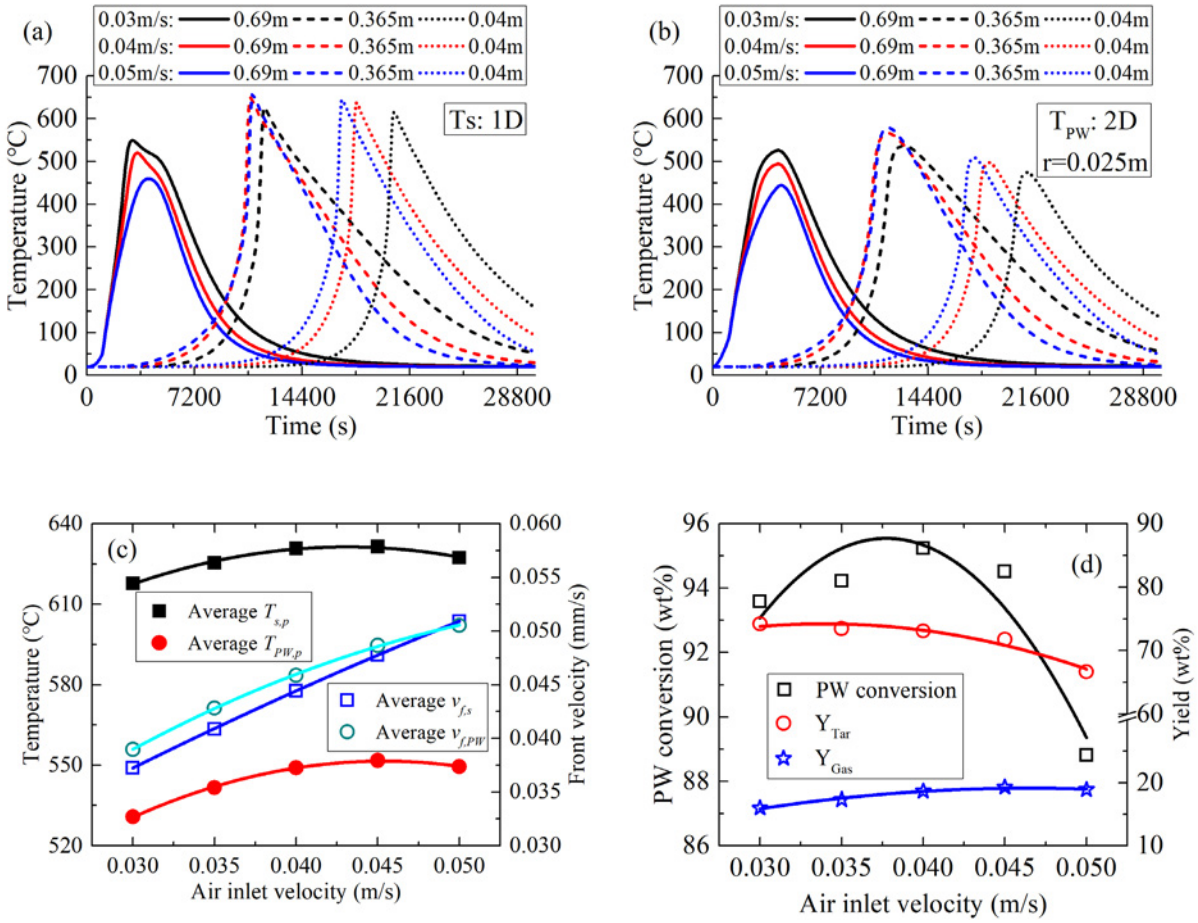

Fig.6.5. The effect of air inlet velocity on (a, b) T_s and T_{PW} (at r=0.025 m) profiles at z=0.04–0.69 m with intervals of 0.325 m, (c) average $T_{s,p}$, $T_{PW,p}$, $v_{f,s}$, and $v_{f,PW}$, and (d) maximum PW conversions, Y_{Tar} and Y_{Gas} distributions.

6.3.4. Effect of char concentration in smoldering chamber

Fig. 6.6a shows the effect of char concentration on the $T_{s,p}$, $T_{PW,p}$, $v_{f,s}$, and $v_{f,PW}$. It should be noted that oxygen is in excess in all cases (3.9%–6.6% consumed). The increase in char concentration leads to an increase in char oxidation energy rate and corresponding increases

local net energy rate, which further increases $T_{s,p}$ [16]. Moreover, the $v_{f,s}$ is also increased as the char concentration increases due to the improved energy out rate from the smoldering front. As discussed in Section 6.3.3, the increase in $T_{s,p}$ and $v_{f,s}$ leads to the increase in input heat flux of the pyrolysis chamber, thereby increasing $T_{PW,p}$ (from 627 °C to 732 °C) and $v_{f,PW}$ (from 0.051 m/s to 0.067 m/s).

Fig. C.6c (Supplementary Material) indicates that the maximum R_{PW} increases drastically from 6.95 $kg \cdot m^{-3} \cdot s^{-1}$ to 17.05 $kg \cdot m^{-3} \cdot s^{-1}$ when the char concentration increases from 2.2 % to 3.0 %. Moreover, the increase in char concentration pushes the pyrolysis front (Fig. C.6e, Supplementary Material) by 0.251 m (0.376–0.125 m) downwards. On the other hand, due to the increased local T_{PW} (Fig. C.6b, Supplementary Material), PW has been completely pyrolyzed at the top of the reactor when the char concentration increases to 2.6 %.

The PW pyrolysis process is shortened by 5160 s (from 18060 s to 12900 s) when the char concentration increases from 2.2 % to 3.0 % (Fig. C.7, Supplementary Material). The increase in T_{PW} caused by the higher energy created with a higher char concentration could accelerate the random scission of C–C bonds in PW [40], which leads to an increase of 7.6 wt% (from 88.8 wt% to 96.4 wt%) in PW conversion. Moreover, the higher temperature can enhance the chain-end scission rate of C–C bonds in tar, which contributes to a dramatically decrease of 25.8 wt% (from 66.7 wt% to 40.9 wt%) in Y_{Tar} and an increase of 33.1 wt% (from 18.9 wt% to 52.0 wt%) in Y_{Gas} due to the (Fig. 6.6b). These results revealed that char concentration could control the composition of plastic pyrolysis products by regulating the temperature distribution in pyrolysis chamber, which provided good insights for the future practical application of

smoldering-driven pyrolysis reactor.

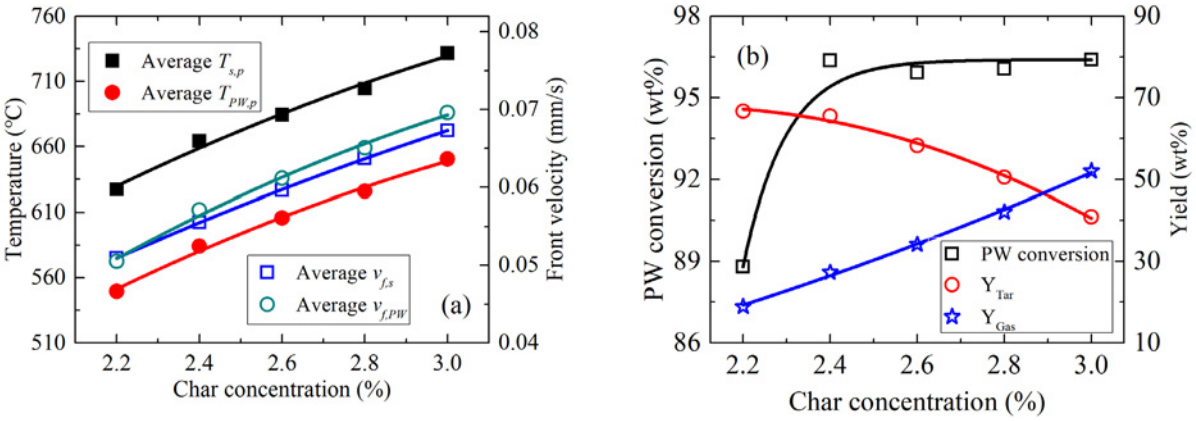

Fig.6.6. The effect of char concentration on (a) average $T_{s,p}$, $T_{PW,p}$, $v_{f,s}$, and $v_{f,PW}$ and (b) maximum PW conversions, Y_{Tar} and Y_{Gas} distributions.

6.3.5. Effect of carrier gas inlet velocity in pyrolysis chamber

Fig. 6.7a demonstrates the effect of carrier gas inlet velocity on the average $T_{s,p}$, $T_{PW,P}$, $v_{f,s}$, and $v_{f,PW}$; and R_{PW}. The increase in carrier gas inlet velocity leads to a decrease in $T_{PW,p}$ due to the enhanced convective cooling by carrier gas, which corresponding increases the heat input from the smoldering chamber and decreases $T_{s,p}$. The increase in the heat input (radial) from the smoldering chamber further decreases the heat leaving the smoldering front in the *z*-axis direction (local energy rate) due to the energy conservation. Consequently, the reduced local energy rate leads to a decrease in $v_{f,s}$, and further decreases $v_{f,PW}$ since the pyrolysis front is driven by the heat generated by smoldering. The maximum R_{PW} decreases from 4.54 $kg \cdot m^{-3} \cdot s^{-1}$ to 3.81 $kg \cdot m^{-3} \cdot s^{-1}$ (Fig. C.8, Supplementary Material) when the carrier gas inlet velocity increases from 0.02 m/s to 0.10 m/s, which is caused by the decrease in T_{PW} that decelerates the random scission rate of C–C bonds in PW.

Fig. C.9 (Supplementary Material) indicates that the decrease in carrier gas inlet velocity

could shorten the PW pyrolysis process slightly by 1260 s (from 18060 s to 16800 s). This is because the lower inlet velocity of carrier gas reduces the boundary heat loss (reflects in the temperature difference between $T_{s,p}$ and $T_{PW,P}$ in Fig. 6.7a) in smoldering chamber, which accelerates the local energy leaving the smoldering front and thus leads to an increase in $v_{f,s}$. Therefore, the $v_{f,PW}$ increased since the pyrolysis front is driven by the boundary heat flux in smoldering chamber. Fig. 6.7b shows that the PW conversion decreases from 95.8 wt% to 88.8 wt% as the carrier gas inlet velocity increases due to the decrease in T_{PW}.

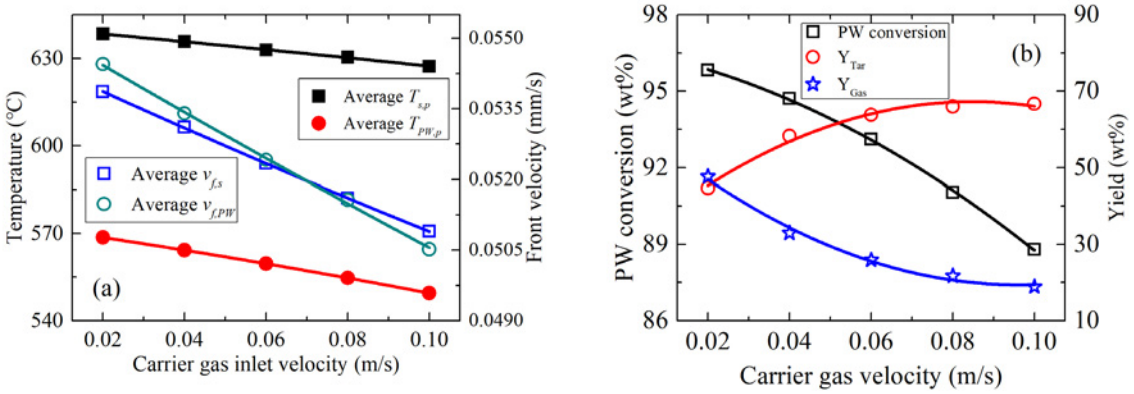

Fig.6.7. The effect of carrier gas inlet velocity on (a) average $T_{s,p}$, $T_{PW,P}$, $v_{f,s}$, and $v_{f,PW}$ and (b) maximum PW conversions, Y_{Tar} and Y_{Gas} distributions.

A detailed evaluation of the effect of carrier gas inlet velocity on R_{Tar}, ρ_{Tar}, and ρ_{Gas} is provided in Fig. 6.8. It should be noted that R_{Tar}, ρ_{Tar}, and ρ_{Gas} values vary greatly at different carrier gas inlet velocities. To compare the tar pyrolysis rate R_{Tar}, tar mass concentration ρ_{Tar}, and pyrolysis gas mass concentration ρ_{Gas}, normalized tar pyrolysis rate R'_{Tar}, tar mass concentration ρ'_{Tar}, and pyrolysis gas mass concentration ρ'_{Gas} was proposed:

$$R'_{Tar} = R_{Tar}\left(\frac{u_{f,in}}{u_{f,in}^{min}}\right) \tag{6.42}$$

$$\rho'_{Tar} = \rho_{Tar}\left(\frac{u_{f,in}}{u_{f,in}^{min}}\right) \tag{6.43}$$

$$\rho'_{Gas} = \rho_{Gas}\left(\frac{u_{f,in}}{u_{f,in}^{min}}\right) \tag{6.44}$$

where R_{Tar}, ρ_{Tar}, and ρ_{Gas} were normalized by the carrier gas inlet velocity, and $u_{f,in}^{min} = 0.02 m/s$.

The maximum R_{Tar} decreases by five times when the carrier gas inlet velocity increases from 0.02 m/s to 0.10 m/s (Fig. 6.8b). The decrease in R_{Tar} can be attributed to three aspects: (i) the enhanced convective cooling by carrier gas reduces the temperature in the pyrolysis chamber and reduces the random scission rate of C–C bonds in PW, thereby decreasing the tar formation rate (Eq. (6.3)), (ii) the decrease in the temperature in the pyrolysis chamber decelerates the chain-end scission rate of C–C bonds in tar, thereby decreasing the tar consumption rate (Eq. (6.6)), and (iii) the shorter residence time of tar inside the pyrolysis chamber leads to a decrease in ρ_{Tar} (Fig. 6.8d) and thus decreases the tar consumption rate for gas generation (Fig. 6.8f). Consequently, the increase in carrier gas inlet velocity leads to an increase of 22.0 wt% in Y_{Tar} and a decrease of 28.8 wt% in Y_{Gas} (Fig. 6.7b). These results reveal that the composition of plastic pyrolysis products can be regulated by the carrier gas inlet velocity in the pyrolysis chamber, which provides meaningful guidance for future practical application of smoldering-driven pyrolysis reactor.

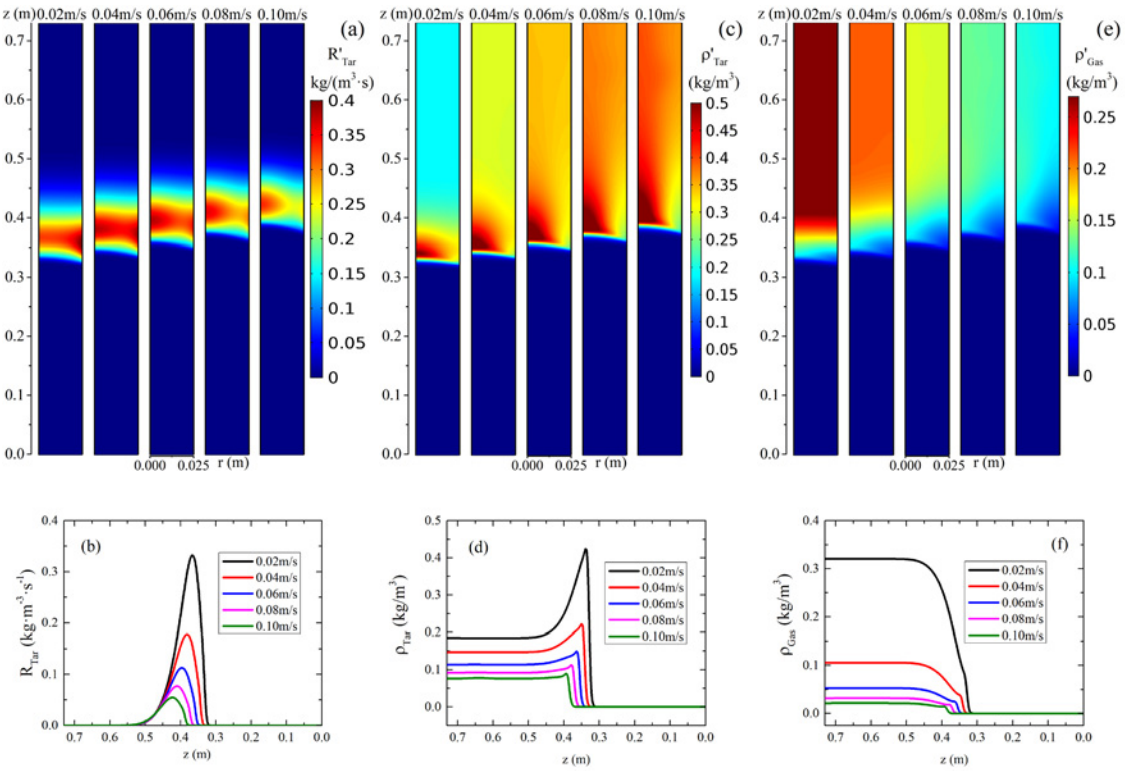

Fig.6.8. The effect of carrier gas inlet velocity on R_{Tar}, ρ_{Tar}, and ρ_{Gas} at t=10800s: (a) Distributions of R'_{Tar}; (b) R_{Tar} profiles at r=0.0125m; (c) Distributions of ρ'_{Tar}; (d) ρ_{Tar} profiles at r=0.0125m; (e) Distributions of ρ'_{Gas}; (f) ρ_{Gas} profiles at r=0.0125m.

6.4. Conclusions

This chapter proposed a novel numerical model for PW pyrolysis driven by char smoldering. The numerical study was performed to ensure the feasibility of the smoldering-driven reactor and evaluate its performance. It is noteworthy that PW was pyrolyzed in a fixed bed. However, the pyrolysis chamber can also process waste in a continuous mode. It is the first time that a multidimensional model was developed to perform the numerical study of PW pyrolysis driven by char smoldering. A comprehensive study of PW pyrolysis tar and gas yields was carried out under consideration of key parameters. The PW pyrolysis process duration, conversion rate, and product composition could be regulated by changing air inlet velocity, char concentration, and carrier gas inlet velocity, since they could control the peak temperature and the front

velocity.

The char smoldering could provide a heat source with stable propagation velocity and peak temperature by adding sand as the porous matrix in the smoldering chamber. PW was continuously pyrolyzed without providing external energy as long as char smoldering continues. Increasing the air inlet velocity in smoldering chamber shortened the PW pyrolysis process. The maximum PW conversion of 95.2 wt% was achieved under the air inlet velocity of 0.04 m/s. The increase in air inlet velocity led to a decrease of 7.5 wt% in tar yield and an increase of 2.9 wt% in gas yield.

The increase in char concentration shorted the PW pyrolysis process and enhance the PW conversion by 7.6 wt%. This also resulted in a decrease of 25.8 wt% in tar yield and an increase of 33.1 wt% in gas yield.

The carrier gas inlet velocity in the pyrolysis chamber had an insignificant effect on the duration of PW pyrolysis process and the PW conversion. A high carrier gas inlet velocity increased tar yield by 22.0 wt% and decreased gas yield by 28.8 wt% mainly by reducing the residence time of tar in the pyrolysis chamber.

Bibliography

[1] PlasticsEurope. An analysis of European plastics production, demand and waste data. Plastics – the Facts 2020.

[2] Weckhuysen, B.M., 2020. Creating value from plastic waste. Science, 370(6515), pp.400-401.

[3] Larrain, M., Van Passel, S., Thomassen, G., Kresovic, U., Alderweireldt, N., Moerman, E. and Billen, P., 2020. Economic performance of pyrolysis of mixed plastic waste: Open-loop versus closed-loop recycling. Journal of Cleaner Production, 270, p.122442.

[4] Gala, A., Catalan-Martinez, D., Guerrero, M. and Serra, J.M., 2021. Simulation-assisted design of a catalytic hydrogenation reactor for plastic pyrolysis fuels. Fuel, 287, p.119400.

[5] Wang, Z., Burra, K.G., Lei, T. and Gupta, A.K., 2021. Co-pyrolysis of waste plastic and solid biomass for synergistic production of biofuels and chemicals-A review. Progress in Energy and Combustion Science, 84, p.100899.

[6] Park, H.J., Park, Y.K., Dong, J.I., Jeon, J.K., Yim, J.H. and Jeong, K.E., 2008. Catalytic degradation of polyethylene over ferrierite. Research on Chemical Intermediates, 34(8), pp.727-735.

[7] Duque, J.V.F., Bittencourt, F.L., Martins, M.F. and Debenest, G., 2021. Developing a combustion-driven reactor for waste conversion. Energy, 237, p.121489.

[8] Mazloum, S., Awad, S., Allam, N., Aboumsallem, Y., Loubar, K. and Tazerout, M., 2021. Modelling plastic heating and melting in a semi-batch pyrolysis reactor. Applied Energy, 283, p.116375.

[9] Yin, L.J., Chen, D.Z., Wang, H., Ma, X.B. and Zhou, G.M., 2014. Simulation of an innovative reactor for waste plastics pyrolysis. Chemical Engineering Journal, 237, pp.229-235.

[10] Debenest, G., Guibert, R., Horgue, P. and Yang, C., 2020. Numerical simulation of solid combustion in microporous particles. Frontiers in Chemistry, p.877.

[11] Zanoni, M.A., Wang, J. and Gerhard, J.I., 2021. Understanding pressure changes in smouldering thermal porous media reactors. Chemical Engineering Journal, 412, p.128642.

[12] Bittencourt, F.L.F., Debenest, G. and Martins, M.F., 2022. Free convection development caused by bed shrinkage in a vacuum-induced smoldering reactor. Chemical Engineering Journal, 430, p.132847.

[13] Zanoni, M.A., Torero, J.L. and Gerhard, J.I., 2019. The role of local thermal non-equilibrium in modelling smouldering combustion of organic liquids. Proceedings of the Combustion Institute, 37(3), pp.3109-3117.

[14] Zanoni, M.A., Torero, J.L. and Gerhard, J.I., 2020. Experimental and numerical investigation of weak, self-sustained conditions in engineered smouldering combustion. Combustion and Flame, 222, pp.27-35.

[15] Ding, K., Xiong, Q., Zhong, Z., Zhong, D. and Zhang, Y., 2020. CFD simulation of combustible solid waste pyrolysis in a fluidized bed reactor. Powder Technology, 362, pp.177-187.

[16] Zanoni, M.A., Torero, J.L. and Gerhard, J.I., 2019. Delineating and explaining the limits of self-sustained smouldering combustion. Combustion and Flame, 201, pp.78-92.

[17] Muhammad, I., Makwashi, N. and Manos, G., 2019. Catalytic degradation of linear low-density polyethylene over HY-zeolite via pre-degradation method. Journal of Analytical and Applied Pyrolysis, 138, pp.10-21.

[18] Sharuddin, S.D.A., Abnisa, F., Daud, W.M.A.W. and Aroua, M.K., 2016. A review on pyrolysis of plastic wastes. Energy conversion and management, 115, pp.308-326.

[19] Pan, R., Martins, M.F. and Debenest, G., 2021. Pyrolysis of waste polyethylene in a semi-batch reactor to produce liquid fuel: optimization of operating conditions. Energy Conversion and Management, 237, p.114114.

[20] Fadaei, H., Sennoune, M., Salvador, S., Lapene, A. and Debenest, G., 2012. Modelling of non-consolidated oil shale semi-coke forward combustion: Influence of carbon and calcium carbonate contents. Fuel, 95, pp.197-205.

[21] Elayeb, M., Debenest, G., Mourzenko, V.V. and Thovert, J.F., 2017. Smoldering combustion in oil shales: influence of calcination and pyrolytic reactions. Transport in Porous Media, 116(2), pp.889-921.

[22] Pozzobon, V., Baud, G., Salvador, S. and Debenest, G., 2017. Darcy scale modeling of smoldering: impact of heat loss. Combustion Science and Technology, 189(2), pp.340-365.

[23] Shi, X., Zhang, Y., Chen, X., Zhang, Y. and Ma, T., 2021. Numerical study on the oxidation reaction characteristics of coal under temperature-programmed conditions. Fuel Processing Technology, 213, p.106671.

[24] Shi, X., Chen, X., Zhang, Y., Zhang, Y., Guo, R., Zhao, T. and Liu, R., 2022. Numerical simulation of coal dust self–ignition and combustion under inclination conditions. Energy,

239, p.122227.

[25] Mazloum, S., Aboumsallem, Y., Awad, S., Allam, N. and Loubar, K., 2021. Modelling pyrolysis process for PP and HDPE inside thermogravimetric analyzer coupled with differential scanning calorimeter. International Journal of Heat and Mass Transfer, 176, p.121468.

[26] Ceamanos, J., Mastral, J.F., Millera, A. and Aldea, M.E., 2002. Kinetics of pyrolysis of high density polyethylene. Comparison of isothermal and dynamic experiments. Journal of Analytical and Applied Pyrolysis, 65(2), pp.93-110.

[27] Kim, S. and Kim, Y.C., 2005. Using isothermal kinetic results to estimate the kinetic triplet of the pyrolysis of high density polyethylene. Journal of Analytical and Applied Pyrolysis, 73(1), pp.117-121.

[28] Miller, R.S. and Bellan, J., 1997. A generalized biomass pyrolysis model based on superimposed cellulose, hemicelluloseand liqnin kinetics. Combustion science and technology, 126(1-6), pp.97-137.

[29] Zanoni, M.A., Torero, J.L. and Gerhard, J.I., 2017. Determination of the interfacial heat transfer coefficient between forced air and sand at Reynold's numbers relevant to smouldering combustion. International Journal of Heat and Mass Transfer, 114, pp.90-104.

[30] Torero, J.L., Fernandez-Pello, A.C. and Kitano, M., 1993. Opposed forced flow smoldering of polyurethane foam. Combustion Science and Technology, 91(1-3), pp.95-117.

[31] Kleinhans, U., Halama, S. and Spliethoff, H., 2017. The role of gasification reactions during pulverized solid fuel combustion: A detailed char combustion model based on

measurements of char structure and kinetics for coal and pre-treated biomass. Combustion and Flame, 184, pp.117-135.

[32] Pecha, M.B., Thornburg, N.E., Peterson, C.A., Crowley, M.F., Gao, X., Lu, L., Wiggins, G., Brown, R.C. and Ciesielski, P.N., 2021. Impacts of anisotropic porosity on heat transfer and off-gassing during biomass pyrolysis. Energy & Fuels, 35(24), pp.20131-20141.

[33] Shi, X., Zhang, Y., Chen, X., Zhang, Y. and Ma, Q., 2021. Characteristics of coal dust ignited by a hot particle. Process Safety and Environmental Protection, 153, pp.225-238.

[34] Pan, R., Lougou, B.G., Shuai, Y., Zhang, G. and Zhang, H., 2019. Heat transfer modeling of a high-temperature porous-medium filled solar thermochemical reactor for hydrogen and synthesis gas production. Journal of Heat Transfer, 141(2).

[35] Shin, D. and Choi, S., 2000. The combustion of simulated waste particles in a fixed bed. Combustion and flame, 121(1-2), pp.167-180.

[36] Xu, Y., Ding, H., Luo, C., Zheng, Y., Xu, Y., Li, X., Zhang, Z., Shen, C. and Zhang, L., 2018. Effect of lignin, cellulose and hemicellulose on calcium looping behavior of CaO-based sorbents derived from extrusion-spherization method. Chemical Engineering Journal, 334, pp.2520-2529.

[37] Xu, Y., Zhang, T., Lu, B., Luo, C., Wu, F., Li, X. and Zhang, L., 2021. Glycine tailored effective CaO-based heat carriers for thermochemical energy storage in concentrated solar power plants. Energy Conversion and Management, 250, p.114886.

[38] Xu, Y., Lu, B., Luo, C., Wu, F., Li, X. and Zhang, L., 2022. Na2CO3 promoted CaO-based heat carrier for thermochemical energy storage in concentrated solar power plants.

Chemical Engineering Journal, p.134852.

[39] Gao, X., Lu, L., Shahnam, M., Rogers, W.A., Smith, K., Gaston, K., Robichaud, D., Pecha, M.B., Crowley, M., Ciesielski, P.N. and Debiagi, P., 2021. Assessment of a detailed biomass pyrolysis kinetic scheme in multiscale simulations of a single-particle pyrolyzer and a pilot-scale entrained flow pyrolyzer. Chemical Engineering Journal, 418, p.129347.

[40] Murata, K., Sakata, Y. and Brebu, M., 2022. Thermal degradation of polyethylene in the presence of a non-acidic porous solid by a continuous flow reactor. Journal of Analytical and Applied Pyrolysis, 161, p.105395.

Chapter 7

A robust two-dimensional model for the pyrolysis of plastic waste driven by self-sustaining smoldering

Summary

Chapter 6 established a two-dimensional (2D) pyrolysis model coupled with a one-dimensional (1D) smoldering model to evaluate the reactor's performance. The boundary heat flux for the 1D smoldering model was determined by the global heat loss coefficient, which was calculated based on experimental data. The difficulty to determine the global heat loss coefficient makes it challenging for the 1D smoldering model to conduct simulations of different reactor sizes.

To improve the robustness of the smoldering-driven pyrolysis model, this chapter established a two-dimensional (2D) mathematical model for plastic waste (PW) pyrolysis driven by self-sustaining smoldering. The PW could be melted and decomposed into value-added volatiles driven by the stable char smoldering heat. The findings revealed that the pyrolysis duration and product distribution could be regulated by the char concentration and Darcy air velocity. Higher PW contents shortened the volatiles' residence time in the pyrolysis chamber and controlled the pyrolysis product yields. The increased PW content could enhance the PW processing capacity and obtain higher economic benefits. Moreover, the reactor's geometry significantly affected the pyrolysis chamber's temperature distribution and the PW processing capacity.

Candidate contribution: Conceptualization, methodology, formal analysis, resources,

data curation, writing - original draft, visualization.

7.1. Introduction

Smoldering combustion is a promising method to remediate the contaminated soils or sands with combustible substances, such as bitumen [1], coal tar [2], heavy oil [3], poly-fluoroalkyl [4-5], sewage [6] and oil [7-8] sludges, char/coal [9-10], etc. Smoldering can self-sustainingly propagate in an inert porous bed (soil/sand) when the local heat released from fuel combustion is higher than heat losses [11-12]. Self-sustaining smoldering is also an efficient technology for waste disposal [13-14] and the valorization of oil shale [15-17] and wastes [18-20].

Self-sustaining smoldering is governed by several parameters, such as Darcy air velocity, oxygen concentration, and fuel concentration. The latter is a key parameter in understanding smoldering extinction. Low fuel concentrations can extinct the smoldering front, since the reaction does not release enough energy for self-sustained propagation [21-22]. In contrast, high fuel concentrations can enhance the local heat release rate and increase the smoldering peak temperature when oxygen is in excess [23]. The increased local heat release rate leads to a higher heat propagation from the front, further resulting in a faster propagation velocity [1]. Higher air injection velocities can increase the peak temperature and propagation velocity due to the enhanced convective heat transfer in most forced smoldering circumstances [24-25]. Duque et al. [26] and Hasan et al. [27] suggested that the increase in air injection velocity led to a virtually linear increase in peak temperature and propagation velocity. Moreover, the increased air injection velocity can enable the substance to combust more completely, improving the thermal robustness of the reactor [28]. Moreover, Lin et al. [29] and Rashwan et al. [30] reported that the geometry of the smoldering reactor is a sensitive parameter for the

thickness of the smoldering front and heat loss to the environment. The findings revealed that larger smoldering reactor radiuses could increase the smoldering front's thickness [29] and enhance the system's energy efficiency [31].

The high peak temperature (above 500 °C) is a critical characteristic of self-sustaining smoldering [32]. Therefore, effective utilization of the high-grade waste heat generated by self-sustaining smoldering can improve the economic benefits of smoldering [33]. The high smoldering temperature is favorable for plastic waste (PW) thermal decomposition [34]. PW can be decomposed into value-added liquid, gas, and solid fuels [35]. The PW pyrolytic liquid and gas fuels are the substitutes for diesel/gasoline and natural gas, respectively [36]. Consequently, it can be concluded that the pyrolysis of PW is an attractive technology because it can both address plastic pollution and reduce carbon emissions.

Pan et al. [9] suggested a smoldering-driven pyrolysis reactor for PW thermal decomposition using the energy generated by smoldering. The reactor consists of a smoldering chamber filled with sand and char and a pyrolysis chamber with the porous-matrix bed and PW particles. The heat generated by char smoldering is transferred to the pyrolysis chamber through the two chambers' boundary. A two-dimensional (2D) pyrolysis model coupled with a one-dimensional (1D) smoldering model was established to evaluate the reactor's performance. The modeling results suggested that the 2D pyrolysis model could successfully reveal the radial heat transfer resistance in the pyrolysis chamber, which exhibited the strong robustness of the 2D pyrolysis model. However, the boundary heat flux for the 1D smoldering model was determined by the global heat loss coefficient, which was calculated based on experimental data. The

difficulty to determine the global heat loss coefficient makes it challenging for the 1D smoldering model to conduct simulations of different reactor sizes.

To improve the robustness of the smoldering-driven pyrolysis model, this study establishes a novel 2D pyrolysis coupled with a 2D smoldering model to address the benefits of a multi-dimensional analysis compared to the 1D smoldering approach. The smoldering and pyrolysis chambers are separated by a thin layer of 2 mm stainless steel, of which the boundary heat transfer is calculated using the thermally thick approximation [37-38]. Moreover, a sensitivity analysis was conducted to investigate the effects of several parameters that can affect smoldering and pyrolysis processes. The model developed in the present study aims to provide a general design tool for the performance, evaluation, and optimization of the smoldering-driven pyrolysis reactor.

7.2. Methodology

7.2.1. Physical model

Fig. 7.1 illustrates the reactor for PW thermal decomposition driven by smoldering. The reactor consists of a pyrolysis chamber (the porous-matrix bed filled with PW particles) and a smoldering chamber (filled with sand and char). The two chambers are separated by 2 mm stainless steel to prevent oxygen in the smoldering chamber from entering the pyrolysis chamber. The reactor is heated by a cone heater for 4320 s [39] to ignite the char in the smoldering chamber. Moreover, the reactor is insulated with 0.02 m ceramic fiber to reduce heat loss to the environment [40]. The cone heater can provide a stable boundary heat flux of 25 kW/m^2. Air is introduced into the smoldering chamber with an injection velocity of 0.05 m/s

when the reactor is heated for 1020 s. The smoldering heat from the smoldering chamber can accumulate over a distance of 0.1 m and then be transported into the pyrolysis chamber via the thin stainless-steel layer. Consequently, the PW in the pyrolysis chamber is first melted and then decomposed into volatiles to spontaneously flow out of the reactor (from the top of the pyrolysis chamber) because of the produced pressure difference. It should be noted that the volatile products are collected from the pyrolysis chamber through two axisymmetric thin tubes. Their presence hardly affects the mass and heat transfer in the pyrolysis and smoldering chambers.

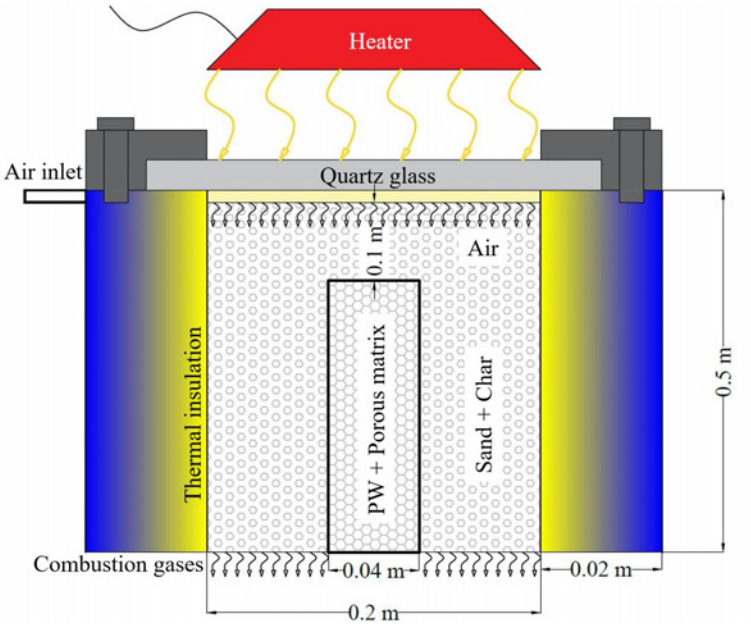

Fig. 7.1. 2D schematic diagram of the PW pyrolysis reactor driven by self-sustaining smoldering.

Table 7.1 lists a sensitivity analysis of several numerical parameters investigating the effects of char concentration (C_C), Darcy air velocity (u_g^{in}), PW content, and pyrolysis chamber's radius. The char concentration ($C_C = \frac{m_C^0}{m_{Sand}} \times 100\%$) is the ratio of the initial char mass (m_C^0) to the sand mass (m_{Sand}). It is noteworthy that the radius of the reactor is fixed at 100 mm. Thus, for instance, the smoldering chamber's radius is 70 mm when the pyrolysis

chamber's radius is set to 30 mm.

Table 7.1. Numerical model parameter settings to study the effects of different parameters.

No.	Char concentration (%)	Darcy air velocity (m/s)	PW content (-)	Pyrolysis chamber's radius (mm)
Base case				
1	3.0	0.030	0.400	20.0
Char concentration				
2	2.2	0.030	0.400	20.0
3	2.4	0.030	0.400	20.0
4	2.6	0.030	0.400	20.0
5	2.8	0.030	0.400	20.0
Darcy air velocity				
6	3.0	0.035	0.400	20.0
7	3.0	0.040	0.400	20.0
8	3.0	0.045	0.400	20.0
9	3.0	0.050	0.400	20.0
PW content				
10	3.0	0.050	0.425	20.0
11	3.0	0.050	0.450	20.0
12	3.0	0.050	0.475	20.0
13	3.0	0.050	0.500	20.0
Pyrolysis chamber's radius				
14	3.0	0.050	0.500	22.5
15	3.0	0.050	0.500	25.0
16	3.0	0.050	0.500	27.5
17	3.0	0.050	0.500	30.0

7.2.2. Reaction kinetics

The smoldering of char (*C*) follows the one-step reaction assumption [39]:

$$C + v_{O_2} O_2 \overset{R_C}{\rightarrow} gases \tag{7.1}$$

$$R_C = A_C \exp\left(-\frac{E_C}{R_g T_s}\right) Y_C Y_{O_2} \tag{7.2}$$

$$Y_C = \frac{m_C}{m_C^0} \tag{7.3}$$

$$Y_{O_2} = \frac{m_{O_2}}{m_{O_2}^0} \tag{7.4}$$

where v_{O_2}, $gases$, R_C, A_C, E_C, R_g, T_s, Y_C, m_C, m_C^0, Y_{O_2}, m_{O_2}, $m_{O_2}^0$ represent the mass stoichiometric coefficient of O_2 (1.15), flue gas (mixture of CO and CO_2), char reaction rate, pre-exponential factor, activation energy, ideal gas constant (8.314 J/mol/K), solid temperature, char mass fraction, char mass, initial char mass, O_2 mass fraction, O_2 mass, and initial O_2 mass, respectively.

PW pyrolysis products consist of C1 to C36 hydrocarbons [34]. The PW pyrolysis mechanism adopts a lumped model to describe the reaction pathway [9].

$$PW \xrightarrow{R_{PW}} v_{L_+}L_+ + v_{L_-}L_- + v_G G + v_{Res}Residue \tag{7.5}$$

$$R_{PW} = A_{PW}\exp\left(-\frac{E_{PW}}{R_g T_{PW}}\right)\rho_{PW} \tag{7.6}$$

where R_{PW}, L_+, v_{L_+}, L_-, v_{L_-}, G, v_G, $Residue$, v_{Res}, T_{PW}, and ρ_{PW} are the PW pyrolysis rate, heavy liquid (> C15), mass stoichiometric coefficient of heavy liquid (0.7206), light liquid (C5 – C15), mass stoichiometric coefficient of light liquid (0.1144), gas (C1 – C4), mass stoichiometric coefficient of gas (0.1285), solid residue, mass stoichiometric coefficient of solid residue (0.0365), PW temperature, and PW bulk density, respectively.

L_+ is further decomposed into L_- and G as follows [41-42]:

$$L_+ \xrightarrow{R_{L_+:L_-}} L_- \tag{7.7}$$

$$L_+ \xrightarrow{R_{L_+:G}} G \tag{7.8}$$

$$R_{L_+:L_-} = A_{L_-}\exp\left(-\frac{E_{L_-}}{R_g T_{PW}}\right)\rho_{L_+} \tag{7.9}$$

$$R_{L_+:G} = A_G\exp\left(-\frac{E_G}{R_g T_{PW}}\right)\rho_{L_+} \tag{7.10}$$

where $R_{L_+:L_-}$, $R_{L_+:G}$, and ρ_{L_+} represent the cracking rate of L_+ into L_-, cracking rate of L_+

into G, L_+ density, respectively. Therefore, the overall reaction rates of L_+ (R_{L_+}), L_- (R_{L_-}), and G (R_G) can be expressed as:

$$R_{L_+} = v_{L_+} R_{PW} - R_{L_+:L_-} - R_{L_+:G} \tag{7.11}$$

$$R_{L_-} = v_{L_-} R_{PW} + R_{L_+:L_-} \tag{7.12}$$

$$R_G = v_G R_{PW} + R_{L_+:G} \tag{7.13}$$

The kinetic parameters of char smoldering, PW pyrolysis, and L_+ secondary cracking reactions are summarized in Table D.1 (Supplementary Material).

7.2.3. Governing equations

Smoldering consumes char and oxygen, and produces flue gas in the air. The mass conservation equations of char and gas are given by:

$$\frac{\partial Y_C}{\partial t} = -R_C \tag{7.14}$$

$$\frac{\partial \varepsilon_{p,smo} \rho_g}{\partial t} + \nabla \cdot (\rho_g \mathbf{u}_g) = \rho_C R_C \tag{7.15}$$

where $\varepsilon_{p,smo}$ is the smoldering bed porosity, ρ_g is the gas density, ρ_C is the char bulk density, and the gas velocity $\mathbf{u}_g$ is determined by the Darcy's Law:

$$\mathbf{u}_g = -\frac{\kappa_{p,smo}}{\mu_g} \nabla p_g \tag{7.16}$$

where $\kappa_{p,smo}$, μ_g, and p_g are the smoldering bed permeability, gas dynamic viscosity, and pressure, respectively.

The oxygen transport in the smoldering chamber follows:

$$\frac{\partial}{\partial t}(\varepsilon_{p,smo} \rho_g Y_{O_2}) + \nabla \cdot (\rho_g \mathbf{u}_g Y_{O_2}) = \nabla \cdot (\varepsilon_{p,smo} \rho_g D_g \nabla Y_{O_2}) - \rho_C v_{O_2} R_C \tag{7.17}$$

where D_g is the gas diffusion coefficient.

The solid and gas energy conservation equations are given by:

$$\frac{\partial}{\partial t}(1-\varepsilon_{p,smo})(\rho_{Sand}C_{p,Sand}+Y_C\rho_C C_{p,C})T_s = \nabla\cdot(1-\varepsilon_{p,smo})(k_{Sand}+\frac{16\sigma d_{p,Sand}{T_s}^3}{3}+$$

$$Y_C C_C k_C)\nabla T_s + h_{sg}\frac{6(1-\varepsilon_{p,smo})}{d_{p,Sand}}(T_g-T_s) - \rho_C \Delta H_C R_C \quad (7.18)$$

$$\frac{\partial}{\partial t}\varepsilon_{p,smo}(\rho_g C_{p,g})T_g + \nabla\rho_g C_{p,g}\mathbf{u}_g T_g = \nabla\cdot\varepsilon_{p,smo}k_g\nabla T_g + h_{sg}\frac{6(1-\varepsilon_{p,smo})}{d_{p,Sand}}(T_s-T_g) \quad (7.19)$$

where ρ_{Sand}, $C_{p,Sand}$, k_{Sand}, $d_{p,Sand}$, $C_{p,C}$, k_C, ΔH_C, σ, T_g, $C_{p,g}$, k_g, and h_{sg} represent the sand bulk density, sand heat capacity, sand thermal conductivity, sand particle diameter, char heat capacity, char thermal conductivity, char combustion enthalpy, Stefan–Boltzmann constant (5.67×10^{-8} W/m^2/K^4), gas temperature, gas heat capacity, gas thermal conductivity, and the interfacial heat transfer coefficient. h_{sg} is calculated by an empirical correlation [39]:

$$Nu = \frac{h_{sg}d_{p,Sand}}{k_g} = 0.001(Re^{1.97}Pr^{1/3}) \quad (7.20)$$

where Nu, Re, and Pr are the Nusselt number, Reynolds number, and Prandtl number.

PW first melts (solid phase PW_s to molten phase PW_m) and then decomposes during pyrolysis. The molten PW (PW_m) is regarded as a stationary fluid due to its high viscosity [43]. The modified apparent heat capacity method (AHCM) is used to simulate the melting process of PW. The energy conservation equation during the PW melting process is given by:

$$((1-\varepsilon_{p,bed})\rho_{bed}C_{p,bed}+\varepsilon_{p,bed}\rho_{PW}^{eff}C_p^{app})\frac{\partial T_{PW}}{\partial t} = \nabla\cdot((1-\varepsilon_{p,bed})k_{bed}+\varepsilon_{p,bed}k_{PW}^{eff})\nabla T_{PW} \quad (7.21)$$

where $\varepsilon_{p,bed}$, ρ_{bed}, $C_{p,bed}$, k_{bed}, ρ_{PW}^{eff}, C_p^{app}, and k_{PW}^{eff} are the porosity of porous-matrix bed, porous-matrix density, porous-matrix heat capacity, porous-matrix thermal conductivity, effective PW density, effective PW heat capacity, and effective PW thermal conductivity, respectively. ρ_{PW}^{eff}, C_p^{app}, and k_{PW}^{eff} follow:

$$\rho_{PW}^{eff} = \theta(T_{PW})\rho_{PW_s} + (1 - \theta(T_{PW}))\rho_{PW_m} \tag{7.22}$$

$$C_p^{app} = \frac{1}{\rho_{PW}^{eff}}\left(\theta(T_{PW})\rho_{PW_s}C_{p,PW_s} + \left(1 - \theta(T_{PW})\right)\rho_{PW_m}C_{p,PW_m}\right) + \Delta H_{pc}\frac{d\alpha_m}{dT_{PW}} \tag{7.23}$$

$$\alpha_m = -\frac{1}{2}\frac{\theta(T)\rho_{PW_s} - \left(1-\theta(T)\right)\rho_{PW_m}}{\theta(T)\rho_{PW_s} + \left(1-\theta(T)\right)\rho_{PW_m}} \tag{7.24}$$

$$k_{PW}^{eff} = \theta(T_{PW})k_{PW_s} + (1 - \theta(T_{PW}))k_{PW_m} \tag{7.25}$$

where $\theta(T_{PW})$, ρ_{PW_s}, C_{p,PW_s}, k_{PW_s}, ρ_{PW_m}, C_{p,PW_m}, k_{PW_m}, ΔH_{pc}, and α_m represent the Heaviside step function, solid PW density, solid PW heat capacity, solid PW thermal conductivity, molten PW density, molten PW heat capacity, molten PW thermal conductivity, phase change enthalpy, and phase transition.

The molten PW is then decomposed into volatiles (L_+, L_-, and G):

$$\frac{\partial}{\partial t}\rho_{PW_m} = -R_{PW} \tag{7.26}$$

The fluid (volatiles) continuity equation is given by:

$$\frac{\partial}{\partial t}\varepsilon_{p,py}\rho_f + \nabla \cdot \rho_f \mathbf{u}_f = R_{L_+} + R_{L_-} + R_G \tag{7.27}$$

where the porosity of smoldering bed $\varepsilon_{p,py} = \varepsilon_{p,bed} - \left(\varepsilon_{p,bed} - \varepsilon_{p,py}^0\right)\frac{\rho_{PW_m}}{\rho_{PW}^0}$, the fluid density obeys the ideal gas law, and the fluid velocity $\mathbf{u}_f$ is determined by:

$$\mathbf{u}_f = -\frac{\kappa_{p,py}}{\mu_f}(\nabla p_f - \rho_f \boldsymbol{g_a}) \tag{7.28}$$

where p_f, μ_f, $\boldsymbol{g_a}$, and $\kappa_{p,py}$ are the pressure, fluid dynamic viscosity, gravitational acceleration, and permeability of the smoldering bed, respectively. $\kappa_{p,py}$ is calculated by:

$$\kappa_{p,py} = \frac{r_c^2\varepsilon_{p,py}^3}{180\left(1-\varepsilon_{p,py}\right)^2} \tag{7.29}$$

where r_c is the porous-matrix equivalent radius.

The transport equation of volatiles (f_i) is given by:

$$\frac{\partial}{\partial t}\left(\varepsilon_{p,py}\rho_{f_i}\right) + \nabla\cdot\left(\rho_{f_i}\mathbf{u}_f\right) = \nabla\cdot\left(\varepsilon_{p,py}D_{f_i}\nabla\rho_{f_i}\right) + R_{f_i} \quad (7.30)$$

where f_i represents L_+, L_-, and G.

The energy conservation equation writes:

$$\frac{\partial}{\partial t}(\rho C_p)_{py}^{eff}T_{PW} + \nabla\cdot(\rho C_p)_{py}^{eff}\mathbf{u}_f T_{PW} = \nabla\cdot k_{py}^{eff}\nabla T_{PW} - R_{PW}\Delta H_{PW} - R_{L_+:L_-}\Delta H_{L_-} - \\ -R_{L_+:G}\Delta H_G \quad (7.31)$$

where ΔH_{PW}, ΔH_{L_-}, ΔH_G, $(\rho C_p)_{py}^{eff}$, k_{py}^{eff} are the PW pyrolysis enthalpy, L_- formation enthalpy (from L_+), G formation enthalpy (from L_+), the effective volumetric heat capacity, and the effective thermal conductivity, respectively. $(\rho C_p)_{py}^{eff}$ and k_{py}^{eff} are calculated by:

$$(\rho C_p)_{py}^{eff} = \left(1-\varepsilon_{p,bed}\right)\rho_{bed}C_{p,bed} + \left(\varepsilon_{p,bed}-\varepsilon_{p,py}\right)\rho_{PW_m}C_{p,PW_m} + \varepsilon_{p,py}\rho_f C_{p,f} \quad (7.32)$$

$$k_{py}^{eff} = \left(1-\varepsilon_{p,bed}\right)k_{bed} + \left(\varepsilon_{p,bed}-\varepsilon_{p,py}\right)k_{PW_m} + \varepsilon_{p,py}k_f \quad (7.33)$$

where $C_{p,f}$ and k_f are the fluid heat capacity and fluid thermal conductivity.

7.2.4. Boundary conditions

The heat exchanges between the smoldering and pyrolysis chambers are calculated by the thermally thick approximation [37-38]:

$$-\mathbf{n}_{smo}\cdot\mathbf{q}_{smo} = -\frac{1}{2}d_{ss}\rho_{ss}C_{p,ss}\frac{\partial T_s}{\partial t} - \frac{T_{PW}-T_s}{d_{ss}/k_{ss}} \quad (7.34)$$

$$-\mathbf{n}_{py}\cdot\mathbf{q}_{py} = -\frac{1}{2}d_{ss}\rho_{ss}C_{p,ss}\frac{\partial T_{PW}}{\partial t} - \frac{T_s-T_{PW}}{d_{ss}/k_{ss}} \quad (7.35)$$

where $\mathbf{q}_{smo}$, $\mathbf{q}_{py}$, d_{ss}, ρ_{ss}, $C_{p,ss}$, and k_{ss} are the smoldering chamber received heat, pyrolysis chamber received heat, stainless-steel thickness (two chamber's boundary), stainless-steel density, stainless-steel heat capacity, and stainless-steel thermal conductivity, respectively.

The reactor is insulated with ceramic fiber [40] to reduce heat loss to the environment. The heat loss to the environment is calculated by:

$$-\mathbf{n}_{smo}\cdot\mathbf{q}_{smo}=-\frac{1}{2}d_{ins}\rho_{ins}C_{p,ins}\frac{\partial T_s}{\partial t}-\frac{T_\infty-T_s}{d_{ins}/k_{ins}} \tag{7.36}$$

where d_{ins}, ρ_{ins}, $C_{p,ins}$, and k_{ins}, and T_∞ are the ceramic fiber thickness, ceramic fiber density, ceramic fiber heat capacity, ceramic fiber thermal conductivity, and environment temperature (20 °C), respectively.

Other initial and boundary conditions are presented in Table 7.2.

Table 7.2. Initial and boundary conditions of smoldering and pyrolysis models.

Initial Condition	Boundary Condition
Smoldering model	
t=0s: $Y_C=1$	-
t=0s: $p_g=101375$ Pa	*z*=0.00m: $\begin{cases} t=(0,1020\text{s}): u_g=0 \\ t=(1020\text{s},30000\text{s}): u_g=u_g^{in} \end{cases}$
	z=0.50m: $p_g=101375$ Pa
t=0s: $Y_{O_2}=0.204$	*z*=0.00m: $Y_{O_2}=0.204$
	z=0.50m: $-\varepsilon_{p,smo}D_g\frac{\partial}{\partial z}(\rho_g Y_{O_2})=0$
t=0s: $T_s=20$ ℃	*z*=0.00m: $\begin{cases} t=(0,4320\text{s}): -k_{smo}^{eff}\nabla T_s=25\ \text{kW/m}^2 \\ t=(4320\text{s},30000\text{s}): -k_{smo}^{eff}\nabla T_s=0 \end{cases}$
	z=0.50m: $-k_{smo}^{eff}\nabla T_s=0$
t=0s: $T_g=20$ ℃	*z*=0.00m: $T_g=20$ ℃
	z=0.50m: $-k_g\nabla T_g=0$
Pyrolysis model	
t=0s: $\rho_{PW}=380\ \text{kg/m}^3$	-
t=0s: $\rho_{f_i}=0\ \text{kg/m}^3$	*r*=0.00m&0.02m: $-\mathbf{n}_{py}\cdot(-D_{f_i}\nabla\rho_{f_i}+\mathbf{u}_f\rho_{f_i})=0$
t=0s: $\varepsilon_{p,py}=0$	-
t=0s: $\begin{cases} \mathbf{u}_f=0\ \text{m/s} \\ p_f=101375\ \text{Pa} \end{cases}$	*z*=0.10m: $p_f=101375$ Pa
	z=0.50m: $\mathbf{u}_f=0$ m/s
	r=0.00m: $\mathbf{u}_f\cdot\mathbf{n}_{py}=0$ m/s
	r=0.02m: $\mathbf{u}_f=0$ m/s
t=0s: $T_{PW}=20$ ℃	*r*=0.00m: $k_{py}^{eff}\nabla T_{PW}=0$

7.3. Results and discussion

7.3.1. Model validation

Fig. 7.2 shows the comparison between the simulated and experimental results. The char concentration and Darcy air velocity are 2.0 % and 0.05 m/s. Other specific parameters can be found in [39]. The findings reveal that the smoldering can self-sustained spread with a stable peak temperature and velocity. The experimental peak temperature and propagating velocity are 631 °C and 3.39 mm/min (Fig. 7.2a). The simulated peak temperature (662 °C) and propagating velocity (3.15 mm/min) have high accuracy with 4.9 % and 6.9 % errors, respectively. Moreover, the simulated pressure is in good agreement with the experimental value, with a 12.5% error (Fig. 7.2b).

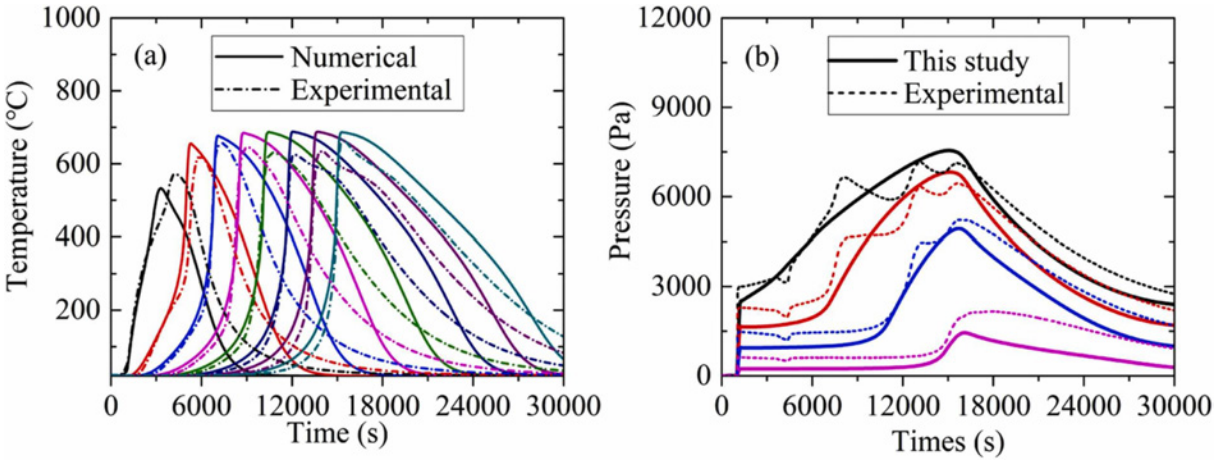

Fig. 7.2. Comparison of experimental and simulated results: (a) T_S at 0.04–0.67 m with 0.09 m intervals; (b) p_g at 0.03–0.66 m with 0.21 m intervals.

7.3.2. Reactor performance evaluation

Fig. 7.3 shows that the smoldering of char (Fig. 7.3a) consumed ~0.083 O_2 (0.204 – 0.121, Fig. 3b). The smoldering front is a thin layer with a thickness of ~0.030 m (Fig. 7.3c). The thin front generates intense heat, of which the peak value is 1.335×10^7 W/m^3 (Fig. 7.3d). Consequently, as depicted in Fig. 7.3e, the peak temperature in the smoldering chamber can reach up to 773 °C due to the intensive smoldering heat generation. It can also be observed that

the temperature in the pyrolysis chamber is lower than the one in the smoldering chamber.

Fig. 7.3f demonstrates the temperature profiles at the smoldering chamber's centerline (T_S), the pyrolysis chamber's centerline (T_{PW}), and the boundary between the two chambers (T_{bound}). The maximum temperature difference between T_S and T_{bound} is ~350 °C at the smoldering front. The heat generated in the smoldering chamber is transferred to the environment and the pyrolysis chamber via the boundaries. Sand with low thermal conductivity slows the heat transfer from the center to the boundary, leading to the significant temperature difference between T_S and T_{bound} in the smoldering chamber. It is noteworthy that there is a relatively noticeable temperature difference between T_{bound} and T_{PW} (~30 °C) in the 0.15 m wide area, which is attributed to the endothermic PW melting and pyrolysis processes. Moreover, Fig. 7.3g reveals that the rapidly rising T_S is due to the local smoldering released in a narrow region (~0.03 m), while the gently increasing T_{PW} is ascribed to the widely distributed (~0.3 m) boundary heat flux.

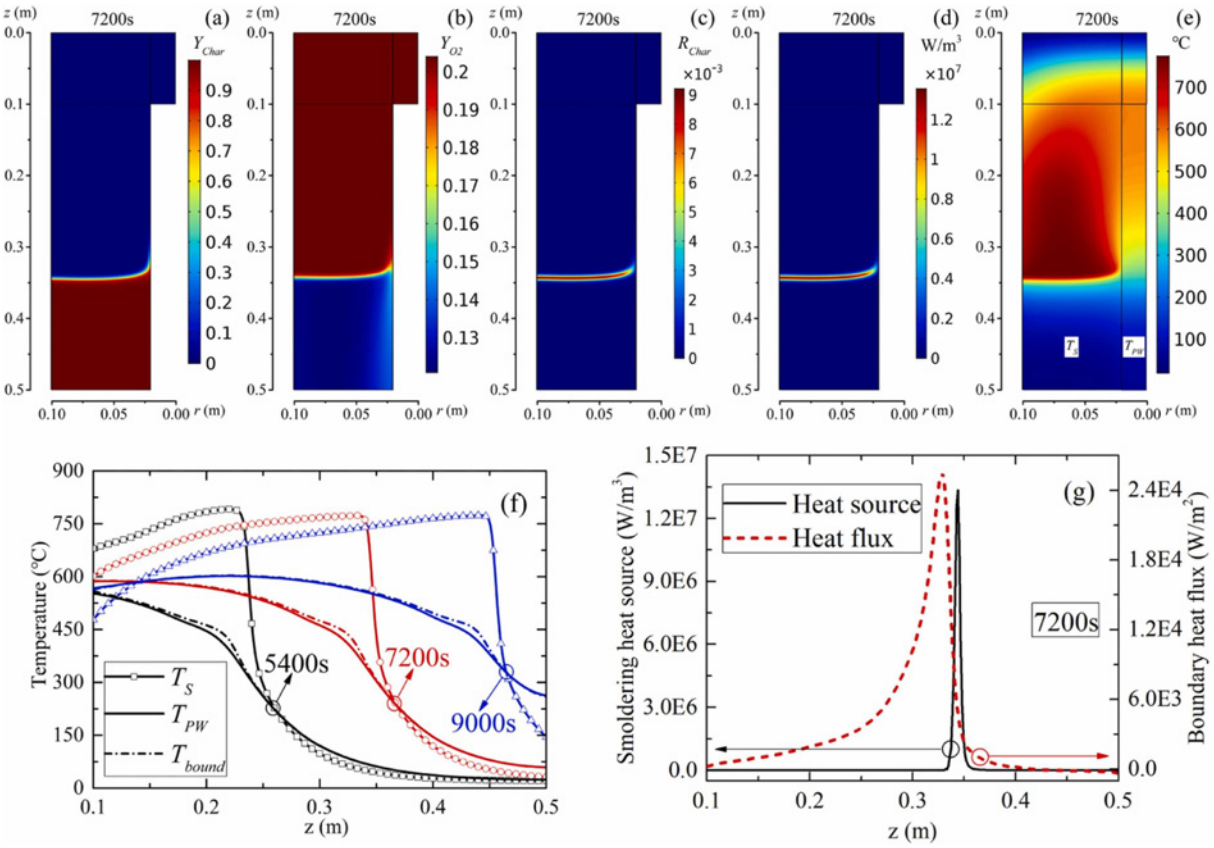

Fig. 7.3. Reactor performance evaluation: (a) Y_{Char}; (b) Y_{O2}; (c) R_{Char}; (d) Smoldering heat source; (e) T_{PW} and T_S; (f) T_{PW} (at r=0.01 m), T_{bound} (at r=0.02 m) , and T_S (at r=0.06 m) profiles; (g) Smoldering heat source (at r=0.06 m) and boundary heat flux (at r=0.02 m).

Fig. 7.4 demonstrates the mechanism of spontaneous efflux of volatile products from the pyrolysis chamber. PW has been decomposed into volatiles (G, L_-, and L_+), increasing the permeability of the bed (Fig. 7.4a). The produced volatiles create a pressure differential (Fig. 7.4b), resulting in a velocity field in the smoldering chamber (Fig. 7.4c). Accordingly, L_+ (Fig. 7.4d), L_- (Fig. 7.4e), and G (Fig. 7.4f) can spontaneously flow out of the smoldering chamber.

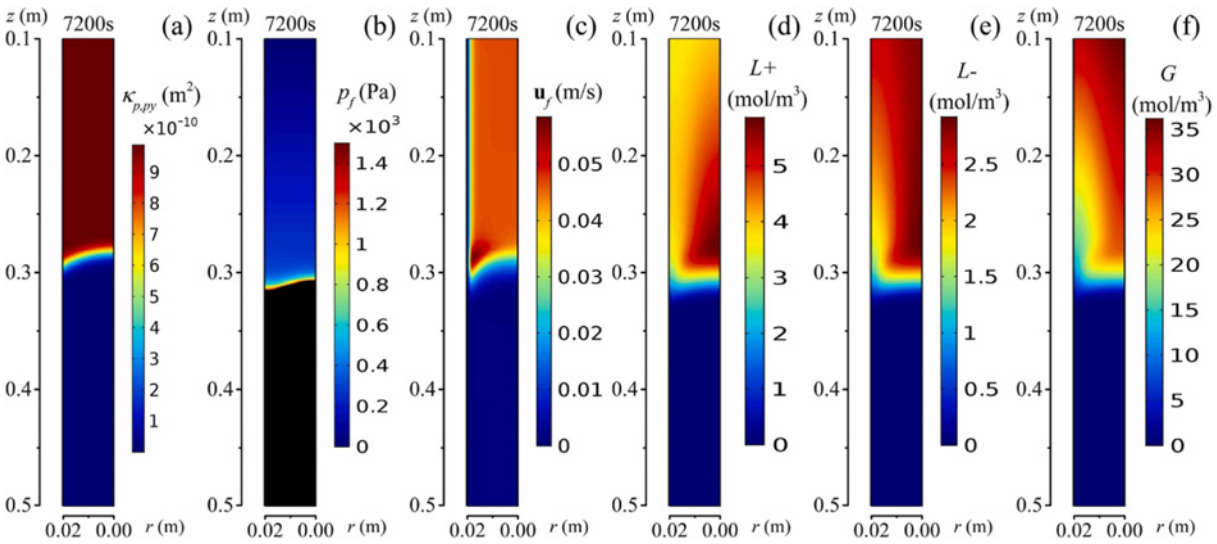

Fig. 7.4. Mechanism of spontaneous efflux of volatile products from the pyrolysis chamber: (a) $\kappa_{p,py}$; (b) p_f; (c) $\mathbf{u}_f$; (d) L_+; (e) L_-; (f) G.

Fig. 7.5a suggests that the temperature can propagate downwards in the pyrolysis chamber. Slowly increasing temperature creates a pyrolysis front with a height of 0.6 m (Fig. 7.5b). Fig. 7.5c intuitively shows the processes of PW pyrolysis. When the temperature exceeds 120 °C, the solid PW (black area) begins to melt. The molten PW (red area) is decomposed into volatiles (blue area) at temperatures above 430 °C, leading the bed porosity in the pyrolysis chamber to increase to 0.4 (Fig. 7.5d). Fig. 7.5e reveals that the real-time L_+ fraction decreases, and L_- and G fractions increase due to the increment in T_{PW} (Fig. 7.3f). The final cumulative G, L_-, and L_+ yields are 33.2 wt%, 15.3 wt%, and 47.8 wt%, respectively (Fig. 7.5f).

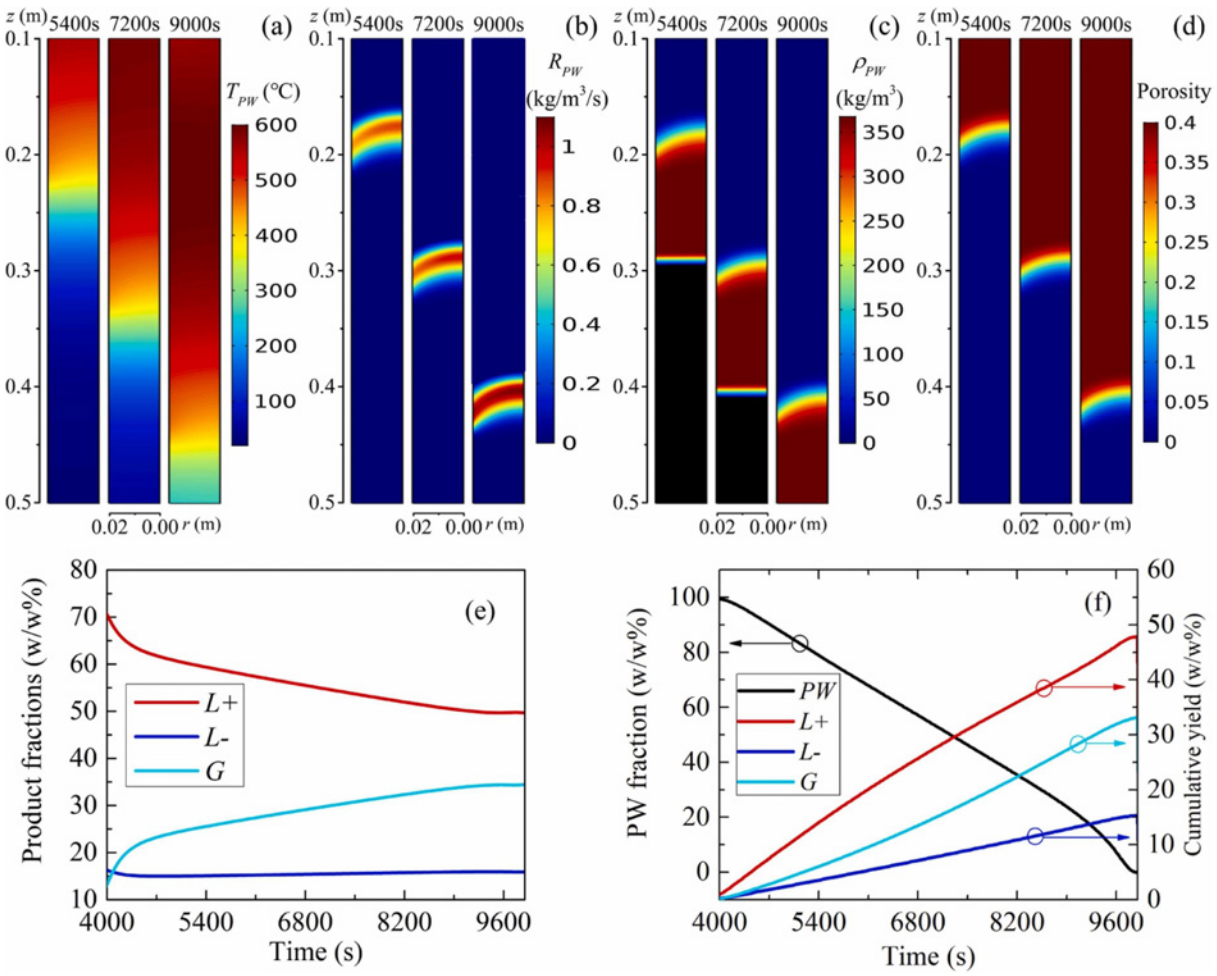

Fig. 7.5. Numerical calculated (a) T_{PW}, (b) R_{PW}, (c) PW density, (d) pyrolysis bed porosity, (e) product fractions, and (f) cumulative product yields and PW mass fraction.

Fig. 7.6 exhibits the comparison between simulated and experimental PW pyrolytic liquid, gas, and residue yields. The experiments were conducted at 500 °C [44-45], and the average T_{PW} in the pyrolysis zone was 469 °C in the present study. However, the simulated volatiles (liquid and gas) yields agreed well with the experimental values, with a 2.4 % error. Although the temperature of the pyrolysis zone was lower than 500 °C, the peak temperature of the pyrolysis chamber was above 500 °C (Fig. 7.3f). L_+ underwent more intense secondary cracking, resulting in product yields similar to those in [44-45].

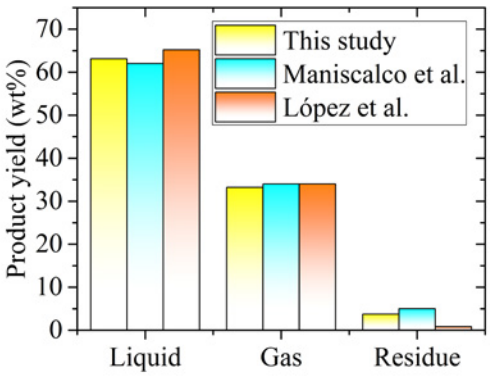

Fig. 7.6. Comparison between experimental and simulated product yields.

7.3.3. Char concentration

Fig. 7.7a illustrates that the peak T_S increases by 59 °C (715–774 °C) when the char concentration rises in the studied range. The increased char concentration can significantly enhance the average peak T_{PW} (T_{PW}^{p}) from 487 °C to 583 °C (Fig. 7.7b). The increased T_S enhances the boundary heat power (Fig. D.1a) and heat input (Fig. D.1c), which is not surprising due to the more smoldering heat released at higher char concentrations. The increment in T_{PW}^{p} is attributed to the higher heat input into the pyrolysis chamber. Fig. 7.7a also demonstrates that the smoldering front has been pushed forward 0.09 m as the char concentration increases. Consequently, the smoldering duration shortens by 2280 s (11970–9690 s, Fig. D.1b), contributing to a shorter pyrolysis duration (12900–9900 s, Fig. 7.7b).

Fig. 7.7c shows that the increased char concentration within the range of 2.2–2.8 % increases L_+ yield and decreases *G* yield, further raising the char concentration to 3.0 % reduces L_+ yield and enhances *G* yield. Higher char concentrations result in the risen temperature in the pyrolysis chamber, which affects the PW thermal decomposition via two

aspects: (i) increasing the PW pyrolysis rate and accelerating the generation rate of volatiles, causing the velocity to increase from 0.037 m/s to 0.047 m/s (Fig. D.1d) and resulting in a shorter produced volatiles' residence time in the pyrolysis chamber; (ii) increasing the L_+ secondary pyrolysis rate [42]. Based on the simulation results, it can be concluded that the shorter residence time of volatiles dominates the product yields when the char concentration increases within the range of 2.2–2.8 %. L_+ is quickly purged out of the pyrolysis chamber to suppress secondary cracking, leading to a higher L_+ yield and a lower *G* yield. However, the increased temperature plays a dominant role in the L_+ secondary cracking as the char concentration increases from 2.8 % to 3.0 %, causing the L_+ yield to decrease by 0.23 wt% (48.06–47.83 wt%) and the *G* yield to increase by 0.45 wt% (32.75–33.20 wt%). Moreover, the L_- yield is more sensitive to changes in the residence time, leading to a decrease of 0.85 wt% when the char concentration increases in the studied range.

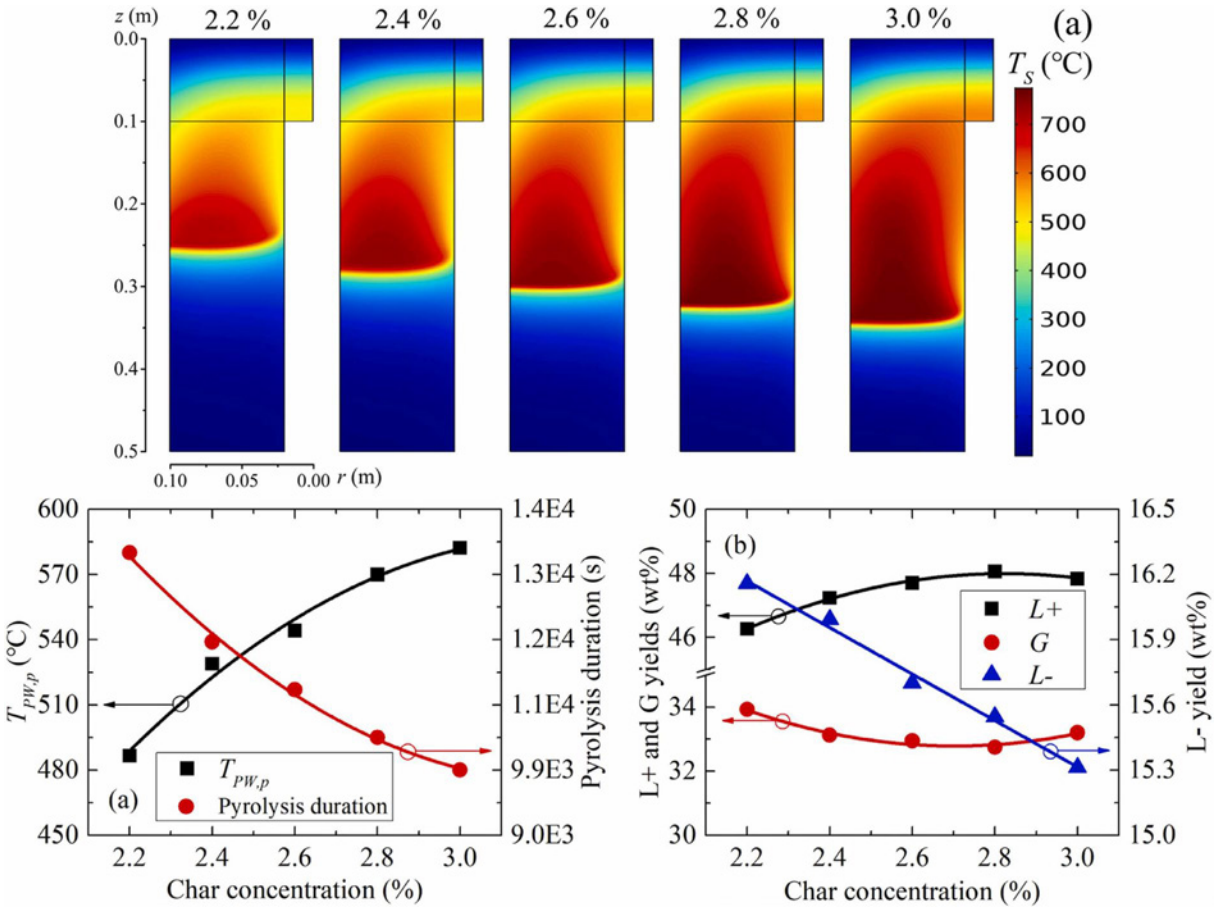

Fig. 7.7. Effect of char concentration on (a) the T_S distribution at t=7200 s in the smoldering chamber, (b) average T_{PW}^{p} and pyrolysis duration, and (c) L_+, L_+, and G yields.

7.3.4. Darcy air velocity

Fig. 7.8a illustrates that the average T_{PW}^{p} is not sensitive to changes in Darcy air velocity, which hovers within 580–586 °C. It is noteworthy that the peak T_S increases from 793 °C at 0.03 m/s to 829 °C at 0.05 m/s (Fig. D.2a) due to the enhanced reaction intensity caused by the increased oxygen flux [7]. The increment in peak T_S increases the boundary heat power from the smoldering chamber to the pyrolysis chamber (Fig. D.2b). However, the boundary heat input into the pyrolysis chamber is hardly affected by the Darcy air velocity (~1000 kJ, Fig. D.2d), resulting in a stabilized average T_{PW}^{p} (Fig. 7.8a). On the other hand, the smoldering duration decreases with the increasing Darcy air velocity (Fig. D.2c), which is attributed to the higher

smoldering propagation velocity. Moreover, the pyrolysis duration is significantly shortened by 2040 s (9900–7860 s, Fig. 7.8a) due to the enhanced smoldering propagation velocity.

Fig. 7.8b reveals that the increase in Darcy air velocity increases L_+ yield and decreases *G* and L_- yields. Higher Darcy air velocities increase the spontaneously generated velocity from 0.049 m/s to 0.067 m/s (Fig. D.2e) because of the enhanced pyrolytic volatiles formation rate in the pyrolysis chamber. Accordingly, the L_+ secondary decomposition is suppressed because of the shorter residence time in the pyrolysis chamber. As the Darcy air velocity increases in the studied range, the L_+ yield increases by 3.39 wt% (47.89–51.28 wt%), and the *G* and L_- yields decrease by 0.37 wt% (15.31–14.94 wt%) and 3.02 wt% (33.15–30.13 wt%), respectively.

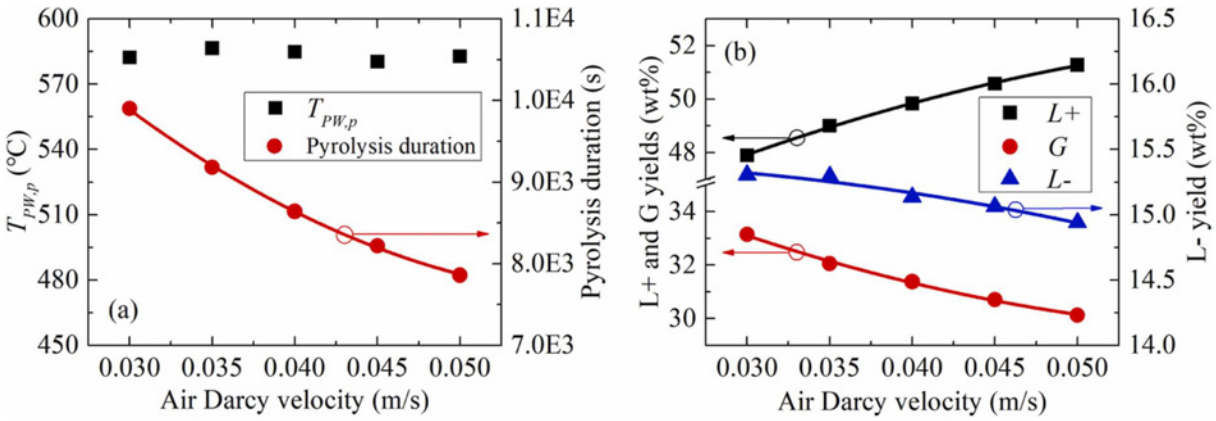

Fig. 7.8. Effect of Darcy air velocity on (a) average T_{PW}^{p} and pyrolysis duration, and (b) L_+, L_+, and G yields.

7.3.5. PW content

Fig. 7.9a demonstrates that the average T_{PW}^{p} hovered within a narrow range of 582–587 °C. Moreover, the PW content hardly affects the peak T_S, which is stabilized at 830 °C (±3 °C, Fig. D.3a). The boundary heat power (Fig. D.3b) and heat input into the pyrolysis chamber (Fig.

D.3d) remain virtually unchanged at different PW contents, resulting in insignificant changes in the average T_{PW}^{p} in the pyrolysis chamber. Although the smoldering duration is practically constant (~7500 s, Fig. D.3c), the pyrolysis duration is prolonged because of the increased thermal resistance in the pyrolysis chamber at higher PW contents (Fig. 7.9a).

Fig. 7.9b shows that the increased PW content enhances L_+ yield and reduces *G* and L_- yields. The velocity increases from 0.067 m/s to 0.082 m/s (Fig. D.3e) at higher PW contents due to the enhanced pyrolytic volatiles generation rate in the pyrolysis chamber. Higher velocities shorten the volatiles' residence time in the reaction zone, thus depressing L_+ to decompose into *G* and L_-, increasing the L_+ yield and decreasing the *G* and L_- yields. However, it is worth noting that the amount of valorized PW increases from 0.191 kg (at PW content of 0.4) to 0.239 kg (at PW content of 0.5), indicating that higher economic benefits are obtained [9]. Therefore, it can be concluded that higher PW contents are favorable for the waste valorization driven by smoldering.

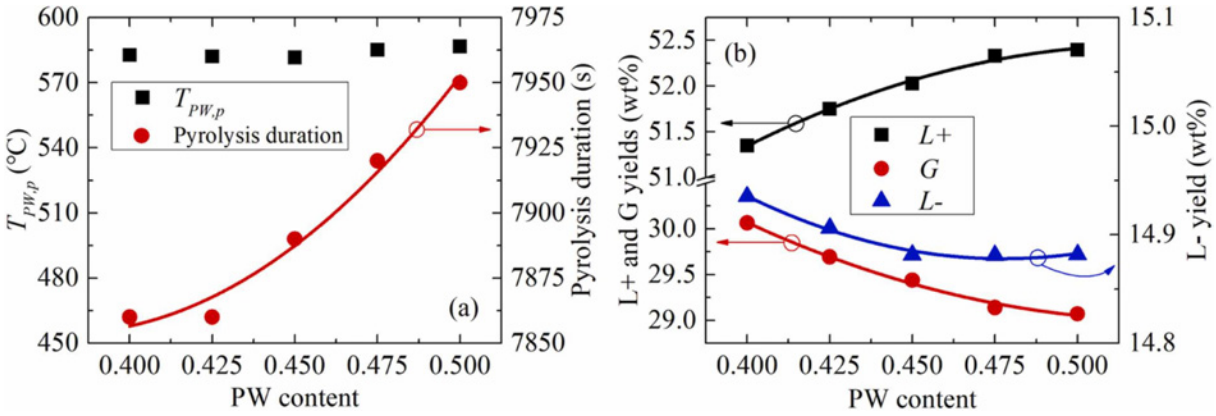

Fig. 7.9. Effect of PW content on (a) average T_{PW}^{p} and pyrolysis duration, and (b) L_+, L_+, and G yields.

7.3.6. Pyrolysis chamber's radius

As depicted in Fig. 7.10a, the increased pyrolysis chamber's radius leads to a lower T_{PW}^{p}

and a longer pyrolysis duration, ascribed to the more heat expenditure and the increased bed thermal resistance of the pyrolysis chamber. It should be noted that the thickness of the smoldering chamber decreases with the increasing pyrolysis chamber's radius due to the overall size of the reactor remaining the same. Fig. D.4a demonstrates that the peak T_S fluctuates within the range of 795–829 °C when the pyrolysis chamber's radius increases from 20.0 mm to 30.0 mm. The local (smoldering front) velocity increases from 0.21 m/s to 0.24 m/s because of the narrower channel in the smoldering chamber (Fig. D.4b). As discussed in Section 7.3.4, higher air velocities are conducive to increasing T_S and shortening the smoldering duration (Fig. D.4d). On the other hand, the boundary heat power (Fig. D.4c) and heat output (Fig. D.4e) from the smoldering chamber increase at higher pyrolysis chamber's radiuses, which are unfavorable to the increment in T_S because of the energy conservation in the smoldering chamber. Given the complex effects of the pyrolysis chamber's radius changes, T_S first decreases from 829 °C at 20.0 mm to 795 °C at 27.5 mm, then increases to 804 °C at 20.0 mm (Fig. D.4a).

The reduced temperature in the smoldering chamber decreases the PW pyrolysis rate, further resulting in a lower velocity (0.082–0.072 m/s, Fig. D.4f) and a prolonged residence time of the pyrolytic volatiles. Therefore, the L_+ yield dramatically decreases by 11.82 wt% (52.40–40.58 wt%), and the L_- and G yields increase by 2.38 wt% (14.88–17.26 wt%) and 9.44 wt% (29.07–38.51 wt%) due to the intensified L_+ secondary cracking (Fig. 7.10b). It should be noted that the PW processing capacity of the reactor has been enhanced by 2.25 times, of which the valorized PW increases from 0.239 kg to 0.537 kg when the pyrolysis chamber's radius increases in the studied range.

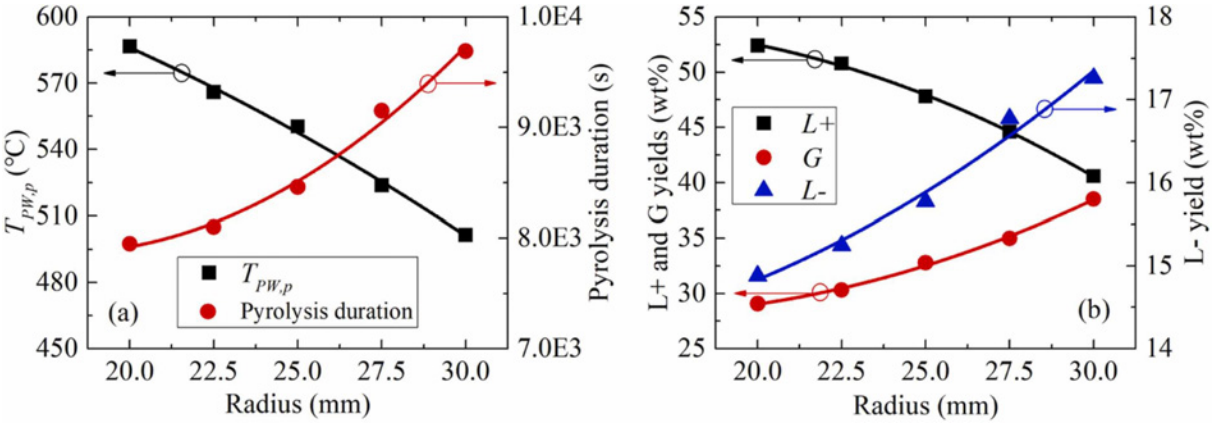

Fig. 7.10. Effect of pyrolysis chamber's radius on (a) average T_{PW}^{p} and pyrolysis duration, and (b) L_{+}, L_{+}, and G yields.

7.4. Conclusions

This study investigated a novel multi-dimensional numerical model approach for a self-sustaining smoldering driven pyrolysis process. Pyrolysis and self-sustaining smoldering are promising methods for waste valorization and contaminated sand/soil remediation. It was the first attempt to establish a robust multi-dimensional model that combines the pyrolysis of plastic waste (PW) driven by self-sustaining smoldering in 2D. The developed model provided a robust tool to guide the design, performance evaluation, and optimization of the smoldering-driven pyrolysis reactor.

Higher char concentrations led to a higher temperature and propagation velocity. The increased temperature enhanced the L_{+} secondary cracking rate (conducive to G and L_{-} yields) and shortened the volatiles' residence time (conducive to L_{+} yield) in the pyrolysis chamber. The findings revealed that the shorter volatiles' residence time dominated the product yields within the range of 2.2–2.8 %. However, the increased temperature played a dominant role as the char concentration raised from 2.8 % to 3.0 %.

Higher Darcy air velocities significantly shortened the pyrolysis duration. The increased Darcy air velocity could decrease *G* and L_- yield and increase L_+ yield.

The increased PW content led to a shorter volatiles' residence time in the reaction zone, thus decreasing the *G* and L_- yields and increasing the L_+ yield. The increase in PW content could enhance the amount of valorized PW and obtain higher economic benefits, which was favorable for the waste valorization driven by smoldering.

Increasing the pyrolysis chamber's radius decreased the temperature (still higher than PW pyrolysis temperature) and prolonged the volatiles' residence time in the pyrolysis chamber. The intensified L_+ secondary decomposition led to an increase in *G* (9.44 wt%) and L_- (2.38 wt%) yields and a dramatic decrease (11.82 wt%) in L_+ yield. Moreover, the PW processing capacity of the reactor was enhanced by 2.25 times when the pyrolysis chamber's radius increased in the studied range.

Bibliography

[1] Zanoni, M.A., Torero, J.L. and Gerhard, J.I., 2019. Delineating and explaining the limits of self-sustained smouldering combustion. Combustion and Flame, 201, pp.78-92.

[2] Switzer, C., Pironi, P., Gerhard, J.I., Rein, G. and Torero, J.L., 2009. Self-sustaining smoldering combustion: a novel remediation process for non-aqueous-phase liquids in porous media. Environmental Science & Technology, 43(15), pp.5871-5877.

[3] Anderson, T.I. and Kovscek, A.R., 2022. Analysis and comparison of in-situ combustion chemical reaction models. Fuel, 311, p.122599.

[4] Duchesne, A.L., Brown, J.K., Patch, D.J., Major, D., Weber, K.P. and Gerhard, J.I., 2020. Remediation of PFAS-contaminated soil and granular activated carbon by smoldering combustion. Environmental Science & Technology, 54(19), pp.12631-12640.

[5] Longendyke, G. Katel, S., and Wang, Y., 2022. PFAS fate and destruction mechanisms during thermal treatment: a comprehensive review. Environmental Science: Processes & Impacts.

[6] Fournie, T., Rashwan, T.L., Switzer, C. and Gerhard, J.I., 2022. Phosphorus recovery and reuse potential from smouldered sewage sludge ash. Waste Management, 137, pp.241-252.

[7] Gan, Z., Zhao, C., Li, Y., Chen, G., Song, Z., Zhang, Z. and Ran, W., 2022. Experimental investigation on smoldering combustion for oil sludge treatment: Influence of key parameters and product analysis. Fuel, 316, p.123354.

[8] Cheng, S., Zhang, H., Chang, F., Zhang, F., Wang, K., Qin, Y. and Huang, T., 2019. Combustion behavior and thermochemical treatment scheme analysis of oil sludges and oil

sludge semicokes. Energy, 167, pp.575-587.

[9] Pan, R. and Debenest, G., 2022. Numerical investigation of a novel smoldering-driven reactor for plastic waste pyrolysis. Energy Conversion and Management, 257, p.115439.

[10] Tang, Y. and Huang, W., 2022. Experimental and theoretical study of the effect of particle size on the forward propagation of smoldering coal. Fuel, 312, p.122903.

[11] Christensen, E.G., Fernandez-Anez, N. and Rein, G., 2020. Influence of soil conditions on the multidimensional spread of smouldering combustion in shallow layers. Combustion and Flame, 214, pp.361-370.

[12] Amin, H.M., Hu, Y. and Rein, G., 2020. Spatially resolved horizontal spread in smouldering peat combining infrared and visual diagnostics. Combustion and Flame, 220, pp.328-336.

[13] Chen, W., Lei, Y., Ma, L. and Yang, L., 2017. Experimental study of high temperature combustion for enhanced shale gas recovery. Energy & Fuels, 31(9), pp.10003-10010.

[14] Song, Z., He, T., Li, M., Wu, D. and You, F., 2022. Self-sustaining smoldering as a novel disposal approach for food waste with high moisture content. Fuel Processing Technology, 228, p.107144.

[15] Sennoune, M., Salvador, S. and Quintard, M., 2011. Reducing CO2 emissions from oil shale semicoke smoldering combustion by varying the carbonate and fixed carbon contents. Combustion and flame, 158(11), pp.2272-2282.

[16] Sennoune, M., Salvador, S. and Quintard, M., 2012. Toward the control of the smoldering front in the reaction-trailing mode in oil shale semicoke porous media. Energy & fuels,

26(6), pp.3357-3367.

[17] Raja, M.A., Chen, H., Zhao, Y., Zhang, X. and Zhang, S., 2017. Process simulation and assessment of hydrogen and high valued hydrocarbon fuels products from oil shale. International Journal of Hydrogen Energy, 42(8), pp.4922-4934.

[18] Wyn, H.K., Konarova, M., Beltramini, J., Perkins, G. and Yermán, L., 2020. Self-sustaining smouldering combustion of waste: A review on applications, key parameters and potential resource recovery. Fuel Processing Technology, 205, p.106425.

[19] Wyn, H.K., Konarova, M., Perkins, G. and Yermán, L., 2021. Fuel Gas Production From Self-Sustaining Smouldering Combustion of Lignocellulosic Waste.

[20] Yan, S., Yin, D., He, F., Cai, J., Schliermann, T. and Behrendt, F., 2022. Characteristics of Smoldering on Moist Rice Husk for Silica Production. Sustainability, 14(1), p.317. https://doi.org/10.3390/su14010317

[21] Zanoni, M.A., Torero, J.L. and Gerhard, J.I., 2020. Experimental and numerical investigation of weak, self-sustained conditions in engineered smouldering combustion. Combustion and Flame, 222, pp.27-35.

[22] Lin, S., Chow, T.H. and Huang, X., 2021. Smoldering propagation and blow-off on consolidated fuel under external airflow. Combustion and Flame, 234, p.111685.

[23] Yermán, L., Wall, H. and Torero, J.L., 2017. Experimental investigation on the destruction rates of organic waste with high moisture content by means of self-sustained smoldering combustion. Proceedings of the Combustion Institute, 36(3), pp.4419-4426.

[24] Song, Z., Huang, X., Jiang, J. and Pan, X., 2020. A laboratory approach to CO2 and CO

emission factors from underground coal fires. International Journal of Coal Geology, 219, p.103382.

[25] Lin, S., Yuan, H. and Huang, X., 2022. A computational study on the quenching and near-limit propagation of smoldering combustion. Combustion and Flame, 238, p.111937.

[26] Duque, J.V.F., Martins, M.F., Bittencourt, F.L. and Debenest, G., 2022. Relevant aspects of propagating a combustion front in an annular reactor for out-of-bed heat recovery. Experimental Thermal and Fluid Science, 133, p.110575.

[27] Hasan, T., Gerhard, J.I., Hadden, R. and Rein, G., 2015. Self-sustaining smouldering combustion of coal tar for the remediation of contaminated sand: Two-dimensional experiments and computational simulations. Fuel, 150, pp.288-297.

[28] Rashwan, T.L., Torero, J.L. and Gerhard, J.I., 2021. The improved energy efficiency of applied smouldering systems with increasing scale. International Journal of Heat and Mass Transfer, 177, p.121548.

[29] Lin, S. and Huang, X., 2021. Quenching of smoldering: effect of wall cooling on extinction. Proceedings of the Combustion Institute, 38(3), pp.5015-5022.

[30] Rashwan, T.L., Torero, J.L. and Gerhard, J.I., 2021. Heat losses in a smouldering system: The key role of non-uniform air flux. Combustion and Flame, 227, pp.309-321.

[31] Rashwan, T.L., Torero, J.L. and Gerhard, J.I., 2021. Heat losses in applied smouldering systems: Sensitivity analysis via analytical modelling. International Journal of Heat and Mass Transfer, 172, p.121150.

[32] Torero, J.L., Gerhard, J.I., Martins, M.F., Zanoni, M.A., Rashwan, T.L. and Brown, J.K.,

2020. Processes defining smouldering combustion: Integrated review and synthesis. Progress in Energy and Combustion Science, 81, p.100869.

[33] Zhong, K.Q., Xiao, Y., Lu, X., Deng, J., Yin, L., Tian, Y. and Shu, C.M., 2021. Nanofluidic two-phase closed thermosyphon-assisted thermoelectric generator for heat recovery from coal spontaneous combustion. Applied Thermal Engineering, 197, p.117397.

[34] Pan, R., Martins, M.F. and Debenest, G., 2021. Pyrolysis of waste polyethylene in a semi-batch reactor to produce liquid fuel: optimization of operating conditions. Energy Conversion and Management, 237, p.114114.

[35] Jahirul, M.I., Rasul, M.G., Schaller, D., Khan, M.M.K., Hasan, M.M. and Hazrat, M.A., 2022. Transport fuel from waste plastics pyrolysis – A review on technologies, challenges and opportunities. Energy Conversion and Management, 258, p. 115451.

[36] Pan, R., Martins, M.F. and Debenest, G., 2022. Optimization of oil production through ex-situ catalytic pyrolysis of waste polyethylene with activated carbon. Energy, 248, p.123514.

[37] Shi, X., Chen, X., Zhang, Y., Zhang, Y., Shi, Z., Che, B. and Xia, S., 2021. Characteristics of self–ignition and smoldering of coal dust layer under inclination conditions. Process Safety and Environmental Protection, 156, pp.1-16.

[38] Shi, X., Chen, X., Zhang, Y., Zhang, Y., Guo, R., Zhao, T. and Liu, R., 2022. Numerical simulation of coal dust self–ignition and combustion under inclination conditions. Energy, 239, p.122227.

[39] Zanoni, M.A., Wang, J. and Gerhard, J.I., 2021. Understanding pressure changes in smouldering thermal porous media reactors. Chemical Engineering Journal, 412, p.128642.

[40] Mazloum, S., Awad, S., Allam, N., Aboumsallem, Y., Loubar, K. and Tazerout, M., 2021. Modelling plastic heating and melting in a semi-batch pyrolysis reactor. Applied Energy, 283, p.116375.

[41] Till, Z., Varga, T., Sója, J., Miskolczi, N. and Chován, T., 2018. Kinetic identification of plastic waste pyrolysis on zeolite-based catalysts. Energy Conversion and Management, 173, pp.320-330.

[42] Pozzobon, V., Salvador, S. and Bézian, J.J., 2018. Biomass gasification under high solar heat flux: Advanced modelling. Fuel, 214, pp.300-313.

[43] Mazloum, S., Aboumsallem, Y., Awad, S., Allam, N. and Loubar, K., 2021. Modelling pyrolysis process for PP and HDPE inside thermogravimetric analyzer coupled with differential scanning calorimeter. International Journal of Heat and Mass Transfer, 176, p.121468.

[44] Lopez, A., De Marco, I., Caballero, B.M., Laresgoiti, M.F. and Adrados, A., 2011. Influence of time and temperature on pyrolysis of plastic wastes in a semi-batch reactor. Chemical Engineering Journal, 173(1), pp.62-71.

[45] Maniscalco, M., La Paglia, F., Iannotta, P., Caputo, G., Scargiali, F., Grisafi, F. and Brucato, A., 2021. Slow pyrolysis of an LDPE/PP mixture: Kinetics and process performance. Journal of the Energy Institute, 96, pp.234-241.

Chapter 8

Conclusion

This thesis aimed to produce the liquid fuel from plastic waste pyrolysis driven by contaminated sand smoldering. Polyethylene (PE) is the first-most component in plastic waste due to its wide range of uses. Therefore, this work investigated the pyrolysis process of waste polyethylene (WPE). This included conducting the kinetic modeling of plastic waste pyrolysis by genetic algorithm (GA) based on different reaction models; using an artificial neural network (ANN) coupled with GA to simulate the plastic waste pyrolysis behavior; adopting ANN coupled with GA to optimize the operating conditions for the maximum oil production derived from plastic waste pyrolysis; investigating the ex-situ catalytic pyrolysis of plastic waste to upgrade the oil's property; developing a multidimensional model of smoldering-driven pyrolysis of plastic waste; and finally, establishing a robust mathematical model to provide a general design tool for the performance, evaluation, and optimization of the smoldering-driven pyrolysis reactor. The following summarized the main achievements and conclusions of this thesis.

The activation energy of plastic waste pyrolysis was determined by three isoconversional methods, which are KAS, Friedman and AIC methods. Three representative reaction models, i.e., reaction-order, extended Prout-Tompkins and Sestak-Berggren models, were also investigated for determining the proper model which could describe the pyrolysis process with

accuracy. Accordingly, GA coupled with the reaction-order model was adopted for calculating the optimal pyrolysis kinetic parameters. The GA calculated activation energy values were in good agreement with that by using of isoconversional methods. Moreover, high consistencies between experimental and GA predicted data were obtained in plastic waste pyrolysis processes at different heating rates. The predicted pyrolysis kinetic parameters by using of GA are relatively reliable and accurate.

A robust model-free method of ANN coupled with GA was adopted to conduct the plastic waste thermal pyrolysis analysis. ANN established mathematical expressions among the plastic waste conversion and the pyrolysis rate, and the operating conditions (temperature and heating rate). ANN was validated using the comparison of the experimental and predicted results. The accuracy of ANN predicted results was investigated by determining the R-squared values of the mass fraction (~ 1) and the pyrolysis rate (> 0.994) compared with the available experimental observations. Subsequently, GA was used to optimize the operating conditions for maximum plastic waste conversions and pyrolysis rates in different temperature ranges.

The oil production from WPE thermal pyrolysis was investigated in a bench-scale semi-batch reactor. Three operating conditions were considered, i.e., the temperature, the residence time, and the carrier gas flow rate. ANN comprehensively described the interactive effects of operating conditions on oil production. Subsequently, genetic algorithm (GA) was adopted to optimize the operating conditions to maximize oil production. The GA optimized oil yield was 83.63 wt% under the operating conditions of 488 °C (temperature), 20 min (residence time) and 20 mL/min (carrier gas flow rate). Moreover, it was found that the operating conditions did not

change the oil's main functional groups. The oils had the same component types under different operating conditions (mostly 1-alkenes and n-alkanes ranging from C7 to C36). However, high temperature, long residence time and high carrier gas flow rate were conducive to formation of the oil's heavy fraction. While low temperature, short residence time and low carrier gas flow rate were beneficial to form light and middle fractions in oil.

The maximum oil yield of WPE ex-situ catalytic pyrolysis was 69.63 wt%, which was lower compared to the WPE thermal pyrolysis oil yield. However, the presence of catalyst (activated carbon, AC) could decrease (from 488 ℃ to 479 °C) the optimal pyrolysis temperature of WPE. Moreover, AC could accelerate the hydrogen-ion abstraction reaction of the WPE hydrocarbon long chain to form more carbonium-ion free radicals, which was conducive to generating shorter chain hydrocarbons with lower carbon numbers.

A 1D smoldering model was coupled with a 2D pyrolysis model to simulate the WPE pyrolysis driven by char smoldering. The char smoldering could provide a heat source with stable propagation velocity and peak temperature by adding sand as the porous matrix in the smoldering chamber. WPE was continuously pyrolyzed without providing external energy as long as char smoldering continues. A comprehensive study of WPE pyrolysis tar and gas yields was carried out under consideration of key parameters. The WPE pyrolysis process duration, conversion rate, and product composition could be regulated by changing air inlet velocity, char concentration, and carrier gas inlet velocity, since they could control the peak temperature and the front velocity.

Finally, a robust mathematical model (2D smoldering model coupled with 2D pyrolysis

model) was established to investigate the self-sustaining smoldering driven pyrolysis process. The thermally thick approximation calculated the boundary heat transfer between smoldering and pyrolysis chambers. Moreover, the modified apparent heat capacity method (AHCM) was used to simulate the melting process of WPE. A sensitivity analysis was conducted to investigate the effects of several parameters that can affect smoldering and pyrolysis processes. The developed model provided a robust tool to guide the design, performance evaluation, and optimization of the smoldering-driven pyrolysis reactor.

Conclusion (Fr)

Cette thèse visait à étudier la production de combustible liquide à partir de la pyrolyse de déchets plastiques en utilisant la combustion lente de sols et sables pollués par des composés organiques.

Le polyéthylène (PE) est le principal composant des déchets plastiques en raison de sa large gamme d'utilisations. Par conséquent, ce travail a étudié, en détail, le processus de pyrolyse des déchets de polyéthylène (WPE). Cela comprenait :

- La réalisation de la modélisation cinétique de la pyrolyse des déchets plastiques par algorithme génétique (GA) basé sur différents modèles de réaction ;
- L'utilisation d'un réseau de neurones artificiels (ANN) couplé à un GA pour simuler le comportement de la pyrolyse de déchets plastiques,
- L'optimisation des conditions opératoires pour permettre une production optimale d'huile issue de la pyrolyse des déchets plastiques ; étudier la pyrolyse catalytique ex-situ des déchets plastiques pour améliorer la propriété du pétrole ;
- Le développement de modèles multidimensionnels de pyrolyse de déchets plastiques entrainée par la combustion lente de résidus organiques ; et enfin,
- L'établissement d' un modèle mathématique robuste pour fournir un outil de conception général évaluer la performance d'un nouveau procédé et l'optimiser.

Ce qui suit résume les principales réalisations et conclusions de cette thèse.

L'énergie d'activation de la pyrolyse des déchets plastiques a été déterminée par trois méthodes d'isoconversion, qui sont les méthodes KAS, Friedman et AIC. Trois modèles de réaction représentatifs, c'est-à-dire l'ordre de réaction, les modèles Prout-Tompkins et Sestak-Berggren étendus, ont également été étudiés pour déterminer le modèle approprié qui pourrait décrire le processus de pyrolyse le plus de consistance. En conséquence, un algorithme GA couplé au modèle d'ordre de réaction a été adopté pour calculer les paramètres cinétiques de pyrolyse optimaux. Les valeurs d'énergie d'activation calculées par GA étaient en bon accord avec celles obtenues via des méthodes isoconvertionnelles. De plus, les accords entre les données expérimentales et celles prédites par GA ont été vérifiés pour ce procédé de pyrolyse de déchets plastiques, et ce, à différentes vitesses de chauffage. Les paramètres cinétiques de pyrolyse prédits à l'aide de GA sont donc fiables et précis.

Une méthode robuste utilisant un modèle ANN couplée à GA a été adoptée pour effectuer l'analyse de la pyrolyse thermique des déchets plastiques. Le modèle réseau de neurones ANN a permis d’établir des expressions mathématiques entre la conversion des déchets plastiques, le taux de pyrolyse, et les conditions de fonctionnement (température et taux de chauffage). L’ANN a été validé en utilisant la comparaison des résultats expérimentaux et ceux prédits via le réseau de neurones. La précision des résultats prédits par l'ANN a été déterminée via la comparaison avec des données expérimentales disponibles et obtenues dans le cadre de cette thèse. Par la suite, l’optimisation via GA a été utilisée pour déterminer les conditions de fonctionnement permettant des conversions maximales de déchets plastiques en huile et les taux de pyrolyse dans différentes plages de température.

La production d'huile à partir de la pyrolyse thermique WPE a été étudiée dans un réacteur semi-batch à l'échelle du laboratoire. Trois conditions opératoires ont été considérées, à savoir la température, le temps de séjour et le débit de gaz vecteur. L'ANN décrit en détail les effets interactifs des conditions opératoires sur la production d'huile issue de plastique. Par la suite, un algorithme génétique (GA) a été adopté pour optimiser les conditions de fonctionnement afin de maximiser la production d'huile. Le rendement en huile optimisé par GA était de 83.63 % en poids dans les conditions de fonctionnement de 488 ℃ (température), 20 min (temps de séjour) et 20 mL/min (débit de gaz vecteur). De plus, il a été constaté que les conditions opératoires ne modifiaient pas les principaux groupes fonctionnels de l'huile. Les huiles avaient les mêmes types de composants dans diverses conditions de fonctionnement (principalement des 1-alcènes et des n-alcanes allant de C7 à C36). Cependant, une température élevée, un long temps de séjour et un débit élevé de gaz vecteur ont favorisé la formation de la fraction lourde d'huile. Par contre, une basse température, un temps de séjour court et un faible débit de gaz porteur étaient bénéfiques pour former des fractions légères et moyennes dans les huiles.

Le rendement maximal en huile de la pyrolyse catalytique ex-situ WPE était de 69.63 wt% en poids, ce qui était inférieur au rendement en huile de la pyrolyse thermique WPE. Cependant, la présence de catalyseur (charbon actif, AC) pourrait diminuer (de 488 ℃ à 479 °C) la température de pyrolyse optimale du WPE. De plus, le catalyseur pourrait accélérer la réaction d'abstraction des ions hydrogène des longues chaînes d'hydrocarbures et ainsi former plus de radicaux libres d'ions carbonium. Ceci est propice à la génération d'hydrocarbures à chaîne plus courte avec un nombre d'atome de carbone inférieur.

Un modèle de combustion lente 1D a été couplé à un modèle de pyrolyse 2D pour simuler la pyrolyse de WPE entraînée par la combustion lente. La combustion lente peut fournir une source de chaleur suffisante pour permettre la pyrolyse tout en maitrisant la vitesse de propagation et la température cible en jouant sur la quantité de réactif dans le sable, utilisé comme matrice poreuse dans la chambre de combustion lente. Le WPE a été pyrolysé en continu sans utilisation d'énergie externe tant que le résidu organique (i.e. charbon) se consume. Une étude approfondie des rendements de goudron et de gaz de pyrolyse issu de WPE a été réalisée en tenant compte des paramètres clés. La durée du processus de pyrolyse WPE, le taux de conversion et la composition du produit pourraient être régulés en modifiant la vitesse d'entrée d'air, la concentration de charbon et la vitesse d'entrée du gaz porteur, car ils pourraient contrôler la température maximale et la vitesse de front de réaction.

Enfin, un modèle mathématique plus robuste (modèle de combustion lente 2D couplé à un modèle de pyrolyse 2D) a été établi pour étudier le processus de pyrolyse auto-entretenu et entraîné par la combustion lente. Nous avons pu estimer le coefficient de transfert de chaleur entre les chambres de combustion lente et de pyrolyse. La méthode de la capacité thermique apparente modifiée (AHCM) a été utilisée pour simuler le processus de fusion du WPE. Une analyse de sensibilité a été menée pour étudier les effets de plusieurs paramètres pouvant affecter les processus de combustion lente et de pyrolyse. Le modèle développé a fourni un outil pour guider la conception, l'évaluation des performances et l'optimisation du réacteur de pyrolyse à combustion lente.

Appendix A

GC-MS chromatograms

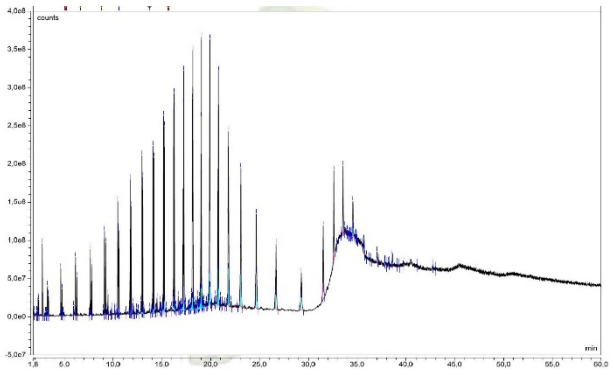

Fig. A.1. GC-MS analysis of the liquid fuel E1 (425 ℃, 20 min, and 20 mL/min).

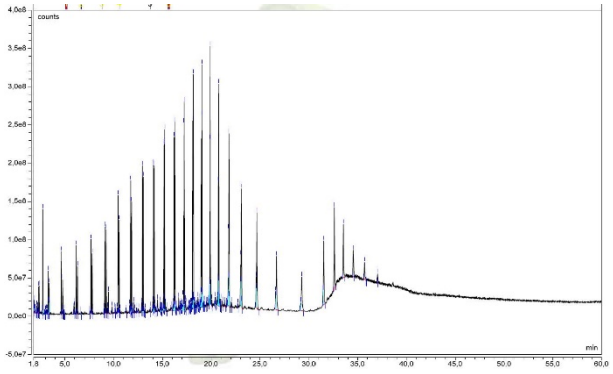

Fig. A.2. GC-MS analysis of the liquid fuel E2 (425 ℃, 20 min, and 100 mL/min).

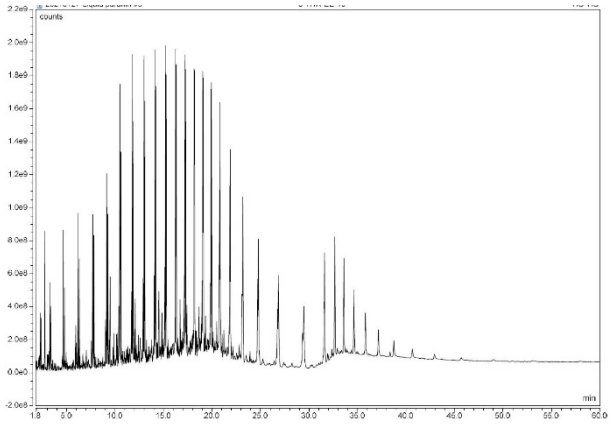

Fig. A.3. GC-MS analysis of the liquid fuel E3 (425 ℃, 40 min, and 60 mL/min).

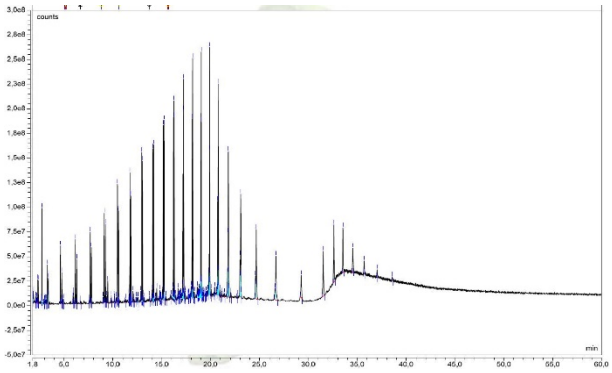

Fig. A.4. GC-MS analysis of the liquid fuel E4 (425 ℃, 60 min, and 20 mL/min).

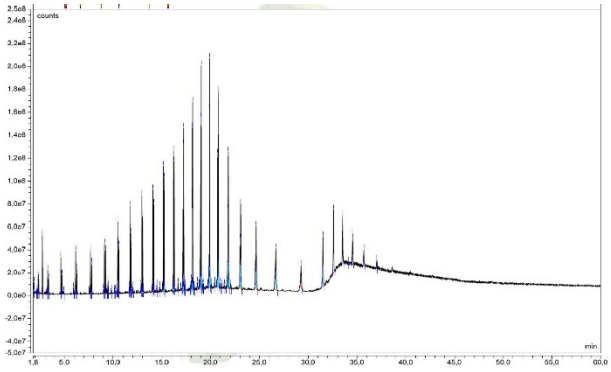

Fig. A.5. GC-MS analysis of the liquid fuel E5 (425 ℃, 60 min, and 100 mL/min).

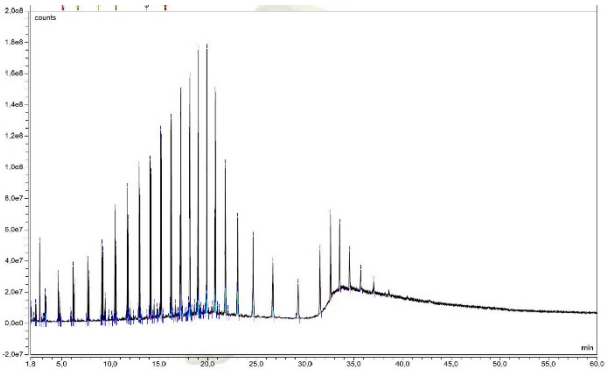

Fig. A.6. GC-MS analysis of the liquid fuel E6 (475 ℃, 20 min, and 60 mL/min).

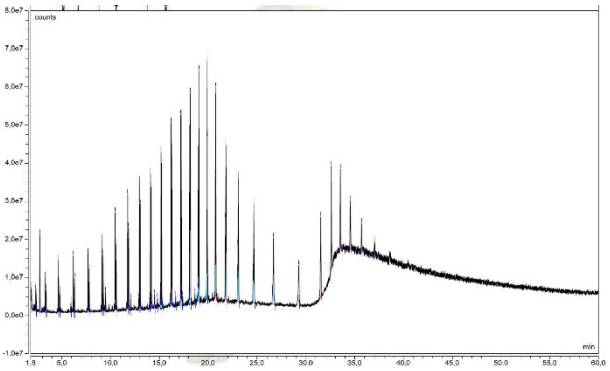

Fig. A.7. GC-MS analysis of the liquid fuel E7 (475 ℃, 40 min, and 20 mL/min).

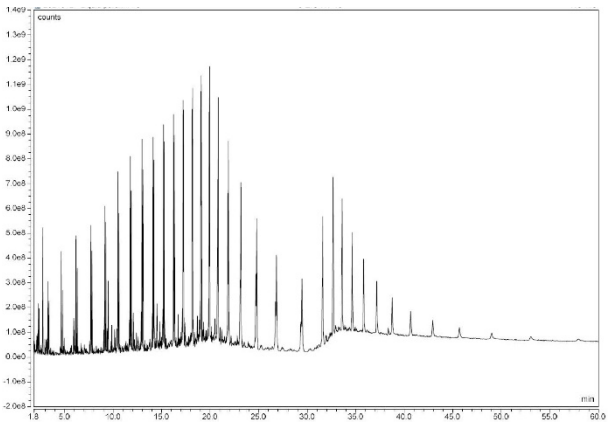

Fig. A.8. GC-MS analysis of the liquid fuel E8 (475 ℃, 40 min, and 60 mL/min).

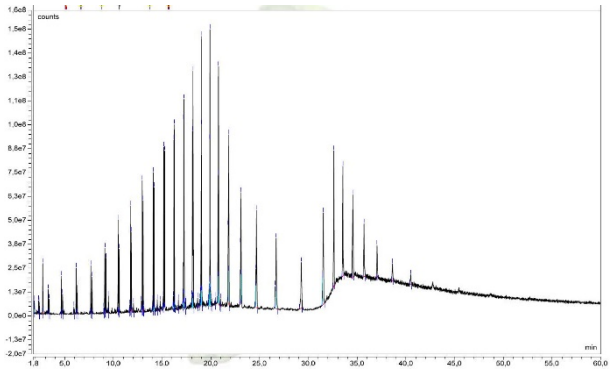

Fig. A.9. GC-MS analysis of the liquid fuel E9 (475 ℃, 40 min, and 100 mL/min).

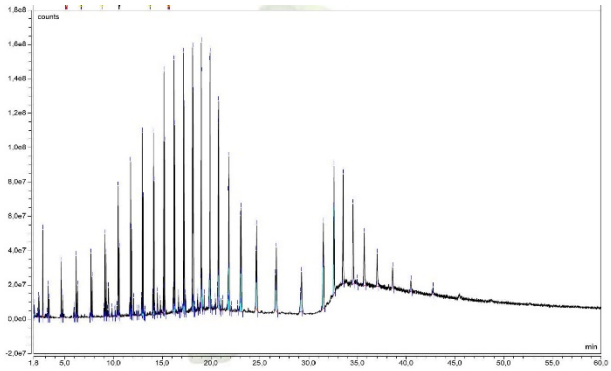

Fig. A.10. GC-MS analysis of the liquid fuel E10 (475 ℃, 60 min, and 60 mL/min).

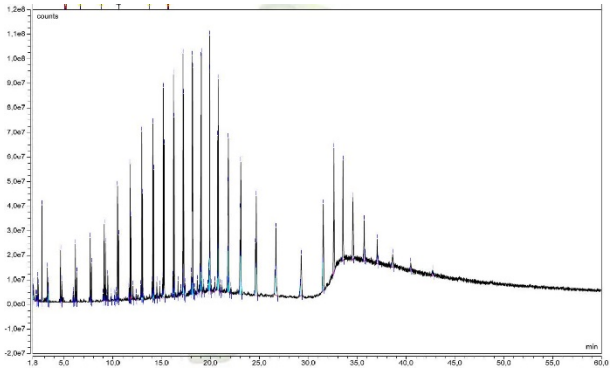

Fig. A.11. GC-MS analysis of the liquid fuel E11 (525 ℃, 20 min, and 20 mL/min).

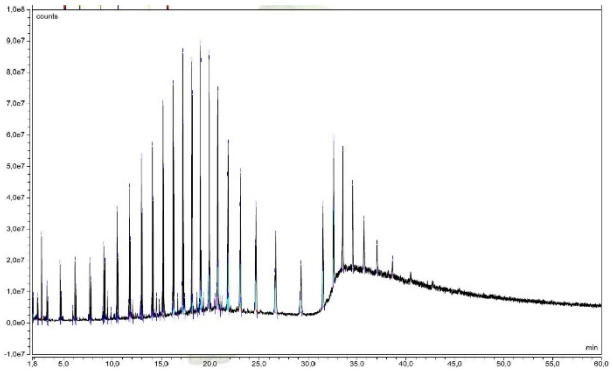

Fig. A.12. GC-MS analysis of the liquid fuel E12 (525 ℃, 20 min, and 100 mL/min).

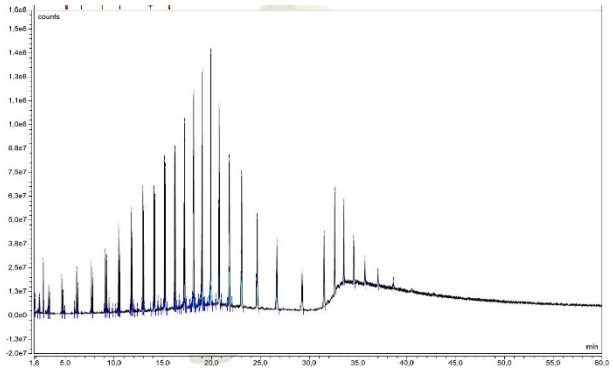

Fig. A.13. GC-MS analysis of the liquid fuel E13 (525 ℃, 40 min, and 60 mL/min).

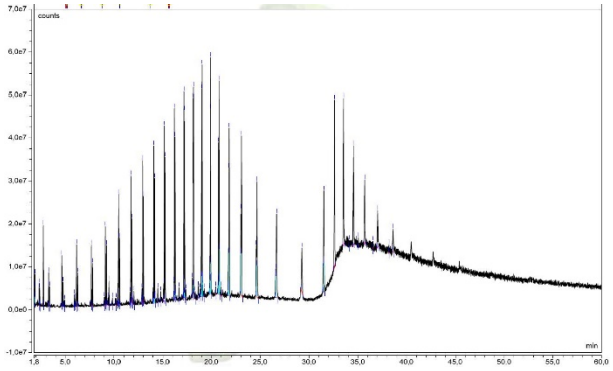

Fig. A.14. GC-MS analysis of the liquid fuel E14 (525 ℃, 60 min, and 20 mL/min).

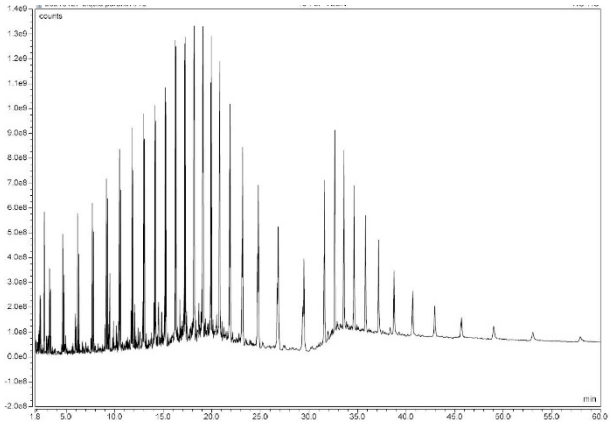

Fig. A.15. GC-MS analysis of the liquid fuel E15 (525 °C, 60 min, and 100 mL/min).

Appendix B

Verification of ANN-GA applicability

In order to verify the applicability of ANN-GA, this study used ANN-GA to optimize the required heat and exergy efficiency during the waste polyethylene (WPE) gasification process [1]. Hasanzadeh et al. [1] investigated the interaction of temperature and steam to polyethylene waste ratio (S/P ratio) on the WPE gasification's required heat and exergy efficiency. They conducted the modeling at S/P ratio of 2 and temperature of 900 °C to study the effects of temperature and S/P ratio on the WPE gasification process. These 2 sets of data could be served as the testing data. Moreover, a total of 13 sets of tests were conducted to obtain the training data. The temperature and S/P ratio were investigated in the ranges of 650–1150 °C and 0.6–3.6, respectively. They used the response surface methodology (RSM) to establish the mathematical expressions of required heat and exergy efficiency expressed in terms of temperature and S/P ratio.

B.1. Required heat (Case 1)

Fig. B.1 shows the flow schematic of ANN-GA for required heat optimization. According to [2], the temperature and S/P ratio were divided into three and two levels, respectively.

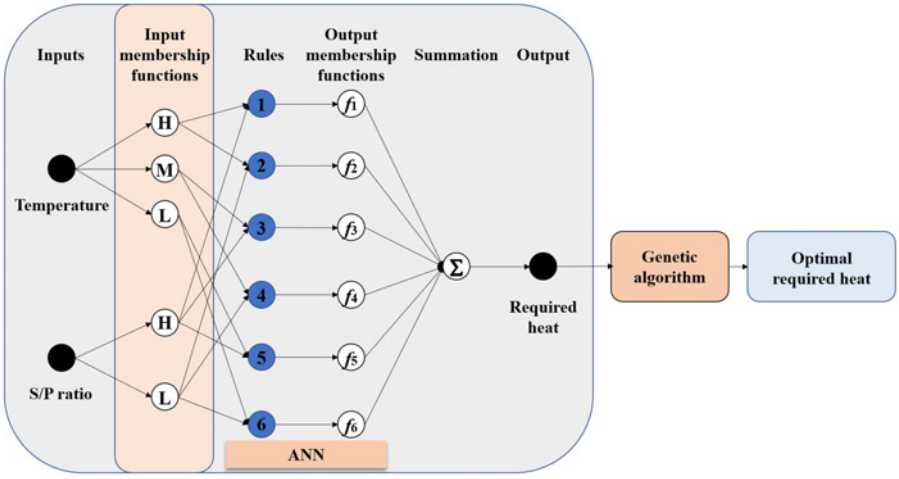

Fig. B.1. Flow schematic of ANN-GA for required heat optimization: Three levels of temperature.

Fig. B.2 demonstrates the comparison of the original data with the predicted required heat values of RSM and ANN-GA (three levels of temperature) in the training set. It can be seen that the ANN-GA predicted required heat values were more consistent with the original ones. Moreover, the R^2 value between the original and ANN-GA predicted results was 0.9798, a value much higher than the RSM predicted results' R^2 value of 0.9159.

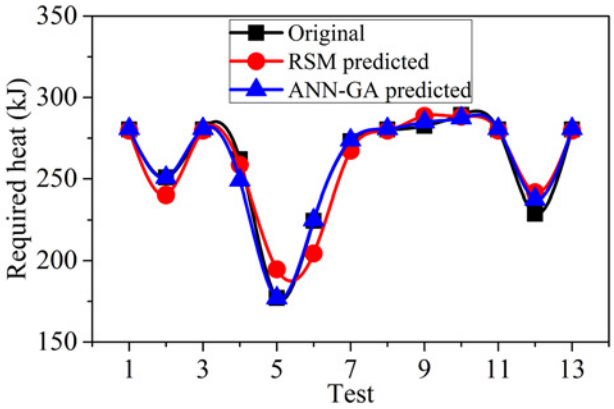

Fig. B.2. Comparison of the original data with the predicted required heat values of RSM and ANN-GA (three levels of temperature) in the training set.

Fig. B.3 illustrates the comparison of the original data with the predicted required heat values of RSM and ANN-GA (three levels of temperature) in the testing set. It can also be seen

that the ANN-GA predicted required heat values were more consistent with the original ones at S/P ratio of 2 and temperature of 900 °C. The R^2 values between the original and ANN-GA predicted results, and between the original and RSM predicted results were 0.9449 and 0.7806, respectively. It can be concluded that the ANN-GA predicted results were much more accurate than the RSM predicted ones.

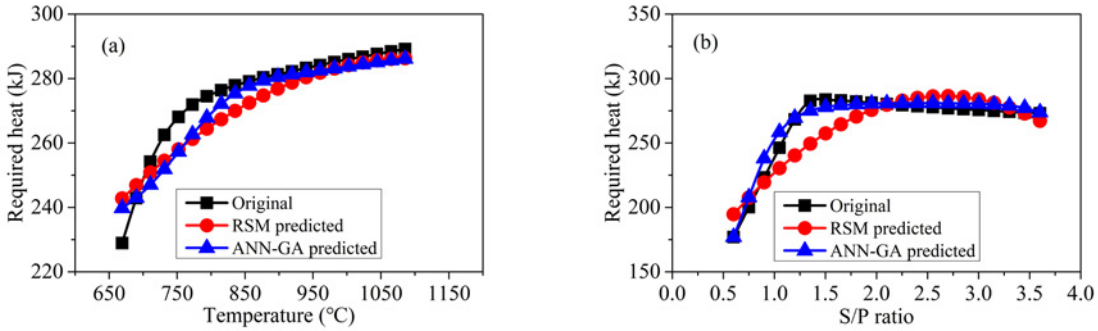

Fig. B.3. Comparison of the original data with the predicted required heat values of RSM and ANN-GA (three levels of temperature) in the testing set: (a) At S/P ratio of 2; (b) At temperature of 900 °C.

Fig. B.4 depicts the interaction of temperature and S/P ratio on the WPE gasification's required heat and the lowest required heat optimized by ANN-GA (three levels of temperature). The lowest required heat was 115.2 kJ at the temperature of 1150 °C and the S/P ratio of 0.6. The optimized temperature was incorrect, because the required heat should be increased with an increase in the temperature. The reason for the incorrect result is that the test design for the training data was not standardized. Although 13 sets of tests were conducted, 5 sets were repeated (Tests 1, 3, 8, 11, and 13). Moreover, only 1 test was conducted at the lowest S/P ratio of 0.6, which caused the ANN-GA predicted results at the lowest S/P ratio to be inaccurate.

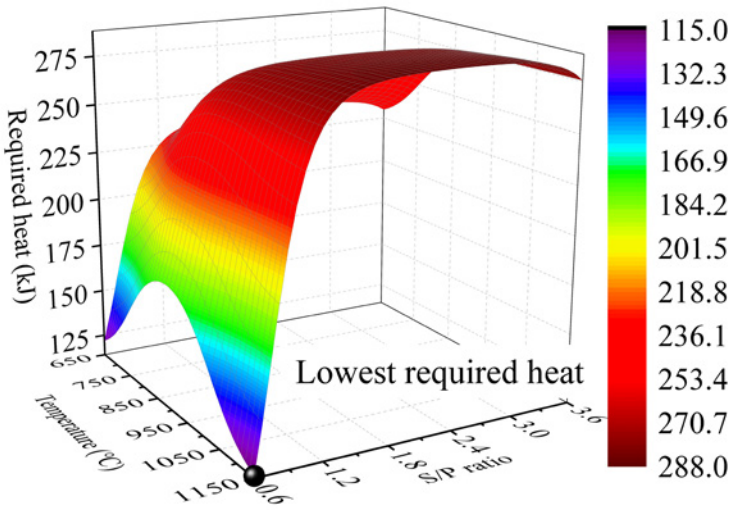

Fig. B.4. The lowest required heat optimized by ANN-GA (three levels of temperature).

In order to improve the accuracy of the predicted value at the lowest S/P ratio, the temperature was divided into two levels. Fig. B.5 shows the flow schematic of ANN-GA with two levels of temperature for the required heat optimization.

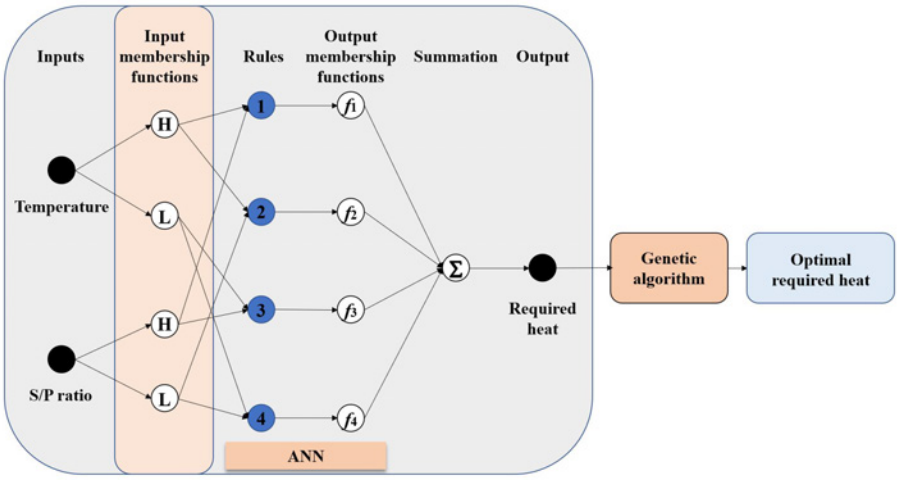

Fig. B.5. Flow schematic of ANN-GA for required heat optimization: Two levels of temperature.

Fig. B.6 shows the comparison of the original data with the predicted required heat values of RSM and ANN-GA (two levels of temperature) in the training set. The R^2 value between the original and ANN-GA (two levels of temperature) predicted results was 0.9273, a value lower

than the ANN-GA (three levels of temperature) predicted results' R^2 value of 0.9798. While the ANN-GA (two levels of temperature) predicted results' R^2 value was still higher than the RSM predicted results' R^2 value of 0.9159.

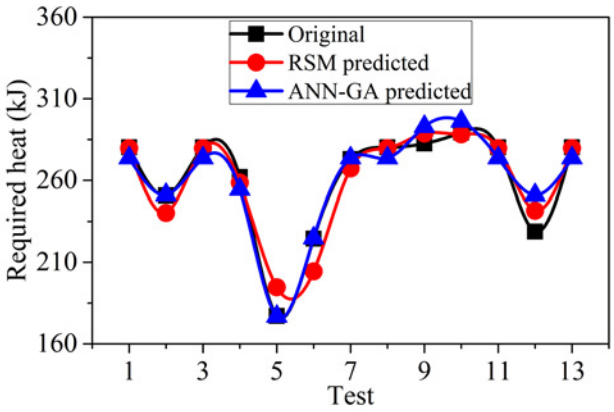

Fig. B.6. Comparison of the original data with the predicted required heat values of RSM and ANN-GA (two levels of temperature) in the training set.

Fig. B.7 depicts the comparison of the original data with the predicted required heat values of RSM and ANN-GA (two levels of temperature) in the testing set. It can be seen that the ANN-GA (two levels of temperature) predicted required heat values were more consistent with the original ones at the temperature of 900 °C. The R^2 values between the original and ANN-GA (two levels of temperature) predicted results, and between the original and RSM predicted results were 0.8679 and 0.7806, respectively. It can also be concluded that the ANN-GA (two levels of temperature) predicted results were much more accurate than the RSM predicted ones.

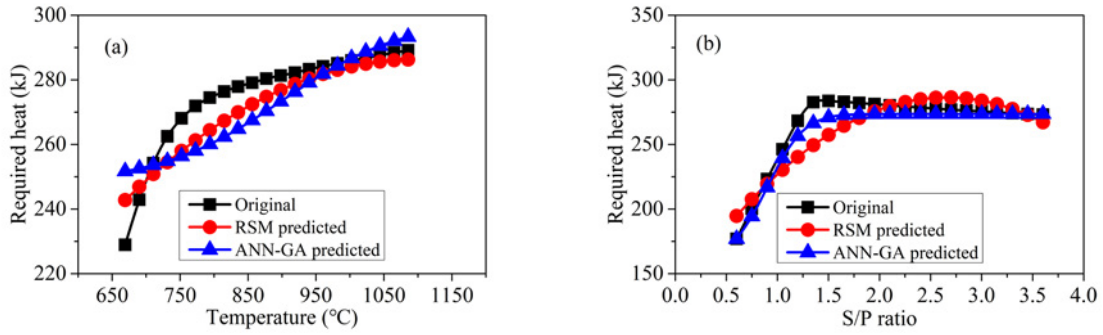

Fig. B.7. Comparison of the original data with the predicted required heat values of RSM and ANN-GA (two levels of temperature) in the testing set: (a) At S/P ratio of 2; (b) At temperature of 900 °C.

Fig. B.8 depicts the interaction of temperature and S/P ratio on the WPE gasification's required heat and the lowest required heat optimized by ANN-GA (two levels of temperature). The ANN-GA (two levels of temperature) predicted the lowest required heat was 173.66 kJ at the temperature of 650 °C and S/P ratio of 0.6. It indicates that low temperature and low S/P ratio can reduce the WPE gasification's required heat, which is consistent with the modeling results [1].

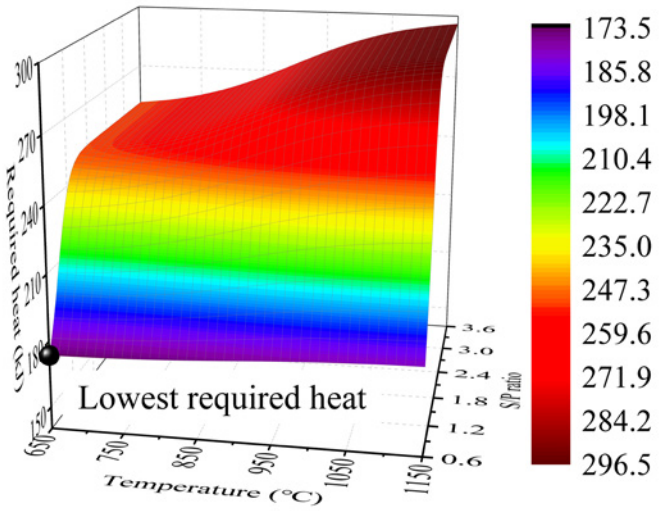

Fig. B.8. The lowest required heat optimized by ANN-GA (two levels of temperature).

B.2. Exergy efficiency (Case 2)

Fig. B.9 compares the original data with the predicted exergy efficiencies of RSM and ANN-GA in the training set. It can be seen that the ANN-GA predicted exergy efficiencies were more consistent with the original ones. Moreover, the R^2 value between the original and ANN-GA predicted results was 0.9912, a value higher than the RSM predicted results' R^2 value of 0.9850.

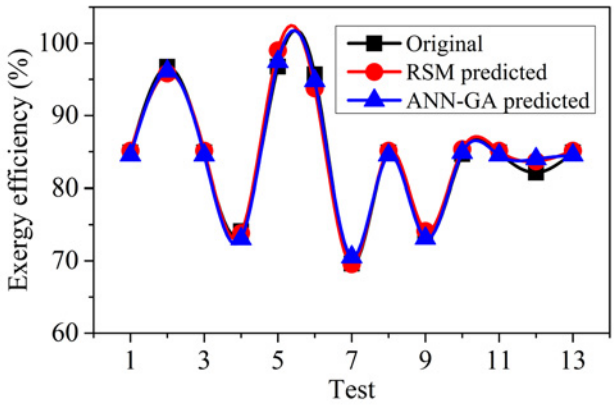

Fig. B.9. Comparison of the original data with the predicted exergy efficiencies of RSM and ANN-GA in the training set.

Fig. B.10 illustrates the comparison of the original data with the predicted exergy efficiencies of RSM and ANN-GA in the testing set. It can be seen that the ANN-GA predicted exergy efficiencies were more consistent with the original ones at the temperature of 900 °C. The R^2 values between the original and ANN-GA predicted results, and between the original and RSM predicted results were 0.9700 and 0.9516, respectively. It can be concluded that the ANN-GA predicted results were much more accurate than the RSM predicted ones.

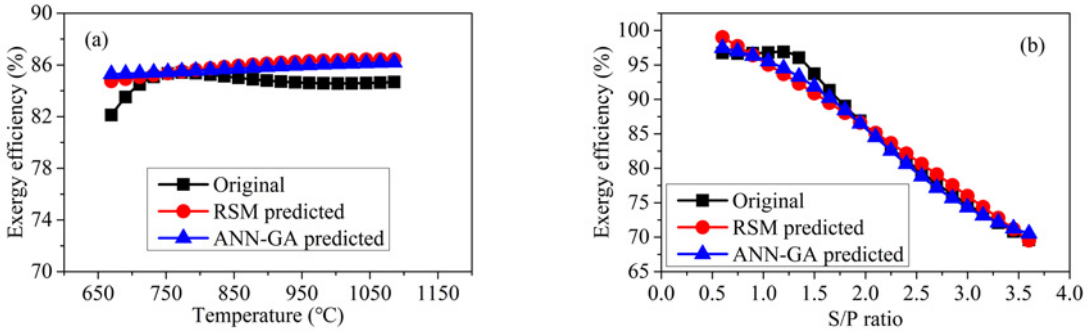

Fig. B.10. Comparison of the original data with the predicted exergy efficiencies of RSM and ANN-GA in the testing set: (a) At S/P ratio of 2; (b) At temperature of 900 °C.

Fig. B.11 demonstrates the interaction of temperature and S/P ratio on the WPE gasification's exergy efficiency and the highest exergy efficiency optimized by ANN-GA. The ANN-GA predicted highest exergy efficiency was 98.17 % at the temperature of 1150 °C and S/P ratio of 0.6.

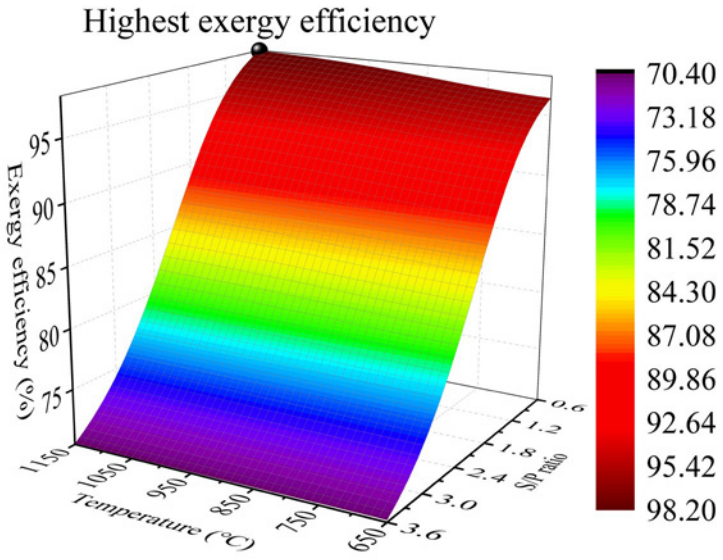

Fig. B.11. The highest exergy efficiency optimized by ANN-GA.

Bibliography

[1] Hasanzadeh, R., Mojaver, M., Azdast, T. and Park, C.B., 2021. Polyethylene waste gasification syngas analysis and multi-objective optimization using central composite design for simultaneous minimization of required heat and maximization of exergy efficiency. Energy Conversion and Management, 247, p.114713.

[2] Quesada, L., Pérez, A., Godoy, V., Peula, F.J., Calero, M. and Blázquez, G., 2019. Optimization of the pyrolysis process of a plastic waste to obtain a liquid fuel using different mathematical models. Energy Conversion and Management, 188, pp.19-26.

Appendix C

1D smoldering model coupled with 2D pyrolysis model

C.1. Grid-independence Test

The grid-independence test is conducted to obtain the numerical results that are not affected by the grid. Fig. C.1a shows the T_{PW} profiles with different mesh elements. The mesh elements of 1000–6000 are 50×20, 100×20, 100×30, 200×20, 200×25, and 200×30 (vertical × horizontal), respectively. It can be found that the T_{PW} differences are not easily distinguished. Therefore, we define the mean variance T_v:

$$T_v = (T_{PW,i} - T_{PW,6000})^2 / \overline{T}_{PW,6000} \quad \text{(C.1)}$$

where $T_{PW,i}$, $T_{PW,6000}$, and $\overline{T}_{PW,6000}$ are the T_{PW} with different mesh elements (1000–5000), the T_{PW} with 6000 mesh elements, and the mean T_{PW} with 6000 mesh elements. As shown in Fig. C.1b, the T_v profiles with 4000, 5000, and 6000 mesh elements are almost completely coincided. By comprehensive comparison of the simulation accuracy and computing cost, we adopt the mesh elements of 4000 for the numerical simulation.

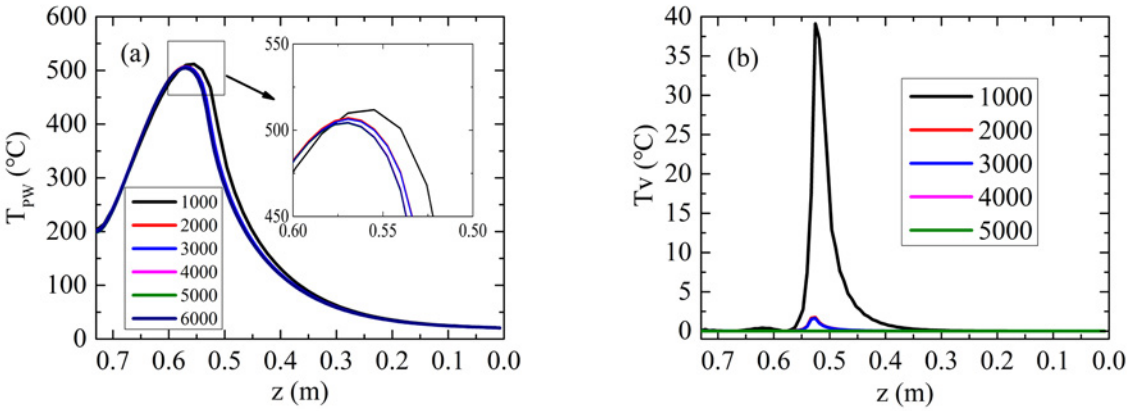

Fig. C.1. T_{PW} and T_v profiles at t=7200s and r=0.025m with different mesh elements: (a) T_{PW}; (b) T_v.

C.2. Assessments of modeling results

Fig. C.2 demonstrates the local peak temperatures $T_{s,p}$ and front velocities $v_{f,s}$. The experimental data is from [1]. Large errors occur at the top of reactor (z=0.069m), which may be due to the smoldering propagation has not yet entered the stable phase. When it continues to propagate downward, the smoldering would stabilize with an average local peak temperature of 631℃ and an average front velocity of 0.057mm/s. This proves that char smoldering can provide a stable heat source.

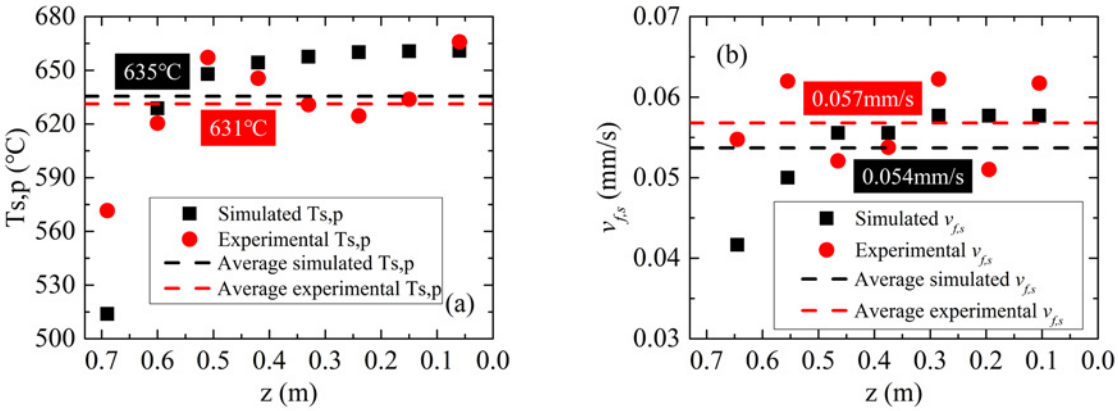

Fig. C.2. $T_{s,p}$; (b) $v_{f,s}$.

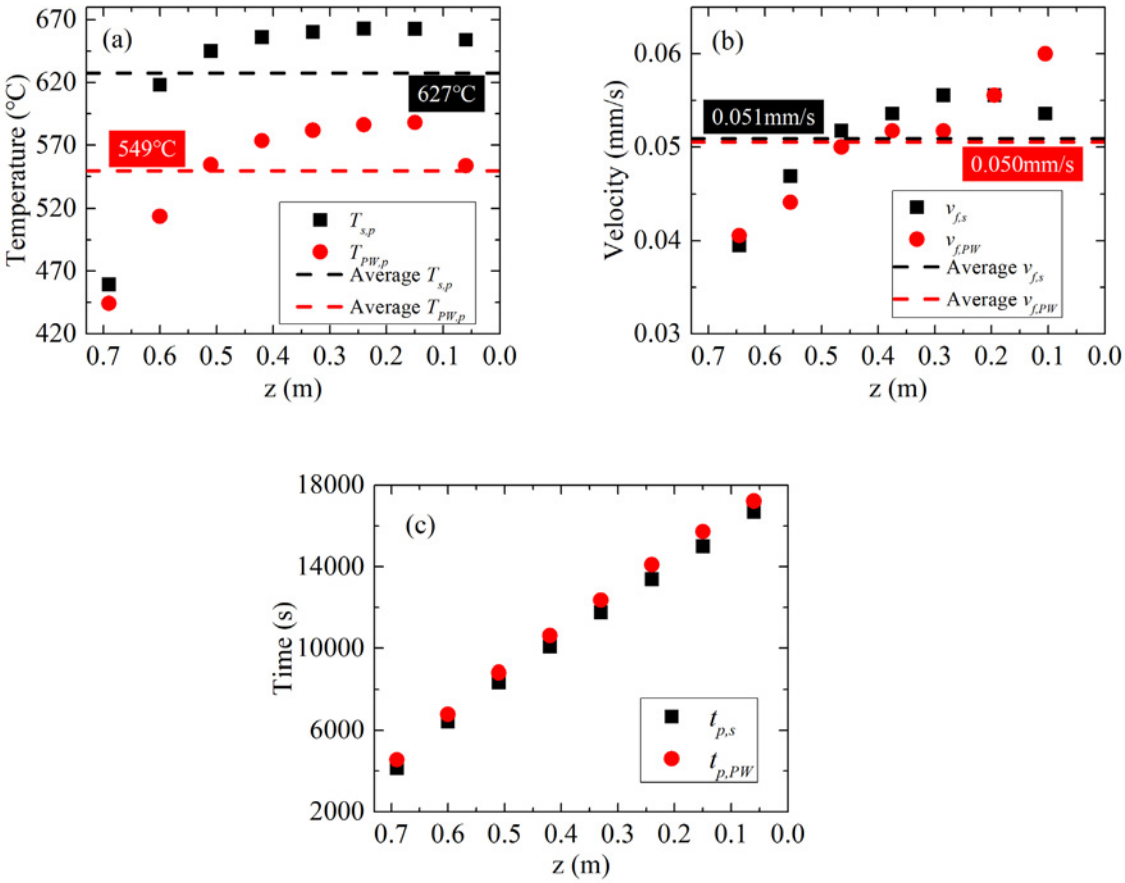

Fig. C.3. Profiles at z=0.06–0.69 m, distributed with a spacing of 0.09 m: (a) $T_{s,p}$ and $T_{PW,p}$; (b) $v_{f,s}$ and $v_{f,PW}$; (c) $t_{s,p}$ and $t_{PW,p}$.

C.3. Effect of air inlet velocity in smoldering chamber

The interactive effect of air inlet velocity on gas-solid convective heat flux and char smoldering reaction rate resulted in the maximum T_s and T_{PW} at 0.04m/s and 7200s (Figs. C.4a–b). The increase of air inlet velocity would monotonously increase T_s and T_{PW} when the time exceeds 7200s. On the other hand, the local T_{PW} reaches its peak earlier under higher air inlet velocities due to the faster heat convection between air and solid in smoldering chamber (determined by Eq. (6.41)).

The increase in air inlet velocity also leads to an increase in R_{PW} due to the higher $T_{PW,p}$

(Fig. C.4c). It can be seen that the air inlet velocity has a complex effect on the temperature front (Fig. C.4d) and pyrolysis front (Fig. C.4e). Pyrolysis front is ahead of temperature front by 0.04m, which occurs at ~490℃. As depicted in Fig. C.4e, PW that has not been completely pyrolyzed at the upper end of the reactor under 0.050m/s due to the low local T_{PW}.

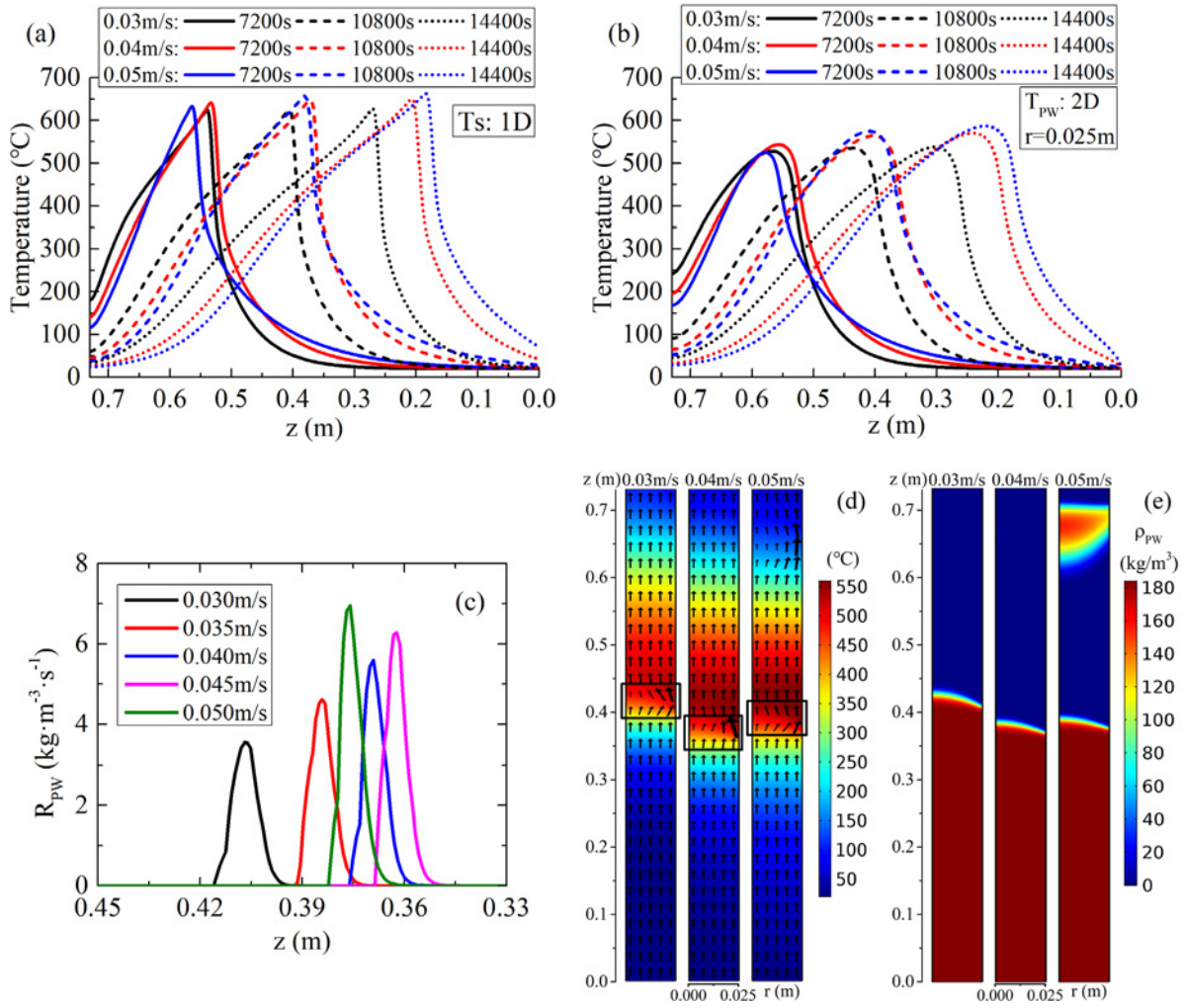

Fig. C.4. The effect of air inlet velocity on (a, b) longitudinal T_s and T_{PW} (at r=0.025m) profiles at t=7200–14400s with intervals of 3600s, (c) R_{PW} at r=0.025m and t=10800s, (d) T_{PW} distribution at t=10800s, and (e) ρ_{PW} distribution at t=10800s.

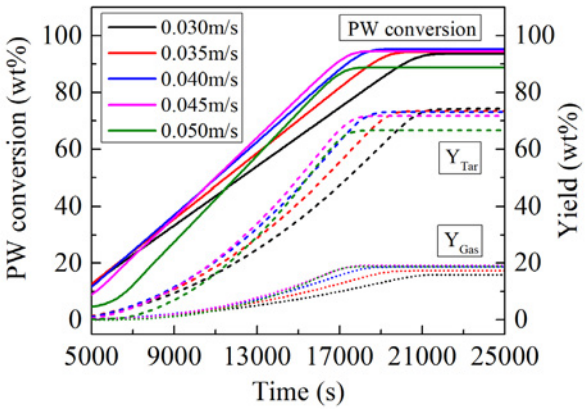

Fig. C.5. The system average PW conversions, Y_{Tar} and Y_{Gas} variations with time under different air inlet velocities.

C.4. Effect of char concentration in smoldering chamber

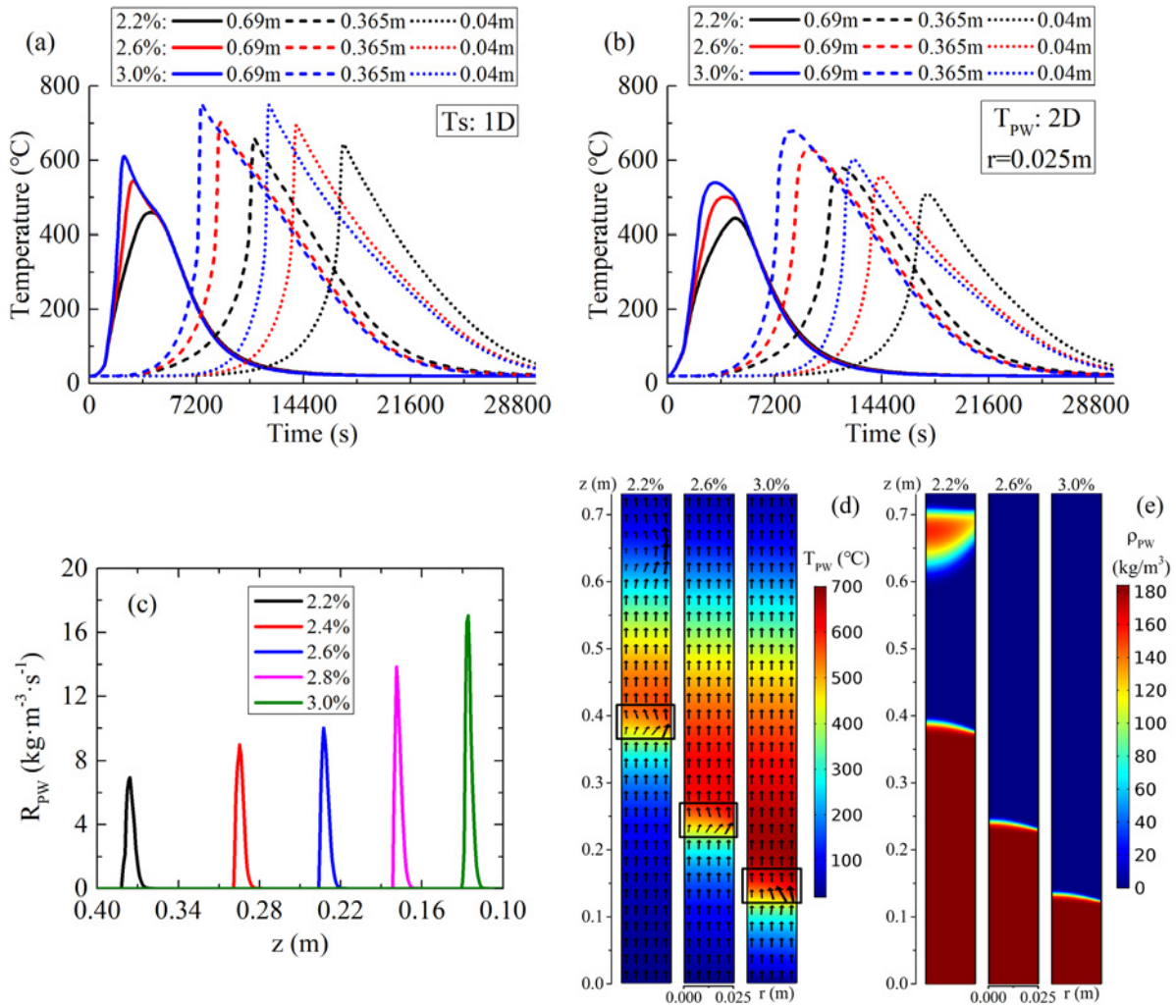

Fig. C.6. The effect of char concentration on (a, b) local T_s and T_{PW} (at r=0.025m) profiles at z=0.04–0.69m

with intervals of 0.325m, (c) R_{PW} at r=0.025m and t=10800s, (e) T_{PW} distribution at t=10800s, and (f) ρ_{PW} distribution at t=10800s.

The incompletely pyrolyzed PW is attributed to the low temperature in the pyrolysis chamber's inlet (z = 0 m).

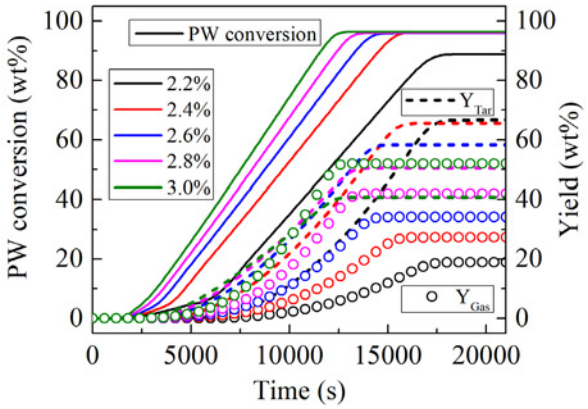

Fig. C.7. The system average PW conversions, Y_{Tar} and Y_{Gas} variations with time under different char concentrations.

C.5. Effect of Carrier Gas Inlet Velocity in Pyrolysis Chamber

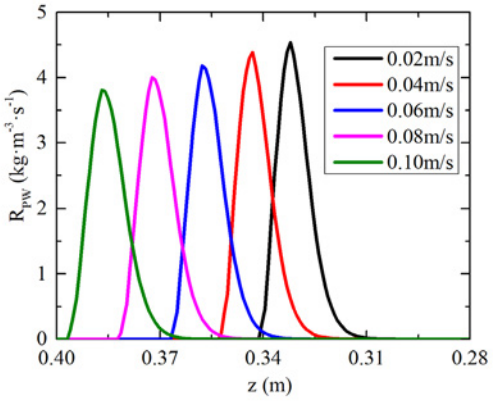

Fig. C.8. The effect of carrier gas inlet velocity on R_{PW} at r=0.0125m and t=10800s.

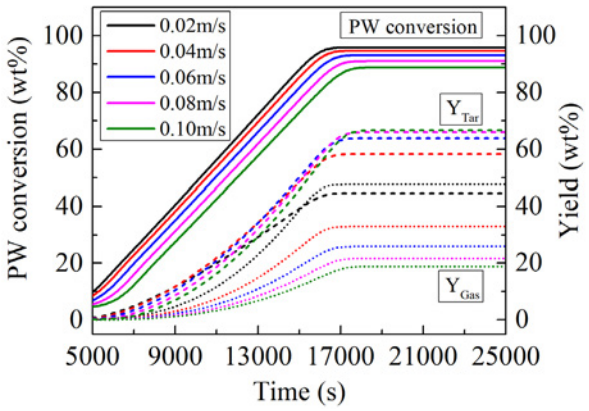

Fig. C.9. The system average PW conversions, Y_{Tar} and Y_{Gas} variations with time under different carrier gas inlet velocities.

Bibliography

[1] Zanoni, M.A., Wang, J. and Gerhard, J.I., 2021. Understanding pressure changes in smouldering thermal porous media reactors. Chemical Engineering Journal, 412, p.128642.

Appendix D

2D smoldering model coupled with 2D pyrolysis model

D.1. Kinetic parameters

Table D.1. Kinetic parameters of char smoldering and PW pyrolysis.

Par.	Value	Unit
A_C	707.9	s^{-1}
E_C	68	$kJ \cdot mol^{-1}$
ΔH_C	-30.82×10^{3}	$kJ \cdot kg^{-1}$
A_{PW}	1.12×10^{22}	s^{-1}
E_{PW}	346.8	$kJ \cdot mol^{-1}$
ΔH_{PW}	323	$kJ \cdot kg^{-1}$
$A_{L\text{-}}$	9.49×10^{-3}	s^{-1}
$E_{L\text{-}}$	0.372	$kJ \cdot mol^{-1}$
$\Delta H_{L\text{-}}$	-42	$kJ \cdot kg^{-1}$
A_G	8.10×10^{-1}	s^{-1}
E_G	18.2	$kJ \cdot mol^{-1}$
ΔH_G	-42	$kJ \cdot kg^{-1}$

D.2. Effect of char concentration

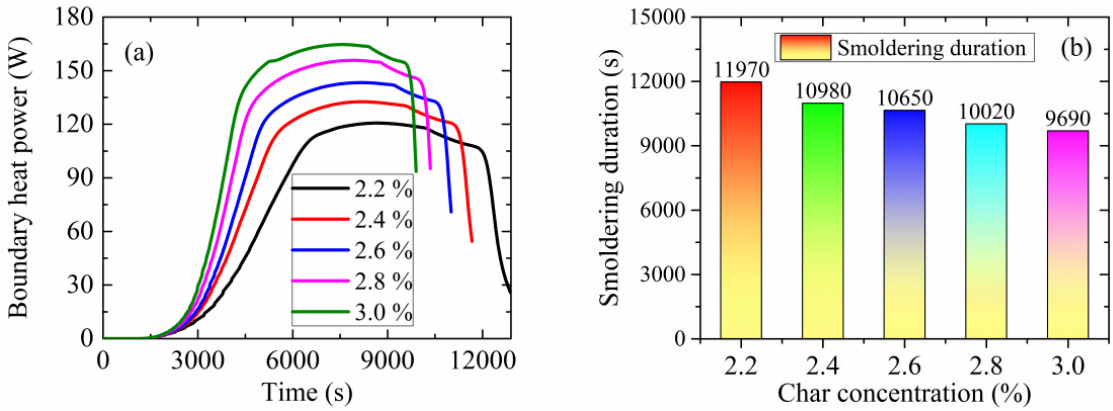

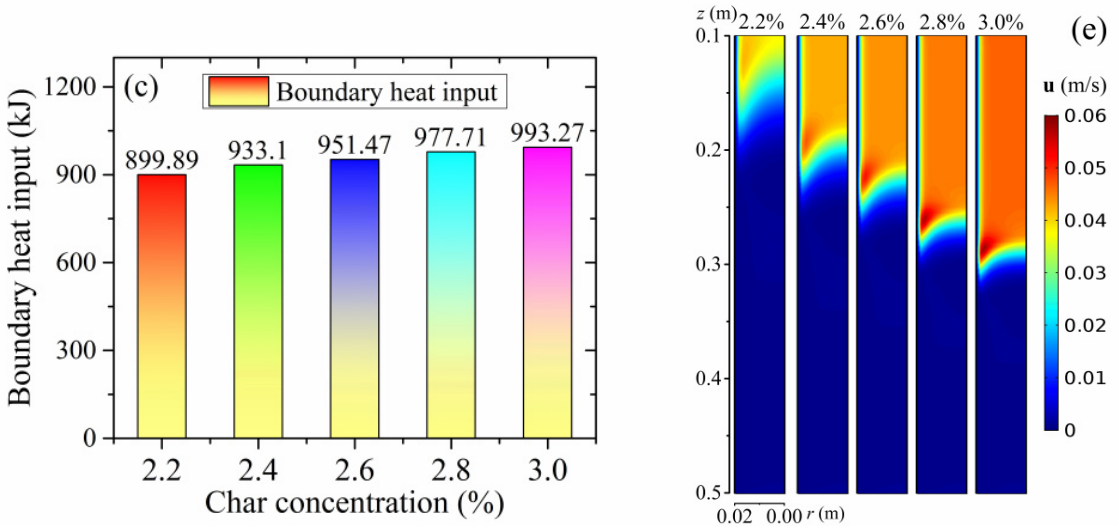

Fig. D.1. Effect of char concentration on (a) the boundary heat power, (b) the smoldering duration, (c) the boundary heat input into the pyrolysis chamber, and (d) the velocity at t=7200 s in the pyrolysis chamber.

D.3. Effect of Darcy air velocity

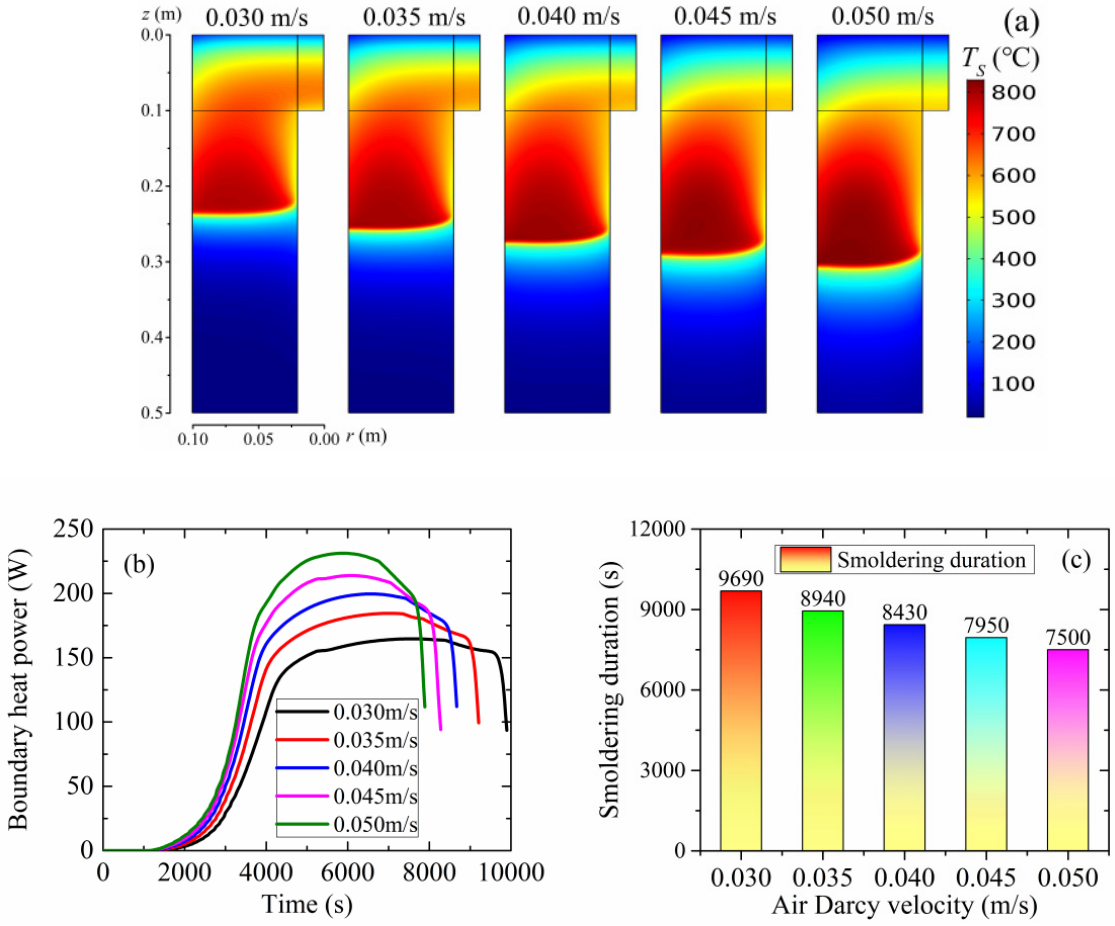

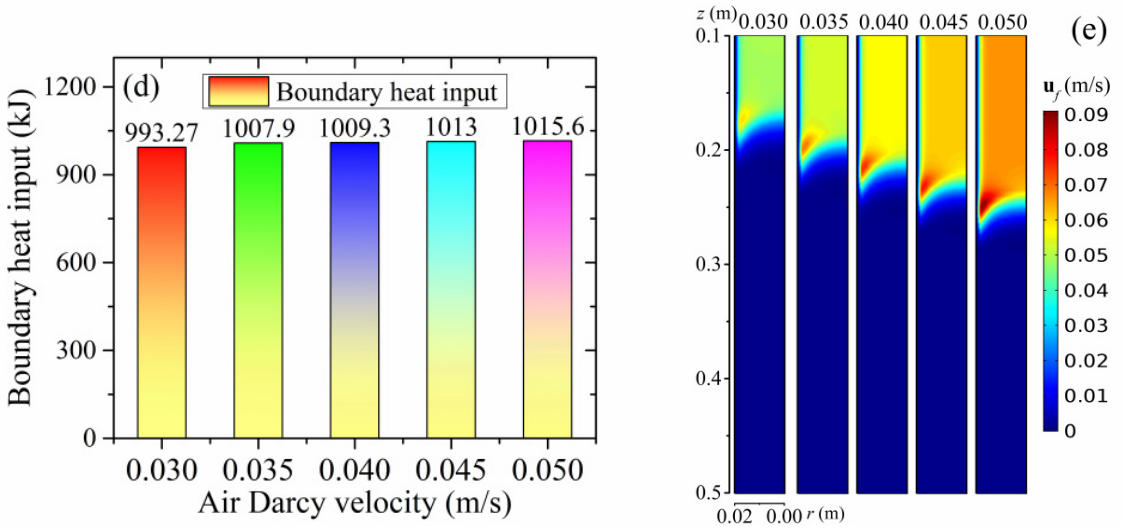

Fig. D.2. Effect of Darcy air velocity on (a) the T_S distribution at t=5400 s in the smoldering chamber, (b) the boundary heat power, (c) the smoldering duration, (d) the boundary heat input into the pyrolysis chamber, and (e) the velocity at t=5400 s in the pyrolysis chamber.

D.4. Effect of PW content

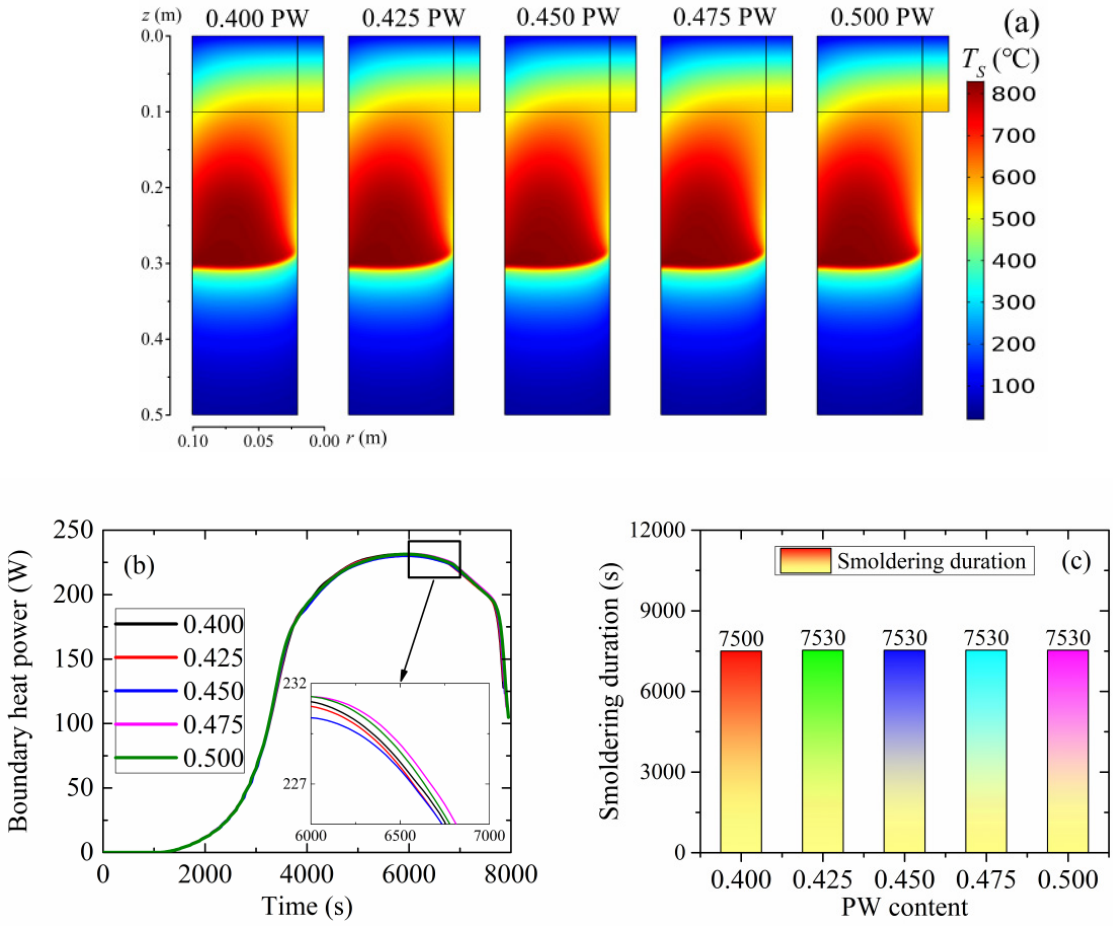

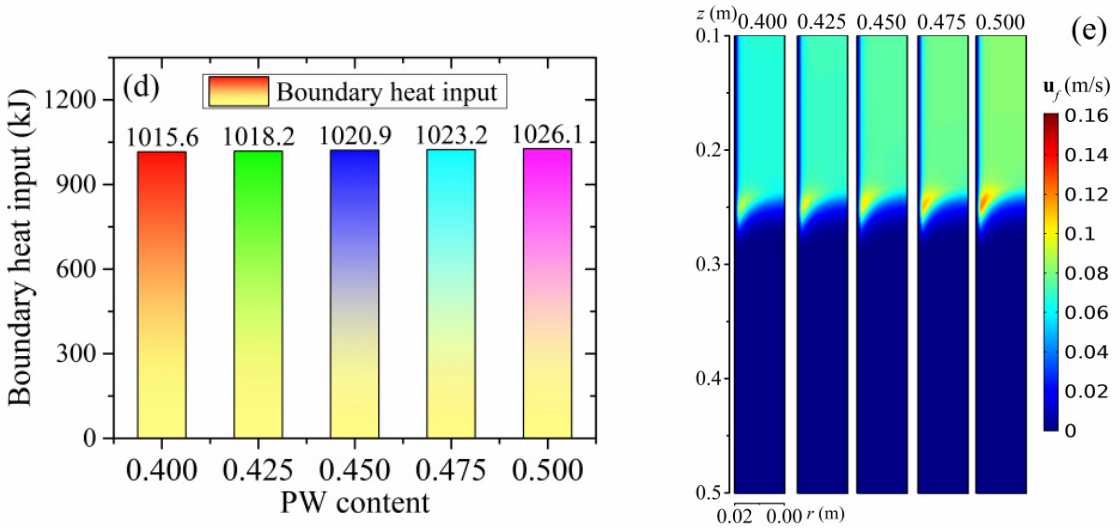

Fig. D.3. Effect of PW content on (a) the T_S distribution at t=5400 s in the smoldering chamber, (b) the boundary heat power, (c) the smoldering duration, (d) the boundary heat input into the pyrolysis chamber, and (e) the velocity at t=5400 s in the pyrolysis chamber.

D.5. Effect of pyrolysis chamber's radius

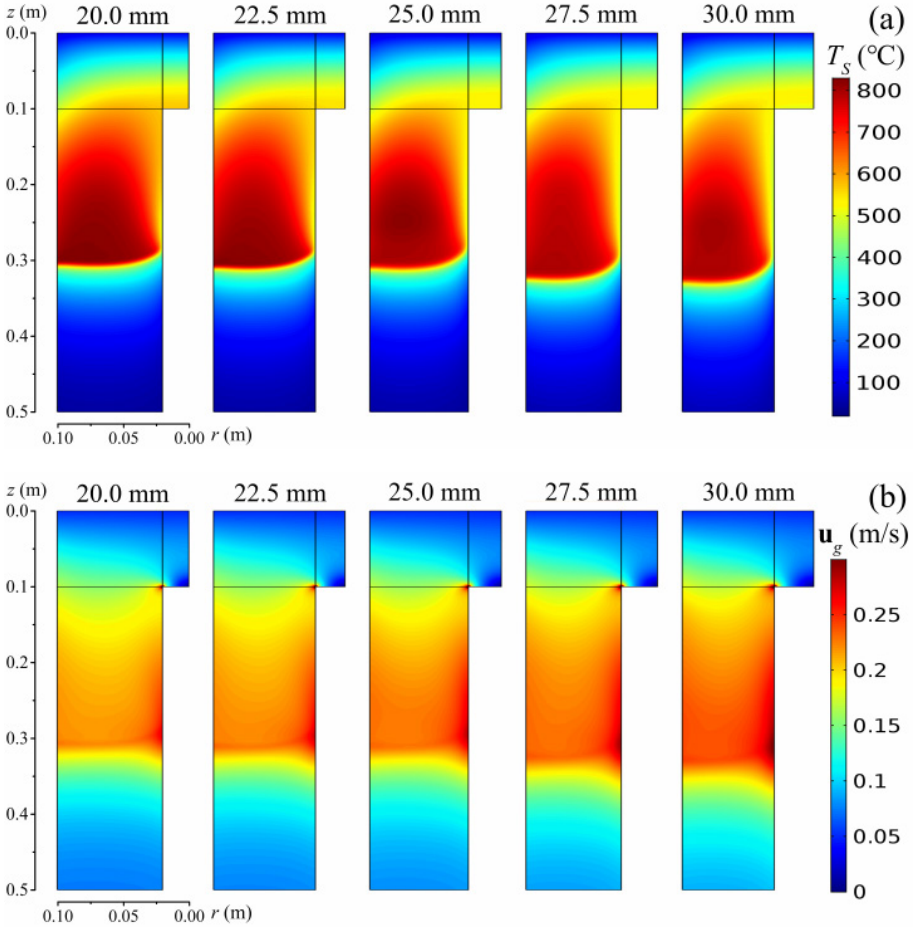

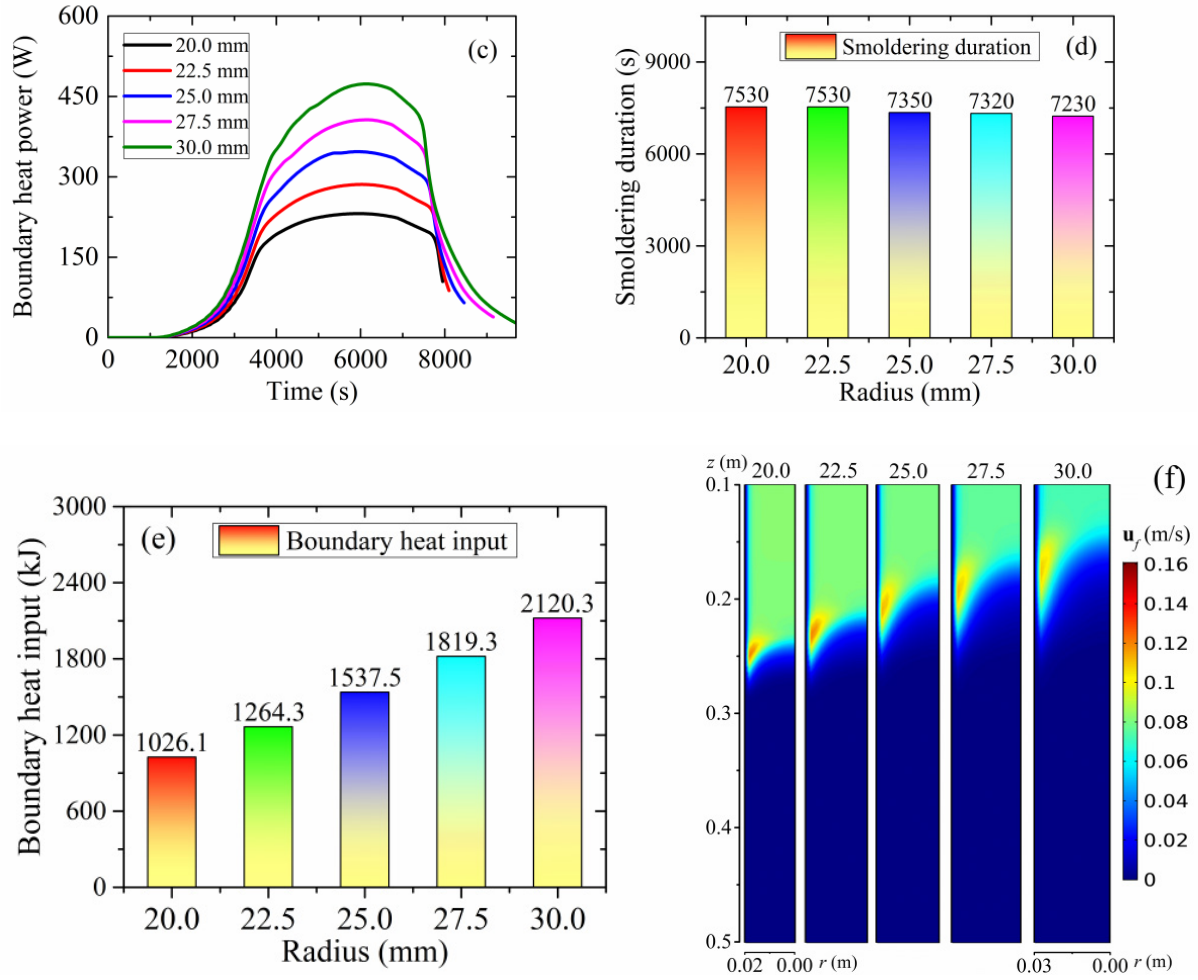

Fig. D.4. Effect of pyrolysis chamber's radius on (a) the T_S distribution at t=5400 s in the smoldering chamber, (b) the $\mathbf{u}_g$ distribution at t=5400 s in the smoldering chamber, (c) the boundary heat power, (d) the smoldering duration, (e) the boundary heat input into the pyrolysis chamber, and (f) the velocity at t=5400 s in the pyrolysis chamber.